HEAT TRANSFER AND FRICTION CHARACTERISTICS OF MULTIPLE V-RIB ROUGHENED SOLAR AIR HEATER

A THESIS

Submitted in partial fulfilment of the requirements for the award of the degree of

DOCTOR OF PHILOSOPHY

by

VISHAVJEET SINGH HANS

ALTERNATE HYDRO ENERGY CENTRE
INDIAN INSTITUTE OF TECHNOLOGY ROORKEE
ROORKEE - 247 667 (INDIA)

SEPTEMBER, 2009

INDIAN INSTITUTE OF TECHNOLOGY ROORKEE
ROORKEE

CANDIDATE'S DECLARATION

I hereby certify that the work which is being presented in the thesis entitled "**HEAT TRANSFER AND FRICTION CHARACTERISTICS OF MULTIPLE V-RIB ROUGHENED SOLAR AIR HEATER**" in partial fulfilment of the requirements for the award of the Degree of **DOCTOR OF PHILOSOPHY** and submitted in **Alternate Hydro Energy Centre** of the Indian Institute of Technology Roorkee, Roorkee, India is an authentic record of my own work carried out during the period from July 2006 to September 2009 under the supervision of **Dr. R.P.Saini,** Associate Professor, Alternate Hydro Energy Centre and **Dr. J.S. Saini,** Former Professor, Mechanical and Industrial Engineering Department, Indian Institute of Technology Roorkee, Roorkee, India.

The matter presented in this thesis has not been submitted by me for the award of any other degree of this or any other institute/university.

VHans

(VISHAVJEET SINGH HANS)

This is to certify that the above statement made by the candidate is correct to the best of our knowledge.

(J. S. Saini)
Supervisor

(R. P. Saini)
Supervisor

Date: 29-9-2009

The Ph.D. Viva-Voce examination of **Shri Vishavjeet Singh Hans**, Research Scholar, has been held on _____

Signature of Supervisors

Signature of External Examiner

ABSTRACT

Ever-increasing gap between demand and supply of energy, growing concerns about the environmental degradation associated with the use of fossil fuels and spiraling cost of energy have forced the scientific community to find and develop alternate sources of energy. There is a need to develop self sustaining units of energy based on local inexhaustible sources of energy which are available in abundance and do not adversely affect the environment. This requires emphasis on harnessing alternate sources of energy such as solar energy, wind energy, hydropower etc. that are reliable, plentiful and environment friendly. The eco-friendly nature and free availability of solar energy in abundance are two factors that have made solar energy the most favorable among other alternate sources of energy. Among the solar collector systems, solar air heater is the cheapest and most commonly used system to convert the incoming radiations into thermal energy, which is extracted by air flowing under the absorbing surface. However, very low heat transfer coefficient between the absorber plate and air results in very poor thermal performance of solar air heaters. In order to improve heat transfer in solar air heaters, artificial roughness, in the form of repeated ribs, is generally used to disturb and produce turbulence in the laminar sub layer region. The ribs are one of the most desirable methods on account of their ability to combine heat transfer coefficient enhancement with limited increase in frictional losses.

A number of experimental investigations involving different types, shapes and orientations of ribs such as transverse, inclined, v-shaped, wire mesh, chamfered, arc shaped and rib-groove arrangements have been reported in literature for performance improvement of solar air heaters. Rib height, pitch, inclination and v-shaping of ribs are some of the important parameters that affect the thermal performance of a solar air

heater having roughened absorber plate. Correlations for Nusselt number and friction factor have been developed.

Thermal performance improvement achieved by the use of artificial roughness in solar air heaters is accompanied by enhanced frictional losses resulting in an increase in pumping power requirement to overcome friction. It has been reported in literature that optimization of roughness geometry parameters of a roughened solar air heater has been carried out on the basis of thermal efficiency, effective efficiency, exergetic efficiency or thermohydraulic performance parameter.

An extensive review of the literature revealed that number of investigators had used v-ribs, having different orientations, to improve the performance of solar air heaters and observed that v-ribs outperform other rib configurations such as transverse and inclined ribs in terms of heat transfer enhancement. Other investigators who used v-ribs for heat transfer enhancement in turbines, nuclear reactors, electric and electronic equipments, also reported similar observations. However, in all the investigations involving v-ribs, a single v-rib has been used along the width of heat transferring surfaces of rectangular duct to improve heat transfer. In the present investigation, multiple v-ribs have been employed along the width of absorber plate of a solar air heater to create artificial roughness for heat transfer enhancement. This arrangement is expected to result in substantial enhancement of heat transfer coefficient due to formation of correspondingly large number of secondary flow cells.

In view of the above, the present work is proposed to include the following objectives:

i. Experimental investigation of effect of multiple v-ribs on heat transfer coefficient and friction factor in duct flow.

ii. Development of correlations for heat transfer coefficient and friction factor in terms of roughness geometry and operating parameters.

iii. Investigation of enhancement of thermal performance of solar air heater having absorber plate roughened with multiple v-ribs.

iv. Thermohydraulic optimization of roughened solar air heater to obtain optimal roughness geometry.

An experimental set up has been designed and fabricated in accordance with the guidelines suggested in ASHRAE standard 93-77 for testing of solar collectors using an open loop system. It consists of a rectangular duct having entry, test and exit sections, a centrifugal blower, two control valves, a calibrated orifice plate and other necessary instruments for measurement of temperature and pressure drop.

Extensive data has been collected on heat transfer and fluid flow characteristics of a rectangular duct roughened with multiple v-ribs. Experimental data pertaining to heat transfer coefficient and friction factor as function of geometrical parameters of roughness namely relative roughness height, e/D, relative roughness width, W/w (ratio of absorber plate width to width of a single v-rib), angle of attack, α and relative roughness pitch, P/e has been recorded. The range of roughness geometry and flow parameters considered in this experimental investigation is given below;

Range of roughness and operating parameters

S. No.	Roughness Parameters	Range
1.	Reynolds number, Re	2000 – 20000 (10 values)
2.	Relative roughness height, e/D	0.019 – 0.043 (4 values)
3.	Relative roughness Width, W/w	1 – 10 (8 values)
4.	Angle of attack, α	30° – 75° (4 values)
5.	Relative roughness pitch, P/e	6 – 12 (4 values)

A total of thirty-eight multiple v-rib roughened absorber plates were tested in this experimental work covering different roughness geometry parameters.

It has been found that Nusselt number and friction factor are strong functions of roughness geometry and flow parameters. Nusselt number increases with an increase in relative roughness width and attains a maximum value corresponding to relative roughness width value of 6 in the range of parameters considered. With further increase in the value of relative roughness width, Nusselt number is found to decrease. However, it has been observed that friction factor increases with increase in relative roughness width ratio and attains a maximum value corresponding to relative roughness width value of 10. Nusselt number and friction factor increase with an increase in angle of attack and attain maximum values corresponding to angle of attack value of 60^{o}. Nusselt number and friction factor attain maximum values corresponding to relative roughness pitch, P/e value of 8 and on either side of this value, decrease in Nusselt number and friction factor has been observed. Nusselt number and friction factor increase monotonically with an increase in relative roughness height, e/D.

The maximum uncertainties in the values of Reynolds number, Nusselt number and friction factor computed are ± 3 %, ± 6.31% and ± 5.97 % respectively.

Experimental data on heat transfer and friction factor has been utilized to develop correlations for Nusselt number and friction factor in terms of relative roughness height, e/D, relative roughness width, W/w, angle of attack, α, relative roughness pitch, P/e and Reynolds number, Re. The correlations are given below;

$$Nu = 3.35 \times 10^{-5}\ Re^{0.92} \left(\frac{e}{D}\right)^{0.77} \left(\frac{W}{w}\right)^{0.43} \left(\frac{\alpha}{90}\right)^{-0.49} \exp\left(-0.1177\,(\ln\,(W/w))^{2}\right)$$
$$\times \exp\left(-0.61(\ln\,(\alpha/90))^{2}\right) \left(\frac{P}{e}\right)^{8.54} \exp\left(-2.0407\,(\ln\,(P/e))^{2}\right)$$

$$f = 4.47 x 10^{-4} \mathrm{Re}^{-0.318} \left(\frac{e}{D}\right)^{0.73} \left(\frac{W}{w}\right)^{0.22} \left(\frac{\alpha}{90}\right)^{-0.39} \exp\left(-0.52 (ln(\alpha / 90))^2\right)$$
$$\times \left(\frac{P}{e}\right)^{8.9} \exp\left(-2.133 (ln(P / e))^2\right)$$

A comparison of experimental values of Nusselt number and friction factor and those predicted by these correlations shows that there is a good agreement between the experimental and predicted values with an average absolute deviation of 4.45% for Nusselt number and 4% for friction factor values. Hence, the designer can use the correlations with reasonably good accuracy.

A computer program has been developed to predict the thermal performance of roughened collector in terms of plate efficiency factor, F', heat removal factor, F_o, and thermal efficiency, η_{Th}, on the basis of these correlations developed for Nusselt number and friction factor. The effect of roughness geometry and operating parameters on thermal performance has been investigated and thermal performance of roughened and smooth collectors was compared in order to determine the enhancement in thermal performance on account of the use of multiple v-rib type of roughness geometry.

It has been observed that thermal performance of roughened solar air heaters is a strong function of roughness geometry parameters. Enhancement in thermal efficiency has been represented in terms of enhancement factor which is defined as the ratio of thermal efficiency of roughened collector to that of conventional smooth collector for the same operating conditions. The value of enhancement factor has been found to vary in the range of 1.13 to 2.45.

As pointed out earlier, the use of artificial roughness in solar air heaters improves the thermal performance considerably; however, this improvement in thermal performance is accompanied by increased frictional losses resulting in an

increase in pumping power requirement to overcome friction. It, therefore, becomes imperative to determine the values of roughness geometry parameters that result in maximum enhancement of heat transfer with minimum increase in friction. In order to determine the values of roughness geometry and flow parameters that yield the optimum performance, thermohydraulic performance of multiple v-rib roughened solar air heater has been evaluated and the following three criteria have been used for optimization of roughness geometry parameters;

(i) Thermal efficiency

(ii) Effective efficiency

(iii) Exergetic efficiency

For given values of operating parameters (temperature rise parameter, $\Delta T/I$ and insolation, I) optimizing parameter values were computed for all possible combinations of roughness geometry parameters. Comparison of the computed values of the optimizing parameter yielded a set of optimal values of roughness geometry parameters.

It has been observed that on the basis of thermal efficiency criterion, a single set of roughness geometry parameters yielded optimum performance for the entire range of operating parameters and is given as;

Relative roughness height, e/D	: 0.043
Relative roughness width, W/w	: 6.0
Angle of attack, α	: 60^{o}
Relative roughness pitch, P/e	: 8.0

No single set of roughness geometry parameters yielded optimum performance on the basis of effective efficiency and exergetic efficiency criteria for the entire range of the operating parameters. The optimum values of roughness geometry parameters depend on the operating parameters (temperature rise parameter and insolation). For instance, the optimum values obtained on the basis of effective efficiency criterion are given below;

Optimum values of roughness parameters on the basis of effective efficiency

Roughness parameter	**Temperature rise parameter range ($K\text{-}m^2/W$)**	**Value of Roughness parameter**
Relative roughness height, e/D	$\Delta T/I < 0.00375$	0.019
	$0.00375 < \Delta T/I < 0.006$	Function of insolation and temperature rise parameter
	$\Delta T/I > 0.006$	0.043
Relative roughness width, W/w	$\Delta T/I < 0.003$	1.0
	$0.003 < \Delta T/I < 0.01375$	Function of insolation and temperature rise parameter
	$\Delta T/I > 0.01375$	6.0
Angle of attack , α	$\Delta T/I < 0.00325$	30^0
	$0.00325 < \Delta T/I < 0.00675$	Function of insolation and temperature rise parameter
	$\Delta T/I > 0.00675$	60^o
Relative roughness pitch, P/e	$\Delta T/I < 0.00575$	12.0
	$0.00575 < \Delta T/I < 0.008$	Function of insolation and temperature rise parameter
	$\Delta T/I > 0.008$	8.0

For given values of temperature rise parameter and insolation, a set of roughness geometry parameters can be obtained from the design plots prepared for each roughness geometry parameter on the basis of effective and exergetic efficiencies. A design procedure has also been proposed to determine the optimum values of roughness geometry parameters for a multiple v-rib roughened solar air heater for given values of temperature rise and the insolation.

Summarizing on the basis of experimental investigation on a solar air heater roughened with multiple v-ribs, it can be stated that considerable enhancement in thermal performance has been obtained in comparison with a smooth conventional solar air heater. Empirical correlations have been developed for Nusselt number and friction factor in terms of roughness geometry and operating parameters. Optimum values of roughness parameters have been determined based on the criteria of thermal efficiency, effective efficiency and exergetic efficiency. Design plots have been prepared which can be utilized to obtain a set of optimum values of roughness geometry parameters that will result in the best thermohydraulic performance for given operating conditions. A design procedure has been proposed to arrive at the optimum roughness geometry for given set of operating parameters of a multiple v-rib roughened solar air heater.

ACKNOWLEDGEMENTS

To pry into Nature's secrets is a stupendous task. Sometimes Nature reveals itself easily and at other times plays hide and seek. The Researcher consistently pursues his avowed objectives with philosophic stoicism. In my humble pursuit, I got unstinted support from an array of people. I consider myself lucky to have the able and inspiring guidance of Dr. R.P. Saini, Associate Professor, Alternate Hydro Energy Centre, Indian Institute of Technology, Roorkee and Dr. J.S. Saini, Former Professor, Mechanical and Industrial Engineering Department, Indian Institute of Technology, Roorkee, which rendered my onerous task so pleasure-able. Their art of passing difficult instructions with easy grace and facile ease made me comfortable. Dr. J.S. Saini's patronage and Dr. R.P. Saini's deft, humane touches inspired me whenever I stumbled. I feel over-whelmed with a deep sense of gratitude to my revered Gurus. Words just fail to express my feelings, though I will ever remain indebted to them and cherish their support as a valuable asset in my academic career.

Author owes a deep sense of gratitude to Dr. Arun Kumar, Head, Alternate Hydro Energy Centre, Indian Institute of Technology, Roorkee for providing vast facilities and all possible help needed in the completion of my work.

I feel grateful to the Director, Indian institute of Technology, Roorkee, the Faculty and all the people, at various levels, who work tirelessly to make the ambience at the Institute so conducive for research work. The Staff at the Laboratories, Library and the Administrative Office always showed concern for work.

My special thanks are due to the Staff of Laboratories, Alternate Hydro Energy Centre, Indian Institute of Technology, Roorkee, who took great pains in the fabrication of experimental set-up, which is verily the backbone of my work. In this regard, the efforts of Shri Avtar Singh who was ever eager to go an extra mile,

deserves a special mention. Author is thankful to Shri Ram Baran Chauhan for extending help in type setting of thesis work.

My thanks are also due to the Authorities of Punjab, Agricultural University, Ludhiana, for their willing cooperation in sponsoring the author to pursue Ph. D. programme.

My sincere thanks are due to the families of my supervisors, Dr. R. P. Saini and Dr. J. S. Saini, who have rendered immense support to them so that they can devote enough of their time to research scholars.

Author is thankful to Prof. Vinod Kumar Coordinator, QIP Centre, IIT Roorkee for his valuable suggestions and encouragements. I express my thanks to the staff of QIP Centre for their co-operation to carry out the official matters during my stay at IIT Roorkee. The financial support provided by MHRD, Govt. of India through AICTE is sincerely and honestly acknowledged.

My sincere thanks to Shri Rathod Praveen Kumar, Shri Rajbir Singh Bhatti, Shri Amarsingh Kanase Patil and Shri Derminder Singh for their support, encouragement and academic inputs during the research work. I will fail in my duty if I do not duly thank Shri Kanwardeep Singh, and Shri Sharad Kumar Yeri for their help in academic matters. I must also thank Shri Sidharath Jain, Shri Anurag Kumar, Shri Harmeet Singh, Mrs. Mamata Kumari Padhy, Shri Ajai Gupta and Shri Aneesh Sachdeva for their moral support to lighten the usual burdens.

Author is greatly indebted to his parents, brother and mother-in-law for their blessings, support and encouragement.

Author is thankful to his wife for shouldering all family responsibilities and all her support during this research work. Cheerfulness and tolerance capacity of my son, who missed many precious moments of fatherly love and care, is really admirable.

My family, my kith and kin made sacrifices in their own way, I rededicate myself to their welfare and service.

It is not possible to name and mention all those people who extended valuable help in my work, it is beyond the scope of this piece. Nevertheless, their assistance will ever remain etched in my memory.

Above all author bestows himself to Almighty God and falls short of words to express thanks for blessings with an opportunity to carry out the present work.

VISHAVJEET SINGH HANS

CONTENT

LIST OF FIGURES

LIST OF TABLES

NOMENCLATURE

Symbol	Title	Unit
A_p	Area of absorber plate	m^2
A_1	Cross section area of pipe	m^2
A_2	Cross section area of orifice	m^2
C_d	Coefficient of discharge for orifice meter	
C_p	Specific heat of air at constant pressure	J/kg K
D_o	Constant	
D	Equivalent diameter of duct	m
D_1	Diameter of pipe	m
D_2	Diameter of orifice-meter	m
e	Roughness height	m
e^+	Roughness Reynolds number (=Re (e/D) $(f/2)^{0.5}$)	
e/D	Relative roughness height	
F'	Plate efficiency factor	
F''	Flow factor	
F_o	Heat removal factor referred to out let temperature	
F_R	Heat removal factor	
f	Friction factor	
f_s	Friction factor of smooth duct	
G	Global irradiation	W/m^2
H	Depth of duct	m

h	Heat transfer coefficient	W/m^2K
h_e	Effective heat transfer coefficient	W/m^2K
h_r	Radiative heat transfer coefficient	W/m^2K
h_w	Wind convective heat transfer coefficient	W/m^2K
I	Intensity of solar radiation (insolation)	W/m^2
k	Thermal conductivity of air	W/m-K
k_i	Thermal conductivity of insulation	W/m-K
L	Length of absorber plate	m
L_g	Air gap between absorber plate and glass cover	m
ln	Natural log	
m	Mass flow rate	kg/s
N	Number of glass covers	
Nu	Nusselt number	
P/e	Relative roughness pitch	
Pr	Prandtl number	
Re	Reynolds number	
St	Stanton number	
T_a	Ambient temperature	K
T_o	Out let air temperature	K
T_p	Average plate temperature	K
T_s	Sky temperature	K
T_{sun}	Sun temperature (5762 K)	K

ΔT	Temperature rise	K
$\Delta T/I$	Temperature rise parameter	$K\text{-}m^2/W$
t_i	Thickness of insulation	m
t_g	Thickness of glass cover	m
t_e	Thickness of collector edge	m
U_b	Back heat loss coefficient	W/m^2K
U_e	Edge loss coefficient	W/m^2K
U_l	Overall heat loss coefficient	W/m^2K
u^+	Dimension less velocity	
V_w	Wind velocity	m/s
V	Velocity of air	m/s
W	Width of duct	m
w	Width of single v-rib	m
W/w	Relative roughness width	
y	Distance from wall	m
α	Rib angle of attack	degree
β	Ratio of orifice diameter to pipe diameter	
θ	Angle of inclination of the collector	degree
δ	Thickness of boundary layer	m
ε_g	Emissivity of glass cover	
ε_p	Emissivity of absorber plate	
ε_s	Emissivity of selective surface	

η_{Th}	Thermal efficiency of solar collectors and power plants	
η_{eff}	Effective efficiency	
η_{exg}	Exergetic efficiency	
η_f	Efficiency of the fan	
η_m	Efficiency of the electric motor	
η_{Tr}	Efficiency of the electrical transmission from power plant	
η_c	Carnot efficiency	
θ	Tilt angle of manometer	degree
ν	Kinematic viscosity of fluid	m^2/s
ρ	Density of fluid	kg/m^3
σ	Stefan-Boltzmann constant	W/m^2K^4
τ	Transmissivity of glass cover	
μ	Dynamic viscosity of fluid	$N\ s\ /\ m^2$
$(\tau\ \alpha)$	Transmittance-absorptance product for absorber-cover combination	

CHAPTER-1

INTRODUCTION AND LITERATURE REVIEW

1.1 INTRODUCTION

Energy is the core of all existence, drives the wheels of modern society and plays a crucial role in the economic development of a nation. Global energy demand and consumption are increasing on account of population growth, economic as well as technological development. About 86% of the energy requirements of the world are derived from fossil fuels with oil and natural gas contributing 58%, coal 28%, nuclear, hydro and other resources providing the balance 14% of the energy requirements. According to Sukhatme and Nayak [1] rate of production of conventional sources of energy such as fossil fuels is on decline and these resources are depleting fast. Hence, the ever-increasing gap between demand and supply of energy, growing concerns about the environmental degradation associated with the use of fossil fuels and spiraling cost of energy have forced the scientific community to find and develop alternate sources of energy.

There is a need to develop self sustaining units of energy based on local inexhaustible sources of energy which are available in abundance and do not adversely affect the environment. This requires emphasis on harnessing alternate sources of energy such as solar energy, wind energy, hydro-power etc that are reliable, plentiful and environment friendly.

The eco-friendly nature and free availability of solar energy in abundance are the two factors that have made solar energy favorite among other alternate sources of energy. Solar energy has a potential to fulfill the energy requirements of all human made systems provided technologies are developed to tap the potential of solar

energy. Considerable efforts are being made to develop the technologies to tap the great potential of solar energy.

1.2 SOLAR ENERGY

The sun is the ultimate source of all the energy available on the earth including solar energy in the form of solar radiations. The sun is a sphere of intensely hot gaseous matter having a diameter of 1.39×10^6 km and is about 1.5×10^8 km from the earth. The surface of the sun has an effective temperature of approximately 5762 K. The temperature in the central interior regions is estimated to vary from 8×10^6 to 40×10^6 K as given by Duffie and Beckman [2]. The sun continuously generates heat by thermo nuclear fusion reactions that convert hydrogen atoms into helium atoms. The sun radiates 3.8×10^{23} kW of energy into space and the earth intercepts only 1.7×10^{14} kW which is about 27000 times the energy requirements of all human made systems in the world.

The solar radiations that reach a receiving surface on the earth consist of three components:

- Beam or direct radiation that reaches the earth surface without change in direction
- Diffused radiation which reaches the earth surface after scattering and re-radiation of solar energy through dust particles, water vapors and air molecules
- Reflected radiations which are received as a result of reflections from nearby surfaces such as buildings, fences, trees and ground

1.3 APPLICATIONS OF SOLAR ENERGY

Solar energy can be used to supply energy demand in the form of thermal as well as power. Some of the important applications [1, 3-13] of solar energy are listed below:

- Solar water heating
- Solar space heating and cooling
- Solar cooking
- Solar crop drying
- Solar distillation
- Solar refrigeration
- Solar power generation
- Solar furnace

In order to make the solar energy utilization economically viable, its efficient collection and storage are essential. The most important component of solar energy utilization system is the solar collector. A brief review of literature in area of solar energy collection is presented below.

1.4 SOLAR COLLECTORS

A solar collector is the most commonly used device for collection of solar energy. It absorbs incoming solar radiant energy, converts it into thermal energy at the absorbing surface and then transfers this energy to a fluid flowing through the collector. Several designs of solar collectors have been reported in literature. However, these collectors may be classified into two categories:

i) Focusing solar collectors

ii) Flat plate solar collectors

1.4.1 Focusing Solar Collectors

A focusing collector is a special form of flat plate solar collector modified by introducing a reflecting surface between the solar radiations and the absorber. Such collectors are generally used to produce high temperatures required for power generation and industrial applications. Concentration of solar radiations is achieved by using a reflecting optical system that directs the solar radiations to an absorber having smaller area surrounded by a transparent cover. Mills et al. [14] and Mills and Giutronich [15] have shown the application of concentrating collector in electric power generation, solar furnaces and some industries where high temperature is required.

From optical point of view, a parabolic reflector gives high enough concentration, which is made possible by tracking the sun throughout the day. Concentration ratio may vary from as low as 1.5 to as high as 10,000 and medium to very high temperature can be achieved. Inability to use diffused radiations, deterioration of reflecting surfaces due to prolonged exposure and complex mounting as well as tracking arrangements are some of the limitations of such collectors.

1.4.2 Flat Plate Collectors

A flat plate collector is a device that is capable of collecting both the beam and diffused solar radiations. These collectors transform solar radiations into low grade thermal energy and temperature up to about 100 plus ambient may be achieved. Low initial cost, simple construction, ease in maintenance and absence of tracking system are some of the advantages associated with these types of collectors.

1.4.3 General Description of Flat Plate Collectors

A flat plate collector basically consists of a flat surface with high absorptivity for solar radiation called absorber plate. The plate is typically metallic, painted black

and facing the sun to intercept solar radiations. It converts the solar radiations intercepted by it into thermal energy and simultaneously transfers this energy to the fluid circulating through it. The top of the collector is covered with transparent covers, generally glass to allow transmission of incident solar radiation and opaque to the infrared radiation emitted by the absorber plate. Thus, the covers reduce convection and radiation losses to the surroundings. Both the bottom and side portions of the collector are properly insulated to prevent thermal losses. Flat plate collectors are usually fixed permanently in position and require no tracking system to face the sun. The flat plate collector, generally, heats either a liquid or a gas.

A liquid heating collector comprises of a glass covered metal box as shown in Fig.1.1. An array of tubes is attached to the absorber plate of the collector and insulation is provided on the back and sides of the collector to prevent thermal losses. The absorber plate, whose sun-facing surface is blackened, absorbs incident solar radiation and transfers heat to liquid flowing in the tubes. Liquid from a storage tank passes through these tubes, absorbs heat from the absorber plate and then returns back to the storage tank.

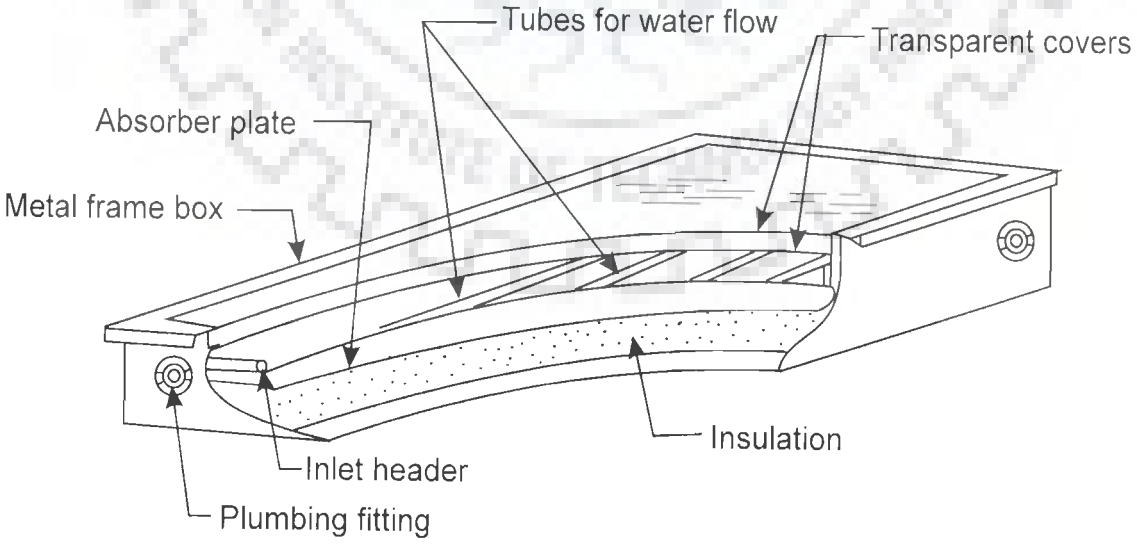

Fig.1.1 Flat plate liquid heating solar collector [16]

An air or gas heating collector is generally known as solar air heater and is shown in Fig.1.2. A conventional solar air heater generally consists of an absorber plate with another parallel plate below it forming a passage for air with a high aspect ratio i.e. ratio of width to depth of the flow cross section.

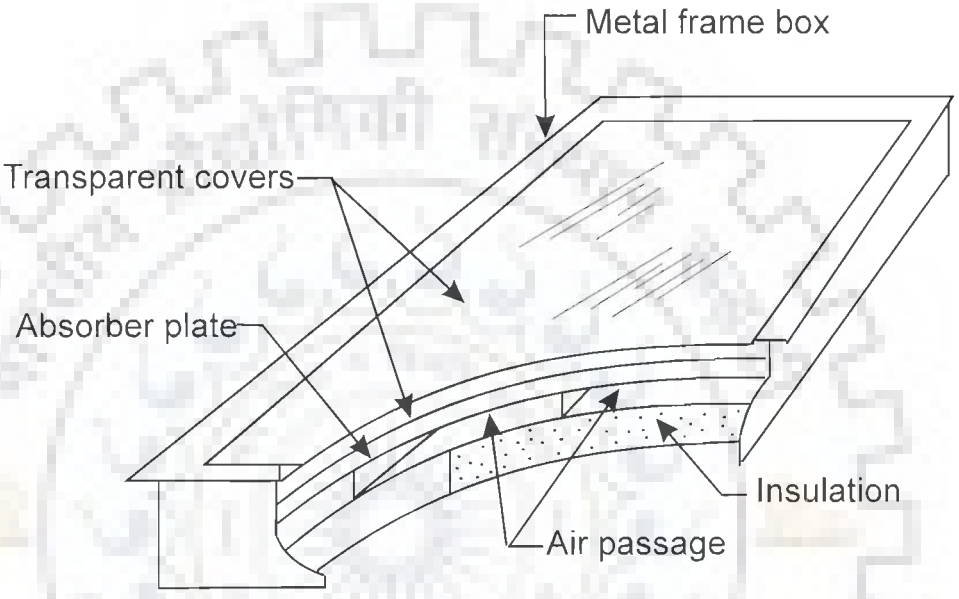

Fig.1.2 Flat plate air heating solar collector [16]

The absorber plate is covered with one or more transparent glass covers and a solid insulation is provided on its back and side walls. The solar radiations pass through the transparent covers and are intercepted by the blackened absorber plate. The energy is then transferred from the absorber plate to air flowing through it. In general, air flows under the absorber plate, however in some designs, air flows over the absorber plate also. The thermal efficiency of solar air heater i.e. ratio of heat transferred to the fluid to the incident solar radiations tends to be significantly lower than that of a solar water heater. This is primarily because of low convective heat transfer coefficient between the absorber plate and the air which results in higher plate

temperature and thus greater thermal losses to the surroundings. A solar air heater has applications in drying agricultural products such as seeds, fruits and vegetables as a low-temperature energy source and for heating buildings to save energy during winters. The use of air as a heat transferring medium instead of water in this type of collector reduces the risks of corrosion, freezing and helps in reducing weight as well as cost of the collector. However, low density and specific heat of air requires high volume flow rate that results in high frictional losses.

1.5 COLLECTOR PERFORMANCE

Thermal performance analysis of solar collectors using air as heat transport medium is essential for providing the basic data required for designing systems incorporating such collectors. A schematic of the collector and thermal network are shown in Fig.1.3 for the most common design of conventional solar air heater. For ensuring generality, two main classes of parameters, as given below, have to be taken into account.

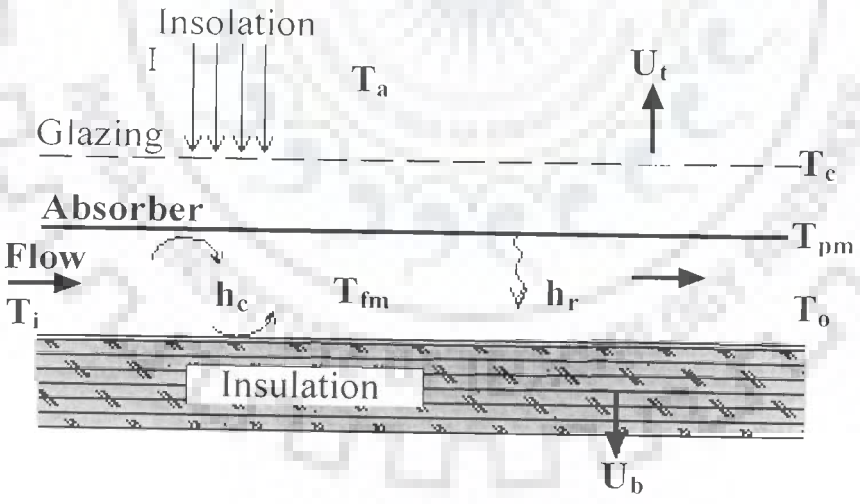

Fig.1.3 Thermal network of a conventional solar air heater [16]

- Environmental parameters: Ambient air temperature, incident solar radiation intensity and wind velocity.
- Operating parameters: Inlet and outlet air temperature and the mass flow rate.

Several investigators [2, 17 and 18] have carried out the analysis of thermal performance of flat plate solar air heaters. The performance of solar air heater is described by an energy balance that indicates the distribution of incident solar energy into the useful thermal gain (Q_u) and various losses (Q_t & Q_b). Whiller [19] analyzed the performance of flat plate solar air heater. The energy balance of the collector can be written as;

$$A_p [IR (\tau\alpha)_e] = Q_u + Q_l \quad (1.1)$$

where,

I : Intensity of insolation incident on horizontal surface, W/m^2

R : A factor to convert radiation on horizontal surface to that on the collector plane

A_p : Collector area, m^2

$(\tau\alpha)_e$: Equivalent transmissivity-absorptivity product of the system

Q_u : Rate of useful energy, W

Q_l : Rate of energy losses ($Q_t + Q_b + Qs$), W

Q_t : Top loss, W

Q_b : Bottom loss, W

Q_s : Side loss, W

The useful energy gain Q_u, can be written in terms of known inlet temperature T_i and other system and operating parameters as,

$$Q_u = A_p F_R[S - U_l (T_i - T_a)] \quad (1.2)$$

where,

S : [= IR $(\tau\alpha)_e$], radiation absorbed by absorber plate, W/m^2

$$F_R = \frac{\dot{m}Cp}{A_p U_l}\left[1 - \exp\left\{-\frac{F'U_l A_p}{\dot{m}Cp}\right\}\right] \qquad (1.3)$$

F_R is termed as collector heat removal factor, which measures the thermal resistance encountered by absorbed solar radiation in reaching the flowing air. It can be represented as ratio of actual useful heat gain to the gain which would occur if the collector absorber plate temperature were maintained at T_i everywhere. As such its value ranges between 0 and 1.

U_l is overall loss coefficient W/m^2K

T_i is inlet fluid temperature, K

T_a is ambient temperature, K

F' is termed as collector efficiency factor and is defined as ratio of thermal resistance between the absorber plate and ambient air to thermal resistance between the fluid and ambient air and can be expressed as:

$$F' = \frac{1}{\left(1 + \frac{U_l}{h_e}\right)} \qquad (1.4)$$

where, h_e is an effective heat transfer coefficient between the absorber plate and air stream,

$$h_e = h\left[1 + \frac{h_r}{h_r + h}\right]$$

h : Convective heat transfer coefficient between absorber plate and air stream

h_r : Radiative heat transfer coefficient between absorber plate and bottom plate

An efficiency equation developed by Whiller–Bliss and reported by Duffie and Beckman [2], where thermal behavior of the collector is expressed as:

$$\eta = F_R\left[(\tau\alpha)_e - U_l\frac{(T_i - T_a)}{I}\right] \tag{1.5}$$

A parameter F'', known as flow factor is written as ratio of heat removal factor, F_R to plate efficiency factor, F' and can be expressed as:

$$F'' = \frac{\dot{m}Cp}{A_p U_l F'}\left[1\text{-}\exp\left\{-\frac{F'U_l A_p}{\dot{m}Cp}\right\}\right] \tag{1.6}$$

Knowing the values of factors F_R, F' and F'', mean fluid and mean plate temperatures can be calculated from the following equations:

$$T_{fm} = T_i + \frac{Q_u}{A_p U_l F_R}(1 - F'') \tag{1.7}$$

$$T_{pm} = T_i + \frac{Q_u}{A_p U_l F_R}(1 - F_R) \tag{1.8}$$

These temperatures may be used to obtain thermal performance of the collector.

Biondi et al. [17] generalized the analysis of performance for conventional solar air heater using two useful parameters namely air mass flow rate per unit collector area and geometric coefficient of the collector, which make collector performance invariant, under the same conditions of design, material choice and ambient values. When collector works as an open cycle, drawing external air, a configuration often utilized for air heaters only, inlet temperatures coincides with the ambient temperature, $T_i = T_a$. Under this working condition, Eq. (1.5) cannot be very useful since the equation of efficiency reduces to: $\eta = F_R(\tau\alpha)_e$. Indeed, this expression

does not allow the real operative temperatures to be shown and it, therefore, becomes less efficacious. Thus, new equation was proposed as:

$$\eta = F_0 [(\tau\alpha)_e - U_l (T_o - T_a)/I] \quad (1.9)$$

where F_o is the heat removal factor referred to outlet temperature and can be expressed as:

$$F_o = G\ Cp\ [exp\ ((U_l F'/GC_p) - 1]/U_l \quad (1.10)$$

where, G is mass flow rate per unit area of the collector (kg/ hr-m^2).

Furthermore, performance can be expressed by another equation containing the temperature gain produced by the collector:

$$\eta = G\ Cp\ (T_o - T_i)/I \quad (1.11)$$

Reddy and Gupta [18] presented a graphical method of determining performance for conventional solar air heater under different operating conditions, using the design data for a system of known characteristics i.e. thermal efficiency (η) versus temperature rise parameter, ($\Delta T_m/I$) curves for different flow rates, with or without air recycling. For a given flow rate, instantaneous collector efficiency can be expressed as:

$$\eta = F' [(\tau\alpha)_e - U_l (\Delta T_m/I)] \quad (1.12)$$

where, ΔT_m is temperature difference between mean temperature of air in collector and temperature of ambient air.

From known data, efficiency, η, is plotted as a function of temperature rise parameter, $\Delta T_m/I$. Given such curves, one can use them to ascertain the collector

efficiency if inlet and outlet temperatures, radiation intensity and flow rate per unit area are given.

For air recycling, Eq. (1.12) can be rewritten as :

$$\eta = F' [(\tau\alpha)_e U_l \{(T_o - T_a) + (T_i - T_a)\}/2I)] \quad (1.13)$$

Eq. (1. 11) can be rewritten as:

$$\eta = 2\ G\ Cp\ \{(T_o - T_a) - (T_i - T_a)\}/\ (2\ I \times 3600) \quad (1.14)$$

Fig.1.4 shows a typical series of efficiency curves for different mass velocities. The abscissa is the sum of the two variables $(T_o - T_a)/2I$ and $(T_i - T_a)/\ 2I$. Using the difference of these two variables, another series of curves can be drawn as shown in Fig.1.5.

Figs. 1.4 and 1.5 are superimposed as in Fig.1.6. For cases of practical interest wherein air inlet and outlet temperatures are specified, mass flow rate and efficiency of the collector can be determined iteratively from Fig.1.6.

When the air heater operates in an open cycle, then $T_i = T_a$ and Eqs.(1.13) and (1.14) reduce to:

$$\eta = F' [\tau\alpha - U_l (T_o - T_a)/\ 2I)] \ \& \quad (1.15)$$

$$\eta = 2GCp\ (T_o - T_a)/\ (2I \times 3600). \quad (1.16)$$

Since the abscissa term $(T_o - T_a)/2I$ is same, only one set of curves is needed and there being only one performance curve, no iteration is required. The unknown parameter can be directly determined from Fig.1.7.

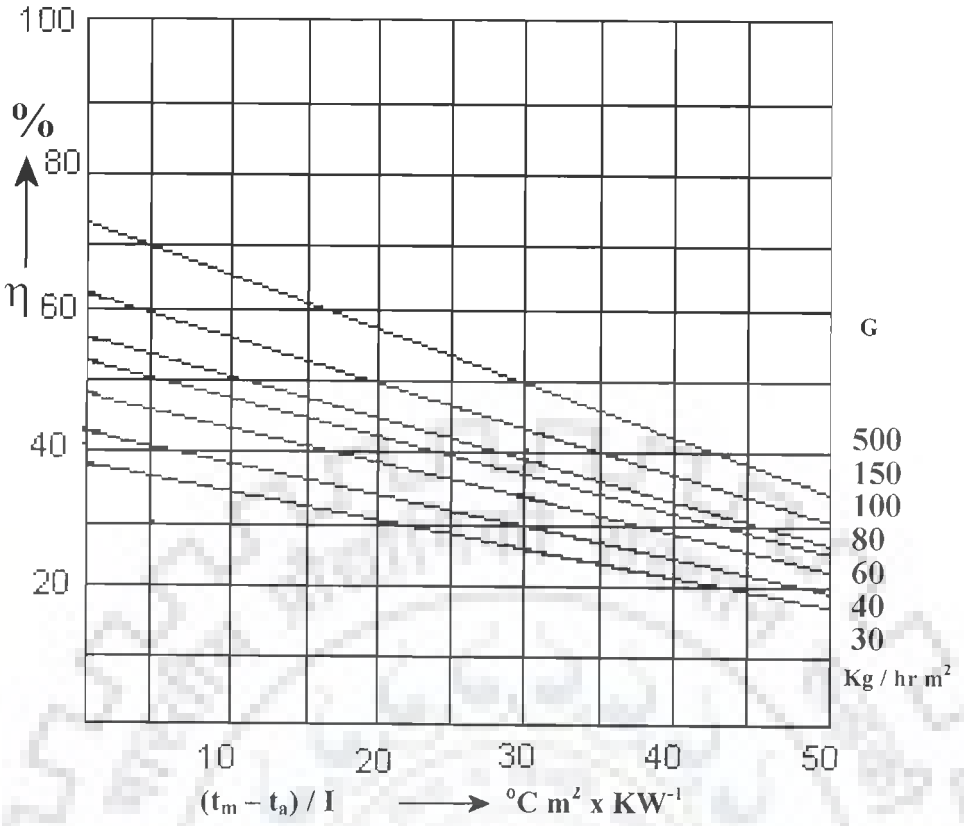

Fig.1.4 Air heater performance curves [18]

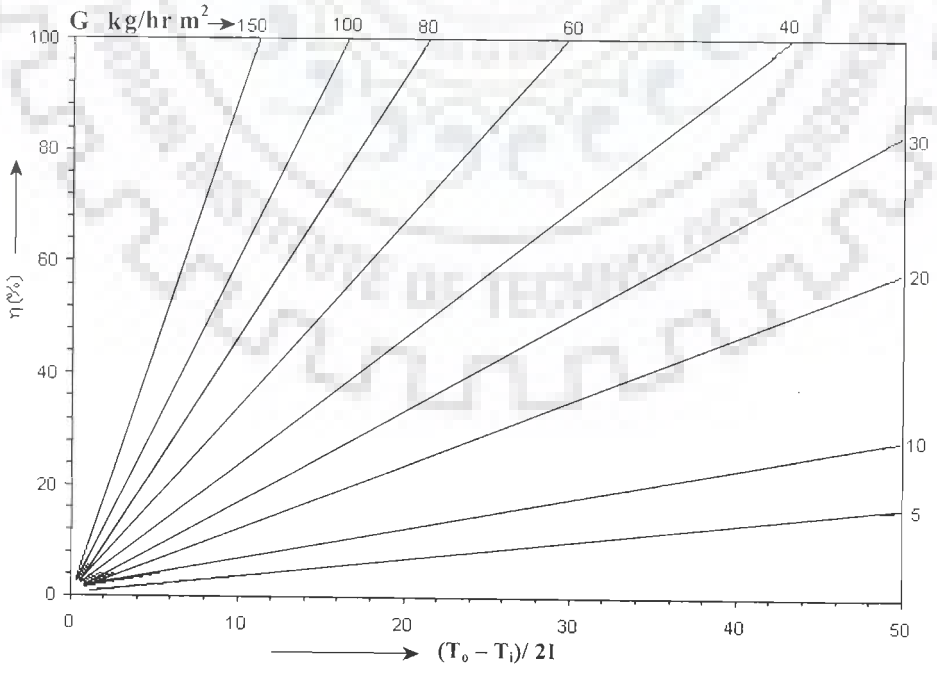

Fig.1.5 Theoretical efficiency curves [18]

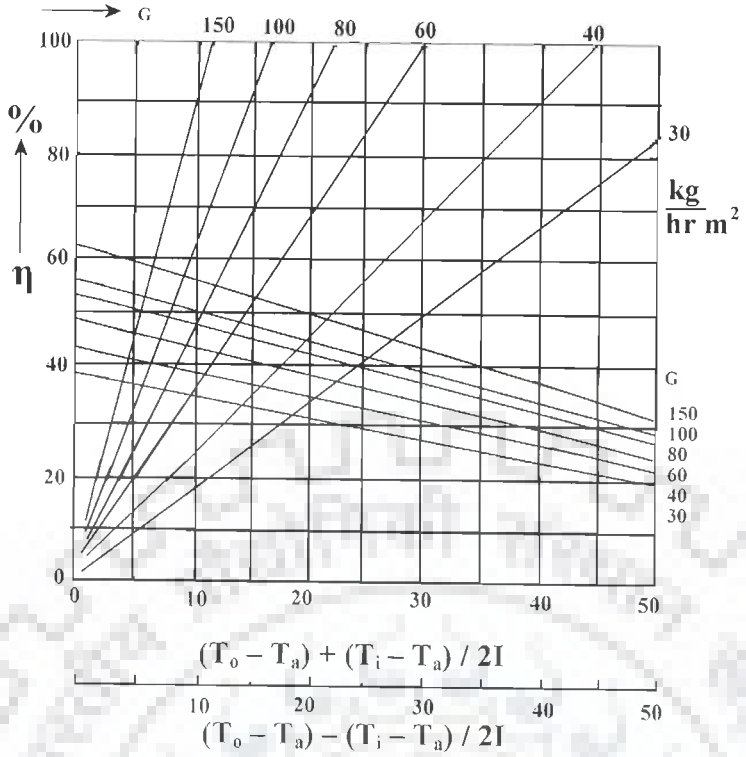

Fig.1.6 Design curves with air recycling [18]

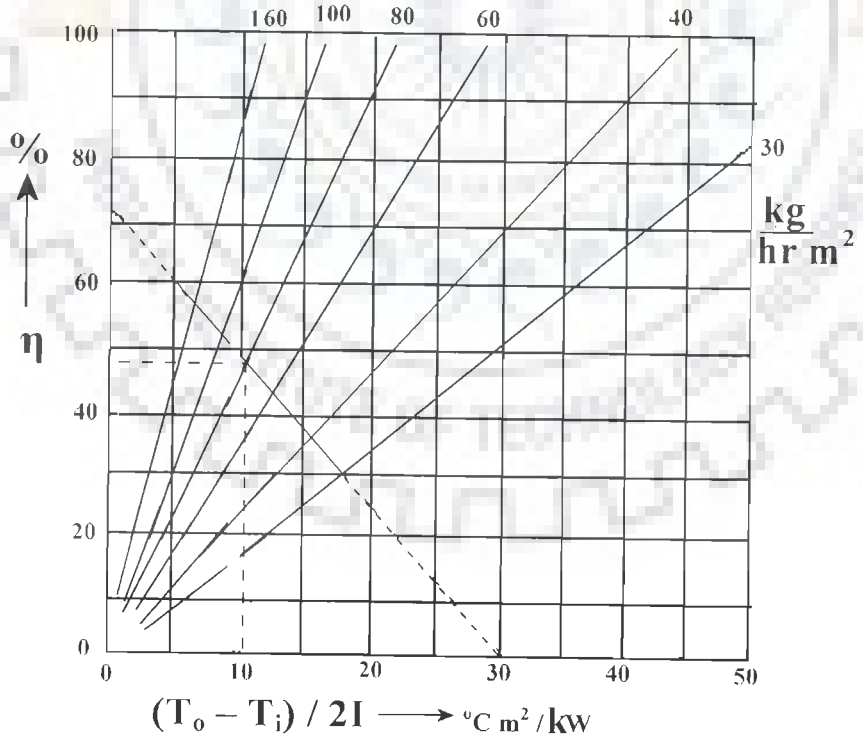

Fig.1.7 Design curves without air recycling [18]

The unknown parameter can be directly determined from Fig.1.7 as shown by the example given below:

Given : $I = 1\ kW/m^2$, $T_a = T_i = 30\ ^oC$ and $T_o = 50\ ^oC$

Required : η and G

Solution : The temperature values give,

$X = (T_o - T_a)/ 2I = 10\ ^oCm^2/kW.$

Proceeding vertically upwards from 10 $^oC\ m^2.kW^{-1}$ in Fig.1.7 to meet the single performance curve at a point corresponding to which G = 85 kg/ hr m^2 and η = 48 %.

1.6 COLLECTOR OVERALL HEAT LOSS COEFFICIENT

From analysis point of view, it is convenient to express heat lost from the collector in terms of an overall loss coefficient defined by the following equation:

$$q_l = U_l\ A_p\ (T_{pm}-T_a) \qquad (1.17)$$

where, U_l, is the overall loss coefficient

T_{pm} is the average temperature of the absorber plate.

The heat lost from collector is the sum of heat lost from top, bottom and the sides. Thus,

$$Q_l = Q_t + Q_b + Q_s \qquad (1.18)$$

where, Q_t is the heat loss rate from glazing top

$= U_t\ A_p\ (T_{pm} - T_a)$

Q_b is the heat loss rate from bottom side

$= U_b\ A_p\ (T_{pm} - T_a)$

Q_s is the heat loss rate from sides

$= U_e\ A_p\ (T_{pm} - T_a)$

which gives the simple form

$$U_l = U_t + U_b + U_e \tag{1.19}$$

The energy loss through the bottom of the collector is sum of two terms, conduction and convection-radiation to the environment. The magnitude of convection and radiation term is negligibly small compared to the conduction term. Therefore, usually back loss coefficient U_b, is approximately expressed as;

$$U_b = ki/\ \delta_i \tag{1.20}$$

where ki and δ_i are thermal conductivity and thickness of back insulation respectively.

In most collectors the evaluation of edge losses is complicated. The losses through the edge should be referred to the collector area. If the edge loss coefficient-area product is $(UA)_{edge}$, then the edge loss coefficient, based on collector area A_p is

$$U_e = \frac{(UA)_{edge}}{A_p} = \frac{(L + W)L_c}{LW\delta_i} k_i \tag{1.21}$$

where, L_c is height of the collector casing.

L is length of absorber plate

W is width of absorber plate

In case of flat plate solar collectors, major heat loss occurs from the top, through the glass covers. The equations for heat loss through a series of glass covers are coupled. Assuming equal resistance between sets of parallel plates, Hottel and Woertz [20] uncoupled these equations. Separating out convection and radiation

terms, they obtained an approximate solution for the top heat loss factor, U_t, of a flat plate collector with N glass covers which is given as:

$$U_t = \left[\frac{N}{C\left[(T_{pm} - T_a)/(N + f_e)\right]^{0.25}} + \frac{1}{h_w}\right]^{-1} + \frac{\sigma\left(T_{pm}^{\ 2} + T_a^{\ 2}\right)\left(T_{pm} + T_a\right)}{\frac{1}{\varepsilon_p} + \left[(2N + f_e - 1)/\varepsilon_g\right] - N} \qquad (1.22)$$

where, h_w is the wind convective heat transfer coefficient, W/m^2-K.

$= 5.7 + 3.8\ V_w$

V_w is the wind speed, m/s

ε_p is emissivity of the absorber plate.

ε_g is emissivity of the glass cover

N is number of glass cover

f_e is an empirical factor

$= (1 + 0.089h_w - 0.1166h_w\varepsilon_p)(1 + 0.07866N)$

C is an empirical factor

$= 620\ (1 - 0.000051\ \beta^2)$ for $0^\circ < \beta < 70^\circ$] for $70^\circ < \beta < 90^\circ$

use $\beta = 70^\circ$.

β is collector tilt angle (degree).

σ is the Stefan – Boltzmann constant (5.6697×10^{-8} W/m^{2}K^4)

Klein [21] improved Eq. (1.22) and extended it for a range of absorber plate temperatures up to 200 °C with selective coating. This relationship fits satisfactorily for U_t for mean plate temperatures between ambient and 200°C within ± 0.3 W/m^{2}C.

$$U_t = \left[\frac{N}{\frac{C}{T_{pm}}\left[\frac{(T_{pm} - T_a)}{(N + f_e)}\right]^e} + \frac{1}{h_w}\right]^{-1} + \frac{\sigma\left(T_{pm}^{\ 2} + T_a^{\ 2}\right)\left(T_{pm} + T_a\right)}{\left(\varepsilon_p + 0.00591Nh_w\right)^{-1} + \frac{(2N + f_e - 1 + 0.133\varepsilon_p)}{\varepsilon_g} - N} \qquad (1.23)$$

where, $e = 0.430(1-100/T_{pm})$

Malhotra et al. [22] developed a correlation for top loss coefficient, U_t, and is given as:

$$U_t = \left[\frac{N}{\frac{C}{T_{Pm}}\left[\frac{(T_{Pm}-T_a)}{(N+f_e)}\right]^{0.252}} + \frac{1}{h_w} \right]^{-1} + \left[\frac{\sigma\left(T_{Pm}^{\ 2}+T_a^{\ 2}\right)(T_{Pm}+T_a)}{\frac{1}{(\varepsilon_P+0.0425N(1-\varepsilon_P))}+\frac{(2N+f_e-1)}{\varepsilon_C}-N} \right] \quad (1.24)$$

where $f_e = \left[\frac{9}{h_w} - \frac{30}{h_w}^2\right]\left[\frac{T_a}{316.9}\right][1+0.019\,N]$

$C = 204.429\,(cos\,\beta)^{0.252}/\,L_s^{\ 0.24}$

Garg and Dutta [23] have made a detailed study of these correlations and have concluded that the correlation suggested by Malhotra et al. [22] agrees the best with the exact iterative solution.

Mullick and Samadarshi [24] proposed a different approach to evaluate the top loss coefficient of a flat plate solar collector with single glass cover. They argued that in case of an absorber with single glass cover it is not necessary to separate the convective and radiative terms to obtain a semi-empirical relation for the heat loss coefficient. The recommended equation for the top loss coefficient is:

$$U_t = \left[\left\{ \frac{12.75\left((T_{Pm}-T_C)\cos\beta\right)^{0.264}}{(T_{Pm}+T_c)^{0.46}L_S^{\ 0.21}} + \frac{\sigma\left(T_{Pm}^{\ 2}+T_C^{\ 2}\right)(T_{Pm}+T_C)}{\frac{1}{\varepsilon_P}+\frac{1}{\varepsilon_C}-1} \right\}^{-1} + \left\{ h_W + \frac{\sigma\varepsilon_C\left(T_C^{\ 4}-T_S^{\ 4}\right)}{(T_C-T_a)} \right\}^{-1} + \frac{t_g}{K_g} \right]^{-1} \quad (1.25)$$

where, T_c is temperature of glass cover, K

L_S is air gap spacing between absorber plate and glass cover, m

T_S is equivalent blackbody sky temperature, K

t_g is thickness of glass cover, m

k_g is thermal conductivity of glass, W/m K

In case the sky temperature, T_s, is assumed to be equal to ambient temperature, T_a, the following relation is obtained for glass temperature, T_c:

$$T_c = T_a + h_w^{-0.38}\left[0.567\varepsilon_p - 0.403 + T_{pm}/429\right]\left(T_{pm} - T_a\right) \qquad (1.26)$$

It has been shown by Samadarshi and Mullick [25] that Eq.(1.23) may give the estimated values with a deviation as high as 33% (overestimate) in certain cases when wind heat transfer coefficient, plate temperature, plate emittance and air gap are all high. Similarly, error resulting from the use of Eq.(1.24) can be as high as 24% (underestimate) when the variables are all low. The computational error resulting from use of Eq.1.25 however remains within ± 3 % in either case.

Akhtar and Mullick [26] developed an improved equation for computing the glass cover temperature of flat-plate solar collectors with single glazing. A semi-analytical correlation for the factor F_1 (the ratio of inner to outer heat-transfer coefficients) as a function of collector parameters and atmospheric variables is obtained by regression analysis. This relation readily provides the glass cover temperature (T_g). The results are compared with those obtained by numerical solution of heat balance equations. Computational errors in T_g and hence in the top heat loss coefficient (U_t) are reduced by a factor of five or more. With such low errors in computation of T_g and U_t, a numerical solution of heat balance equations is not required. The method is applicable over an extensive range of variables with the range of air gap spacing 8 mm to 90 mm and the range of ambient temperature 0°C to 45°C. The maximum error in the calculation of the top heat loss coefficient by using the present method in comparison to that obtained by numerical solution of heat balance equations is about 2%.

$$U_t^{-1} = \left[\frac{\sigma \left(T_p^2 + T_g^2\right)\left(T_p + T_g\right)}{\left(1/\varepsilon_p + 1/\varepsilon_g - 1\right)} + \frac{k\,Nu}{L} \right]^{-1} + \left[\sigma \varepsilon_g \left(T_g^2 + T_a^2\right)\left(T_g + T_a\right) + h_n \right] - 1 + L_g / k_g \qquad (1.27)$$

where $T_g = \dfrac{\left(F_l\, T_p + T_a\right)}{\left(1 + F_l\right)}$

$$F_l = \frac{\left[12 \times 10^{-8} \left(T_a + 0.2T_p\right)^3 + h_w\right]^{-1} + 0.3L_g}{\left[6 \times 10^{-8} \left(\varepsilon_p + 0.0028\right)\left(T_p + 0.5T_a\right)^3 + 0.6L^{-0.2} \left\{\left(T_p - T_a\right)\cos\beta\right\}^{0.25}\right]^{-1}}$$

$$Nu = 1 + 1.44\left[1 - 1708/Ra'\right]^{+}\left\{1 - 1708\left(\sin 1.8\beta\right)^{1.6}/Ra'\right\} + \left[\left(Ra'/5830\right)^{1/3} - 1\right]^{+}$$

1.7 PERFORMANCE ENHANCEMENT METHODS FOR SOLAR AIR HEATERS

Thermal performance of a solar air heater has been found to be poor on account of low thermal capacity of air and absorber to air convective heat transfer coefficient, which needs design considerations, and to the extent possible, compensation. Thermal performance of a solar air heater depends upon the rate of incident solar radiations, losses from the absorber plate and convective heat transfer coefficient between air and the absorber plate. A number of investigations [2, 27 and 28] have been carried out to improve the thermal performance of solar air heaters and different methods have been suggested for this purpose. Broadly speaking, performance enhancement methods for solar air heaters can be classified into following three categories.

- Incident Radiation Enhancement Methods
- Thermal Losses Reduction Methods

- Flow Passage Modification Methods For Convective Heat Transfer Coefficient Enhancement

1.7.1 Incident Radiation Enhancement Methods

Tabor [29, 30] and Patrick [31] suggested the use of concentrating and side mirrors in flat plate solar collectors to increase the amount of radiation reaching the collector in order to attain higher temperatures. It was reported that output of flat plate collectors improved and temperatures above 100 ^{0}C were attained.

Dang [32] compared the performance of flat plate collectors with and without reflector system and reported that collector with reflector system produced an increase of 10-15 ^{0}C in fluid temperature as compared to that without a reflector system. Garg and Harishikesan [33] developed a model to predict the behavior of a system consisting of a flat plate collector and two reflectors. Kumar et al. [34] developed an analytical model to study the effect of four reflectors on the performance of solar collectors. It was reported that for reflectors on the southern and the northern sides, 14 and 44 percent enhancement in solar gain was achieved for the months of May and December respectively. Due to the effect of shadowing, no appreciable solar gain was achieved in case of reflectors on the eastern and the western sides.

Hussein et al. [35] analytically studied the effect of different operational and design parameters of plane reflector-tilted flat plate solar collector systems on daily and yearly solar energy collection. It was reported that the south facing reflector provides higher yearly solar energy collection than the north facing one. For reflector height (L_r) equal to the collector length (L_c), the optimum tilt angle of the collector is about (φ−10°) and (φ+10°) for a south and a north facing reflector, respectively and changing the tilt angle of the south facing reflector at its noon optimum angle up to

twice a year provides more than 13 percent yearly enhancement in the collector solar energy collection.

Souka [36] designed a flat-plate collector to absorb heat from the back side in addition to the front by omitting the usual insulation provided on the back side. The peak energy collection increased by 48 percent, as compared to a conventional flat-plate collector. Suri and Saini [37] studied the performance of single and double exposure solar air heaters as shown in Fig.1.8. They developed a set of generalized performance prediction curves including a chart for designing a new heater as well as for predicting efficiency of the proposed design.

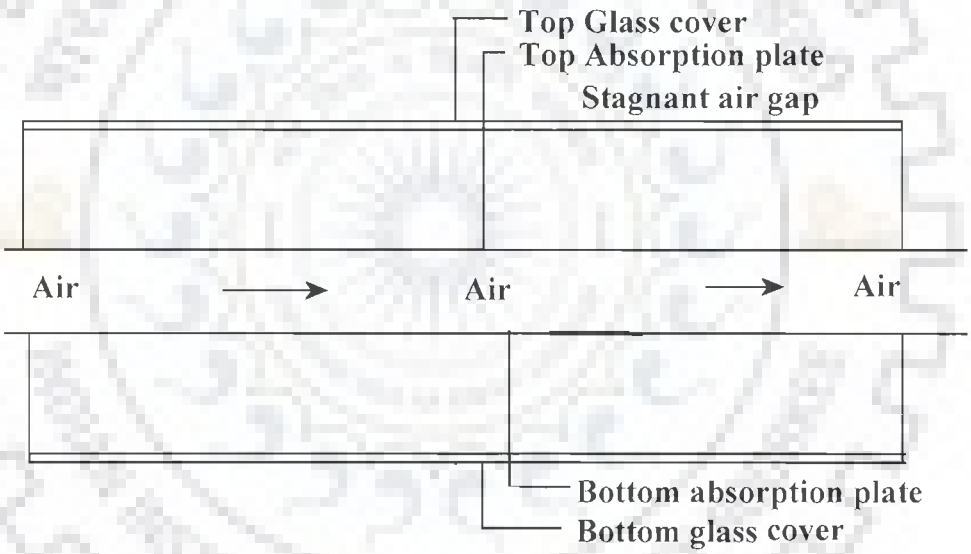

Fig.1.8 Double exposure solar air heater [37]

Bhargava et al. [38] presented a theoretical analysis of three different configurations of double exposure solar air heaters and studied the effect of collector length and reflectance on thermal performance. The outlet air temperature increased with an increase in plate length, however, instantaneous and average efficiencies decreased and a double exposure solar air heater performs better than a single exposure air heater if the reflectance for solar radiation is greater than 10 percent.

1.7.2 Thermal Loss Reduction Methods

Thermal loss reduction methods involve use of more than one glass cover, selective surfaces for absorber plate, honeycomb traps, evacuated glass tubes and two pass arrangements. In order to reduce convective as well as radiative heat losses from the collectors operating at high temperature and wind velocity, two or more glass covers are used. However, use of several glass covers reduces the amount of insolation reaching the absorber plate due to the absorption of the solar radiation by the glass covers leading to decrease in the thermal efficiency [2]. Hence at low temperatures, where thermal loss is small, use of single glass cover gives better efficiency compared to the double one while at higher temperature difference, use of double glass cover is advisable for better performance.

Performance of flat plate solar collectors at high temperatures is adversely affected by thermal losses due to conduction, convection and re-radiation from the hot absorber plate. These thermal losses can be reduced by placing a transparent insulation in the form of thin-walled honeycomb structure between absorber plate and glass cover. Hollands [39] investigated the performance of a flat plate solar collector with a selectively transmitting honeycomb panel mounted between absorber plate and glass cover. An analytical study of natural convection process in such panels has shown that, under certain conditions, natural convection losses can be suppressed. Honeycomb wall thickness also affects the overall efficiency.

Pellete et al. [40] developed a collector with a purpose of attaining high temperature without optical concentration and reported a working temperature in the range of 204 ^{o}C. Buchberg and Edwards [41] reported that use of cylindrical glass honeycomb in solar collectors improved the performance considerably in comparison to conventional single-glazed selective black and double glazed nonselective black absorber collectors especially at high temperatures. The solar collector is shown in Fig.1.9.

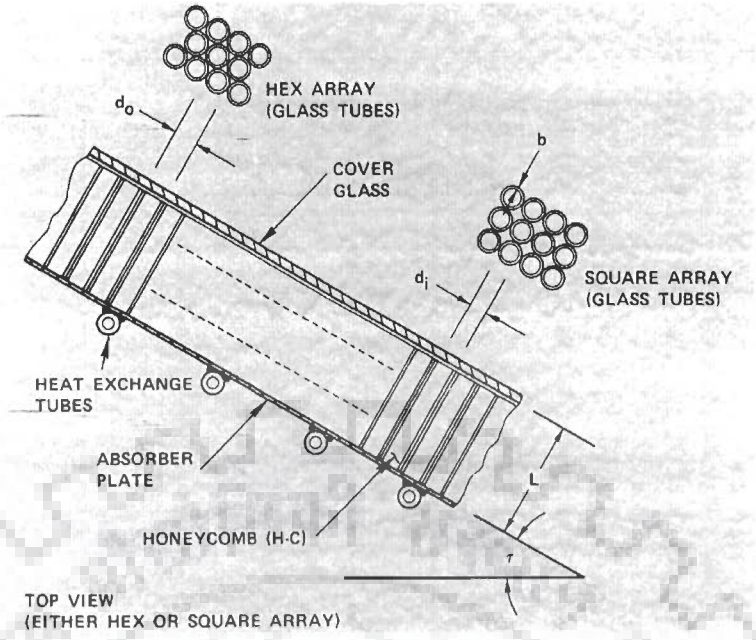

Fig.1.9 Honeycomb flat plate solar collector [41]

Use of selective coatings on the absorber plate results in high absorptance of solar radiations and low emittance of long wave radiations. Ponos et al. [42] carried out an experimental investigation on selective absorber surfaces. They prepared the heat absorbing surfaces by electro-plating copper, cobalt and other suitable metals on the exposed side of the absorber plate and found that the selective coating is suitable for operating at high temperature. They also reported that many combinations of the coatings of semiconductors on highly reflecting surfaces can result in a surface which can absorb more than 85 percent of incident solar radiations and emit less than 20 percent of the absorbed energy at temperature up to 100 °C.

Duffie and Backman [2] have summarized the properties of surface coatings used for flat plate collectors. These are nickel black on galvanized steel, copper black on copper, ebanol carbon on copper and black chrome on nickel plated steel. An absorber plate with highly selective surface requires only one transparent cover even at high operating temperatures.

Herrick [43] designed and tested an evacuated solar collector consisting of a thick phenolic structural foam body, a black painted fiber glass mat absorber, and a closely packed array of evacuated cylindrical glass tubes acting as a collector cover (FMTC). Concentration ratio of such a collector is one and is shown in Fig.1.10. The absorber of the collector has a nearly perfect absorbance and is practically independent of angle of incidence. It was reported that in a steady state simulation at full sun under northern midwinter conditions, the FMTC collector delivered a minimum of 1.9 times more heat per day to a heat storage system as compared to a double glazed water-cooled collector with a non-selective black flat absorber plate.

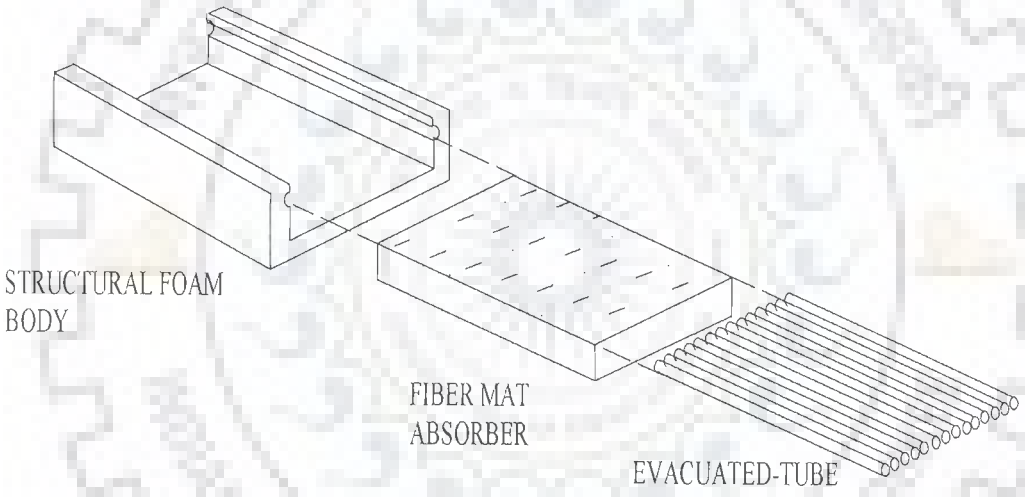

Fig.1.10 An exploded view of the evacuated tube air collector [43]

1.7.3 Flow Passage Modification Methods for Convective Heat Transfer Coefficient Enhancement

In solar air heaters, flow passage can be modified for augmentation of heat transfer between the absorber plate and air. Different methods employed for this purpose are as follow:

- Corrugated absorbers
- Two pass arrangement

- Finned absorber
- Matrix bed absorber having air duct filled with packing material
- Overlapped glass plate absorber
- Artificial roughness on the underside of the absorber plate

1.7.3.1 Corrugated absorber

The use of corrugations on the absorber plate results in increase in the heat transfer area along with increase in absorption of solar radiation. Most of the solar radiations are absorbed after multiple reflections occurring on the sides of corrugations in addition to the cavity effect. Chaudhary et al. [44] fabricated a single pass solar air heater without glass covers to provide hot air for agricultural uses as shown in Fig.1.11. It was reported that in order to obtain higher air temperature, lower air mass flow rate through the air heater and longer air channel are desirable. A narrow channel results in an improvement in the performance of the system.

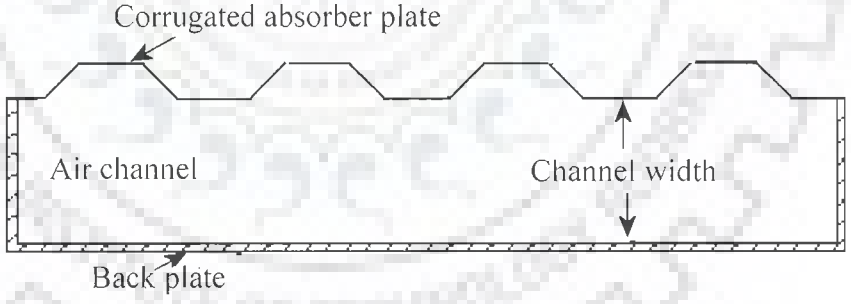

Fig.1.11 Solar air heater with corrugated absorber plate [44]

Gupta and Garg [45] carried out an experimental study on the solar air heaters having corrugated absorber plate and reported that such air heaters are capable of supplying hot air up to about 30 °C above ambient with an overall efficiency of 60%. Thermal efficiency is found to be maximum when the corrugated sheet is at right angles to the air flow and the channel depth is kept to be minimum.

1.7.3.2 Two pass air flow

The solar collector design can be improved by two pass airways like splitting the air stream, which increases the heat absorbing area and decreases the convective losses from the heated surface. In this type of solar air heater, the air flows either between two covers or between the inner cover and the absorber plate and then pass through the passage under the plate. The concept of a two pass air heater was first introduced by Satcunanathan and Deonarine [46]. The collector consists of two glass covers, absorber plate, and a rear plate. The air was first made to pass through the channel formed by the two glass covers and then through the channel formed by the rear plate. They found that the outer glass cover temperatures were significantly lower and much nearer to atmospheric temperature compared to the condition when the collector was operated in the conventional single pass manner. Additionally, each air layer between two successive glass panels provides a transparent insulation for heat losses from the metal plate to the atmosphere. Consequently, the performance of the two-pass mode shows an improvement of about 17 percent over the single pass mode.

Wijeysundera et al. [47] studied another arrangement both analytically and experimentally, in which inlet air flows first above the absorber plate and then under it. The collector performance was examined over a wide range of system and operating conditions and two pass designs was found to perform better than the single pass mode. Persad and Satcunanathan [48] developed an analytical model for predicting the performance of a two-glass cover solar air heater when operating in either the single-pass or the two-pass mode. Performance analysis shows that the two pass mode of operation is consistently superior in efficiency to the single pass mode by some 2 to 9 percent.

1.7.3.3 Finned absorber plate

Considerable enhancement in heat transfer from the absorber plate to air can be achieved by attaching fins perpendicularly on the lower side of the absorber plate of a solar air heater on account of turbulence generation as flow is interrupted and an increase in heat transfer area. However, enhancement in heat transfer is accompanied by a corresponding increase in pressure drop, which is also an important factor in the selection of a solar air heater. Liu et al. [49] showed that the efficiency of a solar air heater can be increased by providing extended surfaces. An experimental study was carried out with pin fin of hollow brass tubes soldered on the plates in staggered pattern. Significant increase in energy collection was predicted due to depression of plate temperature.

Yeh et al. [50] presented a design for double flow operation with fins attached over and under the absorbing surface. Considerable improvement in collector efficiency was obtained. The effect of the flow rate ratio of the two streams of air flowing over and under the absorbing plate on the enhancement of collector efficiency was also investigated.

Issacci et al. [51] presented an investigation of a reflective fin solar air heater. This collector made of a multitude of specularly reflective parallel fins has several interesting features, including high solar absorptance and reduced heat losses, leading to high efficiencies. Solar radiation penetrates and undergoes multiple reflections among the fins until they are completely absorbed.

Pottler et al. [52] optimized fin spacing for the highest net energy gain as shown in Fig.1.12. They recommended 5 to 10 mm spacing for continuous fins. Due to higher pressure losses, offset strip fins show reduced net energy gains compared to optimally spaced continuous fins.

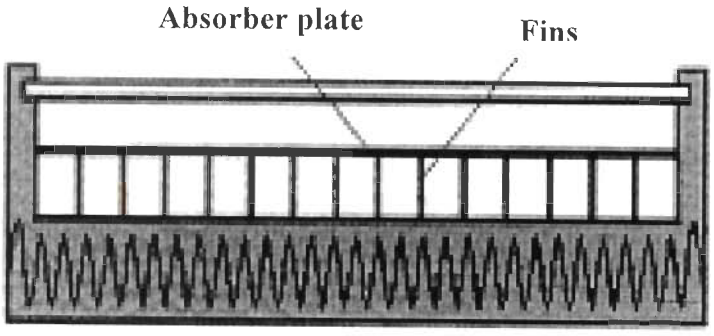

Fig.1.12 Schematic description finned solar air heater [52]

1.7.3.4 Overlapped glass plates

Selcuk [53] carried out the thermal analysis of an overlapped glass plate solar air heater. The collector consists of a series of overlapped parallel glass plates with the lower glass plate blackened as shown in Fig.1.13. It is reported that at higher air velocities of the order of 1 m/s, the thermal efficiency is about 75 percent where as at one-third of this velocity, the efficiency is only about 60 percent. The increased efficiency at the higher velocities is to be expected, however, the temperature rise of the incoming air is correspondingly reduced.

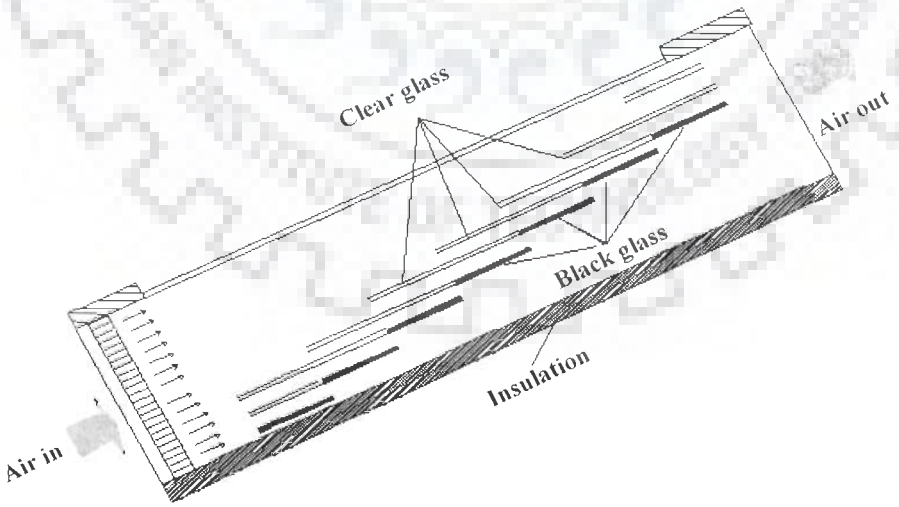

Fig.1.13 Overlapped Glass Plate Absorber [53]

1.7.3.5 Solar collector with metal matrix absorber

In the matrix air heater, air flows through a porous matrix receiving solar radiation directly, radiation penetrates the matrix and is gradually absorbed. This type of solar air heater is different from the non-porous absorber surface in which radiation is absorbed at the surface only. The inlet air is introduced at the top and is heated through the matrix. The advantage of this pattern is that near the inlet, both the glass cover and top surface of the matrix are in contact with the incoming air and are at the lowest possible temperatures resulting in top loss being minimum. Most commonly used porous matrix absorbers are wire meshes, slit and expanded metal.

Kays and London [54] presented detailed data for heat transfer and flow friction as applicable to compact heat exchangers using wire screens inside the heat exchanger tubes. Hamid and Beckman [55] studied the thermal behavior of air-cooled radiatively heated and randomly stacked copper wire mesh screen matrices in a bed. Chiou et al. [56] and Chiou and El-Wakil [57] determined the volumetric heat transfer coefficient and friction factor for a collector having its duct packed with slit and expanded aluminum foil matrices. Their results revealed that the volumetric heat transfer coefficient is generally higher for beds with lower porosities.

Ozturk and Demirel [58] experimentally investigated the thermal performance of a solar air heater having its flow channel packed with Raschig rings. They found that the energy and exergy efficiencies of the packed bed solar air heater were increased as the outlet temperature of heat transfer fluid was increased.

The thermohydraulic investigations of a solar air heater packed with wire screen matrices for different geometrical parameters were done by Mittal and Varshney [59] as shown in Fig.1.14. A design criterion was suggested to select a

matrix for packing the flow channel which would result in best thermal performance with minimum pumping power penalty.

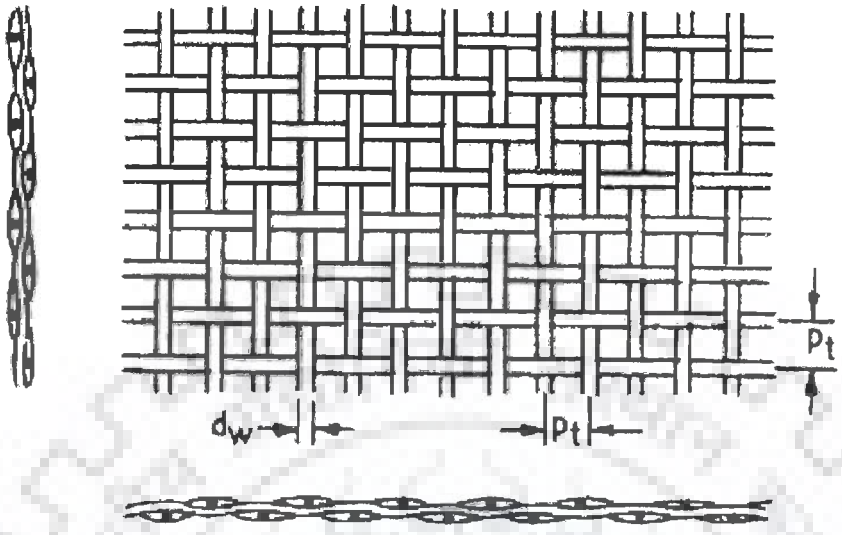

Fig.1.14 Schematic of wire screen used as packing element [59]

Prasad et al. [60] carried out an experimental study on a packed bed solar air heater using wire mesh as packing material and reported that an enhancement of the order of 76.9–89.5 percent in thermal efficiency can be obtained.

1.7.3.6 Artificially roughened solar air heater

The artificial roughness in the form of repeated ribs is the most effective and economic way of improving the performance of a solar air heater as shown in Fig.1.15. Ribs break the viscous sub layer and create local wall turbulence due to separation and reattachment of flow without disturbing the core turbulent flow resulting in improvement of convective heat transfer coefficient between air and the absorber plate. However, the use of artificial roughness results in higher friction losses leading to larger power requirement to make air flow through the duct. It is, therefore, desirable that the turbulence must be created only in the region very close to the heat transferring surface i.e. within the viscous sub-layer region only where heat transfer takes place and the core flow should not be unduly disturbed so as to

avoid excessive friction losses. This can be done by keeping the height of the roughness elements to be small in comparison with the duct dimensions as suggested by Saini [61].

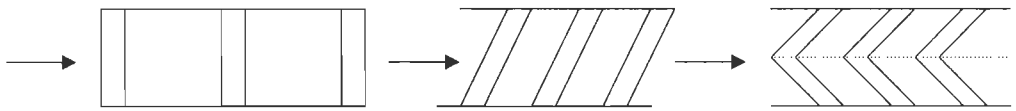

(a) (b) (c)

Fig.1.15 Different rib arrangements

The artificial roughness is one of the most desirable methods on account of its ability to combine heat transfer coefficient enhancement with limited frictional losses. Several investigators [62–76] have used different geometries of artificial roughness on wetted side of the absorber plate to study the enhancement of heat transfer with corresponding increase in the friction factor. Most of the studies [62, 64, 67, and 76] were performed in laboratory under simulated conditions. They reported that there is substantial enhancement in the thermal performance of a solar air heater by using artificial roughness on wetted side of the absorber plate of solar air heater. The details of these studies have been discussed later in a separate section.

1.8 CONCEPT OF ARTIFICIAL ROUGHNESS

As the air flows through the duct of a solar air heater, a viscous sub-layer is formed over the absorber surface that impedes the heat transfer to the flowing air, thereby, adversely affecting heat transfer between air and the absorber plate resulting in poor thermal performance of solar air heaters. The primary mechanisms for thinning the boundary layer are increased free stream velocity and turbulent mixing. Artificial roughness provided on the underside of the absorber plate creates local wall turbulence. Secondary recirculation flows further enhance the convective heat transfer. Flows from the core to the surface reduce the thickness of boundary layer

and secondary flows from the surface to the core flow promote mixing. Energy for creating turbulence has to come from a blower and excessive turbulence results in greater power requirements for the blower. So, it becomes necessary that turbulence must be created in viscous sub layer region where heat transfer takes place. In order to select height of the artificial roughness element, it becomes imperative to know the thickness of the viscous sub-layer which is expressed by an equation given by Bhatti and Shah [77].

$$\delta_t = 5 \times \nu/u_t \qquad (1.28)$$

There are several parameters that characterize the arrangement and shape of the roughness geometry, though, roughness element height, e, and pitch, P, are the most important roughness geometry parameters. These parameters are usually specified in terms of dimensionless parameters, namely, relative roughness height, e/D and relative roughness pitch, P/e. The roughness elements can be two dimensional ribs or three dimensional discrete elements, transverse or inclined ribs or v-shaped continuous or broken ribs. Although square ribs are the most common, chamfered, circular, semi-circular and grooved sections have also been investigated in order to determine the most beneficial arrangement from thermohydraulic point of view [61].

The studies on the effect of roughness geometry parameters on the heat transfer and friction factor have been carried out to determine the most efficient configuration and optimum dimensions of the roughness geometry elements. Some of the important geometries and the related parameters that characterize the roughness geometry and substantially influence the performance are given in Table 1.1.

Table1.1 Rib geometries and parameters

S .No	Rib Geometry	Parameter
1	Transverse ribs	e/D, P/e
2	Continuous angled Ribs	e/D, P/e, α,
3.	Angled ribs with gaps	e/D, P/e, α, g/p, d/W
4.	V-shaped ribs	e/D, P/e, α
5.	V-shaped staggered discrete ribs	e/D, P/e, α, B/S, P'/P, S'/S
6	Transverse-chamfered ribs	e/D, P/e, Φ
7.	Grooved-ribbed arrangement	e/D, P/e, g/P
8.	Arc shaped ribs	e/D, P/e, α,
9.	W-shaped discrete ribs	e/D, P/e, α
10.	Wire mesh	e/D, P/e, L/e, S/e

The most important effect produced due to the presence of a rib on the flow pattern, is the generation of two flow separation regions, one on each side of the rib. The vortices so generated are responsible for the turbulence and hence the enhancement in heat transfers along with corresponding increase in friction losses. Taslim and Spring [78] carried out an experimental investigation to determine the heat transfer coefficient and friction factor in roughened channels.

The effects of rib geometry and rib parameters are discussed as follows:

1.8.1 Effect of Rib Height and Pitch

The effect of rib height on laminar sub layer has been investigated by Prasad and Saini [72] and is shown in Fig.1.16 . Figs.1.17 and 1.18 show the flow patterns downstream of a rib with variation in rib height and pitch as given by Prasad and Saini [73]. Due to flow separation over a rib, reattachment of the shear layer does not occur for a relative roughness pitch ratio, P/e, value less than about 8.

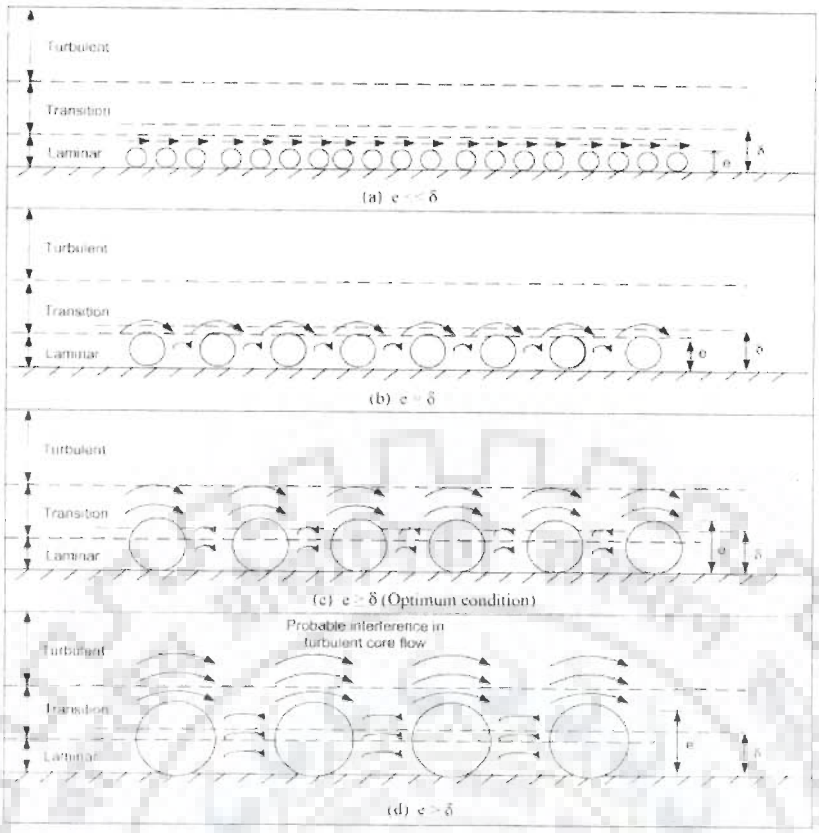

Fig.1.16 Effect of rib height on laminar sub layer [72]

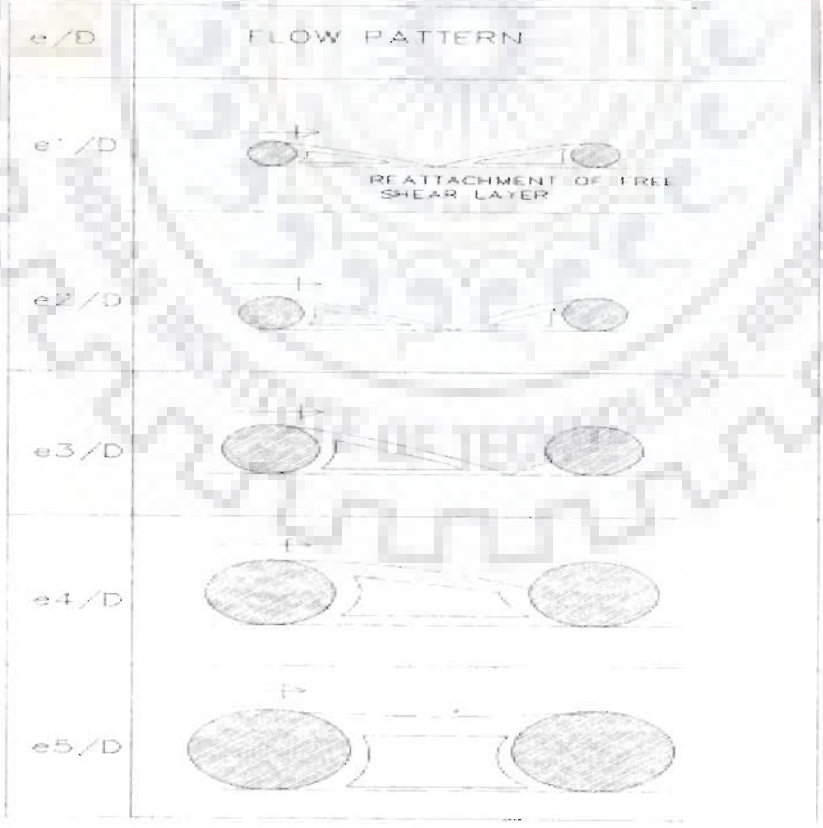

Fig.1.17 Effect of rib roughness height on flow pattern [75]

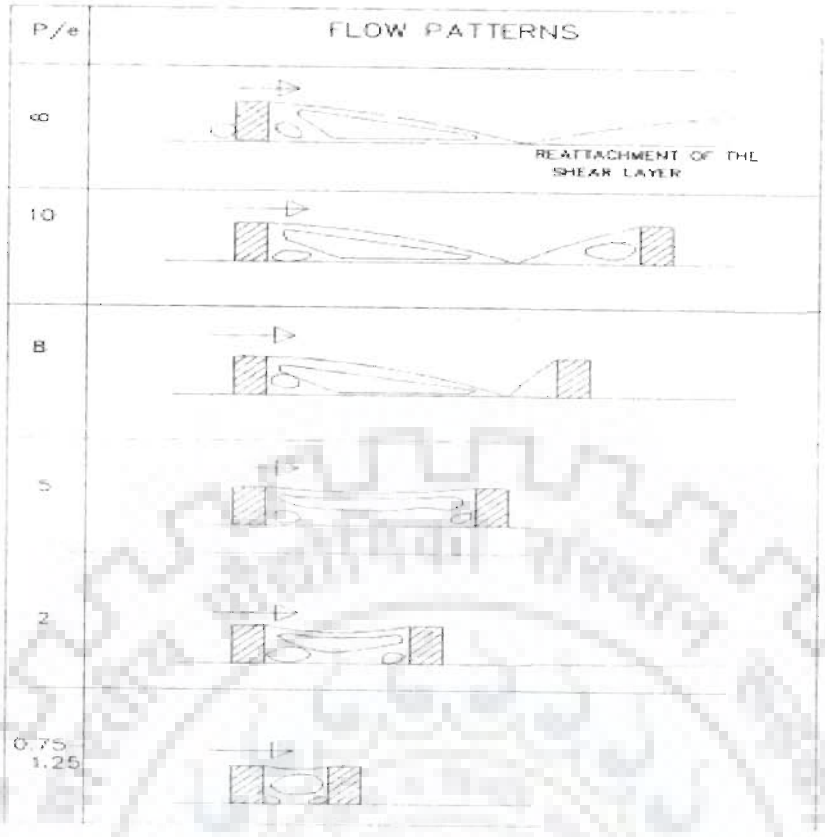

Fig.1.18 Flow pattern of rib as a function of relative roughness pitch [72]

Maximum heat transfer has been found to occur in the vicinity of a reattachment point. It is reasonable to expect that a similar effect can be produced by decreasing the relative roughness pitch, P/e for a fixed value of relative roughness height. For relative roughness pitch, P/e value considerably less than about 8, the reattachment will not occur at all resulting in the decrease of heat transfer enhancement. However, an increase in relative roughness pitch value beyond about 10 also results in decrease of enhancement. It can be, therefore concluded that there occurs an optimum combination of pitch and height of ribs that will result in maximum enhancement of heat transfer.

1.8.2 Effect of Inclination of Rib

The angling of the rib with respect to flow creates counter-rotating secondary flow along the span that causes span wise variation of heat transfer coefficient. The

vortices move along the rib to subsequently join the main stream i.e. the fluid enters at the leading end of the rib and comes out near the trailing end as shown in Fig.1.19. The moving vortices bring the cooler channel fluid in contact with leading end, raising heat transfer rate while the trailing end heat transfer is relatively low. This results in strong span wise variation of heat transfer as reported by Taslim et al. [79].

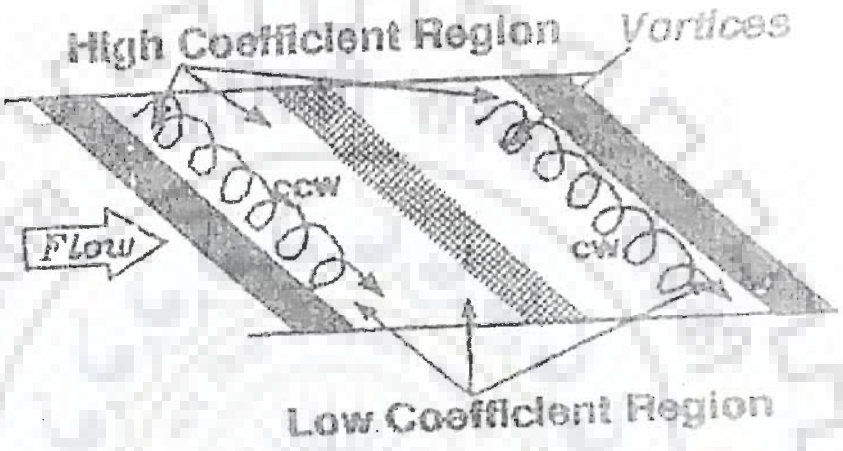

Fig.1.19 Effect of inclination of rib [79]

1.8.3 Effect of Width and Position of Gap in Continuous Inclined Rib

With the introduction of a gap in a rib, secondary flow along the rib joins the main flow to accelerate it, which in turn, energizes the retarded boundary layer flow along the surface resulting in enhancement of heat transfer. Position of gap with respect to leading and trailing edge has a considerable effect on heat transfer enhancement. Position of the gap near the trailing edge, results in more contribution of secondary flow in energizing the main flow through the gap and recirculation loop in the remaining part of the rib, thereby, increasing the heat transfer rate as reported by Aharwal [76] and shown in Fig.1.20.

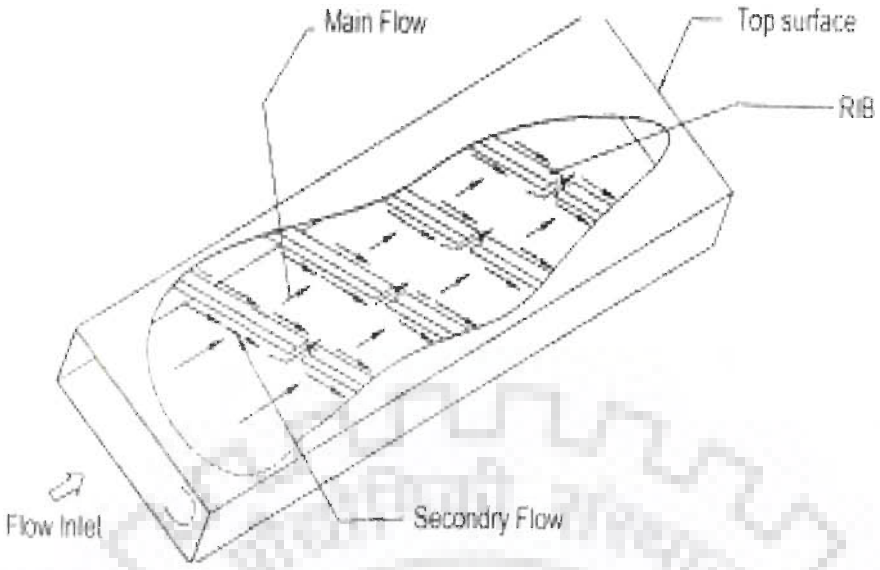

Fig.1.20 Effect of width and position of gap in broken inclined rib [76]

1.8.4 Effect of V-shaping of Rib

Shaping of a long, angled rib into v-shape helps in the formation of two leading ends (where heat transfer rate is high) and a single trailing end (where heat transfer is low) resulting in much large increase of heat transfer. V-shaped ribs form two secondary flow cells as compared to one in case of a continuous angled rib resulting in higher overall heat transfer coefficient in case of v-shaped rib as shown in Fig.1.21. V-shaped rib with apex facing downstream has a higher heat transfer as compared to that of with apex facing upstream [79].

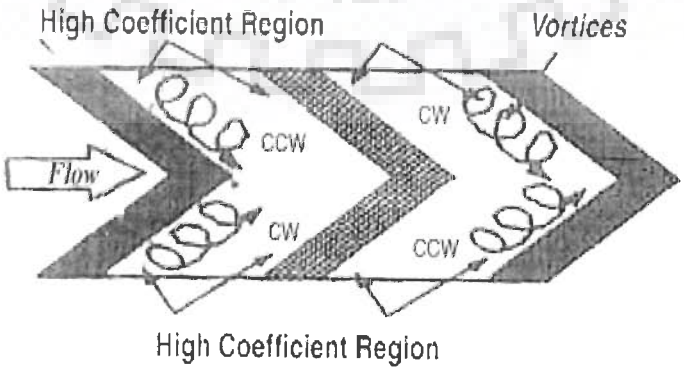

Fig.1.21 Effect of v-shaping of rib [79]

1.8.5 Effect of Discretizing of V-shaped Ribs

The v-shaped ribs along with staggered rib pieces in between further increase the number and area of heat transfer regions. Additional rib parameters related to the size and positioning of rib pieces (length ratio, B/S, segment ratio, S'/S and staggering ratio, P'/P) with respect to main rib produce complex interaction of secondary flow as reported by Mulluwork et al. [71].

1.8.6 Effect of Rib Cross-Section

Sparrow and Hossfeld [80] reported that rib cross-section affects the size of separated region and level of disturbance in the flow. The friction factor is less for circular cross-section ribs in comparison to that of rectangular or square cross-section ribs on account of reduction in the size of separated region. This results in decrease in inertial losses and increase in skin friction, thereby, decreasing the friction factor. As the size of separated region diminishes, level of disturbance in flow also decreases which affects the heat transfer adversely. Another possible factor contributing to the Nusselt number decrease is the reduction in heat transfer surface area associated with circular cross-section ribs.

1.8.7 Fluid Flow and Heat Transfer Characteristics of Roughened Surface

The effect of roughness on friction factor and velocity distribution was first investigated by Nikuradse [81], who conducted series of experiments on pipes roughened by sand grains. He developed the law of wall similarity for roughness in pipes using different grades of closely packed sands of different sizes ($0.004 < e/D < 0.0679$). He proposed the following correlations for friction factor:

$$f = 2[A + B \ln(v^* e/\upsilon) - 2.456 \ln (2e/D)]^{-2} \qquad (1.29)$$

where, 'A' and 'B' are parameters that depend upon the regimes of flow, υ^* is friction velocity ($=\sqrt{\frac{\tau_o}{\rho}}$), m/s and (v^*e/υ) is Roughness Reynolds number, (e^+).

The Roughness Reynolds number, e^+, also defined in terms of e/D, Re and f can be expressed as follows

$$e^+ = Re\ (e/D)\sqrt{f/2} \tag{1.30}$$

Rearranging the above equation, one can obtain,

$$f = 2[A+B \ln e^+ - 2.456 \ln (2e/D)]^{-2} \tag{1.31}$$

Nikuradse [81] proposed the law of wall similarity by correlating the measured velocity distribution data for these sand roughened tubes by a non-dimensional equation in the form of

$$u^+ = \frac{u}{v^*} = 2.5 \ln (y/e) + A \tag{1.32}$$

From this similarity, Nikuradse [81] deduced the value of "A" as

$$A = \sqrt{2/f} + 2.5 \ln (2e/D) + 3.75 \tag{1.33}$$

Thus
$$A = u^+ - 2.5 \ln (y/e) = \sqrt{2/f} + 2.5 \ln (2e/D) + 3.75 \tag{1.34}$$

The non-dimensional parameter "A" is called by different investigators as the roughness parameter [82] or momentum transfer roughness function [83] or roughness function [72 and 73] and it is generally denoted by $R(e^+)$. The usual relation for this function is given as

$$R(e^+) = \sqrt{2/f} + 2.5 \ln (2e/D) + E \tag{1.35}$$

The constant, E, in Eq.(1.37) is termed as geometric parameter whose value depends on the configuration of the duct. Nikuradse [81] reported a value of this parameter as 3.75 for pipe and the same value was used by Dipprey and Sabersky [83] in their investigation. However, there is no general agreement on the value of constant "E". The plot of the roughness function, $R(e^+)$, against roughness Reynolds number (e^+) obtained by Nikuradse [81] is shown in Fig.1.22. The three flow regions namely, hydraulically smooth flow region, transition rough flow region and fully rough region are shown in Fig.1.22.

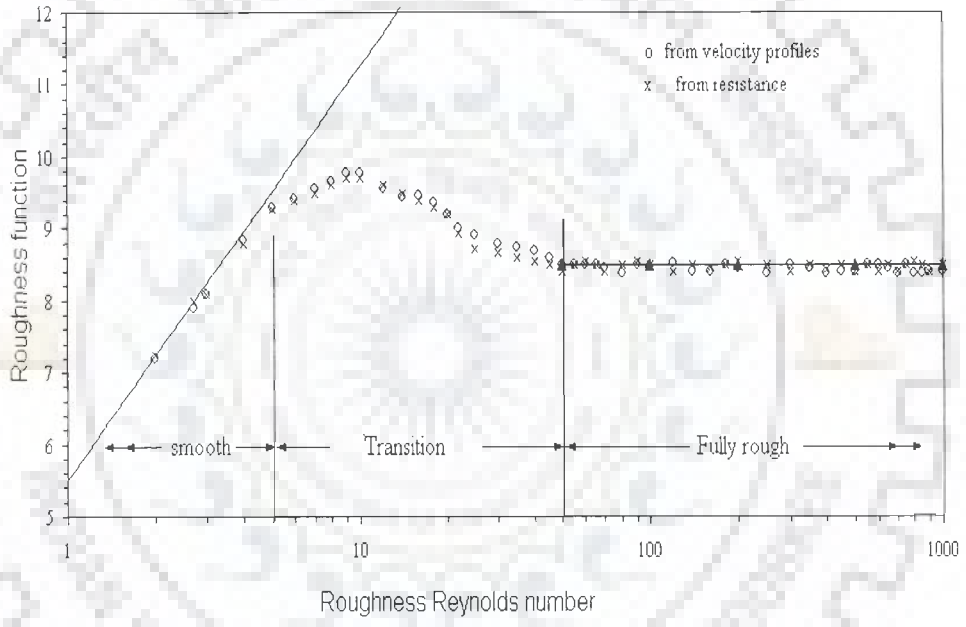

Fig.1.22 Variation of momentum transfer roughness function with roughness[81]

i) Hydraulically smooth flow ($0 < e^+ < 5$)

In this flow region, the roughness has no effect on the friction factor and for all values of relative roughness height, e/D, the friction factor values coincides with those of a smooth pipe. The measured pressure loss data in this regime were correlated by Nikuradse [81] in the form of $R(e^+)$ as under,

$$R(e^+) = 5.5 + 2.5 \ln(e^+) \qquad (1.36)$$

ii) Transitionally rough flow ($5 \leq e^+ \leq 70$)

In transition zone, the influence of roughness becomes noticeable to a greater degree; the friction factor increases with increase in roughness Reynolds number (e^+). This zone is particularly characterized by the fact that the friction factor depends on the Reynolds number as well as on the relative roughness height. The thickness of viscous sub-layer (δ) is of the same order of magnitude as the average roughness height (e) and individual projection extends through the boundary layer which produces vortices causing additional loss of the energy. As the roughness Reynolds number increases, the number of projections passing over the viscous sub-layer increases because of reduction in its thickness with increase in Reynolds number. Thus, the additional energy loss increases with increase in the roughness Reynolds number.

iii) Fully rough region ($e^+>70$)

In this flow region, the roughness function was found to be independent of the roughness Reynolds number and it attains a constant value. The projections of the roughness extend beyond the viscous sub layer.

Webb et al. [84] and Webb and Eckert [85] developed correlations for heat transfer coefficient and friction factor for fully rough flow region in tubes. The friction factor correlation is based on the law of wall similarity as proposed by Nikuradse [81] for sand grain roughness. The heat transfer correlation is based on the application of heat-momentum transfer analogy to flow over a rough surface, which was first used by Dipprey and Sabersky [83] for sand grain roughness. They used the repeated ribs aligned normal to the direction of main flow. The correlations were verified with experimental data taken with $0.01 < e/D < 0.04$, $10 < p/e < 40$ and $0.71 < Pr < 37.6$. These correlations were successfully used to correlate friction loss and

heat transfer results by many investigators [86-94] for different types of roughness geometry, in the fully rough region.

Han and his associates [88-94] conducted extensive experiments to simulate the effect of artificial roughness on cooling turbine blade passages. Han and Park [88] investigated the combined effect of rib angle of attack and channel aspect ratio on heat transfer and friction characteristics of developing flow in short rectangular channel with a pair of opposite rib roughened walls for Reynolds number range of 10,000 to 60,000. They found that the maximum heat transfer and the maximum pressure drop is obtained at an angle of attack of 60° in the square channel while the maximum heat transfer and the maximum pressure drop occurs at the angle of attack of 90° in the rectangular channel of an aspect ratio of 4.0.

Han [89] investigated the effect of the ratio of rib pitch to height, and rib height to equivalent hydraulic diameter on friction factor and heat transfer coefficient for Reynolds number range of 7,000 to 90,000, relative roughness pitch range of 10 to 40, and relative roughness height range of 0.021 to 0.063. It was reported that the maximum values of friction factor and Stanton number occur at a relative roughness pitch of 10. Both the friction factor and Stanton number increase with increase in the relative roughness height.

Han et al. [90] conducted experiments with sixteen plates of different geometries for relative roughness pitch of 5 to 20, relative roughness height of 0.032 to 0.102, angle of attack of 20° to 90° and Reynolds number range of 3,000 to 30,000. They developed a correlation for heat transfer coefficient based on the law of the wall similarity and heat-momentum analogy to relate it with rib shape, rib spacing and angle of attack. They found that for small value of relative roughness pitch (p/e = 5), the flow which separates on each rib does not reattach before it reaches the next rib, whereas at a relative roughness pitch value of about 10, the flow reattaches close to

the next rib and for large rib spacing, the reattachment point exists and the boundary layer begins to grow before the next rib is encountered, reducing both the average shear stress and heat transfer.

Han et al. [91] investigated the effect of surface heat flux ratio on heat transfer augmentation in square channels roughened with parallel, cross and v-shaped angled ribs for Reynolds number range of 15000-80000, rib height to hydraulic diameter ratio, e/D value of 0.0625 and rib pitch to height, P/e value of 10. It was reported that effect of wall heat flux ratio reduced with increase in Reynolds number and v-shaped ribs performed better than parallel ribs.

Han et al. [92] investigated the effect of the rib orientation angle on the local heat transfer distribution and pressure drop in a square channel with two opposite rib roughened walls for Reynolds number range of $15x10^3$ to $90x10^3$ for e/D value of 0.0625 and P/e value of 10. The rib configuration includes 90°, 60° and 45° parallel ribs, 60° and 45° crossed ribs, 60° and 45° V- shaped ribs, and 60° and 45° Λ-shaped ribs. They observed that the v-shaped ribs shows better heat transfer compared to that of the angled ribs because of the development of two vortices cells in place of only one cell in case of inclined ribs.

Han et al. [93] observed the effect of the rib angle of attack on the distribution of local heat transfer coefficient and friction factor in low aspect ratio channel (W/H = ½ & ¼) having two opposite roughened walls. The results indicate that the low aspect ratio channels show better heat transfer performance than those with high aspect ratio channels for a constant pumping power.

Han and Zhang [94] conducted experimental study to investigate the effect of orientation of the broken ribs on the local heat transfer distribution and pressure drop in a square duct with two opposite roughened walls. Top view of the rib configuration

is shown in Fig 1.23. The results show that 60° parallel broken ribs or 60° v-shaped broken ribs yield higher heat transfer augmentation than 45° broken or 45° v-shaped broken ribs. It has also been observed that 60° broken ribs or 60° v-shaped broken ribs perform better than 60° continuous ribs or 60° v-shaped continuous ribs. The heat transfer augmentation is about 2.5 to 4 times of that of the broken rib configuration and about 2 to 3 times of that of the continuous rib configuration with about 7 to 8 times higher pressure drop penalty. Similar results were obtained by Kukreja et al. [95] during their experimental investigations on the turbulent heat/ mass transfer of air flow in a square duct in which two opposite walls were roughened with aligned arrays of full length ribs and V-shaped ribs.

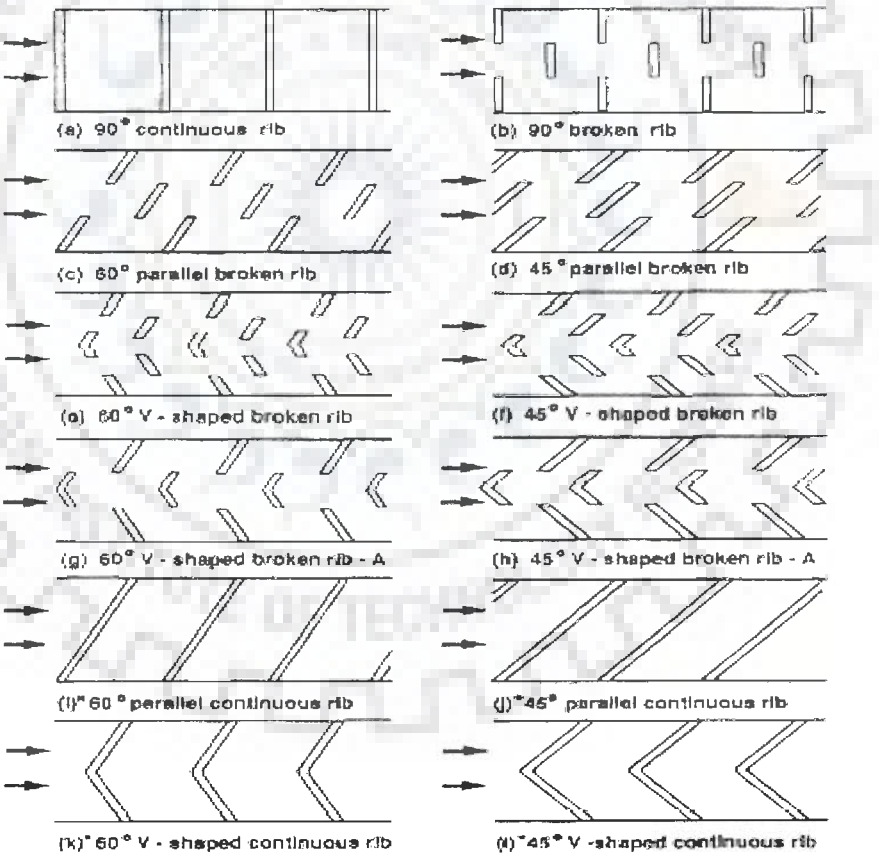

Fig.1.23 Top view of rib configuration used by Han et al. [94]

Liou and Hwang [96, 97] experimentally investigated the heat transfer and friction factor characteristics in a channel with various shapes of ribs mounted on two

opposite walls. They reported that semicircular, triangular or square ribs at two opposite side walls yield about a 4-8 fold, 5-10 fold and 7-15 fold increase in friction factors respectively and 1.6-2.1 fold, 1.7-2.2 fold and 1.9 - 2.7 fold increase in the heat transfer coefficient respectively. They have also developed the correlations for heat transfer and friction factor.

Kiml et al. [98] studied the effect of rib height on heat transfer performance of a high aspect ratio channel with inclined ribs by using flow visualization technique for rib height range of 1 mm to 3 mm. They found that the heat transfer decreases with the decrease of the rib height because of weakening of rib-induced effects namely turbulence production and secondary flow production.

Chandra et al. [99] investigated the heat transfer and friction behavior of a fully developed turbulent air flow in a square channel with transverse ribs on one, two, three and all the four walls for Reynolds number ranging from 10,000 to 80,000, the pitch to rib height ratio, P/e of 8 and rib height to duct hydraulic diameter ratio, e/D of 0.0625. They concluded that the channel with two opposite ribbed walls, three ribbed walls and four ribbed walls yielded around 6, 5 and 7 percent increase in heat transfer respectively as compared to that of the one ribbed walls case.

Lau et al. [100] in a similar experimental investigation, studied the turbulent heat transfer and friction characteristics of fully developed flow of air in a square channel with two opposite walls roughened by aligned array of v-ribs, with 45°, 60°, 120°, 135°, and transverse full ribs. The 60° v-rib yields the highest heat transfer performance.

Taslim et al. [79] investigated the heat transfer and friction characteristics of a channel roughened with angled and V-shaped ribs. They found that v- ribs pointing downwards have much higher heat transfer coefficient compared to that of the v- ribs

pointing upwards. Gao and Sunden [101] have also reported that the v- ribs pointing downward perform better than the ribs pointing upward.

Tanda [102] carried out experimental investigation using liquid crystal thermography to study the heat transfer from a rectangular duct having aspect ratio of 5 with one surface heated at uniform heat flux which is roughened by repeated ribs. The ribs, having rectangular or square sections, were fixed transversely to the main direction of flow or having v-shaped ribs with an angle of 45° or 60° relative to the flow direction. They showed that the features of the inter-rib distribution on heat transfer coefficient are strongly related to rib shape and geometry.

Wright et al. [103] experimentally investigated the heat transfer distribution and friction loss in rotating and non-rotating channels roughened with angled, v-shaped and W-shaped full and discrete ribs. They reported that w-shaped and discrete w-shaped ribs show better thermal performance for both rotating and non rotating channels. It is also observed that these two rib configurations also incurred the highest frictional losses while the discrete V-shaped and discrete angled ribs resulted in the lowest pressure drop. Based on the heat transfer enhancement and pressure drop penalty, the discrete v-shaped and discrete w-shaped ribs exhibit the best overall thermal performance for both rotating and non rotating channels.

Gao and Sunden [104] conducted experiments in rectangular ducts with 90°, 60°, 45° and 30^0 ribs using PIV (Particle Image Velocimetry) system to investigate the effect of the rib inclination on the fluid flow field for a constant value of the system parameters such as ratio of rib height to hydraulic diameter value of 0.06, pitch to rib height ratio value of 10 and Reynolds number value of 5800. The PIV results obtained for 90° ribs were compared with the data available by LDV (Laser Doppler Velocimetry) system, which showed good agreement. All the three inclined rib configurations altered the span-wise profile of the stream-wise velocity component,

leading to high stream-wise velocity component in the region of the upstream end of the ribs and low values at its downstream end.

Bonhoff et al. [105] investigated the flow structure of coolant channel roughened with 45^0 inclined ribs on two opposite surfaces using PIV system. They measured the flow parameters of fluid flowing through the rough surfaces in two planes as shown in Fig.1.24. They compared the numerical analysis results with PIV results and found a good agreement between the two.

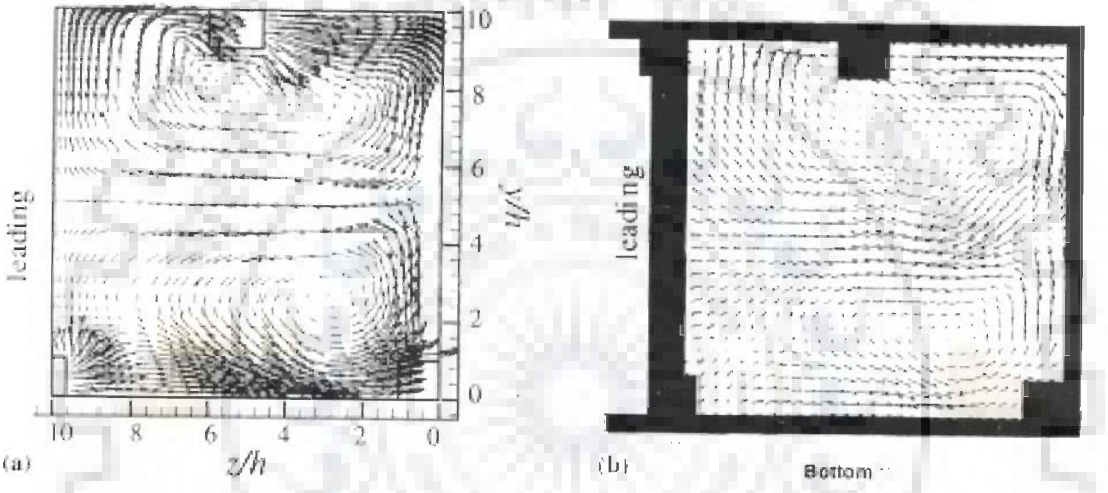

(a) Predicted with RSM model (b) Experimental, Bonhoff et al. [105]

Fig.1.24 Comparison of flow field in principal flow direction

Gao and Sunden [106] experimentally investigated the flow field in the rectangular ducts roughened with different rib arrangements, namely staggered parallel ribs, cross ribs and v-shaped ribs by using PIV system. They investigated the flow structure in three planes and reported that the PIV technique is capable of obtaining the detailed flow structures between two consecutive ribs with reasonable resolution. Some results reported by them are shown in Fig.1.25 (a-f).

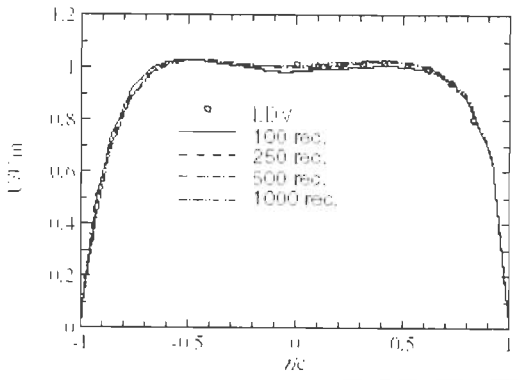

(a) Comparison of stream wise velocity components as observed by LDV and PIV

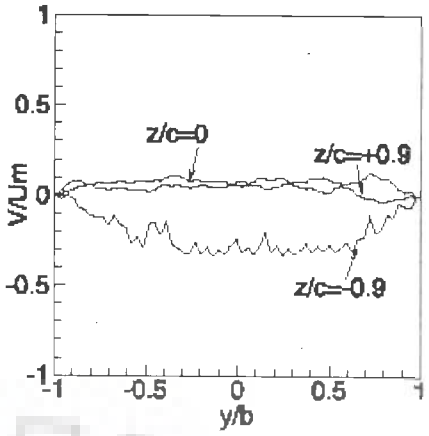

(b)Normalized span wise velocity Components

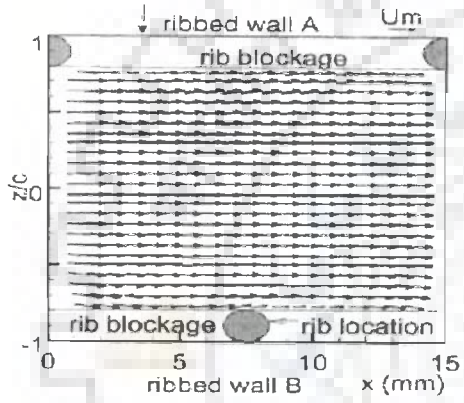

(c) Velocity profile in principal flow Direction

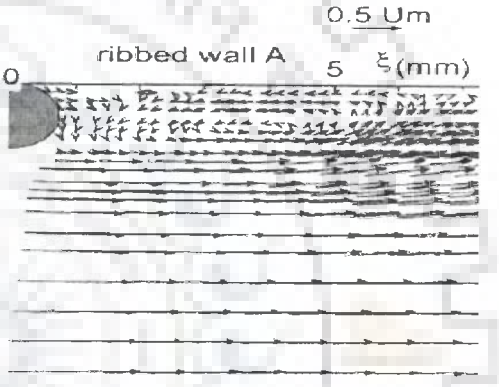

(d) Velocity vector for staggered parallel rib roughened duct

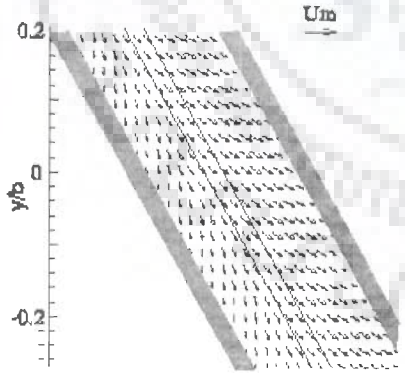

(e) Velocity profile in plane A

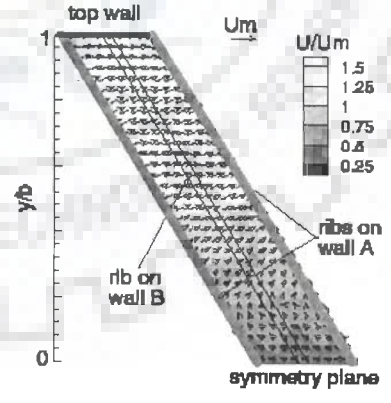

(f) Normalized U/Um velocity Component

Fig.1.25 Flow field over artificially roughened surfaces [106]

Lau et al. [107] conducted experiments to study the effect of replacement of the 90° full ribs with discrete ribs on heat transfer and friction characteristics of flow in the rectangular duct. In this study, the discrete ribs have shown superior heat transfer coefficient and relatively lower friction loss compared to other forms of rib geometries. The rib configurations examined were 90° full ribs and 90° discrete ribs with parallel and cross rib arrangements. The rib height to hydraulic diameter ratio and the rib pitch to height ratio were 0.0625 and 10 respectively. The Reynolds number ranged from 10,000 to 80,000. Results showed that the average Stanton number for 90° discrete rib case was about 10 to 15 percent higher than that of 90° full rib case. Angling of discrete ribs on the opposite walls at an angle of 60°, 45°, or 30° respectively with respect to the main flow, increased in the average Stanton number by 10 to 20 percent compared to that of the 90° discrete ribs.

Lau et al. [108] conducted comparative study on full and staggered discrete rib arrays as shown in Fig 1.26 (a-f) and reported that for a constant pumping power, 60° and 45° discrete ribs enhance the ribbed wall heat transfer by about 5 to 19 percent and 11 to 32 percent respectively compared to the corresponding full ribs case.

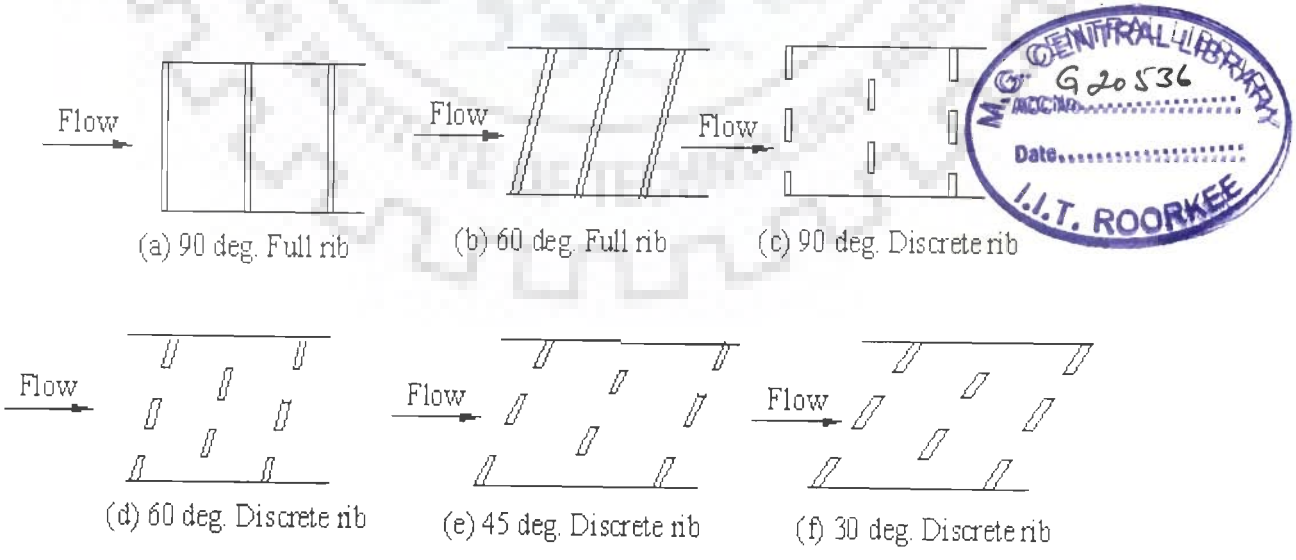

Fig.1.26 Top view of rib configurations used by Lau et al. [108]

Wang and Sunden [109] experimentally investigated the heat transfer and fluid flow characteristics of a rectangular duct roughened with broken v-shaped ribs. They used Liquid Crystal Thermography (LCT) to investigate the detailed heat transfer distribution at the ribbed wall. The feature of the heat transfer were correlated and explained by the detailed velocity structure obtained by PIV system. They found that broken ribs give better heat transfer compared to the continuous ribs.

Chyu and Natrajan (110) have investigated the effect of a slit in a conventional transverse rib on heat transfer from a rib roughened wall using naphthalene sublimation technique. They tested three rib configurations namely, full rib without slit, in line slitted-rib and staggered slitted-rib and observed that the thermo-hydraulic performance of the inline slit ribs and staggered slit ribs respectively are about 6 percent and 13 percent higher than the full ribs.

Cho et al. [111] examined the combined effect of rib angle and length of discrete ribs on heat transfer and friction loss in roughened rectangular ducts. The discrete ribs were made by dividing each continuous rib into two, three or five pieces as shown in Fig.1.27 (a-h). They reported that 90° discrete ribs with two or three pieces shows highest enhancement of heat transfer while the discrete ribs with five pieces show less enhancement in the heat transfer. For 45° ribs, heat transfer distributions of the discrete ribs are similar to those for the angled continuous ribs due to the dominating effects of the rotating secondary flow along the angled ribs on the flow field in the vicinity of the ribbed wall. They further reported that the friction factor of 90 degree discrete ribs with two or three pieces are almost two times higher as compared to that of the continuous ribs.

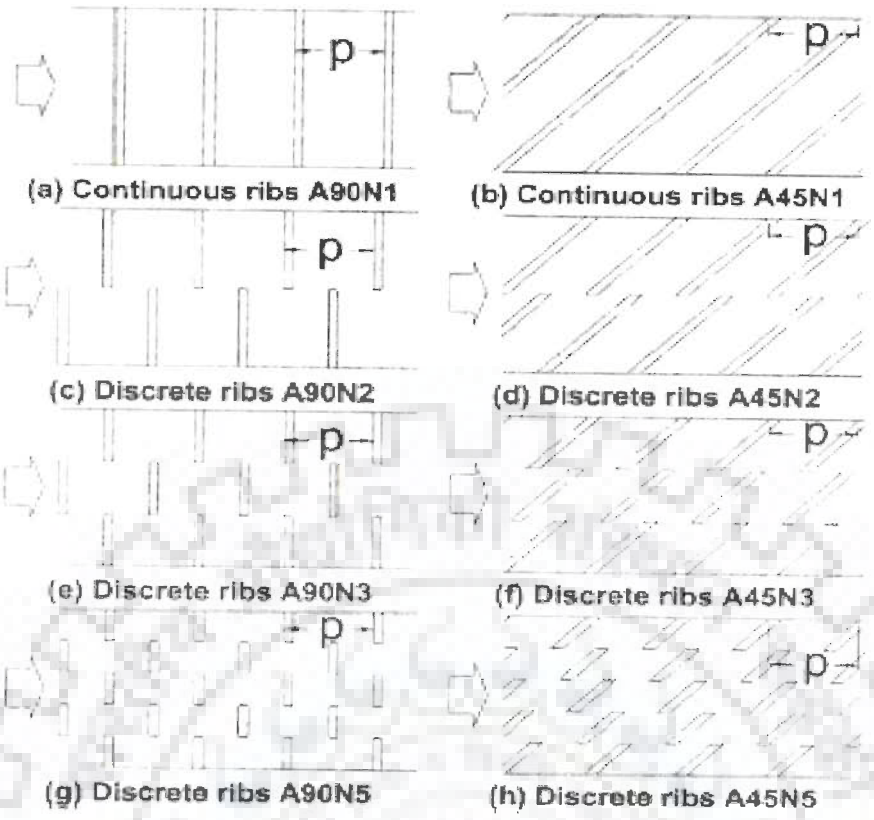

Fig.1.27 Top view of discrete ribs used by Cho et al. [111]

In an another study, Cho et al. [112] investigated the effect of a gap in the inclined ribs on heat transfer in a square duct with rib to pitch height ratio of 8, and angle of attack of 60°. They maintained the gap width same as the rib width and the gap positions has varied over the duct width for parallel and cross rib arrangement on two opposite walls as shown in Fig.1.28 (a-f). They found that the angled ribs with a gap enhance the heat transfer coefficient because the gap flow promotes local turbulence and flow mixing near the ribbed surface, while the rib induced secondary flow is maintained in the duct. They reported that the inclined rib arrangement with a gap position towards the trailing edge of the rib shows higher enhancement in heat transfer compared to that of the continuous inclined rib arrangement.

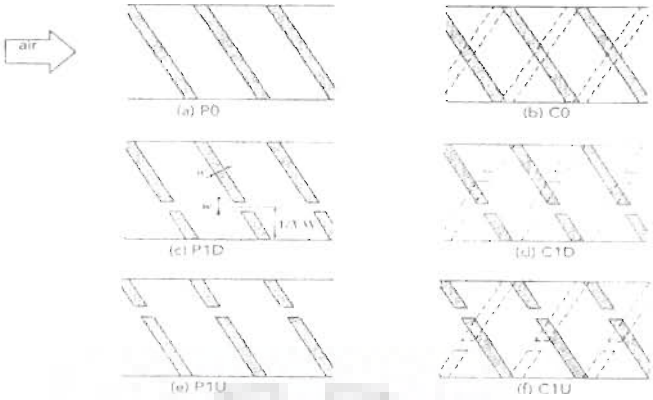

Fig 1.28 Top view of ribs arrangements used by Cho et al. [112]

The enhancement of heat transfer and friction factor for discrete rib roughened ducts as compared to smooth duct is given in Table 1.2.

Table 1.2 Heat transfer and pressure drop enhancement for discrete rib roughness in ducts

Reference	Rib configuration	Range of Reynolds No. $Rex10^{-3}$	Heat transfer enhancement w.r.t. all smooth walls	Pressure drop enhancement w.r.t. all smooth walls
Han et al. [92]	60° V-shaped full rib vs smooth	15 to 90	2.88 to 3.28 fold	8 to 11 fold
Han et al. [93]	60° discrete ribs vs smooth	10 to 80	3 to 4 fold	7 to 8 folds
Han and Zhang [94]	90° Parallel transverse vs smooth	15 to 90	2.38 fold	7 to 9 fold
Lau et al. [107 and 108]	90° transverse discrete vs smooth	10 to 800	2.61 to 2.73 fold	7 to 8 fold
Cho et al. [112]	60° V-shaped discrete ribs vs smooth	25 to 60	2.5 to 3.3 fold	8 to 10 fold

Olsson and Sunden [113] investigated the secondary flow patterns, pressure drop and heat transfer in rectangular channels roughened with cross ribs, parallel ribs, cross v-ribs, parallel v-ribs, and multiple v-ribs (Swirl Flow Tube) as shown in Fig.1.29. The flow patterns were investigated by using smoke wire visualization and LDV measurements. The smoke wire experiments have been performed at Re=1100 and the LDV measurements at Re=3000 at periodic fully developed conditions. The heat transfer and pressure drop are described by j and f factors for Reynolds numbers from 500 to 15 000. Large mean velocities and small fluctuations are found in regions where the secondary flow is directed towards a surface, while small mean velocities and large fluctuations are found in regions where the secondary flow is directed away from a surface. The Swirl Flow Tube provides a significant increase in the j factor at Reynolds numbers from 1000 to 2000, with corresponding increase in the f factor. At higher Reynolds numbers, the j and f factors of the Swirl Flow Tube are of the same order of magnitude as for the other rib-roughened channels. At Reynolds numbers above 4000, this channel provides the highest j/f ratio if the v-ribs are pointing upstream; while it provides the lowest j/f ratio of all rib configurations, if the v-ribs are pointing downstream.

Aliaga et al. [114] used infrared (IR) thermo-graphy technique to measure heat transfer of a square rib roughened surface and reported that a minimum heat transfer coefficient occurring at down-stream face of the rib due to re-circulating flow whereas a local maximum heat transfer coefficient value occurs at reattachment points. The distance of the reattachment point from rear face of a rib was determined to lie between three to four rib heights from the rear face of the rib. A decrease of the local heat transfer coefficient after reattachment continued until a minimum value occurred at the point of flow separation. The distance from the separation point to the downstream rib was about one to two rib heights.

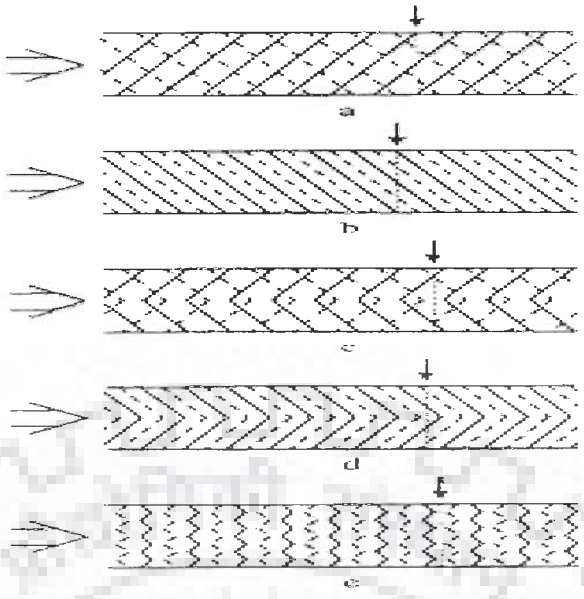

Fig.1.29 Rib configurations: (a) cross rib-roughened; (b) parallel rib-roughened; (c) cross v-rib-roughened; (d) parallel v-rib-roughened; (e) swirl flow tube [113]

Khanna and Kant [115] reported that enhancement of heat transfer associated with pressure drop due to the use of in-line propellers in a pipe flow under constant heat flux condition in turbulent flow regime. Fractional increase in average Nusselt number, fanning friction factor and efficiency were determined as a function of Reynolds number and number of propellers.

Wu and cooper [116] used hemispherical indentations as roughness elements on absorber plates and showed that heat transfer is enhanced by a factor 1.7 to 1.9 over that for smooth absorbers. The friction factor of the wholly rough surface has been correlated by the expression

$$fr = 0.0854\ (Re)^{-0.0325} \qquad (1.37)$$

The smooth and roughened duct Nusselt number data were correlated by the relations:

$$Nus = 0.0321\ (Re)^{0.771} \qquad (1.38)$$

$$Nur = Nus\ (fr/fs)^{0.5} \qquad (1.39)$$

Hosni and Coleman [117] investigated the effect of truncated cone roughness elements on Stanton number and skin coefficient friction and compared the experimental data with previously reported results obtained in the same test facility under similar flow conditions. Predictions of Stanton number and skin friction coefficient distributions from the finite difference solutions of discrete element equations have been compared with the experiments.

Hsieh and Hong [118] used smoke-flow-visualization techniques to observe vortices being shed periodically in the curved shear layer from the downstream sharp corner of the ribs. The flow in the re-circulating regions between two consecutive ribs exhibits a definite pattern. It was characterized by two separation vortices, one formed on the upstream face and the other formed on the downstream face of the ribs. It appears that the separation point of these two vortices shifts further downstream as the Reynolds number increases.

Kim and Kim [119] optimized the shape of rib-roughened surface by numerical optimization technique coupled with RANS analysis of flow and heat transfer in case of single surface roughened in two dimensional channel. Computed reattachment length was found to be shorter than the measurement. Discrepancies were also found on the surfaces of the rib, which probably result from the approximation of heat flux distribution. However, the analysis yielded generally good prediction enough to estimate the overall heat transfer performance of specific rib shape.

1.9 ARTIFICIAL ROUGHNESS GEOMETRIES USED IN SOLAR AIR HEATERS

The use of artificial roughness in solar air heaters owes its origin to several investigations carried out in connection with the enhancement of heat transfer in nuclear reactors, cooling of turbine blades and electronic equipment. It was pointed out earlier that thermal efficiency of a solar air heater can be improved by using artificial roughness in the form of ribs or wires having different shapes and orientations to break the viscous sub layer. As a result convective heat transfer coefficient between air and the absorber plate increases, thereby; thermal performance of solar air heater is considerably improved. Some of the important roughness geometries employed in solar air heaters for thermal performance improvement are discussed as:

1.9.1 Transverse Continuous Ribs

Prasad and Mullick [120] studied the effect of protruding wires on friction factor, heat transfer coefficient and plate efficiency factor of a solar air heater used for drying of agricultural products. High mass flow rates were used to have turbulent flow in the ducts and protruding wires of 1mm diameter tripped the laminar sub-layer. They compared the Nusselt number, friction factor and plate efficiency factor of roughened corrugated and roughened plane absorber plates with that of corrugated without roughness and smooth absorber plates. The protruding wires enhanced the heat transfer coefficient for the roughened air heaters and plate efficiency factor improved from 0.63 to 0.72 resulting in 14% improvement in the performance.

Prasad and Saini [72, 73] studied the effect of roughness and flow parameters such as relative roughness height, e/D and relative roughness pitch, P/e on heat transfer and friction factor. The type and orientation of roughness geometry used has been shown in Fig.1.30. They developed expressions for the heat transfer and friction

factor for a fully turbulent flow. It was observed that maximum heat transfer occurred in the vicinity of reattachment points and reattachment of free shear layer doers not occur if relative roughness pitch, P/e is less than about 8 to 10. Optimal thermohydraulic performance is achieved for roughness height slightly higher than the transition sub layer thickness. For relative roughness height, e/D value of 0.033 and relative roughness pitch, P/e value of 10, maximum enhancement in Nusselt number and friction factor was reported to be 2.38 and 4.25 times respectively in comparison with smooth duct.

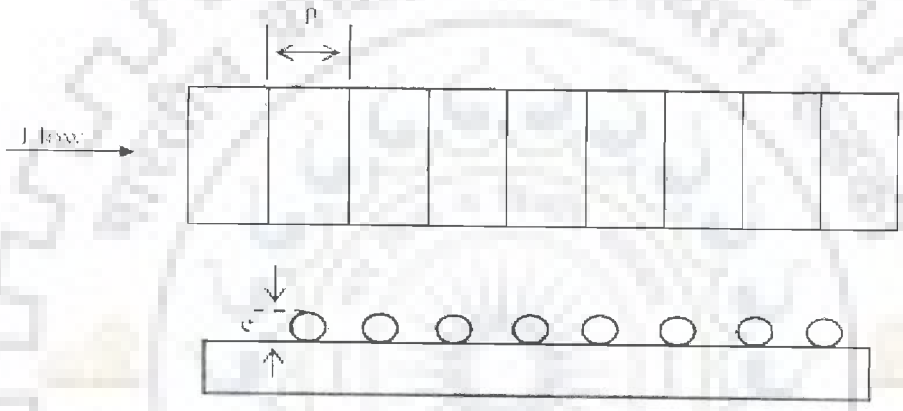

Fig.1.30 Roughness geometry used by Prasad and Saini [72]

With the previous investigations carried out for fully rough flow conditions ($e^+>70$), Gupta et al. [63] carried out an experimental investigation for transitionally rough flow region ($e^+<50$) in which most of the solar air heaters operate and developed correlations for friction factor and Nusselt number over a wide range of roughness geometry parameters. They studied heat transfer and friction characteristics of a rectangular duct roughened with transverse wires, with relative roughness height, e/D varying from 0.018 to 0.052, aspect ratio, W/H range of 6.8-11.5 and Reynolds number, Re range of 3000-18000 for a fixed value of relative roughness pitch, P/e of 10. It was observed that for fully rough flow region, Stanton number decreased monotonously with increase in Reynolds number, Re for a given roughness

configuration. In a transitionally rough flow region, Stanton number increased with increase in Reynolds number, Re and attained a point of maxima for Reynolds number value of about 12000. The point of maxima shifted towards lower values of Reynolds number, Re as the value of relative roughness height, e/D is increased.

Verma and Prasad [121] carried out an outdoor experimental investigation for thermohydraulic optimization of the roughness geometry and flow parameters for Reynolds number, Re, range of 5000-20000, relative roughness pitch, P/e range of 10-40 and relative roughness height, e/D range of 0.01-0.03. The optimal value of roughness Reynolds number, e^+ was found to be 24 and corresponding to this value, thermohydraulic efficiency parameter value was found to be 71%. Heat transfer enhancement factor was found to vary between 1.25 and 2.08 for the range of parameters investigated. Correlations for heat transfer and friction factor were developed.

Karwa [122] experimentally investigated the effect of repeated rectangular cross-section ribs on heat transfer and friction factor for duct aspect ratio, W/H range of 7.19 to 7.75, relative roughness pitch, P/e value 10, relative roughness height, e/D range of 0.0467 - 0.050, Reynolds number range of 2800-15000. It was explained that vortices originating from the roughness elements beyond the laminar sub layer are responsible for heat removal as well as increase in friction factor. The enhancement in the Stanton number was reported to be 65-90% while friction factor was found to be 2.68-2.94 times over smooth duct.

1.9.2 Transverse Broken Ribs with Circular Cross-Section

Sahu and Bhagoria [123] investigated the effect of 90^0 broken ribs on the enhancement of the thermal performance of solar air heaters for fixed roughness height, e value of 1.5 mm, duct aspect ratio, W/H value of 8, pitch, P in the range of

10- 30 mm and Reynolds number range of 3000-12000. Roughened absorber plate increased the heat transfer coefficient by 1.25-1.4 times as compared to smooth rectangular duct under similar operating conditions. Corresponding to roughness pitch, P value of 20 mm, maximum value of Nusselt number was obtained that decreased on the either side of this roughness pitch, P value. Based on the experimental investigation, the thermal efficiency of roughened solar air heater was found to be in the range of 51-83.5% depending upon the flow conditions. The investigated geometry ha been shown in Fig.1.31.

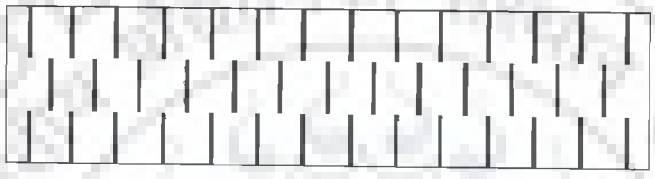

Fig.1.31 Transverse broken ribs [123]

1.9.3 Inclined Continuous Ribs

Gupta et al. [63] experimentally investigated the effect of relative roughness height, e/D, inclination of rib with respect to flow direction and Reynolds number on the thermohydraulic performance of a roughened solar air heater for transitionally rough flow region ($5<e^{+}<70$). The roughness geometry investigated has been shown in Fig.1.32. It was reported that with increase in relative roughness height, value of Reynolds number decreased for which value of effective efficiency was found to be maximum. The effective efficiency also increased with increase in insolation. For a roughened solar air heater, maximum enhancement in heat transfer and friction factor was reported to be of the order 1.8 and 2.7 times respectively for an angle of inclination of 60^0 and 70^0 respectively. Best thermohydraulic performance was reported for relative roughness height value of 0.023 and Reynolds number value of 14000.

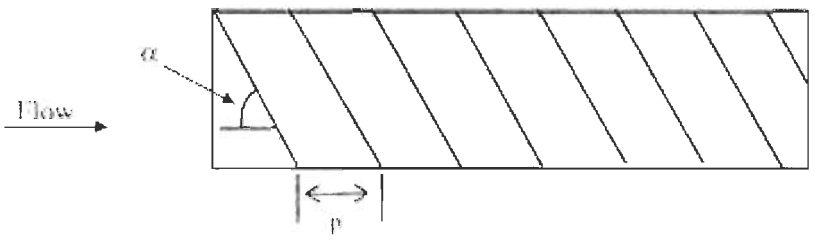

Fig.1.32 Roughness geometry used by Gupta et al. [63]

Karwa [122] experimentally investigated the effect of repeated, 60° inclined rectangular cross-section ribs on heat transfer and friction factor for aspect ratio, W/H range of 7.19 - 7.75, relative roughness pitch, P/e value of 10, relative roughness height, e/D range of 0.0467-0.050 and Reynolds number, Re range of 2800-15000. The enhancement in the Stanton number was reported to be 22-32% and increase in friction factor was of the order of 1.12-1.16 times over transverse ribs.

1.9.4 Inclined Ribs with Gap

Aharwal et al. [76] experimentally studied the effect of width and position of gap in an inclined split ribs having square cross-section on heat transfer and friction characteristics of a rectangular duct. The duct had an aspect ratio, W/H of 5.84, relative roughness pitch, P/e of 10, relative roughness height, e/D of 0.0377, angle of attack, α of 60°, relative gap width, g/e range of 0.5-2 and relative gap position, d/W varied from 0.1667-0.667 for Reynolds number, Re, range of 3000-18000. For the split - rib and continuous rib roughened ducts, the enhancement in heat transfer was reported to be in the range of 1.71–2.59 times and 1.48–2.26 times respectively under similar operating conditions. The maximum values of heat transfer, friction factor ratio (f/f_s) and thermohydraulic parameter obtained were corresponding to relative gap width value of 1.0 and relative gap position value of 0.25 for the range of parameters investigated. PIV (Particle Image Velocimetry) system was used to visualize the effects of rib geometry on the flow behavior. The geometry investigated has been shown in Fig.1.33.

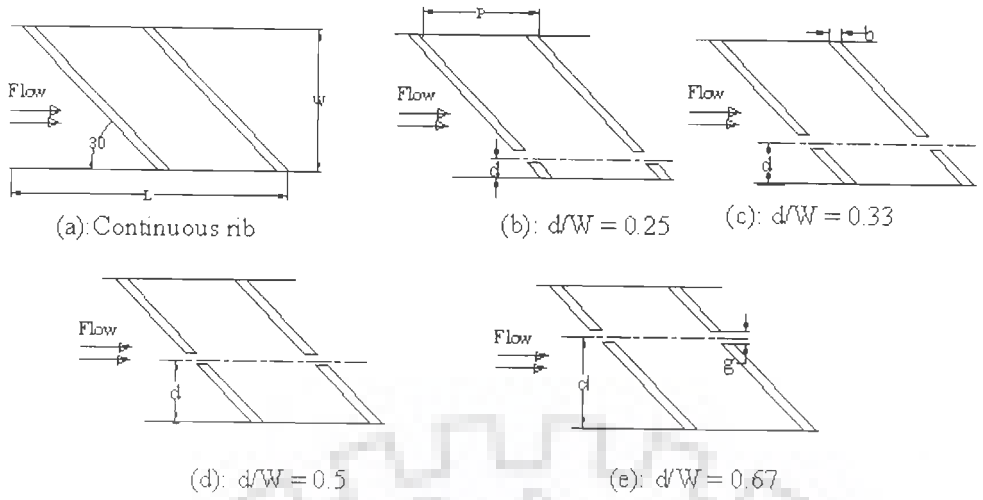

Fig.1.33 Inclined ribs with gap [76]

1.9.5 Expanded Mesh Metal

Saini and Saini [75] carried out an experimental investigation to study the effect of wire mesh roughened absorber plate on heat transfer augmentation and friction characteristics of solar air heaters as shown in Fig.1.34. The investigation considered relative longway length of mesh, L/e,in range of 25-71.87, relative shortway length of mesh, S/e in range of 15.62-46.87, relative roughness height, e/D in range of 0.012-0.039 and Reynolds number, Re, in range of 1900-13000. It was reported that the maximum heat transfer of order 4 times over the smooth duct were obtained corresponding to angle of attack of 61.9^0, relative longway length of mesh, L/e, value of 46.87 and relative shortway length of mesh, S/e, value of 25. Maximum value of friction factor was reported for angle of attack of 72^0, relative longway length of mesh, L/e value of 71.87 and relative shortway length of mesh, S/e value of 15. Correlations for Nusselt number and friction factor were developed.

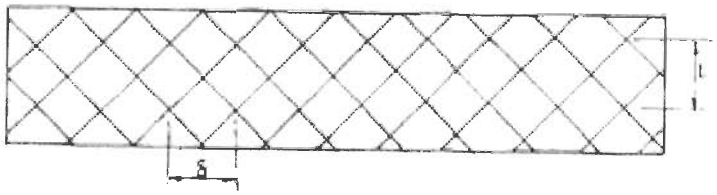

Fig.1.34 Roughness geometry used by Saini and Saini [74]

1.9.6 V-shaped Ribs

Momin et al. [69] experimentally investigated the effect of geometrical parameters of v-shaped ribs, shown in Fig.1.35, on heat transfer and fluid flow characteristics of a rectangular duct of a solar air heater. The investigation covered a Reynolds number, Re range of 2500-18000, relative roughness height, e/D range of 0.02-0.034 and angle of attack, α range of $30-90°$ for a fixed relative roughness pitch, P/e of 10. Rate of increase of Nusselt number was observed to be lower than the rate of increase of friction factor with an increase in Reynolds number, Re. The maximum enhancement of Nusselt number and friction factor as a result of providing artificial roughness had been found to be 2.30 and 2.83 times respectively over the smooth duct for an angle of attack, α value of 60°. It was reported that for relative roughness height, e/D value of 0.034 and angle of attack, α value of 60°, v-shaped ribs enhanced the value of Nusselt number by 1.14 and 2.30 times over inclined ribs and smooth absorber plate respectively. Correlations for heat transfer and friction factor were developed.

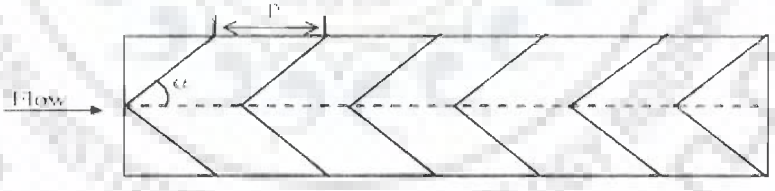

Fig.1.35 Roughness geometry used by Momin et al. [69]

Mulluwork et al. [70] compared the thermal performance of staggered discrete v-apex up and down ribs with corresponding transverse staggered discrete ribs as shown in Fig.1.36. They studied the effect of relative roughness length ratio, B/S, relative roughness segment ratio, S'/S, relative roughness staggering ratio, P'/P and angle of attack, α on heat transfer and friction factor. It was observed that Nusselt number increased with the increase in relative roughness length ratio, B/S. Nusselt

number for v-down discrete ribs was found to be higher than the corresponding v-up and transverse discrete roughened surfaces. Nusselt number increased with increase in relative roughness staggering ratio, P'/P and attained a maximum value of Nusselt number for relative roughness staggering ratio, P'/P value of 0.6. Heat transfer and friction factor attained maximum values for angle of attack of 60^0 and 70^0 respectively. Correlations for Nusselt number and friction factor were developed.

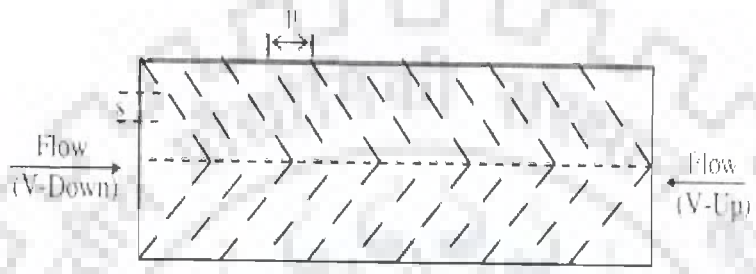

Fig.1.36 Discrete v-ribs [70]

Karwa [122] carried out a comparative experimental study of augmented heat transfer and friction in a rectangular duct having rectangular cross-section ribs arranged in transverse, inclined, v-continuous and v-discrete pattern for duct aspect ratio, W/H range of 7.19 -7.75, relative roughness pitch, P/e value 10, relative roughness height, e/D range of 0.0467-0.050 and Reynolds number, Re range of 2800-15000. The enhancement in the Stanton number over the smooth duct was reported to be in range of 65-90%, 87-112%, 102-137%, 110-147%, 93-134% and 102-142% for transverse, inclined, v-up continuous, v-down continuous, v-up discrete and v-down discrete rib arrangement respectively. The friction factor ratios corresponding to these arrangements were found as 2.68-2.94, 3.02-3.42, 3.40-3.92, 3.32-3.65, 2.35-2.47 and 2.46-2.58 respectively. The performance of v-down ribs was observed to be better than that of v-up ribs, which was in confirmation with the findings of Mulluwork et al. [70]. The rib configurations investigated in the study have been shown in Fig.1.37.

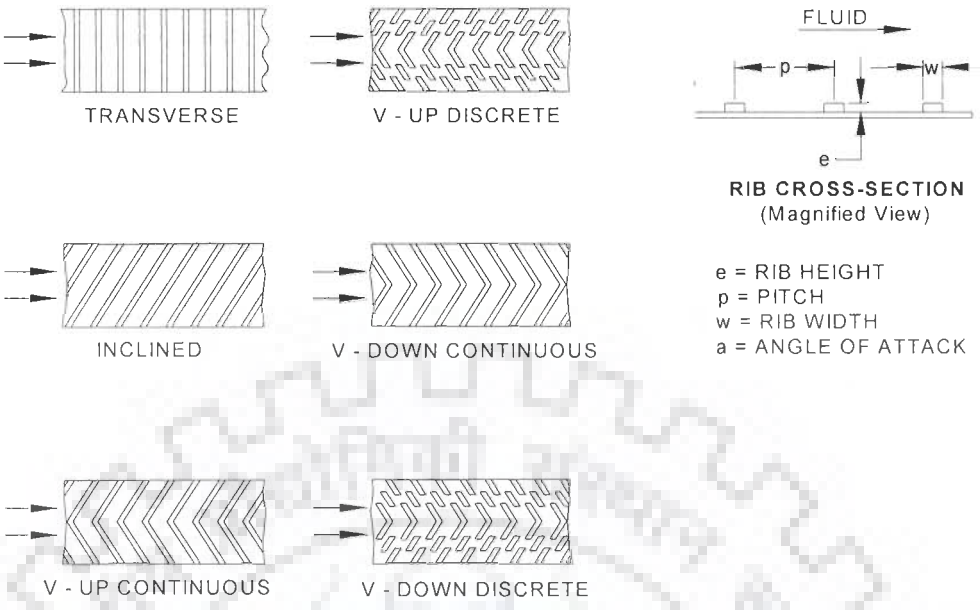

Fig.1.37 Roughness geometries used by Karwa [122]

Karwa et al. [124] experimentally studied the heat transfer and friction in a high aspect ratio, W/H rectangular duct with repeated rectangular cross-section ribs on one broad wall in v-discrete and discontinuous patterns at angles of inclination of 45° and 60°, relative roughness pitch, P/e value of 10.63, relative roughness length, B/S values 3 and 6 with Reynolds number, Re varied from 2850 to 15500. It was observed that corresponding to relative roughness length, B/S value of 6, the highest and the lowest values of Stanton number ratio, St/St_s were obtained for 60° v-down discrete and 60° v-up discontinuous ribs respectively. Friction factor ratio, f/f_s values were found to be maximum and minimum for 60° v-down discrete and 45° v-up discrete ribs corresponding to relative roughness length, B/S value of 3. Stanton number and friction factor values were reported to be higher for v-down pattern in comparison with v-up pattern and 60° v-shaped ribs performed better than the 45° v-shaped ribs. Rib pattern had a strong effect on the Stanton number and friction factor with discrete ribs performing better than other rib configurations from

thermohydraulic performance point of view. The various v-rib configurations investigated have been shown in Fig.1.38.

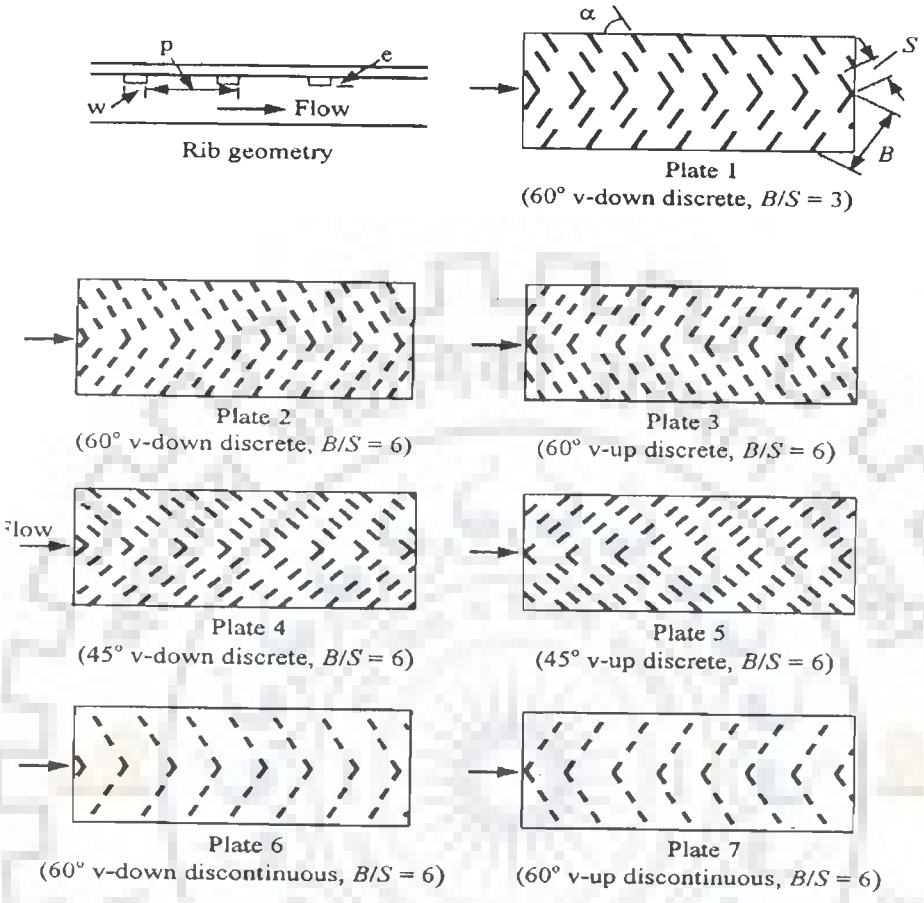

Fig.1.38 Different v-rib geometries [124]

1.9.7 Chamfered Ribs

Karwa et al. [66] performed an experimental investigation of heat transfer and friction for rectangular ducts having aspect ratio, W/H in the range of 4.8-12, and roughened with repeated integral chamfered ribs as shown in Fig.1.39. The roughness geometry and flow parameters considered for the investigation were Reynolds number, Re range of 3000-20000, relative roughness height, e/D range of 0.014 - 0.0328, relative roughness pitch, P/e range of 4.5 - 8.5 and chamfer angle, Φ varying from -15^0 to 18^0. Stanton number and friction factor increased with increase in chamfer angle and attained maximum value corresponding to chamfer angle value of

15^0. It was reported that Stanton number decreased while friction factor increased with increase in aspect ratio, W/H. As compared to the smooth duct, the presence of chamfered ribs on one of the broad wall of duct yielded up to about two-fold and three-fold increase in the Stanton number and the friction factor respectively in the range of parameters investigated. Heat transfer and friction factor correlations were developed.

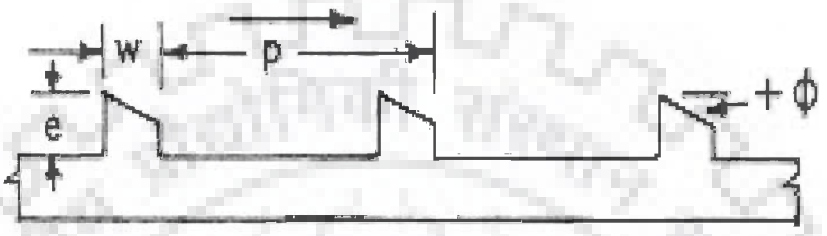

Fig.1.39 Chamfered rib geometry [66]

1.9.8 Wedge Shaped Ribs

Bhagoria et al. [125] experimentally studied heat transfer and flow characteristics in a solar air heater with absorber plate roughened with wedge shaped transverse integral ribs as shown in Fig.1.40. The investigation encompassed the Reynolds number, Re range of 3000-18000, relative roughness height, e/D range of 0.015- 0.033 and rib wedge angle, Φ range of $8\text{-}12^0$. It was reported that Nusselt number and friction factor increased by 2.4 and 5.3 times over smooth duct in the range of parameters investigated. Statistical correlations for Nusselt number and friction factor were developed.

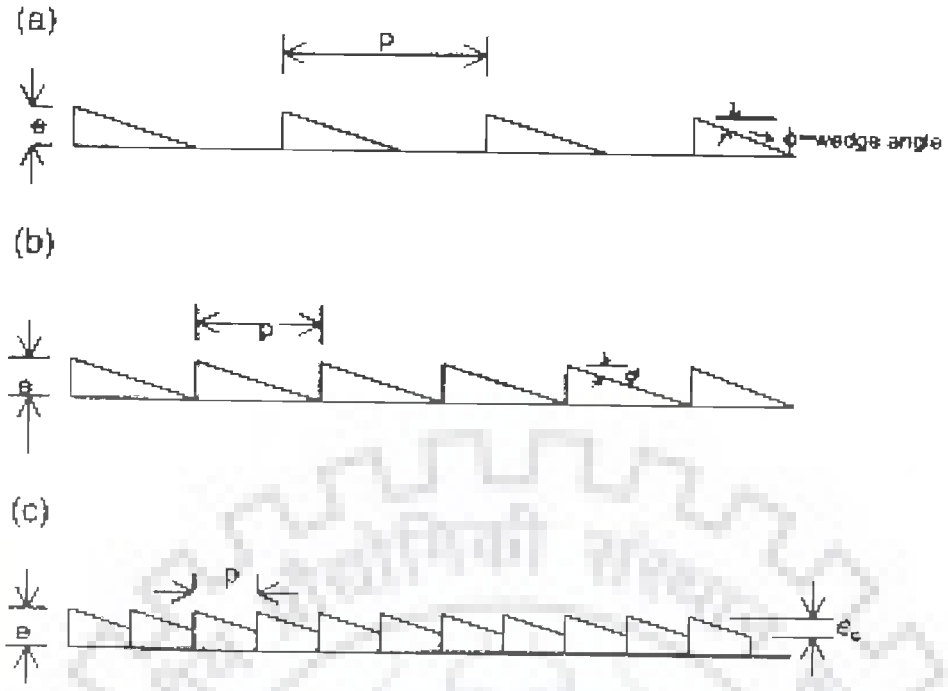

Fig.1.40 Roughness geometry used by Bhagoria et al. [125]

1.9.9 Arc Shaped Ribs

Saini and Saini [126] studied the effect of arc shaped ribs on the heat transfer coefficient and friction factor of rectangular ducts with Reynolds number, Re, relative roughness height, e/D, and relative arc angle, α varying from 2000-17000, 0.0213 – 0.0422 and 0.3333-0.6666 respectively. It was reported that relative arc angle, α had an opposite effect on heat transfer enhancement and friction factor. With decrease in relative arc angle value, Nusselt number value increased while friction factor value decreased. Enhancement of Nusselt number and friction factor was reported to be of order 3.6 and 1.75 times respectively over smooth duct for relative arc angle, α value of 0.3333 and relative roughness height, e/D value of 0.0422. Based on the experimental results, correlations for Nusselt number and friction factor were developed. The investigated geometry has been shown in Fig.1.41.

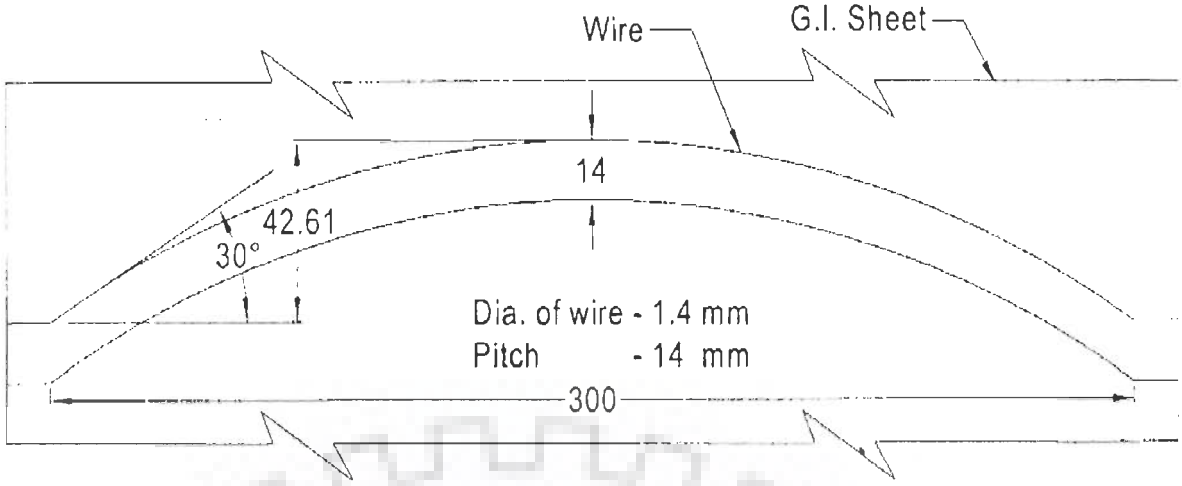

Fig.1.41 Roughness geometry used by Saini and Saini [126]

1.9.10 Dimpled Surfaces

Saini and Verma [127] studied the effect of roughness geometry and operating parameters on heat transfer and friction factor in a roughened duct provided with dimple-shape roughness geometry for the range of Reynolds number, Re from 2000 to 12,000, relative roughness height, e/D from 0.018 to 0.037 and relative roughness pitch, P/e from 8 to 12. For the range of parameters investigated, Nusselt number was found to be maximum corresponding to relative roughness height, e/D value of 0.0379 and relative roughness pitch, P/e value of 10. For fixed value of relative roughness pitch, P/e, of 10, friction factor attained the maximum and minimum values corresponding to relative roughness height, e/D values of 0.0289 and 0.0189 respectively. Correlations for Nusselt number and friction factor have been developed. The geometry investigated has been shown in Fig.1.42.

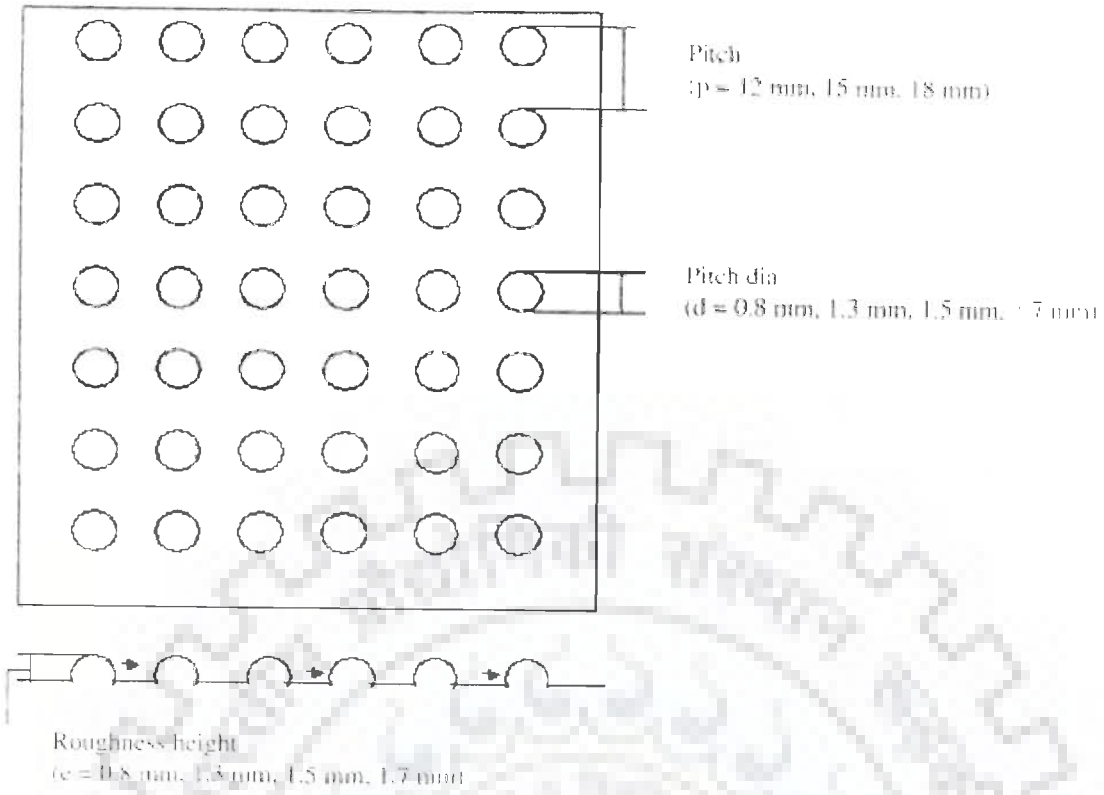

Fig.1.42 Dimpled roughness geometry [127]

1.9.11 Metal Grit Ribs

Karmare and Tikekar [128] experimentally investigated the heat transfer and friction characteristics of a rectangular duct having absorber plate roughened with defined grid of metal ribs of circular cross-section and the investigated roughness geometry has been shown in Fig.1.43. The investigation considered relative roughness height, e/D range of 0.035 - 0.044, relative roughness pitch, P/e range of 12.5–36, relative grit length, l/s range of 1.72–1 and Reynolds number, Re range of 4000–17,000. Enhancement in Nusselt number was found to be 187% and the friction factor increased by 213% and optimum performance was observed for relative grit length, l/s, value of 1.72, relative roughness height, e/D value of 0.044, and relative roughness pitch, P/e value of 17.5 for the range of parameters studied. Based on experimental data, correlations for Nusselt number and friction factor were developed.

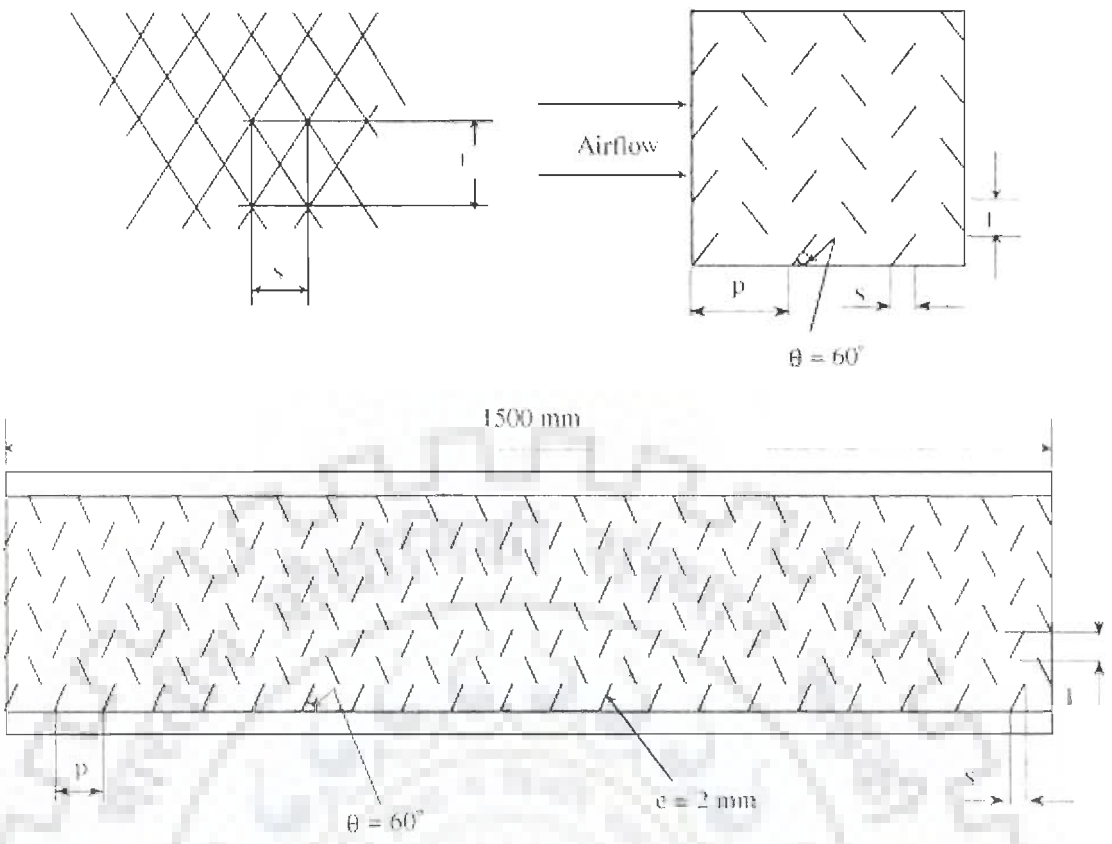

Fig.1.43 Metal grit ribs [128]

1.9.12 Discrete W-Shaped Ribs

Kumar and Bhagoria [129] studied heat transfer and friction characteristics of a rectangular channel having discrete w-shaped roughness provided on one broad wall as shown in Fig.1.44. The experiment encompassed the Reynolds number, Re range from 3000-15000, relative roughness height, e/D range from 0.0168 - 0.0338, relative roughness pitch, P/e value 10, and angle of attack, α range from 30^0 - 75^o. It was reported that maximum enhancement of Nusselt number and friction factor in comparison to smooth duct was of order of 2.16 and 2.75 times respectively for an angle of attack, α value of 60^o. Flow separation and secondary flow resulting due to the presence of discrete w-shaped rib combined to provide an optimum value of angle of attack, α. Discretization was found to have significant effect on heat transfer enhancement. Correlations for Nusselt number and friction factor were developed.

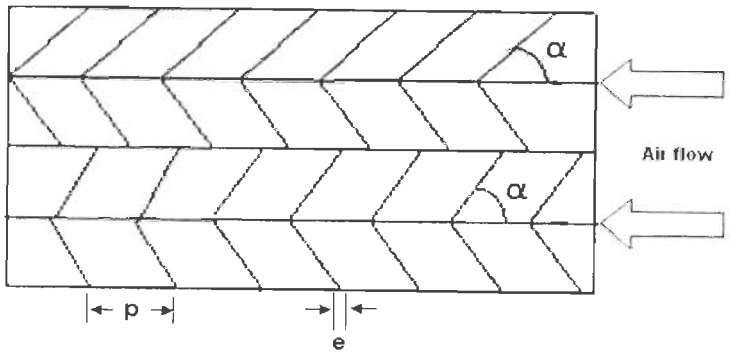

Fig.1.44 Discrete W-shaped ribs [129]

1.9.13 Combination of Different Roughness Elements

Jaurker et al. [64] experimentally investigated the heat transfer and friction characteristics of rib-groove roughened rectangular duct as shown in Fig.1.45. The effect of relative roughness pitch, P/e, relative roughness height, e/D and relative groove position, g/P on heat transfer coefficient and friction factor has been studied. The presence of rib-grooved artificial roughness enhanced Nusselt number and friction factor up to 2.7 and 3.6 times respectively in comparison to smooth absorber plate. The maximum heat transfer occurred for a relative roughness pitch, P/e of about 6 and relative groove, g/P value of 0.4. Correlations for Nusselt number and friction factor were developed.

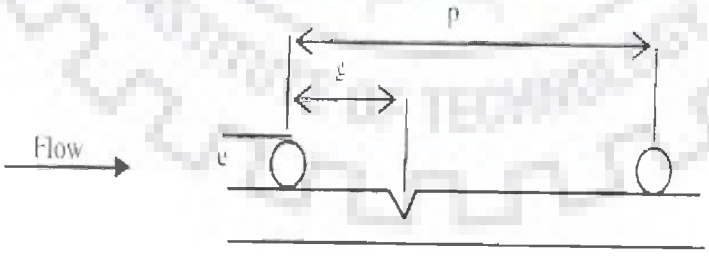

Fig.1.45 Rib-groove-1 geometry [64]

Layek et al. [67] carried out an experimental investigation to study the heat transfer and friction for repeated transverse compound rib-groove arrangement on absorber plate of a solar air heater. Four relative rib-groove positions, g/P values of

0.3, 0.4, 0.5 and 0.6 were investigated for fixed relative roughness height, e/D and relative roughness pitch, P/e values of 0.03 and 10 respectively. It was found that relative roughness pitch, P/e value of 10, relative groove position, g/P value of 0.4 provided about 2.42 and 2.6 times increase in the Nusselt number and friction factor respectively for entire range of Reynolds number, Re studied. Correlations for Nusselt number and friction factor were developed. The investigated geometry has been shown in Fig.1.46.

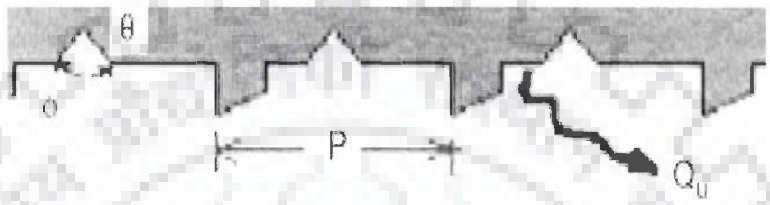

Fig.1.46 Rib-Groove-2 geometry [67]

Varun et al. [130] carried out an experimental study on heat transfer and friction characteristics by using a combination of inclined and transverse ribs on the absorber plate of a solar air heater with Reynolds number, Re ranging from 2000 to 14 000, relative roughness pitch, P/e range of 3–8, relative roughness height, e/D value of 0.030, duct aspect ratio, W/H value of 10 and roughness height, e value of 1.6 mm. For relative roughness pitch, P/e value of 8, the best thermal performance was reported. Correlations for Nusselt number and friction factor were developed. The investigated geometry has been shown in Fig.1.47.

Fig.1.47 Inclined and transverse ribs [130]

1.9.14 U-Shaped Ribs

Bopche and Tandale [131] carried out an experimental investigation to study the heat transfer coefficient and friction factor of a rectangular duct roughened artificially with u-shaped turbulator. The experimental encompassed Reynolds number, Re range from 3800 to 1800, ratio of turbulator height to hydraulic mean diameter, e/D is varied from 0.0186 to 0.03986, relative roughness pitch, P/e, range of 6.67 to 57.14 and value of angle of attack, α is kept constant at 90^0. The u-shaped roughness geometry shows appreciable heat transfer enhancement even when Reynolds number value is less than 5000 where ribs are generally inefficient. At Reynolds number value of 3800, maximum enhancement in Nusselt number and friction factor are reported to be 2.388 and 2.50 respectively.

1.9.15 Computational Analysis

Chaube et al. [132] carried out a computational analysis using Fluent 6.1 software to investigate flow and heat transfer characteristics of two-dimensional rib roughened rectangular ducts with one wall subjected to uniform heat flux of 1100 W/m^2. They compared the predictions of different turbulence models with experimental results available in the literature and reported good matching of predictions of shear stress transport (SST) K-ω turbulence model. They used SST K-ω turbulence model for analyzing the performance of nine different roughness elements and compared the predictions on the basis of heat transfer enhancement, friction characteristics and performance index. The results obtained from two-dimensional model were reported to be closer to the experimental results and these models required less memory and computational time as compared to three-dimensional models. The highest heat transfer was reported in case of chamfered ribs, however, the best performance index was found to be for rectangular rib of size 3 x 5 mm with in the range of parameters investigated.

Sharad [133] analyzed the effects of arc shaped roughness geometry on heat transfer and friction by computational fluid dynamics (CFD). The results obtained from different models of computational analysis were compared with Dittus-Boelter empirical relationship for smooth duct and it was found that the Renormalization (RNG) k-ε model had least variation as compared to other CFD models.

1.10 HEAT TRANSFER AND FRICTION FACTOR CORRELATIONS

In most of the solar air heaters roughened artificially for heat transfer enhancement, correlations have been developed for heat transfer coefficient and friction factor in terms of roughness geometry parameters. Some of the correlations developed for heat transfer coefficient and friction factor are given in Table 1.3.

1.11 THERMOHYDRAULIC PERFORMANCE OF ARTIFICIALLY ROUGHENED SOLAR AIR HEATERS

It is evident from the above discussion that use of artificial roughness brings about a considerable improvement in the thermal performance of a solar air heater along with corresponding increase in pressure drop resulting in greater pumping power requirements to make air flow through the duct of a solar air heater. Therefore, geometry and orientation of roughness elements should be chosen in such a way that enhancement in heat transfer occurs at minimum possible pressure drop. It becomes imperative to evaluate thermal as well as hydraulic performance of roughness geometry in order to obtain the optimum roughness geometry parameters. To account for the pressure drop in the performance of roughness geometry, researchers have suggested number of criteria that combine thermal and hydraulic performance of a roughness geometry.

The existence of optimum conditions, for a given rough surface, was proposed by Sheriff and Gumley [134]. It was reported that the characteristics of a roughened surface necessary to give minimum pumping power in the channel can be written as:

Table 1.3 Summary of heat transfer and friction factor for artificially roughened solar air heaters

Investigators	Type of Roughness	Roughness parameter Range					Correlation	
		e/D	P/e	α	e^+	W/H	Heat Transfer	Friction factor
Gupta et al. [63]	*Oblique wire roughness*	0.018-0.052	10	40- 90		6.8-11.0	$Nu = 0.00247\ (e/D)^{0.001}$ $(W/H)^{-0\ 06}\ Re^{1.084}$ $[exp\{-0.04(1-\alpha/60^0)^2\}]$ for $e^+<35$ $Nu = 0.007\ (e/d)^{-0.24}(W/H)^{-0.028}$ $Re^{0\ 88}[exp\{-0.475(1-\alpha/60^0)^2\}]$ for $e^+ > 35$	$f = 0.1991(e/D)^{0.196}$ $(W/H)^{-0\ 093}\ Re^{-0.165}\ [exp\{-0.0993(1-\alpha/70^0)^2\}]$
Jaurker et al. [64]	*Rib groove-1 compound roughness*	0.0181-0.0363	4.5-10	90	-	7	$Nu = 0.002062Re^{0.936}\left(\frac{e}{D}\right)^{0.349}\left(\frac{P}{e}\right)^{3.318}\left(\frac{g}{p}\right)^{1\ 108} exp\left[-0.868\left\{ln\left(\frac{P}{e}\right)\right\}^2\right] exp\left[2.486\left\{ln\left(\frac{g}{P}\right)\right\}^2 + 1.406\left\{ln\left(\frac{g}{P}\right)\right\}^3\right]$	$f = 0.001227\ (Re)^{-0.199}\left(\frac{e}{D}\right)^{0.585}\left(\frac{P}{e}\right)^{7\ 19}\left(\frac{g}{P}\right)^{0.645} exp\left(-1.854\left\{ln\left(\frac{P}{e}\right)\right\}^2\right) exp\left(1.513\left\{ln\left(\frac{g}{P}\right)\right\}^2 + 0\ 8662\left\{ln\left(\frac{g}{P}\right)\right\}^3\right)$

Layek et al. [67]	Chamfered rib-grooved	0.018-0.036	4.5-10	90	-	-	$Nu=0.00225\ Re^{0.92}((e/d))^{0.52}(p/e)^{1.72}$ x exp [-0.22 $(\ln \Phi)^2$] x exp[-0.46{ln(p/e)}^{2}] $(g/P)^{-1.21}$ $\Phi^{1.24}$ x exp [-0.74{ln(g/P)}^{2}]	$f= 0.00245$ x $Re^{-0.124}((e/d))^{0.365}(p/e)^{4.32}(g/P)^{-1.124}$ x exp[-1.09 {ln((p/e))}^{2}] x exp[-0.68{ln(g/P)}^{2}] x exp[0.005Φ]
Momin et al. [69]	*V shaped wire roughness*	0.02- 0.034	10	30, 45, 60, 90	5- 60	10	$Nu = 0.067\ (e/D)^{0.424}\ Re^{0.888}\ (\alpha/60^0)^{-0.077}$ [*exp*{-0.782 (*ln* $(\alpha/60^0))^2$]	$f= 6.266\ (e/D)^{0.565}Re^{-0.425}\ (\alpha/60)^{-0.093}$ [*exp*{-0.719 (*ln* $(\alpha/60^0))^2$]
Mulluwork [70]	*V-shaped discrete*	0.01-0.05	-	30-90	-	12.6	$Nu = 0.00534\ Re^{1.2991}\ (B/S)^{1.3496}\ (S'/S)^{1.112}(e/D_h)^{0.27}(P'/P)^{0.762}$ *exp*[-2.25 (*ln*(P'/P))^2] *exp*[-0.376 (*ln* (1-(α/60))^2]	$f= 0.717Re^{-2.991}\ (B/S)^{0.0636}\ (S'/S)^{0.0712}(e/D_h)^{0.113}\ (P'/P)^{-0.00936}$ *exp*[-1.26 (*ln* (1-(α/70))^2]
Prasad and Saini [72, 73]	*Transverse wire roughness*	0.02 - 0.033	10, 20	90	20	-	$St = (f/2)/\ [1+\sqrt{(f/2)}\{4.5\ Pr^{0.57}\ (e^+)^{0.28} - 0.95(P/e)^{0.53}\}]$	$f= 2/\ [0.95(P/e)^{0.53} + 2.5\ ln\ (D/2e) - 3.75]$
Saini and Saini [75]	*Expanded metal mesh*	0.012-0.039	-	-	-	11.6	$Nu = 4\times10^{-4}Re^{1.22}(e/D)^{0.625}\ (S/10e)^{2.22}(L/10e)^{2.66}$[*exp*{-1.25 (*ln* (S/10e))^2}][*exp*{-0.824(*ln* (L/10e))^2}]	$f= 0.815\ Re^{-0.361}\ (L/e)^{0.266}\ (S/10e)^{-0.19}\ (10e/D)^{0.591}$

Aharwal et al. [76]	Inclined rib with gap	0.0377	10	60°	-	5.84	$Nu=0.002\ Re^{1.08\,(p/e)1.87}$ x $\exp[-0.45(\ln(p/e))^2]$ $(\alpha/60)^{0.006}$ x exp [-0.65(ln $\alpha/60)^2$] $(d/W)^{-0.32}$ x exp[-0.12 (ln $d/W)^2$] $(g/e)^{-0.03}$ x exp[-0.18 $(\ln g/e)^2$] $(e/D)^{0.5}$	$f=0.071\ Re^{-0.133\,(p/e)1.83}$ $\exp[-0.44(\ln(p/e))^2]$ x $(d/W)^{-0.43}$ x exp[-0.14 (ln $d/W)^2$] $(g/e)^{-0.052}$ x $(\alpha/60)^{0.67}$ $(\exp[0.12\ (\ln g/e)^2]$ $(e/D)^{0.69}$
Bhagoria et al. [125]	*Wedge rib roughness*	0.015 0.033	7.12- 12.1	90	5- 60	5	$Nu = 1.89 \times 10^{-4}(e/D)^{0.426}Re^{1.21}$ $(P/e)^{2.94}[exp(-0.71\ (ln\ (P/e))^2]$ $(\varphi/10)^{-0.018}$ $[exp\{-1.50\ (ln\ (\varphi/10^0))^2\}]$	$f = 12.44\ (e/D)^{0.99}\ Re^{-0.18}$ $(P/e)^{-0.52}\ (\alpha/10^0)^{0.49}$
Saini and Saini [126]	Arc shaped rib	0.021- 0.042,	10	0.33- 0.66	-	-	$Nu=0.001047\ Re^{1.3186}\ (e/D)^{0.3772}$ x $(\alpha/90)^{-0.1198}$	$f=0.14408\ Re^{-0.17103}$ $(e/D)^{0.1765}\ (\alpha/90)^{0.1185}$
Saini and Verma [127]	Dimple shape rib	0.018- 0.037	8-12	-	-	-	$Nu= 5.2 \times 10^{-4}Re^{1.27}\ \{(p/e))^{3.15}$ x $[\exp(-2.12)(\log((p/e)))^2]$ $(e/D)^{0.033}$ x $[\exp(-1.3)(\log((e/d)))^2]$	$f=0.642\ Re^{-0.423}\ (p/e)^{-0.465}$ $[\exp(0.054)(\log((p/e)))^2]$ x $(e/D)^{-0.0214}$ $[\exp(0.84)(\log((e/d))^2]$

Karmare and Tikekar [128]	Metal grit rib	0.035-0.044	12.5 – 36	-	-	-	$Nu = 2.4 \times 10^{-3} \times Re^{1.3} \times (e/D)^{0.42} (l/s)^{-0.146} \times (p/e)^{-0.27}$	$f = 15.55 \times Re^{-0.263} \times (e/D)^{0.91} (l/s)^{-0.27} \times (p/e)^{-0.51}$
Kumar and Bhagoria [129]	Discrete W-shaped ribs	0.0168-0.0338	10	30°-75°		8	$Nu_r = 0.105 \times (Re)^{0.873} \times (e/D_h)^{0.453} \times (\alpha/60°)^{-0.081} \times \exp[-0.59 \times (\ln(\alpha/60°))^2]$	$f_r = 5.68 \times (Re)^{-0.40} \times (e/D_h)^{0.59} \times (\alpha/60°)^{-0.081} \times \exp[-0.579 \times (\ln(\alpha/60°))^2]$

$$\frac{f}{f_s} < \left(\frac{St}{St_s}\right)^3 \qquad (1.40)$$

Kovarik and Lesse [135] proposed that collection of heat can be optimized by controlling the flow rate in such a way that some given criterion of performance attains its maximum value. The simplest criterion of the performance is expressed in terms of j(m) given by equation:

$$j(m) = -\int[Q(T,M) - S(m)]dt \qquad (1.41)$$

where Q(T, M) is the thermal output rate at temperature, t_c, and mass flow rate, m and S(m) is the thermal equivalent of power spent in maintaining a flow rate, m. The thermal output, Q(T,m) depends on the fluid requirement at collector entry, and mass flow rate. The optimal flow rate, m, if it exists reduces j(m) to its lowest possible value.

As discussed above, it is beneficial to make thermohydraulic considerations as the basis of selection of optimum artificial roughness geometry. This criterion requires selection of a set of roughness geometry parameters that yield the maximum value of thermohydraulic performance of the collector for the given set of design parameters. The computational procedure requires the determination of thermohydraulic performance for a given set of design conditions for all possible roughness geometries. A set of roughness parameters that yields the maximum thermohydraulic performance is then selected as optimal design geometry.

An approximate analytical solution to determine the optimal flow rate through solar collectors was proposed by Winn and Hull [136] to yield the maximum value of a parameter that is integral of the difference between useful energy and gain and pumping cost incurred in collecting the solar energy. The optimum mass flow rate has been given as:

$$m=\frac{\left(F'\right)^2 U_L A_c}{\left[2C_p\left(F'-f\right)\right]} \qquad (1.42)$$

Lewis [137] proposed a model for transverse roughness elements by choosing form drag coefficients for different rib shapes instead of taking specific shapes of these ribs in the parametric study to investigate the performance of rough surfaces. An optimization parameter called thermohydraulic performance parameter, ε, was proposed to evaluate thermohydraulic performance of roughened surfaces and is expressed as :

$$\varepsilon = (St/St_s)^3/(f/f_s) \qquad (1.43)$$

It can be seen that a roughness geometry that yields a value of this parameter greater than unity is useful and out of various values of possible sets, the one that yields the maximum value of this parameter should be used. Prasad and Saini [72] and Ahrawal et al. [76] used the optimization method suggested by Lewis [137] to obtain optimal thermo-hydraulic conditions in artificially roughened solar air heaters when the roughness element height is slightly higher than the laminar sub layer thickness.

A parameter that facilitates the simultaneous consideration of thermal and hydraulic performance is given by Williams et al. [138] as thermo-hydraulic performance ratio (TPR);

$$TPR=\frac{\left(\frac{St}{f^{1/3}}\right)_{rough}}{\left(\frac{St}{f^{1/3}}\right)_{smooth}} \qquad (1.44)$$

Cortes and Piacentini [139] proposed that the performance of a solar collector cannot be optimized by simply subtracting the fan power from the thermal output of the collector, because the former has to be produced at thermal power plant and then

transmitted, losing a considerable part of the energy in conversion and transmission. In order to evaluate the thermo-hydraulic performance of a solar collector, they proposed a parameter called effective efficiency, η_{eff}, and is expressed as:

$$\eta_{eff} = \frac{Q_u - \frac{Pm}{C}}{I A_p} \qquad (1.45)$$

where, C is the conversion factor to account for the conversion of high grade mechanical energy to thermal energy and is given by:

$$C = \eta_F \eta_m \eta_{tr} \eta_{th}$$

where, η_F is the efficiency of the fan,

η_m is the efficiency of the electric motor,

η_{tr} is the efficiency of electrical transmission from the power plant, and

η_{th} is the efficiency of thermal conversion of the power plant.

The value of C as recommended by Cortes and Piacentini [139] is 0.18 (typical values of efficiency factors being: $\eta_F = 0.65$, $\eta_m = 0.88$, $\eta_{tr} = 0.925$ and $\eta_{th} = 0.344$).

Gupta et al. [63] plotted the variation of thermal energy gain and pumping power of a solar air heater as a function of flow rate as shown in Fig.1.48. It has been observed that thermal energy gain and pumping power increase with increase in flow rate. In the low flow rate range, thermal energy gain increases sharply with increase in flow rate while rate of pumping power consumption is low, resulting in higher value of effective efficiency. Beyond this range of flow rate, the rate of increase of pumping power is very high while the rate of useful energy gain becomes nearly constant resulting in decrease in the value of effective efficiency. At very high values of flow

rate, useful energy gain becomes equal to or less than the energy required to move the air through the collector, thereby, affecting the effective efficiency adversely.

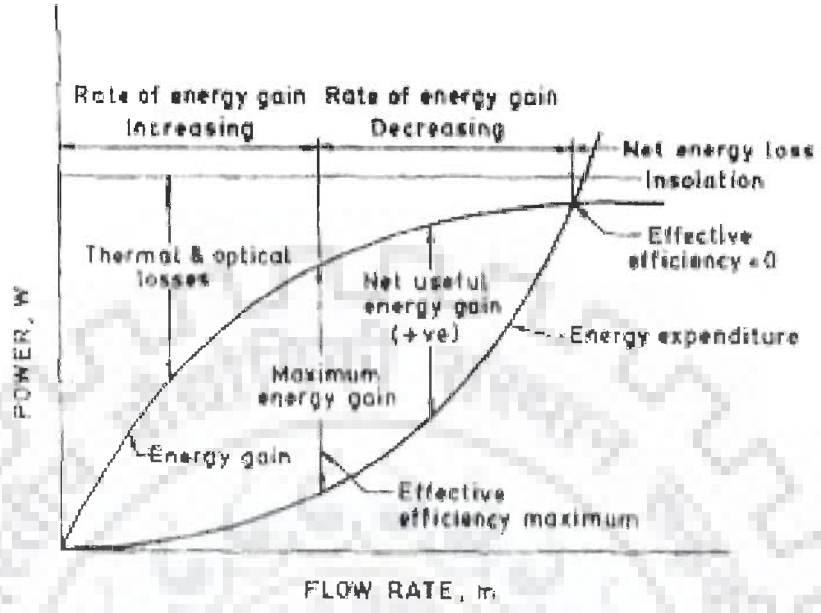

Fig.1.48 Variation of energy gain and losses with flow rate [63]

A number of investigators [63, 68, 69, 70, 74, 76 and 126] evaluated the thermohydraulic performance of a roughened solar air heater using the criterion suggested by Cortes and Piacentini [139]. The design of a solar air heater using artificial roughness was proposed to be based on the criteria of the best thermohydraulic performance where thermal performance is expressed in terms of useful energy gain by the collector.

Gupta et al. [63] used the criterion defined by Eq.1.44 to show the thermo-hydraulic advantage of wire-roughened solar air heater. The optimum condition has been found to be affected mainly by Reynolds number, roughness geometry parameters and insolation.

Saini [74] presented a composite performance plot where a clear relationship between thermal and effective efficiency were depicted as a function of design parameter i.e., temperature rise parameter for the artificial roughness in the form of

expanded metal matrix on the absorber plate, as shown in Fig.1.49. It is found that for higher values of temperature rise parameter, the effective efficiency values closely follow the thermal efficiency values whereas there is a perceptible difference in the lower range of temperature rise parameter values. For high fluid flow rates or for low temperature rise parameter values the solar air heater having smooth duct becomes thermohydraulically more efficient in comparison to a roughened air heater even though the thermal efficiency of a roughened solar air heater will be higher than that of the smooth one.

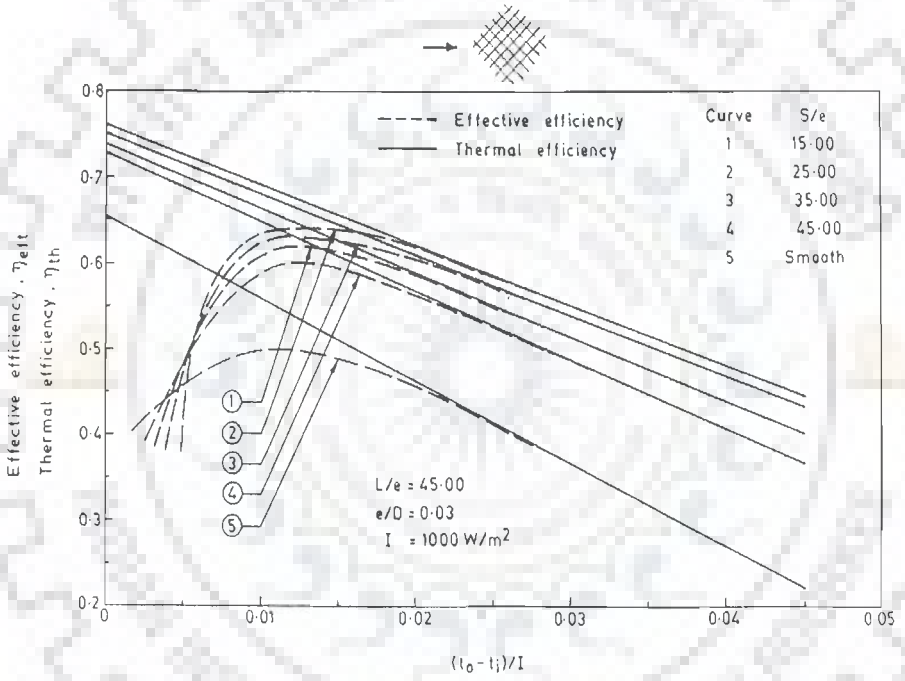

Fig.1.49 Efficiency as function of temperature rise parameter for different values of S/e [74]

Exergy analysis, based on second law of thermodynamics, of renewable energy systems is gaining popularity amongst researchers and scientists as it deals with minimization of irreversibility and can indicate the possibilities of thermodynamic improvement of the process under consideration. Recently, the concept of exergy has been applied by many scientists [140-147] to optimize the performance of solar air heaters.

Fujiwara [140] analyzed the performance of solar collectors from exergy point of view and stated that friction process, which is an energy conversion from mechanical energy to thermal energy, can be treated as exergy loss. An optimum control is established by comparing the exergy loss with the exergy gain extracted from insolation and a simple principle is obtained which is that in the range of $T_i \leq \sqrt{(T_{st}\ T_a)}$ (K), the average fluid temperature should be constant at $\sqrt{(T_{st}\ T_a)}$ (K) and in the range $T_i \geq \sqrt{(T_{st}\ T_a)}$ (K), the mass flow rate should be constant, while the collector performance declines.

Suzuki [141] presented an exergy balance equation for a solar flat plate collector and an evacuated tubular collector. It was reported that both types of solar collectors have nearly equal capabilities in exergy gain despite large differences in technological efforts and expenses to produce them.

Said and Zubair [142] analyzed the performance of two flat-plate solar collectors and a photovoltaic panel based on first as well as second law of thermodynamics. Second law efficiency values of 17 percent and 11 percent were obtained for photovoltaic and flat plate collectors respectively.

Kurtbas and Durmus [143] experimentally evaluated the energy efficiency, friction factor and dimensionless exergy loss of a solar air heater having five solar sub-collectors of same length and width arranged in series in a common case for different values of Reynolds number. It was reported that temperature difference (T_o-T_i) of air, pressure loss and collector efficiency are the major parameters that affect the exergy loss.

Naphon [144] presented a mathematical model for predicting the heat transfer characteristics, thermal performance and entropy generation of a double pass solar air heater having longitudinal fins. Effect of height and number of fins on the entropy

generation was considered and it was found that with increase in height and number of fins, entropy generation decreases while thermal efficiency increases.

Ucar and Inalli [145] experimentally compared the performance and second law efficiency of flat plate solar collector having absorber plates of different shapes and orientations and reported that the least value of second law efficiency is obtained in case of a conventional collector.

Gupta and Kaushik [146] undertook a comparative study to evaluate the performance of solar air heaters roughened with different roughness geometries on the basis of energy, effective and exergy efficiencies. It was found that artificial roughness on absorber surface effectively increased the efficiencies in comparison to smooth surface. The thermal efficiency in general increased in the following sequence: smooth surface, circular ribs, v - shaped ribs, wedge shaped rib, expanded metal mesh, rib-grooved, and chamfered rib–groove. The effective efficiency based criteria also follows same trend of variation among various considered geometries, and trend was reversed at very high values of Reynolds number. The exergy efficiency based criteria also follows the same pattern; however, the trend was reversed at relatively lower value of Reynolds number and for higher range of Reynolds number, the exergy efficiency approaches zero or may be negative. It was found that for the higher range of Reynolds number, circular ribs and v-shaped ribs yield higher value of exergy efficiency while for low Reynolds number range, chamfered rib–groove yields higher value of exergy efficiency.

Altfeld et al. [147] stated that in solar air heating systems, the compression energy needed to overcome friction losses could, essentially, reduce the benefit obtained from solar heat. Thus, the design of solar air heaters with high heat transfer rates and low friction losses is of particular interest. The net exergy flow has been proposed to be a suitable quantity for optimization. By maximizing the net exergy

flow the sum of exergy losses, including exergy losses by absorption of radiation at the absorber temperature level, is minimized and reasonably optimized design of absorbers and flow ducts were found. The net exergy flow is defined as the increase in exergy of air while passing through the collector; it is maximized for optimization. Neglecting changes of kinetic and potential energy and treating air as a perfect gas, the net exergy flow is expressed as: $\dot{E}_n$

$$\dot{E}_n^* = I\, A_p\, \eta_{th}\, \eta_c - P_m(1-\eta_c). \tag{1.46}$$

The first term represents the exergy of the absorbed solar energy transferred to the fluid while the second one represents the exergy losses due to friction.

In the nutshell, in order to compare the performance, the two forms of energy i.e. thermal and mechanical, should be considered appropriately; the mechanical energy needed to overcome friction must be converted to the corresponding thermal energy expenditure. The second law efficiency is introduced to measure the entropy generation or exergy destruction by the system. The decrease in exergetic efficiency is due to the amount of entropy generation during the processes occurring in the solar air collectors.

To compare the exergy dissipated fraction $\dot{E}_n^*$, to the availability of the solar radiation, $\dot{E}_s$ the following equation given by Bejan [148] is used.

$$\dot{E}_s = \dot{Q}\left[1 - \frac{T_a}{T_s}\right] \tag{1.47}$$

The exergetic efficiencies can be defined as;

$$\eta_{II} = \frac{\dot{E}_n}{\dot{E}_s} \tag{1.48}$$

Jaurker [149] and Layek et al. [150] evaluated the performance of artificially roughened solar air heaters by using Eq.1.48, which was developed on the basis of second law of thermodynamics. Fig.1.50 shows the results of such studies [150] where parameters of optimal set of roughness geometry are plotted to yield design plots. The designers can directly make use of such plots to select suitable roughness geometry parameters corresponding to given design conditions.

1.12 GAPS IN KNOWLEDGE

The literature review shows that the use of artificial roughness in different forms and shapes is an effective and economic way of improving the performance of solar air heaters. Number of experimental investigations involving roughness elements of different shapes, sizes and orientations with respect to flow direction have been carried out in order to obtain an optimum arrangement of roughness element geometry. Correlations for heat transfer and friction have been developed which are applicable to wide range of rib configurations and operating parameters.

It is found that in case of transverse ribs, two fluid vortices immediately upstream and downstream of rib are stagnant on account of which fluid temperature as well as wall temperature increase resulting in low heat transfer. However, in comparison to conventional smooth solar air heater, transverse rib roughened solar air heater enhances the heat transfer coefficient by about 1.7 times. Angling of transverse rib further enhances the heat transfer on account movement of vortices along the rib and formation of a secondary flow cell near the leading end, which results in local wall turbulence. V-shaping of a long angled rib helps in the formation of two secondary flow cells as compared to one in case of an angled rib resulting in higher heat transfer rate [79].

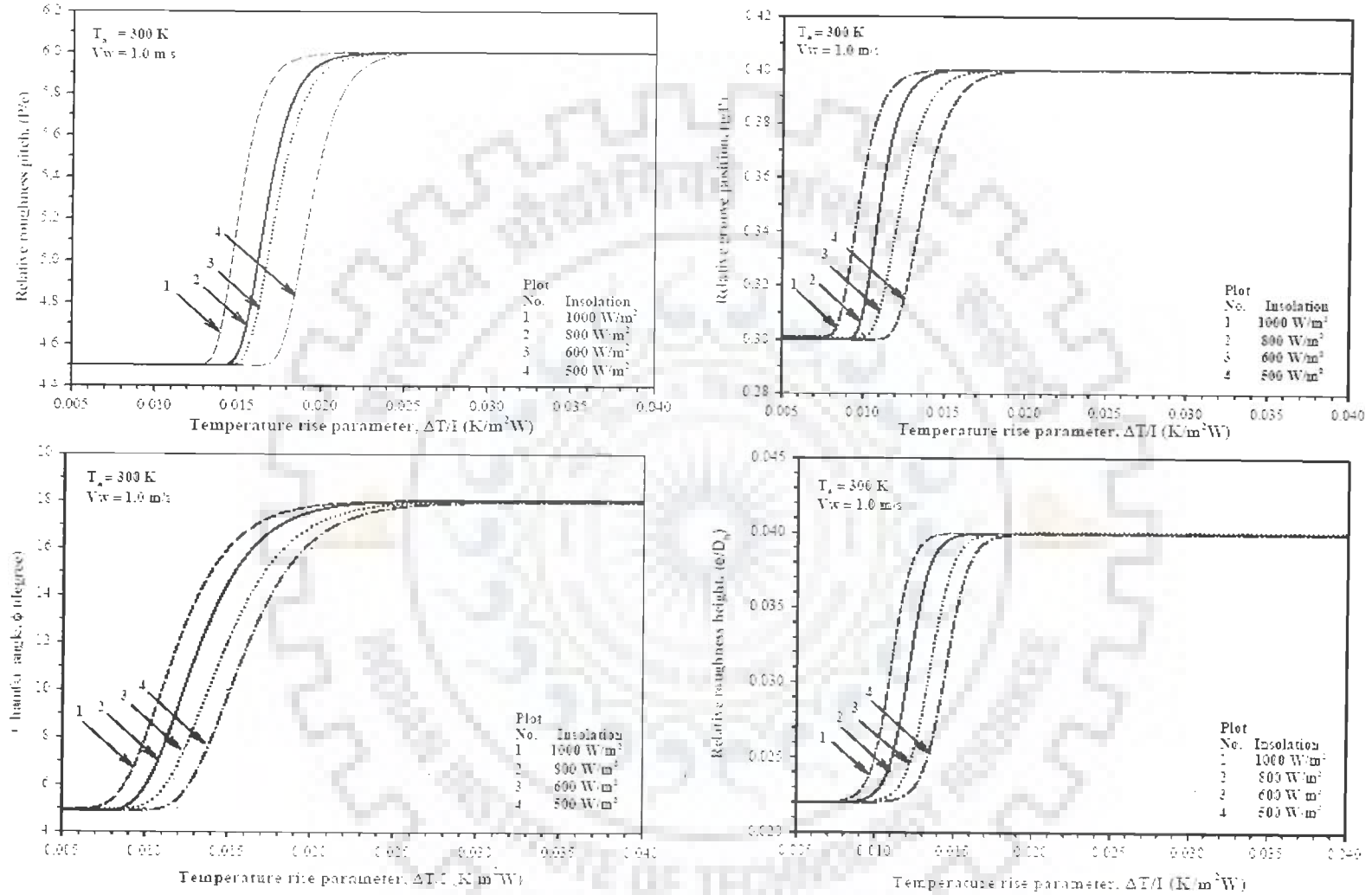

Fig.1.50 Design plots proposed by Layek et al. [150]

Several studies have been reported in literature [68, 69, 78, 91, 92, 94, 95, 102, 103, 106, 113, 122 and 124] to investigate the effect of different v-shaped rib arrangements such as upstream and downstream, staggered without gaps, discrete, broken, parallel with gaps and having an angle of attack as 45^0 and 60^0, on heat transfer enhancement and friction factor. Wright et al. [103] have proposed w-shaped and discrete w-shaped rib geometries orientated at 45^0 and compared their performance with v-shaped and discrete v-shaped rib geometries for turbine blade cooling. They reported that w-shaped ribs (two V-ribs along the width of the duct) fared better. Similarly, Olsson and Sunden [113] investigated the effect multiple v-shaped ribs (four v-ribs along the width of the duct) attached to the walls of swirl flow duct of rectangular cross section. However, detailed studies of heat transfer and friction of surfaces roughened with multiple v-ribs covering wide range of system and operating parameters (width of a single v-rib in multi v-rib configuration, angle of attack, α range of Reynolds number) have not been carried out so far.

In the context of the foregoing discussion, it appears that there is a need for a study of heat transfer and friction characteristics in a rectangular duct with one wall roughened with multiple v-ribs, covering wide range of system and operating parameters as applied to a solar air heater. The basic reason for the use of multiple v-ribs for heat transfer enhancement is that a single v-rib along the width of the duct creates two secondary flow cells as compared to one in case of a single angled rib resulting in higher heat transfer and with multiple v-ribs along the width of the duct, number of secondary flow cells formed will be more resulting in further enhancement of the heat transfer.

Therefore, multiple v-ribs are proposed for use in solar air heaters. The proposed geometrical parameters whose effects are to be investigated on the heat transfer and friction in a rectangular duct with one wall roughened include width ratio, W/w (Ratio of width of duct to width of a single v-rib in multiple v-rib

configurations), angle of attack, α, relative roughness height, e/D, relative roughness pitch, P/e and range of Reynolds numbers, Re.

1.13 OBJECTIVES OF THE PRESENT WORK

In view of the above discussion, the present work is proposed to include the following objectives:

i. To investigate the effect of multiple v-ribs on the heat transfer coefficient and friction factor in the duct flow.

ii. To develop correlations for heat transfer coefficient and friction factor in terms of roughness and operating parameters.

iii. To investigate the thermal performance of solar air heater having absorber plate roughened with multiple v-ribs.

iv. To investigate the thermohydraulic performance of solar air heater having artificially roughened absorber plate with multiple v-ribs to obtain optimal roughness geometry.

CHAPTER-2

EXPERIMENTAL INVESTIGATION

2.1 GENERAL

The review of literature revealed that use of artificial roughness on heat transferring surface of a heat exchanger brings about a considerable enhancement in heat transfer accompanied by an increase in pressure drop penalty. Extensive experimentation has been carried out, employing artificial roughness in the form of small diameter wires, square, triangular, semicircular, wedge or chamfered shaped ribs, for heat transfer enhancement in rectangular ducts. Majority of the experimental investigations involving artificial roughness in rectangular ducts have been conducted to improve heat transfer coefficients in gas turbine blade cooling passages, nuclear reactors, and electronic equipments [84-94, 101, 103, 106 and 113]. However, in the last two decades, several investigators have proposed the use of artificial roughness in solar air heaters and reported substantial improvement in thermal performance of solar air heaters at the expense of frictional losses [62-76, 120, 125-130]. In order to determine the optimum roughness geometry, that maximizes heat transfer enhancement for a minimum pressure drop penalty, a number of roughness geometries having different shapes, forms and orientations have been employed in solar air heaters. It has been reported that v-shaped roughness geometry performs better in terms of heat transfer enhancement in comparison to transverse and inclined roughness geometries [68, 67 and 79] on account of formation of more number of secondary flow cells. Wright et al. [103] proposed w-shaped rib geometry (two v-ribs along the width of the duct) orientated at 45^0 to the flow direction and reported that w-shaped rib geometry outperformed v-shaped roughness geometry in turbine blade cooling applications. Kumar et al. [129] used discrete w-shaped roughness geometry for performance enhancement of solar air heaters. Similarly, Olsson and Sunden [113]

investigated the effect of multiple v-shaped ribs (four v-ribs along the width of the duct) attached to the walls of swirl flow duct of rectangular cross section. However, optimum number of v-ribs along the width of the duct has not been suggested and effect of multiple v-ribs on the performance of rectangular duct with a single roughened and three smooth walls, an arrangement most commonly used in solar air heaters, has also not been investigated. In context of the above, an experimental investigation has been planned to carry out detailed studies of heat transfer and friction in rectangular ducts roughened with multiple v-ribs covering wide range of system and operating parameters.

An indoor test facility has been designed and fabricated to generate heat transfer coefficient and friction factor data for the roughened duct at flow rates suitable for solar air heaters as well as for a range of roughness geometry parameters such as relative roughness height, e/D, relative roughness width, W/w, angle of attack, α and relative roughness pitch, P/e. Experimental investigation on roughened duct was preceded by data collection for smooth rectangular duct under similar operating condition for the purpose of validation of the experimental set-up and comparison of the heat transfer coefficients and friction factors of roughened and smooth conventional rectangular ducts. The test facility has been designed in accordance with the guidelines suggested in ASHRAE standard 93-77 [151] for testing solar collectors using an open loop system. The details of the experimental set-up, data collection and processing have been presented in the following sections.

2.2 EXPERIMENTAL SET-UP

The experimental set-up comprises of an open loop system and it consists of a rectangular duct having entry, test and exit sections, a centrifugal blower, two control valves, a calibrated orifice plate and other necessary instruments for measurement of temperature and pressure drop. The schematic diagram of the experimental set-up

including the test section is shown in Fig.2.1 and a photograph of the same is given in Fig.2.2. The test facility consists of a rectangular duct connected to the suction side of a 3.0 kW centrifugal blower by means of a transitional section reducer and a circular pipe. Atmospheric air, entering the rectangular duct, flows under the absorber plate, which is electrically heated and a variac controls the energy input to the absorber plate. Temperature of air at inlet and outlet of the test section as well as that of the absorber plate are recorded with the help of copper constantan thermocouples, connected to a digital micro voltmeter. For measurement of mass flow rate of air through the duct, a calibrated orifice meter with an inclined U-tube manometer connected across it has been provided. A micro-manometer has been used to measure the pressure drop across the test section. The flow rate through the test section is controlled by means of two gate valves provided at the entrance and exit of the blower. The detailed description of the major components of the experimental set-up is given below.

2.2.1 Solar Air Heater Duct Details

Fig.2.3 shows the sectional view of the rectangular duct, which has been designed and fabricated as per the recommendations of ASHRAE Standard 93-77 [151]. The duct, fabricated from wooden planks of different cross sections, is 2400 mm long with a flow cross section of 300 mm width, W and 25 mm depth, H. A section 1000 mm long is used as a test section, with an entry section of length 525 mm before it and an exit section of length 875 mm after the test section. It may be noted that ASHRAE Standard 93-77 [151] recommends a minimum entry and exit length of 433 mm ($5\times\sqrt{(W\times H)}$) and 217 mm ($2.5\times\sqrt{(W\times H)}$) respectively for the turbulent flow regime. Consequently, the flow can be assumed to be fully developed turbulent flow in the entire length of the test section. A longer exit section of 875 mm length has been provided in order to minimize the end effects.

The bottom of the duct has been made of 19 mm thick wooden plank with 6mm thick plywood fixed on it and followed by 1 mm thick mica laminate pasted on top of the plywood to give a smooth finish to the bottom of the duct. The sidewalls of the duct are made of 25 mm wooden plank with 1 mm thick mica laminate pasted on the inner sides to have smooth finish. Topside of the rectangular the duct comprised of galvanized iron (G.I.) plate and on the lower side of the G.I plate artificial roughness, in the form of multiple v-ribs, has been provided. Topside of the G.I. plate has been covered with a wooden box made of 12 mm thick plywood, having size of 2400 mm×360 mm×100 mm. The hollow inner space of the heater box is filled with glass wool (i.e. 76 mm thick) to minimize the heat losses. The air is thoroughly mixed in the mixing section before the bulk air temperature is measured. The entire length of the rectangular duct is insulated by means of 50 mm thick polystyrene (Thermo Cole) having thermal conductivity of 0.037 W/m-K followed by black foam sheet of 10 mm thickness, to ensure minimum heat losses to the environment.

2.2.2 Heater Assembly

An electric heater having a size of 1525 mm × 310 mm has been fabricated by combining series and parallel loops of Ni-Chrome wires on 8 mm thick asbestos sheet, as shown in Fig.2.4. Six series loops have been connected in parallel to give a maximum heat flux of about 1250 W/m^2. The heater assembly is connected to 220 AC through a Variac in order to control the heat supply to the heater plate assembly.

In order to minimize the heat loss from the topside of the heater assembly, the electric heater is fitted over a box made of 12 mm thick plywood, having a size of 2400 mm×360 mm×100 mm. The hollow inner space of the heater box is filled with glass wool (i.e. 76 mm thick) to minimize the thermal losses. The cross-sectional view of the heater assembly has been shown in Fig.2.5. Electrical power supplied by the heater is determined from the measurement of current and voltage of supply by a digital voltmeter and an ammeter.

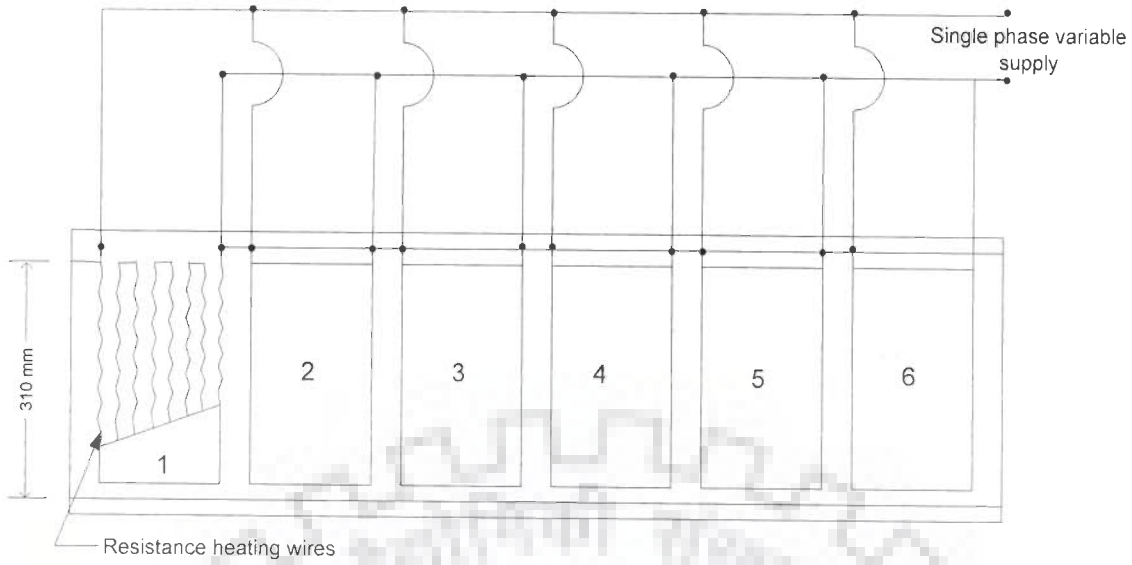

Fig.2.4 Heater plate assembly

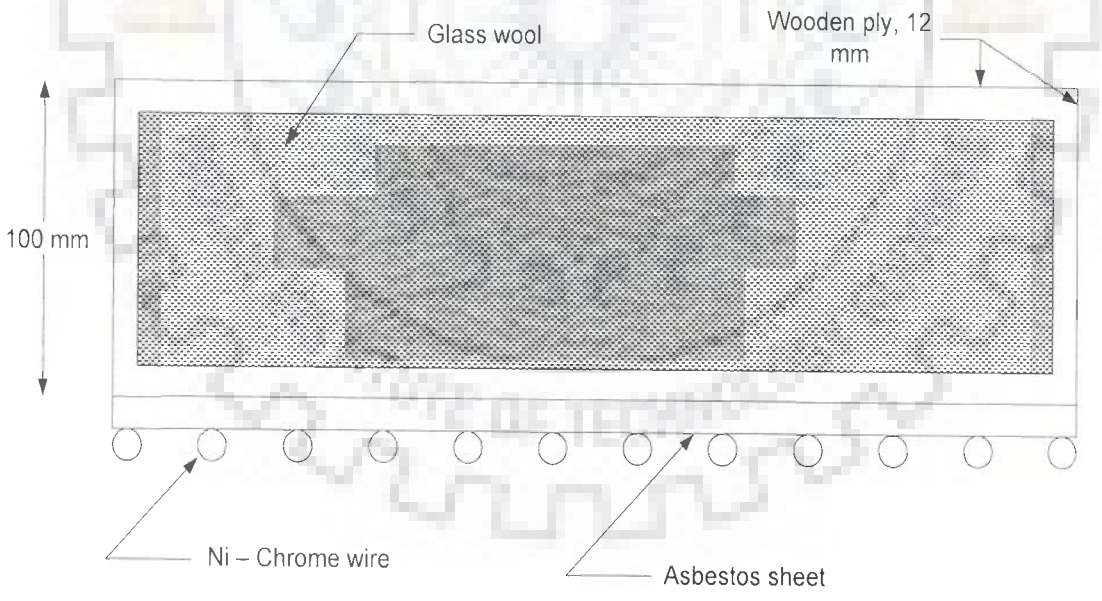

Fig.2.5 Cross–sectional view of heater assembly

2.2.3 Air Handling Equipment

Atmospheric air, sucked through the entry section, passes through the rectangular duct and is delivered from the system to the atmosphere by a centrifugal blower, driven by a 3-phase, 440 V, 3.0 kW and 2880-rpm motor. The exit end of the duct is connected to the blower by means of an 81 mm diameter pipe provided with a calibrated orifice plate and a rectangular to circular transition section. Two gate valves have been used to control the airflow rate through the system. The orifice plate assembly and the control valves are connected through a flexible plastic pipe of 600 mm length in order to minimize the transmission of vibrations from blower to the rectangular duct. The transition section and the orifice plate assembly are insulated with 25 mm thick glass wool followed by black foam sheet of 10 mm thickness, in order to minimize the heat losses to the surrounding. In addition to this, all connecting parts are joined with gaskets and seals to prevent air leakages. Soap solution has been used to check any leakages at the joints, and remedial actions taken wherever necessary.

2.2.4 Temperature Measurement

Calibrated, butt-welded, copper-constantan 0.3 mm diameter (24 SWG) thermocouples with fiberglass insulation all along the leads have been used to measure air and the absorber plate temperatures at different locations. Such thermocouples are usually recommended for temperature measurement in the range of 0–400 ^{o}C [152] The thermocouple output is measured by a digital micro-voltmeter, connected through a selector switch as shown in Fig.2.6 to indicate the output of the thermocouples in degree centigrades. To ascertain the accuracy of temperature measurement, thermocouples have been calibrated under laboratory conditions against a dry block temperature calibrator (Presys Instruments T-25N) [153], having least count of 0.01 °C.

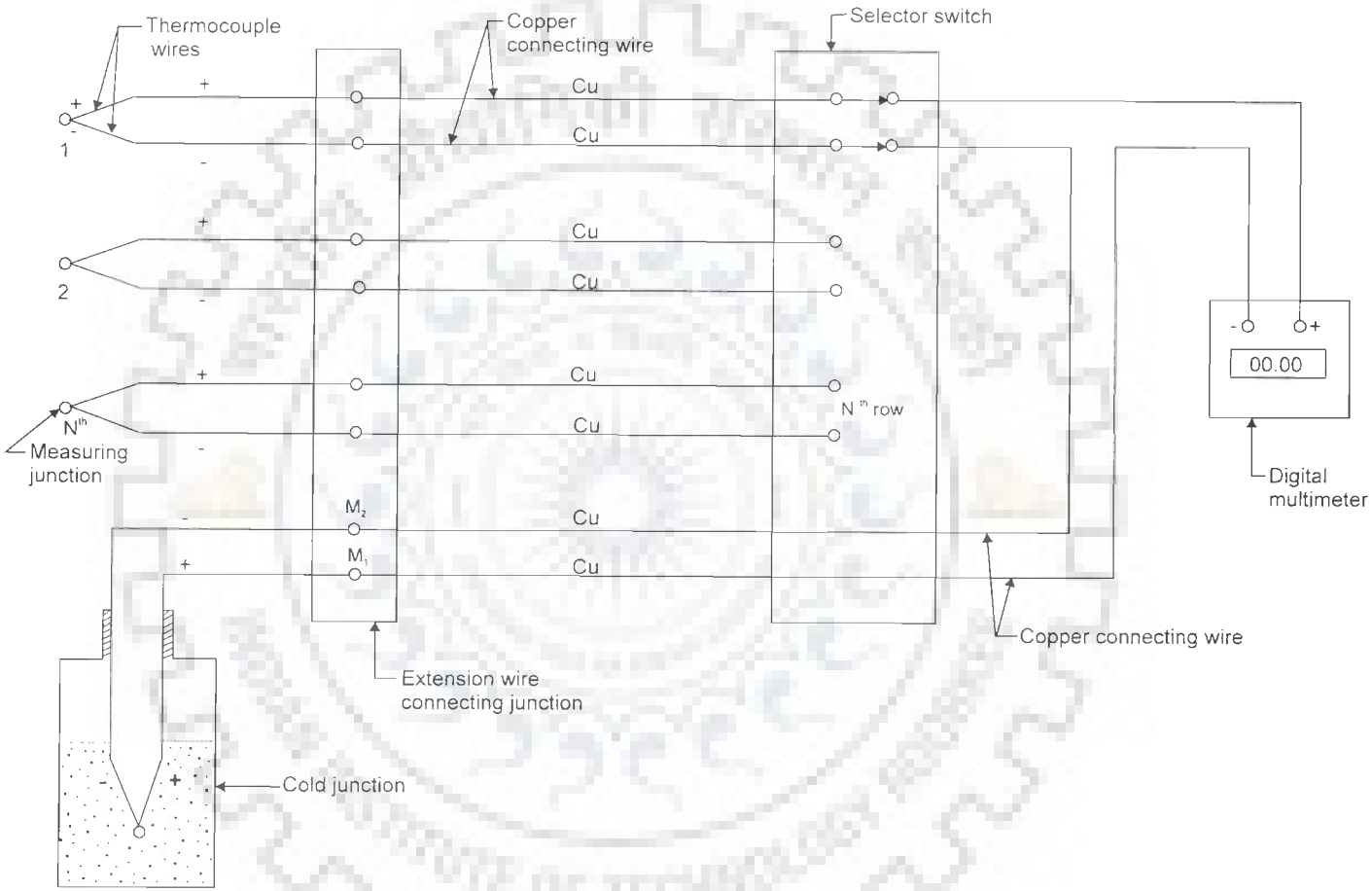

Fig.2.6 Thermocouple circuit

Fig.2.7 shows the photographic view of the calibrator. The thermocouple to be calibrated is placed in the calibration bath where constant temperature is maintained and the response of the thermocouple and the standard probe were noted with the help of a digital temperature indicator for various pre-set values of the standard probe, and the error between the reading of standard probe and the thermocouple were calculated.

If this error is more than certain limit of the calibrator then the thermocouple is rejected and if this error is less than tolerance limit of the calibrator then the thermocouple is accepted. This process was repeated in several steps of increasing as well as decreasing temperature range. The calibration curve is presented in Fig.2.8 and a typical set of observations of calibration is shown in Table 2.1.

Table 2.1 Observations of thermocouple calibration.

S. No.	Step of calibration (Pre-set value) (°C)	Probe reading (°C)	Thermocouple reading (°C)	Error (°C)
1	0	-0.06	-1.0	0.94
2	10	9.99	9.7	0.29
3	20	20	19.8	0.2
4	30	30.01	30	0.01
5	40	40.1	40	0.10
6	50	50.2	49.9	0.30
7	60	60.02	60.2	-0.18
8	70	70.01	70.4	-0.39
9	80	80.07	80.2	-0.13
10	90	90.12	90.2	-0.08
11	100	100.13	100.3	-0.17
12	110	110.2	110.3	-0.1

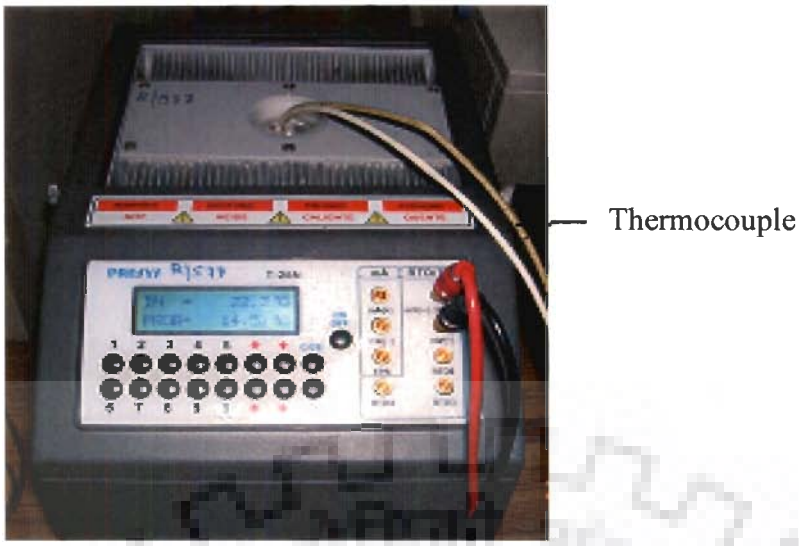

Fig.2.7 Photographic view of dry block thermo-couple calibrator

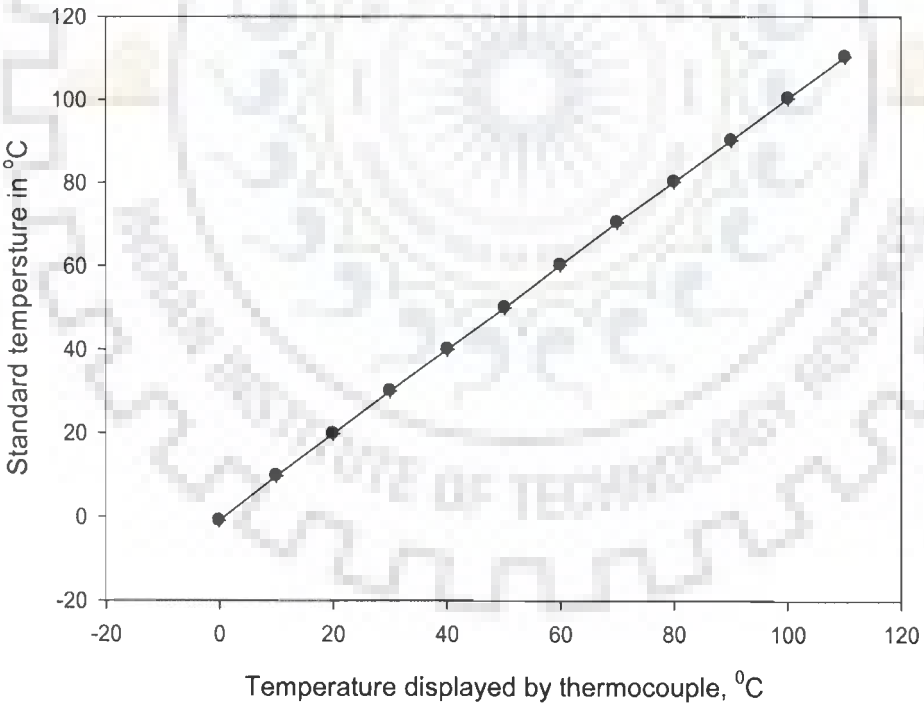

Fig.2.8 Calibration curve for thermocouples

A total of nineteen thermocouples have been used to measure the temperature of top surface of the absorber plate. Out of nineteen thermocouples, nine are fixed along the axial centerline starting from a location, which is at a distance of 525 mm from the inlet of the duct and these thermocouples are at a distance of 125 mm from each other. Five thermocouples each, at a distance of 250 mm from each other and at a distance of 125 mm on the either side of the central line, have been fixed to measure the span wise variation of absorber plate temperature as shown in Fig.2.9. Temperature of air inside the duct as well at the exit of the test section was recorded at different locations as shown in Fig.2.10. Shallow grooves are machined on the top surface of the absorber plate to hold the thermocouples in place and epoxy applied over it. Good physical contact between the thermocouple and plate surface has been ensured.

2.2.5 Airflow Rate Measurement

The airflow rate in the duct has been measured by means of a calibrated orifice plate of thickness 3 mm and having 38 mm throat diameter. The orifice plate has been fitted in an 81 mm diameter pipe and an inclined U tube manometer having kerosene as manometric fluid has been used to determine the pressure drop across the orifice plate. Fig.2.11 shows the details of the orifice plate assembly along with vena-contracta taps. The orifice plate has been designed as per recommendation of Moore [154] and calibrated against a standard Pitot tube. The calibration curve has been shown in Fig.2.12. The upstream and downstream edges of the orifice plate were free from burrs, dents and other irregularities and in order to achieve this, special care was taken during machining. The orifice plate has been fitted between two flanges, so that it remains concentric with the pipe. The length of the circular pipe provided is based on the pipe diameter D, which is minimum of 10xD on the upstream side and 5×D on the downstream side of the orifice plate as recommended by Ehlinger [155].

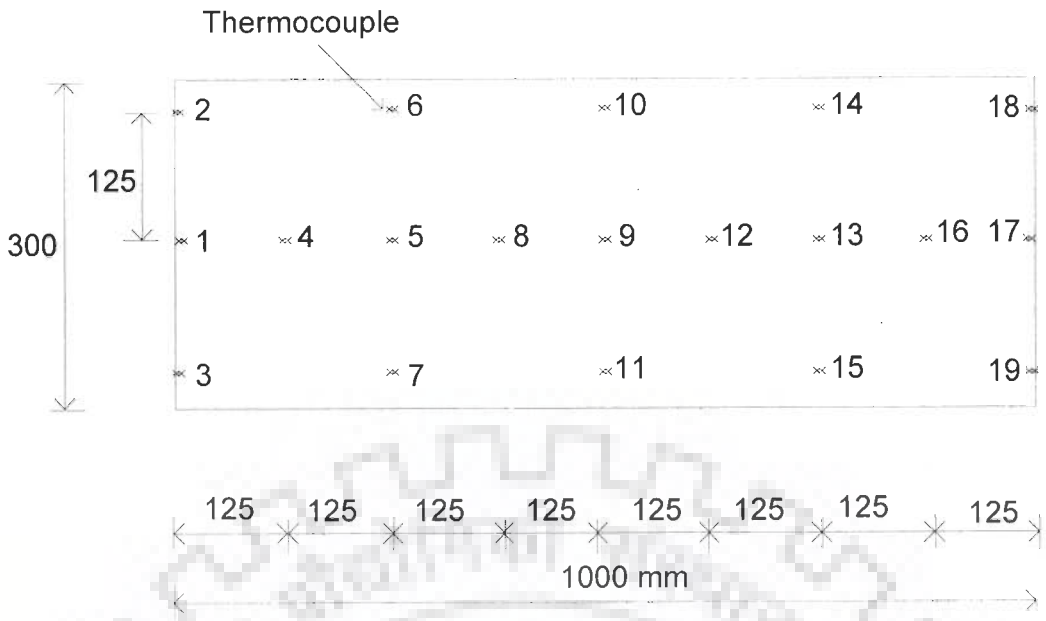

Fig.2.9 Location of thermocouples on absorber plate

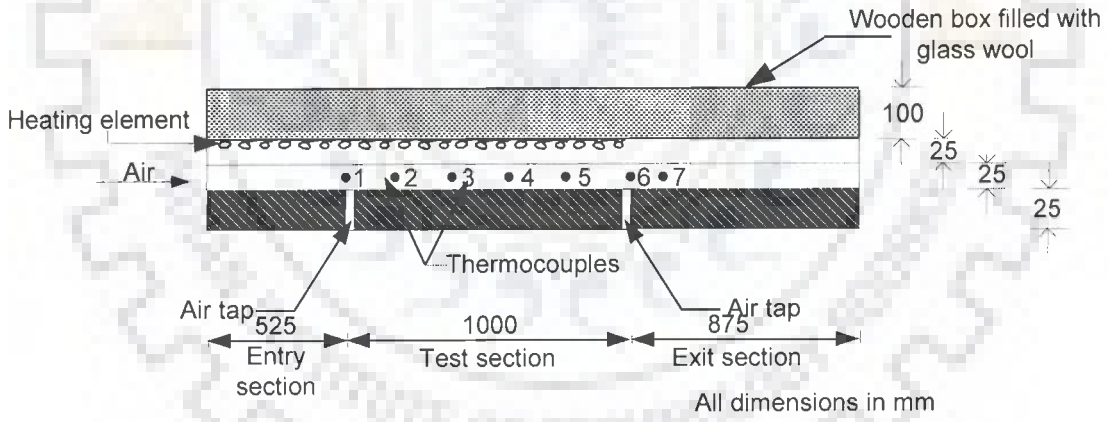

Fig.2.10 Location of thermocouples and air taps in air duct

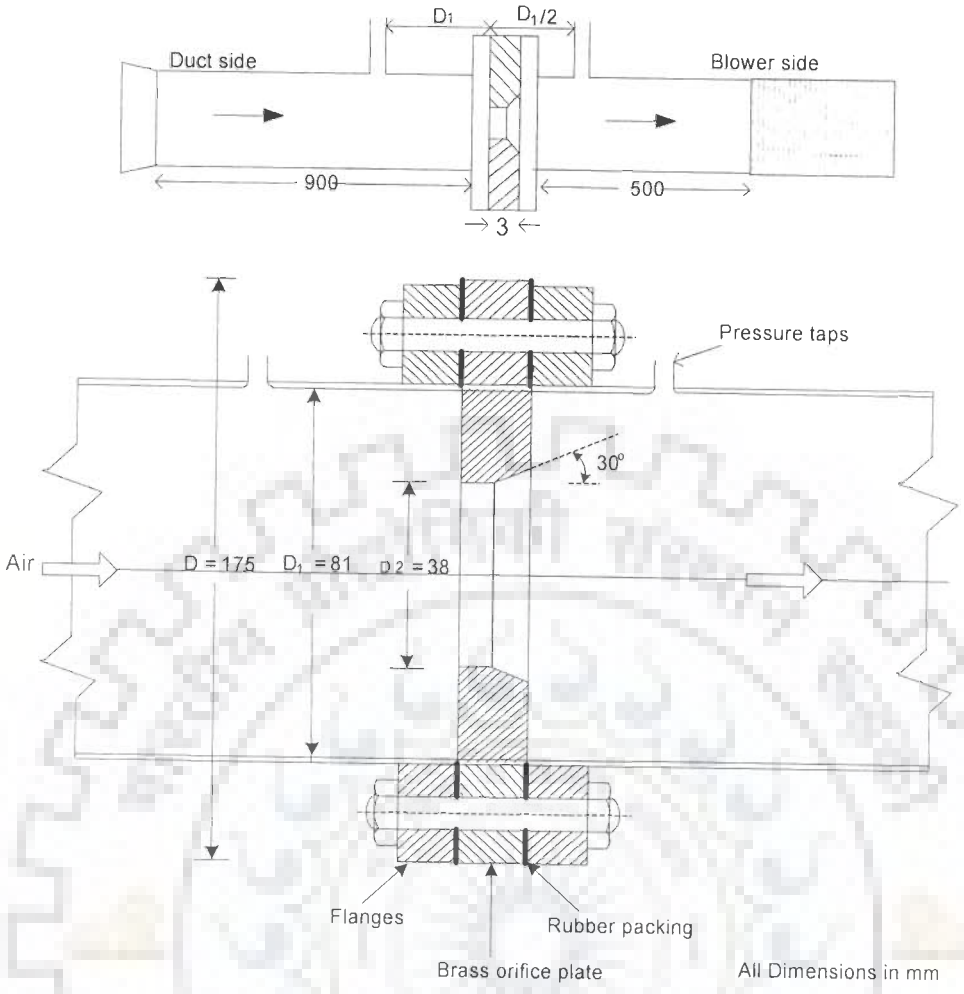

Fig.2.11 Orifice plate assembly

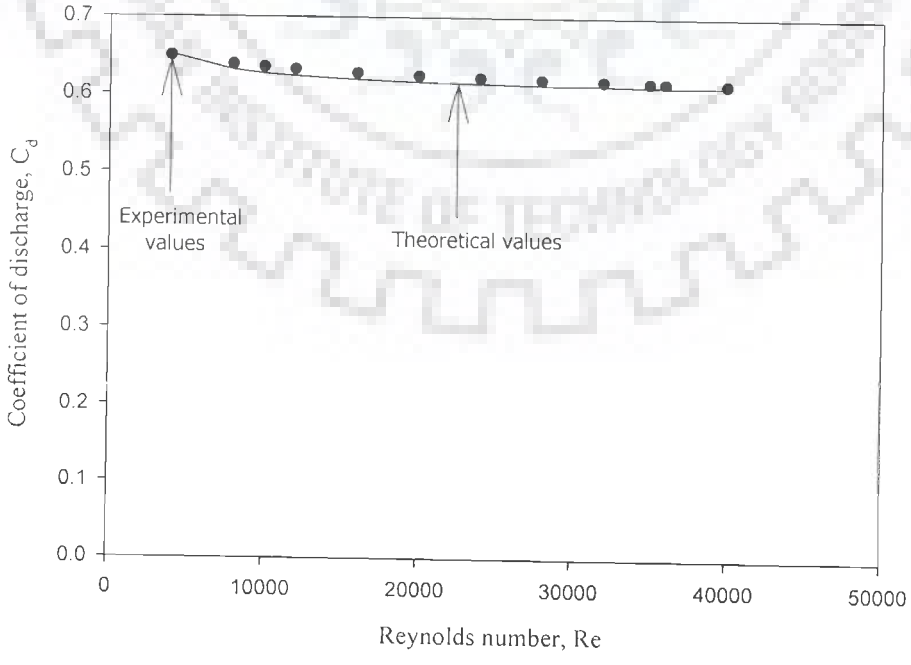

Fig.2.12 Calibration curve of orifice meter

The length of the pipe provided on the upstream side of orifice plate is 900 mm (11.1x D) and on the downstream side is of 500 mm (6.7×D) in order to make the flow fully developed at the orifice plate. Vena contracta taps of 3 mm diameter are located 1 pipe diameter (D) upstream and ½ pipe diameter downstream of the orifice plate (both measured from the upstream face of the orifice plate). The corners of the holes at the inner surface of the pipe were free from burrs and were smoothed off by slightly rounding up by emery cloth.

2.2.5.1 Calibration of orifice-meter

The orifice-meter has been calibrated against a standard Pitot tube on the basis of comparison of mass flow rate measured by orifice-meter and Pitot tube. Pitot tube measures the velocity distribution across the pipe cross-section and velocity area integration method is applied to compute the mass flow rate. The mass flow rate thorough the orifice-meter can also be measured by measuring the pressure drop across it using a U- tube manometer, if the coefficient of discharge is known. By comparing these two mass flow rates, an experimental value of coefficient of discharge, C_d, has been determined. The value of the coefficient of discharge was also estimated using an empirical correlation proposed by Benedict [152]. The experimental and empirical values of coefficient of discharge show reasonable agreement. The procedure for determination of the experimental and empirical values of coefficient of discharge is given as under:

(a) Experimental values of coefficient of discharge

The actual mass flow rate through the pipe is measured by means of a Pitot tube inserted inside the pipe and moving it along the diameter of the pipe. Velocity at each 5 mm distance along two perpendicular diametric planes has been measured and average of the two set of readings has been used for further calculation. Following relationship is used to determine the flow velocity at any point,

$$V = C_t \sqrt{\frac{2 \Delta P_h}{\rho_m}} \qquad (2.1)$$

where, C_t is taken as unity for the calibration of the Pitot tube for pipe Reynolds number, Re_P greater than 1000 under usual flow conditions [152]. These values are used for integration over the pipe area to evaluate the area average velocity of flow through the pipe.

$$V_{av} = \frac{1}{2\pi} \int_0^R 2\Pi r V dr \qquad (2.2)$$

The actual mass flow rate, m, is given by:

$$m = \rho_m V_{av} A_1 \qquad (2.3)$$

(ii) Discharge through orifice-meter

Mass flow rate of air is determined from pressure drop measurement across the orifice-meter using the following relationship.

$$m = C_d A_2 \sqrt{\frac{2\rho(\Delta P)_o}{(1-\beta^4)}} \qquad (2.4)$$

where, $\rho = \frac{P_a}{RT}$

m is the mass flow rate of air.

$(\Delta P)_0$ is the pressure drop across the orifice plate.

$\beta = D_2/D_1$,

D_2 is the throat diameter of the orifice-plate,

D_1 is the pipe diameter

The coefficient of discharge, C_d is then determined using Eqs.2.3 and 2.4. The variation of experimental values of C_d with Reynolds number is shown in Fig.2.12, which gives average value of coefficient of discharge C_d as 0.624.

(b) Empirical value of coefficient of discharge

Stolz presented an equation that was reported by Benedict [152] for the calculation of coefficient of discharge for orifices, which is amenable to hand calculations. *Stolz*'s equation, called the ISO–ASME orifice coefficient equation is given as;

$$C_{ds}=0.5959+0.0312\beta^{2.1}-0.184\beta^{8}+0.0029\beta^{2.5}\left(\frac{10^{6}}{Re_{o}\beta}\right)+\frac{0.09L_{1}\beta^{4}}{1-\beta^{4}}-0.033L_{2}\beta^{3} \qquad (2.5)$$

where C_{ds} is the *Stolz* discharge coefficient,

Re_o is Reynolds number based on throat diameter,

L_1 is the dimensionless location of the up-stream pressure tap with respect to the upstream face of the orifice,

L_2 is the dimensionless location of the down-stream pressure tap with respect to the down-stream face of the orifice,

Stolz equation is "universal" in the sense that it applies equally well to flange tap, Vena contracta taps (D and ½ D tap) and corner tap installations.

The detailed procedure of calculating of C_d followed in this work is given below:

Pipe diameter, $D_1 = 81$ mm

Orifice diameter, $D_2 = 38$ mm

$\beta = D_2 / D_1 = 0.47$

For *Vena contracta taps* connection $L_1 = D_1$ and $L_2 = 0.5\ D_1$

(i). Velocity at the throat of the orifice plate, V_o is calculated from

$$V_o = \frac{m}{A_2 \rho}$$

(ii). Reynolds number based on throat diameter of the orifice plate, Re_o

$$Re_o = \frac{V_o D_2}{\nu}$$

(iii). The coefficient of discharge can be calculated using the *Stolz* equation (Eq.2.5) as;

$C_{ds} = 0.6265$ at $Re_o = 10000$ and

$C_{ds} = 0.6123$ at $Re_o = 35000$.

The theoretical value of coefficient of discharge, C_d, determined from Eq.2.5 has been compared with the experimental value of coefficient of discharge obtained from Eq.2.4 in Fig.2.12. The experimental and theoretical values have been observed to be in good agreement with maximum deviation of 1.25%. For the entire range of throat Reynolds number, the value of coefficient of discharge varies between 0.648 and 0.613. Since this variation is small, the average value of coefficient of discharge (= 0.624) has been used for all further calculations of mass flow rate.

2.2.6 Duct Pressure Drop Measurement

The pressure drop across the test section of the duct has been measured by using a micro-manometer. The micro-manometer consists of a digital micrometer having a least count of 0.001 mm, a moveable reservoir, a fixed reservoir and an inclined transparent tube connecting these reservoirs by means of flexible tubing. The moveable reservoir has been mounted on a sliding arrangement in such a way that the reservoir movement takes place in vertical plane only. The up and down movement of the moveable reservoir has been recorded with the digital micrometer. The two reservoirs have been connected to air taps provided at the inlet and outlet of the test section. Kerosene having specific gravity of 0.7698 has been used as a manometric fluid to further increase the accuracy. The manometric fluid meniscus is maintained at

a prescribed fixed mark by moving the movable reservoir in upward or downward direction and the movement is recorded which yields the pressure difference across the test section. The location of the air taps is shown in Fig.2.9.

The photographic view of the micro-manometer various instruments used for measurement of data pertaining to heat transfer and friction factor are shown in Fig.2.13 and Fig.2.14.

2.3 ROUGHNESS GEOMETRY AND RANGE OF PARAMETERS

In this experimental investigation, a GI sheet (1 mm thick) 1000 mm x 300 mm in size has been used as an absorber plate in the test section of the rectangular duct and multiple v-ribs, with apex facing downstream, have been used as roughness elements as downstream v-ribs perform better than the upstream v-ribs in terms of heat transfer enhancement [79]. Aluminum wires of circular cross-section have been used to create artificial roughness on the underside of the absorber plate. Aluminum wires in single v-rib patterns, with apex pointing down stream, were fixed with an adhesive along the width of the duct on the underside of the absorber plate, for the length covering the entrance and test sections of the rectangular duct. In order to ensure good surface contact between roughness elements and the absorber plate, the roughness elements were pressed from top against the absorber plate. Single v- rib patterns of Aluminum wires, with an angle of attack, α value of 30^{o} and relative roughness pitch, P/e value of 10, were fixed on the absorber plates for four different values of relative roughness height, e/D as given in Table 2.2. Similarly, Aluminum wires in multiple v-rib patterns such as two v-rib, three v-rib, four v-rib, five v-rib, six v-rib, eight v-rib and ten v-rib with apex pointing downstream, were fixed along the width of the duct on the underside of the absorber plate for all the values of relative roughness height, e/D.

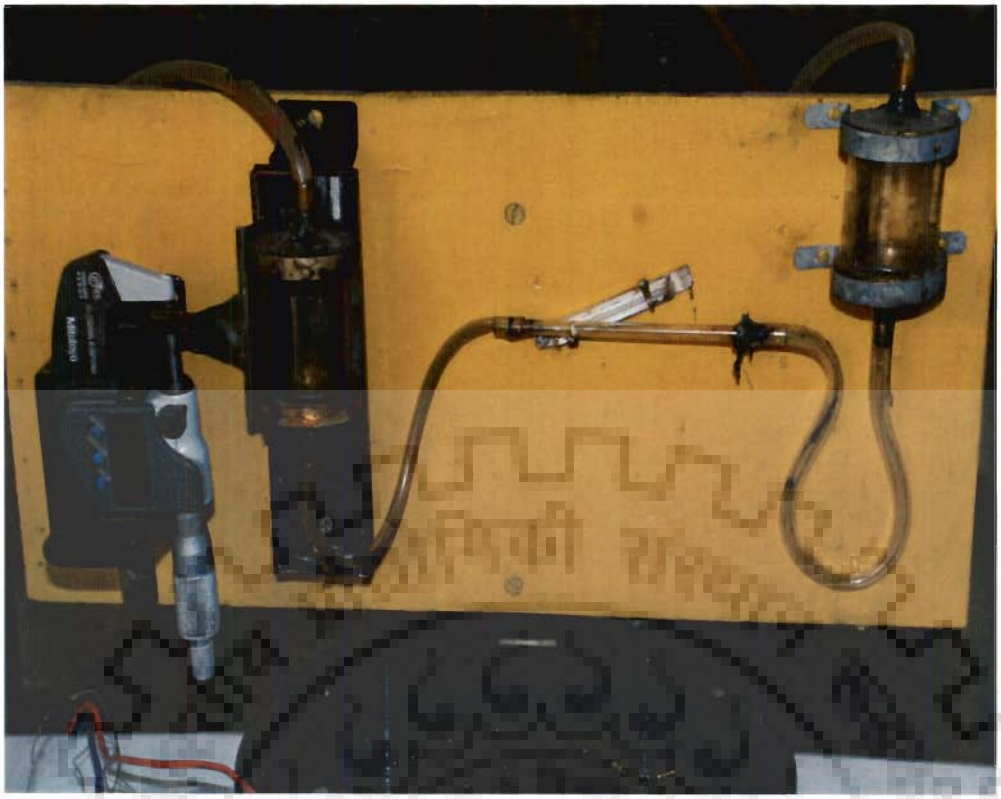

Fig.2.13 Photographic view of micro-manometer

Fig.2.14 Photographic view of instruments

In order to study the effect of angle of attack, α on the performance of multiple v-rib roughened ducts, Aluminum wires in six v-rib pattern having relative roughness pitch, P/e value of 10 and relative roughness height, e/D value of 0.043 were fixed on the underside of the absorber plate for different values of angles of attack, α.

Similarly, in order to bring out the effect of relative roughness pitch, P/e on the performance of multiple v-rib roughened ducts, Aluminum wire in six v-rib patterns having angle of attack, α value of 60° and relative roughness height, e/D value of 0.043 were fixed on the underside of the absorber plate for different values of relative roughness pitch, P/e as given in Table 2.2.

Table 2.2 Range of roughness geometry and operating parameters

S. No.	Roughness parameters	Range
1.	Reynolds number, Re	2000 – 20000 (10 values)
2.	Relative roughness height, e/D	0.019 – 0.043 (4 values)
3.	Relative roughness Width, W/w	1 – 10 (8 values)
4.	Angle of attack, α	30° – 75° (4 values)
5.	Relative roughness pitch, P/e	6 – 12 (4 values)

A total number of thirty-eight multiple v-rib roughened absorber plates were tested in this experimental work covering different roughness parameters.

In order to investigate the effect of multiple v-ribs on heat transfer enhancement and friction factor, relative roughness width, W/w parameter was considered and defined as,

$$\text{Relative roughness width } \left(\frac{W}{w}\right) = \frac{\text{Width of absorber plate}}{\text{width of a single v-rib}} \qquad (2.6)$$

The roughness geometry and operating parameters considered in the present experimental investigation are given in Table 2.2 and the specifications of roughness elements provided on each absorber plate are given in Table 2.3. The orientation and

arrangement of multiple v-ribs on the absorber plate have been shown in Fig.2.15 and photographic view of the roughened absorber plates is shown in Fig.2.16.

2.4 EXPERIMENTAL PROCEDURE

The experimental data pertaining to heat transfer and flow friction was collected in accordance with recommendation of ASHRAE 92-77 [151] for testing in open loop flow mode. In the present experimental study, thirty-eight roughened surfaces, having different values of roughness parameters, were investigated in addition to smooth surface operating under similar flow conditions for the purpose of comparison with the roughened absorber surfaces. For each set of experiment, before the start of the experimentation, all the measuring instruments, joints of the duct, plenum and pipes were thoroughly checked to ensure that there was no leakage. Ten values of airflow rates were considered for each roughened surface at a fixed heat flux of 1000 W/m^2. The micro-manometer and U-tube manometer were leveled properly and the inclination of U-tube manometer was measured using a combination set. Blower was switched on and the flow control valves were adjusted to give a predetermined mass flow rate of the air through the duct. The power input to the heater is adjusted using a variac to get the desired temperature rise.

A voltage stabilizer was used to ensure constant voltage supply to the heater plate. All the data were collected under steady state conditions that were assumed to have been attained when the absorber and outlet air temperatures did not deviate over a period of ten minutes. Initially, for each test run, steady state condition was attained in about 2-3 hours. The following parameters were measured for each set of readings:

(i) Absorber plate temperature at 19 points.

(ii) Air temperature inside the duct.

(iii) Outlet air temperature at five points in span wise directions of the duct.

(iv) Ambient temperature.

(v) Pressure drop across the test section.

(vi) Pressure difference across the orifice meter.

Table 2.3 Specifications of roughened absorber plates

Plate No.	Rib height, e (mm)	Pitch, P (mm)	Angle of attack, α	Relative rib roughness height (e/D)	Relative roughness pitch (P/e)	Relative roughness width (W/w)
1	0.9	9	30	0.019	10	1
2	0.9	9	30	0.019	10	2
3	0.9	9	30	0.019	10	3
4	0.9	9	30	0.019	10	4
5	0.9	9	30	0.019	10	5
6	0.9	9	30	0.019	10	6
7	0.9	9	30	0.019	10	8
8	0.9	9	30	0.019	10	10
9	1.2	12	30	0.026	10	1
10	1.2	12	30	0.026	10	2
11	1.2	12	30	0.026	10	3
12	1.2	12	30	0.026	10	4
13	1.2	12	30	0.026	10	5
14	1.2	12	30	0.026	10	6
15	1.2	12	30	0.026	10	8
16	1.2	12	30	0.026	10	10
17	1.6	16	30	0.035	10	1
18	1.6	16	30	0.035	10	2
19	1.6	16	30	0.035	10	3
20	1.6	16	30	0.035	10	4
21	1.6	16	30	0.035	10	5
22	1.6	16	30	0.035	10	6
23	1.6	16	30	0.035	10	8
24	1.6	16	30	0.035	10	10
25	2.0	20	30	0.043	10	1
26	2.0	20	30	0.043	10	2
27	2.0	20	30	0.043	10	3
28	2.0	20	30	0.043	10	4
29	2.0	20	30	0.043	10	5
30	2.0	20	30	0.043	10	6
31	2.0	20	30	0.043	10	8
32	2.0	20	30	0.043	10	10
33	2.0	20	45	0.043	10	6
34	2.0	20	60	0.043	10	6
35	2.0	20	75	0.043	10	6
36	2.0	20	60	0.043	6	6
37	2.0	20	60	0.043	8	6
38	2.0	20	60	0.043	12	6

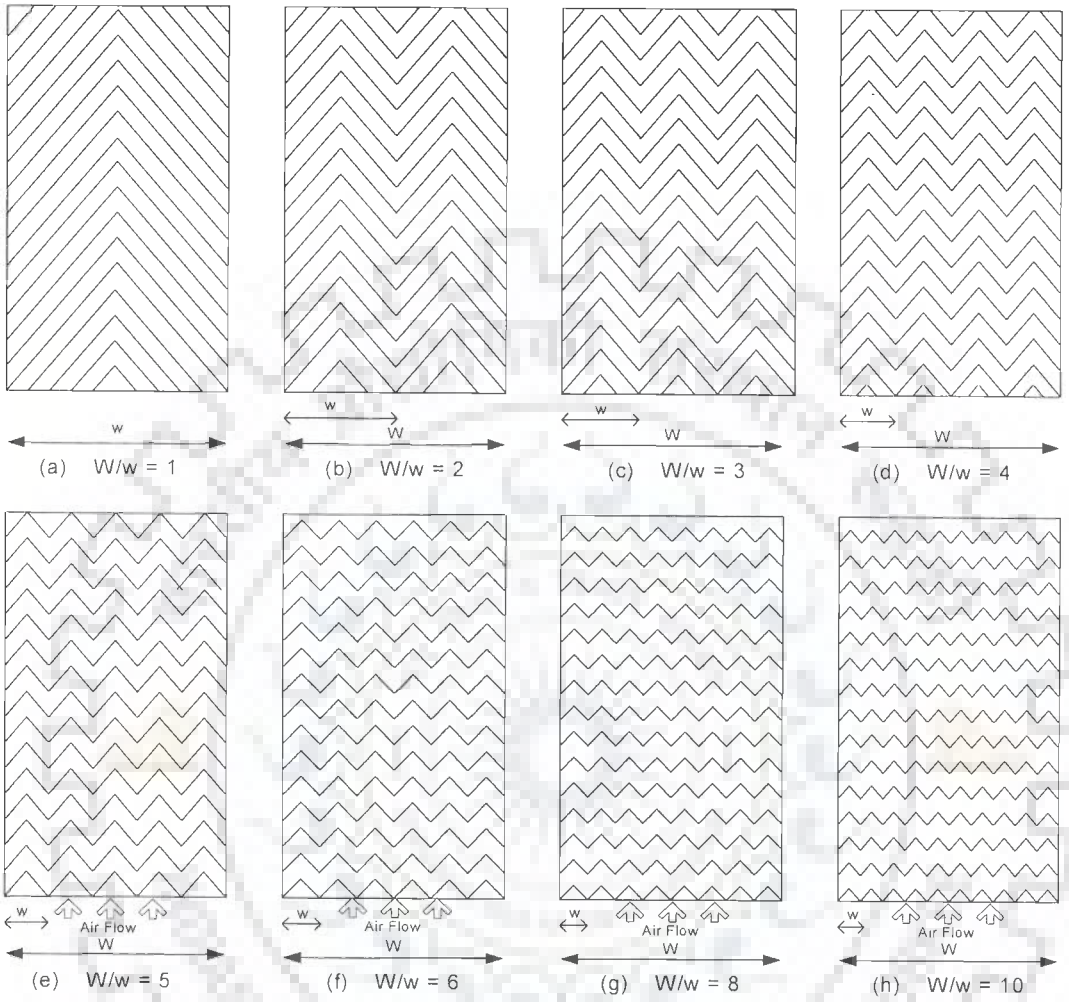

Fig.2.15 Roughened absorber plates with different values of W/w

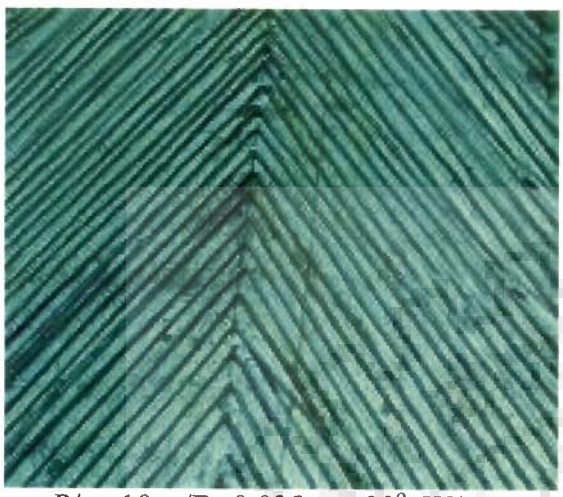

P/e =10, e/D=0.035, α= 30°, W/w=1

P/e =10, e/D=0.043, α= 30°, W/w=2

P/e =10, e/D=0.026, α= 30°, W/w=3

P/e =10, e/D=0.026, α= 30°, W/w=4

Fig.2.16 (a) Photographic view of roughened absorber plates

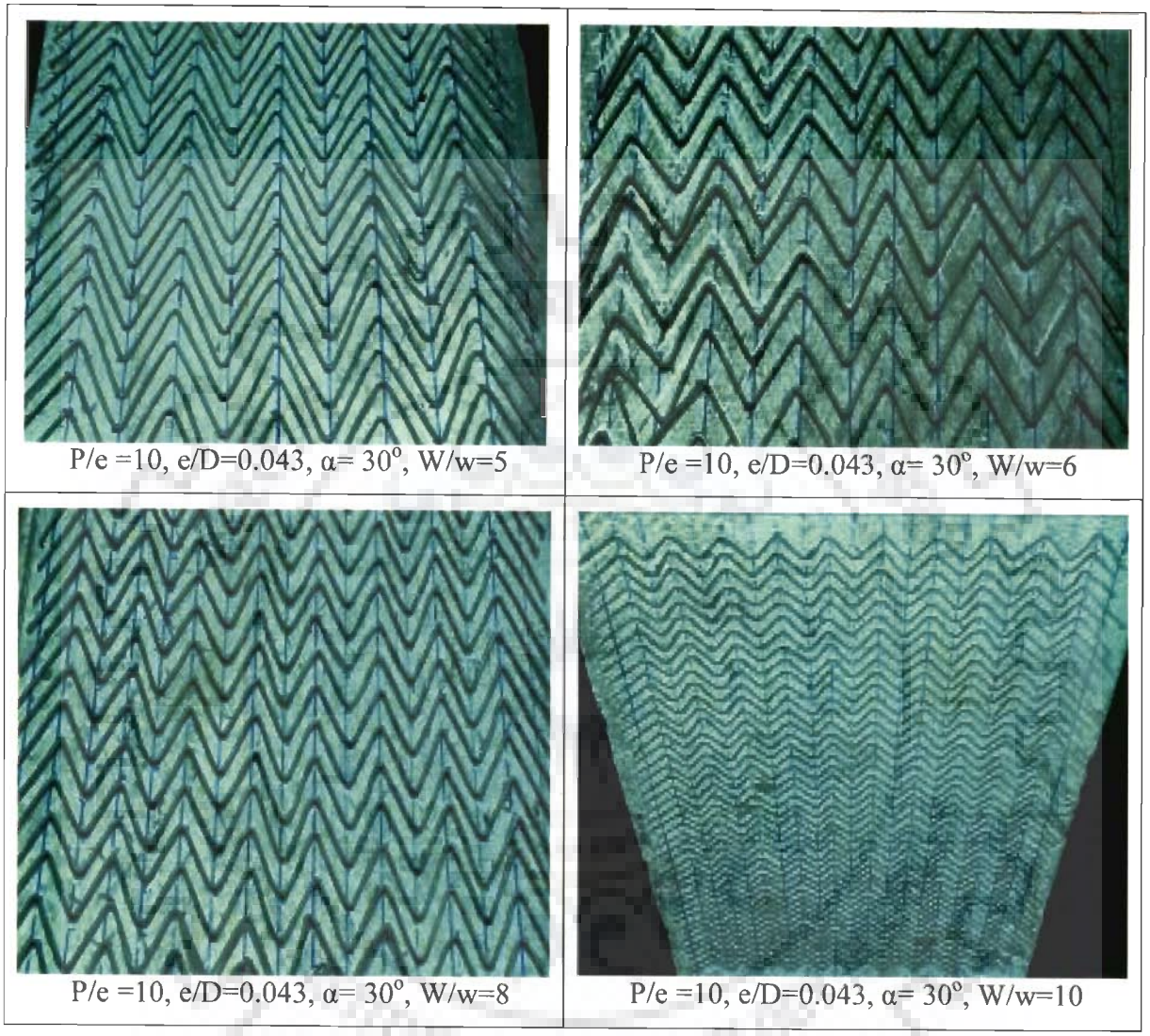

Fig.2.16 (b) Photographic view of roughened absorber plates

2.5 TEMPERATURE PROFILE ALONG THE DUCT

Fig.2.17 shows the variation of temperature of the absorber plate and air along the length of the duct. It has been observed that temperature of plate varied linearly in the flow direction and variation in plate temperature in a direction normal to flow was found to be negligible. Variation in temperature of air inside the duct was also found to vary linearly in the flow direction with negligible variation in temperature occurring in span wise direction. The slight fall in plate temperature observed towards the end appears to be on account of the end effects and this drop in temperature was also reported by Gupta [62] and Karwa [65].

2.6 EXPERIMENTAL DATA

The experimental data for plate and air temperatures at various locations in the duct has been recorded under steady state conditions for a given heat flux and mass flow rate of air for all the thirty-eight plates roughened with multiple v-ribs.

Experiments have been conducted for ten different values of mass flow rate for each roughened plate, thereby, making a total of 380 test runs. Sample experimental data collected for a typical set have been shown in Table 2.4.

2.7. VALIDITY TEST

The Nusselt number and friction factor determined from experimental data for smooth duct have been compared with the values obtained from Dittus Boelter Equation [156] and Modified Blasius Equation [77] for Nusselt number and friction factor respectively.

Dittus Boelter Equation: $Nus = 0.023\ Re^{0.8}\ Pr^{0.4}$ (2.7)

Modified Blasius Equation: $fs = 0.085\ Re^{-0.25}$ (2.8)

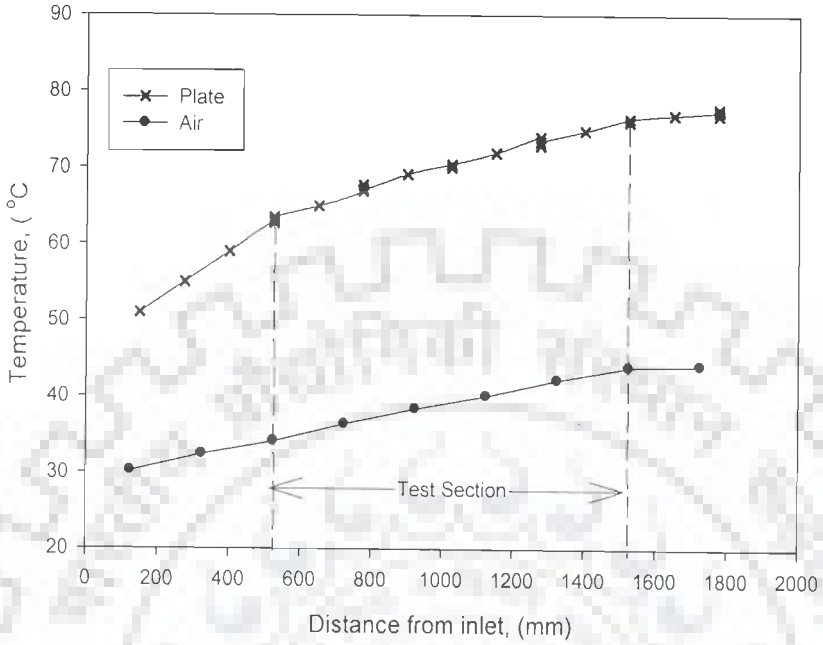

Fig.2.17 Plate and air temperature profile along the test duct

The comparison of the experimental and predicted values of Nusselt number and friction factor is shown in Figs.2.18 and 2.19 respectively. The average deviation of experimental values of Nusselt number is ±2.7% from the predicted values given in Eq.2.7 and the average deviation of experimental values of friction factor is ±2.67% from the predicted values given by Eq.2.8. This shows good agreement between experimental and predicted values, which ensures the accuracy of the data collected with the experimental set-up.

2.8 DATA REDUCTION

The data collected has been used to compute heat transfer coefficient, Nusselt number and friction factor. Relevant expressions for the computation of above mentioned parameters and some intermediate parameters have been given below;

2.8.1 Average Plate and Air Temperature

The mean plate temperature T_P is the average of the temperatures recorded at various locations on the absorber plate as shown in Fig.2.9 and is given as;

$$T_P = \frac{T_1 + T_2 + T_3 + T_4 + T_5 + T_6 + T_7 + T_8 + T_9 + T_{10} + T_{11} + T_{12} + T_{13} + T_{14} + T_{15} + T_{16} + T_{17} + T_{18} + T_{19}}{19} \quad (2.9)$$

The bulk mean air temperature, T_f is the arithmetic mean of the measured values of air temperature at the entry and exit to the test section,

$$T_f = \frac{T_o + T_i}{2} \quad (2.10)$$

where $T_i = T_{20}$ and T_o is the average temperature at the outlet which is calculated by using the following equation,

$$T_o = \frac{T_{26} + T_{27} + T_{28} + T_{29} + T_{30}}{5} \quad (2.11)$$

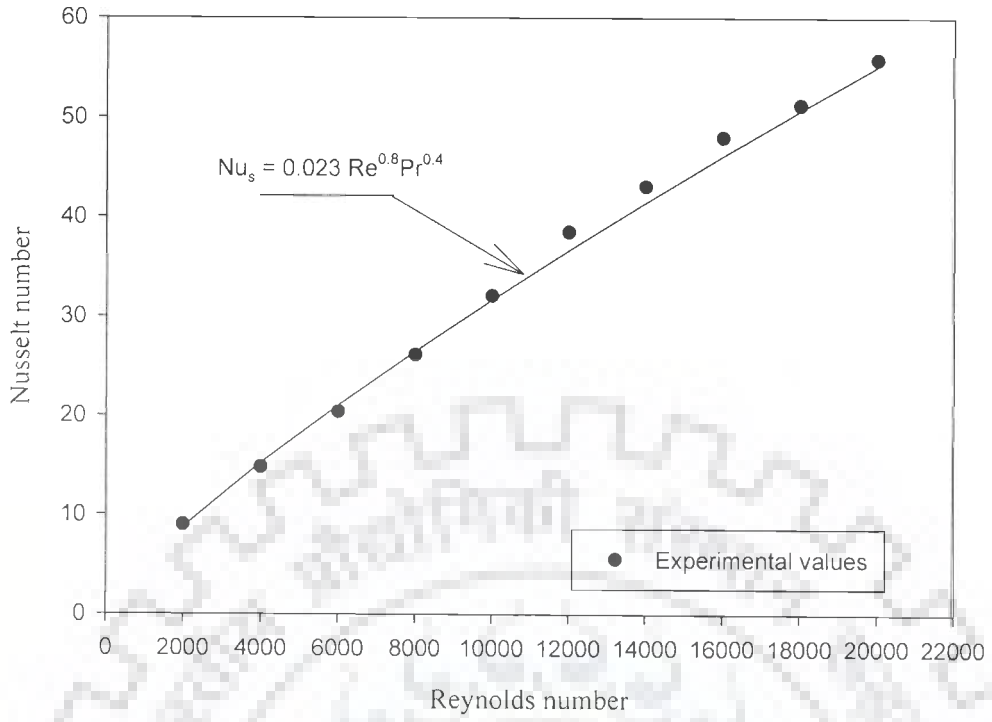

Fig.2.18 Comparison of experimental and predicted values of Nusselt number for smooth duct

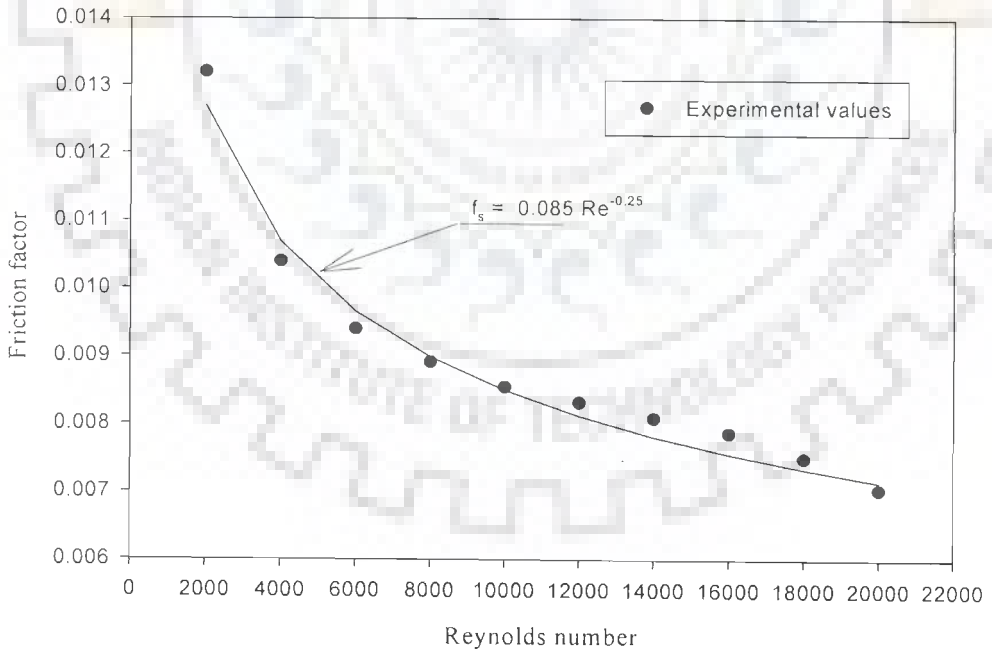

Fig.2.19 Comparison of experimental and predicted values of friction factor for smooth duct

Table 2.4 Experimental data recorded for roughened duct (plate no. 22)

Rib height, e : 1.6 mm
Relative roughness width, W/w : 6
Pitch, P : 16 mm
Angle of attack, α : 30°
Relative roughness pitch, P/e : 10
Manometric fluid density ρ : 769.8 kg/m^3 (kerosene)

Relative roughness height e/D_h : 0.035
Duct width W : 300.0 mm
Duct depth, H : 25.0 mm
Test plate length L : 1.0 m
Inclination of the manometer θ : 45°

Absorber Plate Temperatures

Run No.	ΔP_o mm	ΔP_d mm	Plate temperature (°C)																	
			T_1	T_2	T_3	T_4	T_5	T_6	T_7	T_8	T_9	T_{10}	T_{11}	T_{12}	T_{13}	T_{14}	T_{15}	T_{16}	T_{17}	T_{18}	T_{19}
1	7	0.165	62.3	61.5	60.8	76.9	78.7	77.1	78.1	83.5	89.3	87.1	86.1	91.3	93.9	92.8	93.1	95.4	97.2	96.2	96.5
2	24	0.42	65.4	64.8	65.3	71	71.8	71.2	71.4	75.6	79.4	78.8	78.5	81.7	84.8	83.8	84.1	87.3	88	86.8	87.3
3	54	0.864	61.2	60.8	61.2	63.8	64.8	64.6	64.2	67	70.9	70.2	70.7	73.9	74.7	74.2	73.9	75.7	76.8	76.3	76.5
4	96.5	1.395	55	54.7	54.9	55.9	56.9	56.7	56.6	59.1	62.3	61.9	62	63.9	66	65.6	65.8	67.9	68.4	68	67.7
5	154	2.135	49.6	49.1	49.3	50.7	52.2	51.8	52	54.6	57.6	57.3	57.6	58.7	60.6	60.5	60.3	62.6	62.9	62.6	62.7
6	225	2.9	46.8	45.8	46.0	47.3	48.5	47.8	47.7	50.8	53.5	53	52.5	54	55.6	55	54.8	56.5	58.5	58	57.6
7	308	3.76	45.2	45	44.8	46.1	47.7	47.5	47.2	49.2	50.1	49.6	49.7	52	53.4	53.2	53	53.2	53.3	53.1	53
8	395	4.5	43.1	42.8	42.9	44.3	45.6	45.2	45.43	46.8	48.5	48	47.9	48.9	50.1	49.8	49.9	50.3	50.5	49.9	50.2
9	495	5.27	42	41.7	41.7	42.4	43.5	43	43.3	44.3	46.2	45.9	46	47	48	47.8	47.9	49	49.8	49	49.5
10	585	5.84	40.8	40.7	40.4	40.9	41.2	40.9	41	42.2	43.5	42.9	43	44	45.8	45	45.4	47.2	49	48.7	48.5

Cont.-----

Air Temperatures

Test run	T_a (°C)	Air Temperature (°C)					
		Inlet	Outlet				
		T_{20}	T_{26}	T_{27}	T_{28}	T_{29}	T_{30}
1	27.5	44	60.1	65.4	67.5	66.4	68.1
2	27.5	43.5	56.1	63.1	62.5	65.1	63.2
3	27.6	39.2	52.2	54.4	53.8	53.9	54.2
4	27.6	35.4	48	47.1	48.3	48.1	49
5	27.6	33.1	44	43.2	43.8	44	45
6	27	32.2	42.3	41	41.6	41.1	43
7	27.5	31.1	39.5	39.6	39.8	39.9	40.7
8	27.7	30.4	39.4	37.8	37.6	37.6	38.6
9	27.5	29.9	39.8	39.1	38.9	38.9	40.2
10	27.4	29.3	35.6	34.6	35.1	35	36.2

2.8.2 Mass Flow Rate of Air

Mass flow rate of air has been determined from the pressure drop measurement across the calibrated orifice meter using the following relationship.

$$m = 0.624 \cdot A_o \cdot \left[\frac{2 \cdot \rho \cdot (\Delta P)_o}{1 - \beta^4} \right]^{0.5} \qquad (2.12)$$

where $(\Delta P)_o = 9.81 \cdot (\Delta h)_o \cdot \rho_m \cdot \mathrm{Sin}(\theta)$

Here, θ is the inclination of U- tube manometer from the horizontal and kept equal to 45°.

2.8.3 Velocity of Air Through Duct

The velocity of air is calculated from the knowledge of mass flow rate and area of flow as,

$$V = \frac{m}{\rho \cdot W \cdot H} \qquad (2.13)$$

2.8.4 Equivalent Hydraulic Diameter

The hydraulic diameter of the rectangular section of the duct is determined from the relationship as given below,

D = (4 x Area of flow)/ Perimeter

$$= \frac{4 \cdot (W \cdot H)}{2 \cdot (W + H)} \qquad (2.14)$$

2.8.5 Reynolds Number (Re)

The Reynolds number of airflow in the duct is calculated from the following relationship,

$$\mathrm{Re} = \frac{V \cdot D}{\upsilon} \tag{2.15}$$

2.8.6 Friction Factor (f)

The friction factor is determined from the measured values of pressure drop $(\Delta P)_d$ across the test section length using Darcy Wiesbach equation as below,

$$f_s = \frac{2 \cdot (\Delta P)_d \cdot D}{4 \cdot \rho \cdot L \cdot V^2} \tag{2.16}$$

where, $(\Delta P)_d = 9.81 \cdot (\Delta h)_d \cdot \rho_m$

2.8.7 Heat Transfer Coefficient (h)

Heat transfer rate "Q_u" to the air is given by

$$Q_u = m\, C_p\, (T_o - T_i) \tag{2.17}$$

The heat transfer coefficient for the heated test section is calculated from the relationship given below;

$$h = \frac{Q_u}{A_p (T_p - T_f)} \tag{2.18}$$

where T_p and T_f are the average absorber plate and the fluid temperatures respectively, as discussed above.

2.8.8 Nusselt Number (Nu)

The heat transfer coefficient calculated using Eq.2.18 is used to determine the Nusselt number as below;

$$Nu = \frac{h \cdot D}{k} \qquad (2.19)$$

Table 2.5 lists the values of these parameters calculated from the raw data given in Table 2.4. The details of this sample calculation are given in Appendix A.

Table 2.5 Results of roughened duct (Plate no. 22) corresponding to data of Table 2.4

Test run	T_i (°C)	T_o (°C)	T_f (°C)	T_p (°C)	m (Kg/s)	Re	Qu (W)	h (W/m^2-K)	Nu	Nu_s	f	f_s
1	44	65.5	54.75	84	0.00642	2017	139	15.8	25.76	9	0.04114	0.0132
2	43.5	62	52.75	77.7	0.01193	3761	222.5	29.72	48.7	14.8	0.03054	0.0104
3	39.2	53.7	46.45	69.6	0.01804	5747	263.5	37.9	63.2	20.4	0.02793	0.0094
4	35.4	48.1	41.75	61.6	0.02432	7845	311.1	52.2	88.1	26.13	0.02523	0.0089
5	33.1	44	38.55	56.48	0.03088	10024	338.8	63.0	107.3	32.1	0.02420	0.0086
6	32.2	41.8	37	52.13	0.03725	12191	360	79.31	135.7	38.5	0.02248	0.0083
7	31.1	39.9	35.5	49.8	0.04389	14370	388.9	90.6	155.6	43.11	0.02131	0.0081
8	30.4	38.2	34.3	47.4	0.04980	16352	391	99.5	171.5	48.05	0.01988	0.0079
9	29.9	36.8	33.35	45.68	0.05582	18365	387.8	104.8	181.1	51.27	0.01858	0.0077
10	29.3	35.3	32.3	43.8	0.06076	20021	367	106.4	184.4	55.87	0.01742	0.0070

2.9 UNCERTAINTY ANALYSIS

An error analysis relevant to the experimental results has been carried out on the basis of uncertainty analysis proposed by Kline and McClintosh [157]. The details of the analysis are given in Appendix-B. The maximum possible measurement errors in the values of major parameters are given below:

Reynolds number : 3.0%

Heat transfer coefficient : 6.3%

Nusselt number : 6.31%

Friction factor : 5.97%

CHAPTER-3

RESULTS AND DISCUSSION

3.1 INTRODUCTION

The major objective of this investigation is to examine how the heat transfer coefficient and friction factor are affected when the absorber plate of the conventional solar air heater is artificially roughened by employing multiple v-ribs. Literature review shows that enhancement of heat transfer coefficient due to artificial roughness in the flow passage of a solar air heater is always accompanied by an increase in frictional losses. This increases the pumping power required to maintain flow in the duct resulting in reduction of net energy gain. It is, therefore, desirable that the roughness parameters are selected in such a way that the friction factor should be maintained as low as possible whereas, the heat transfer coefficient is increased to the maximum possible extent. Such a selection is possible only if heat transfer and fluid flow characteristics of the roughened duct are known.

In this chapter, the results of experimental investigation on heat transfer and friction characteristics of rectangular ducts roughened with multiple v-ribs are presented as function of flow and roughness geometry parameters. Results have also been compared with those of the conventional smooth (without roughness) duct under similar flow and thermal boundary conditions to examine the enhancement in heat transfer coefficient and corresponding increase in friction factor.

3.2 HEAT TRANSFER CHARACTERISTICS

Turbulence generation, on account of presence of artificial roughness in laminar sub layer region, results in heat transfer enhancement from the heated surface of rectangular ducts. The shape and orientation of roughness geometry has a

significant effect on turbulence intensity. In this experimental investigation, effect of multiple v-rib roughness geometry parameters such as relative roughness height, e/D, relative roughness width, W/w, angle of attack, α and relative roughness pitch, P/e on heat transfer and friction has been studied extensively and discussed below.

3.2.1 Effect of Relative Roughness Height

Figs. 3.1 to 3.8 show the effect of relative roughness height on Nusselt number as a function of Reynolds number. These plots have been prepared for a given value of relative roughness width and fixed values of other roughness geometry parameters. It has been observed from these plots that Nusselt number increases monotonically with increase in Reynolds number for a fixed value of relative roughness height. In order to bring out the effect of relative roughness height on Nusselt number, the experimental data presented in Fig.3.6 has been re-plotted in Fig.3.9 for different values of Reynolds number and fixed values of other roughness geometry parameters. It has been observed that Nusselt number increases with increase in relative roughness height and maximum value of Nusselt number has been obtained corresponding to relative roughness height value of 0.043. It may be attributed to the fact that as relative roughness height increases, ribs protrude beyond laminar sub layer in to core flow, causing more turbulence which results in increase in heat transfer.

It has been observed that rate of increase of Nusselt number is high as relative roughness height increases from 0.019 to 0.035 and for increase in relative roughness height from 0.035to 0.043, rate of increase in Nusselt number decreases. Table 3.1 shows the percentage variation of Nusselt number with increase in relative roughness height.

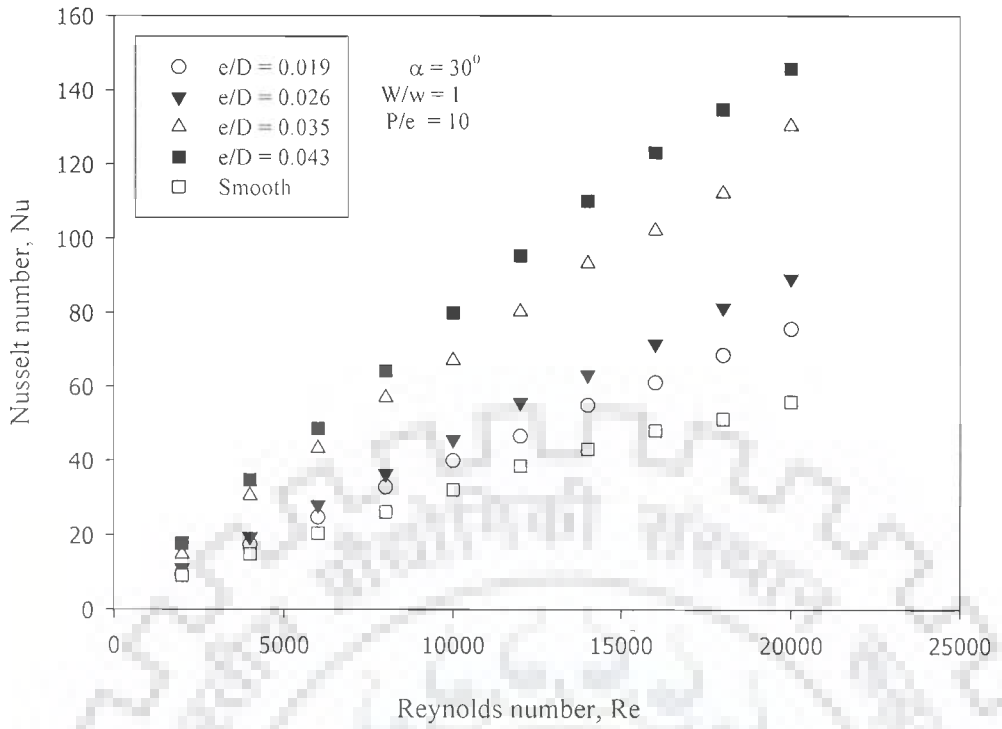

Fig.3.1 Effect of relative roughness height on Nusselt number for W/w = 1

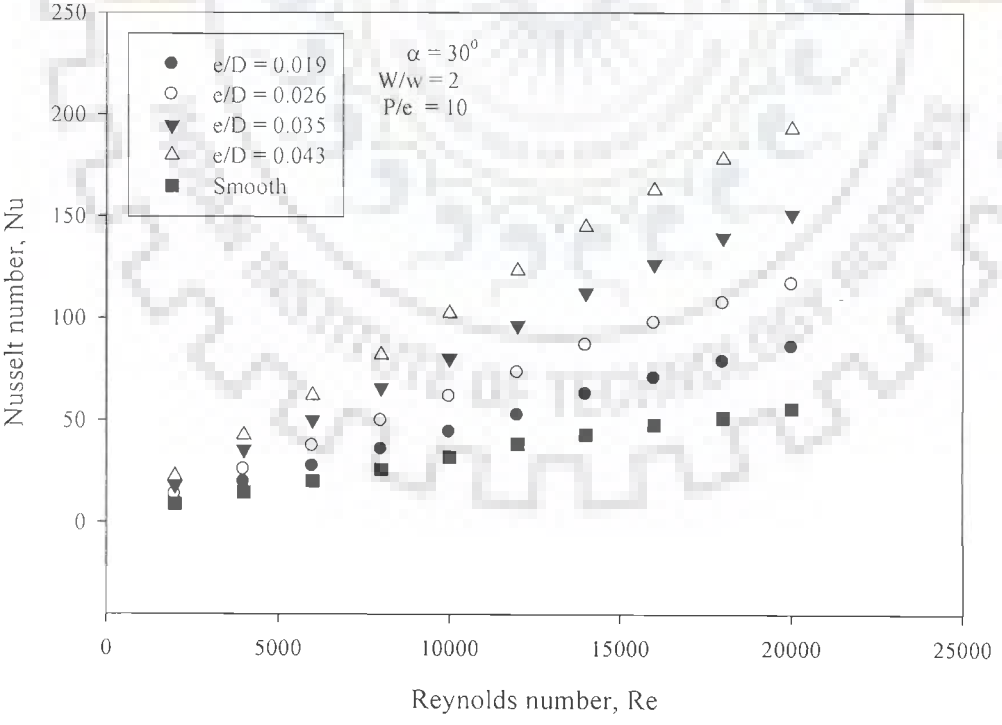

Fig.3.2 Effect of relative roughness height on Nusselt number for W/w = 2

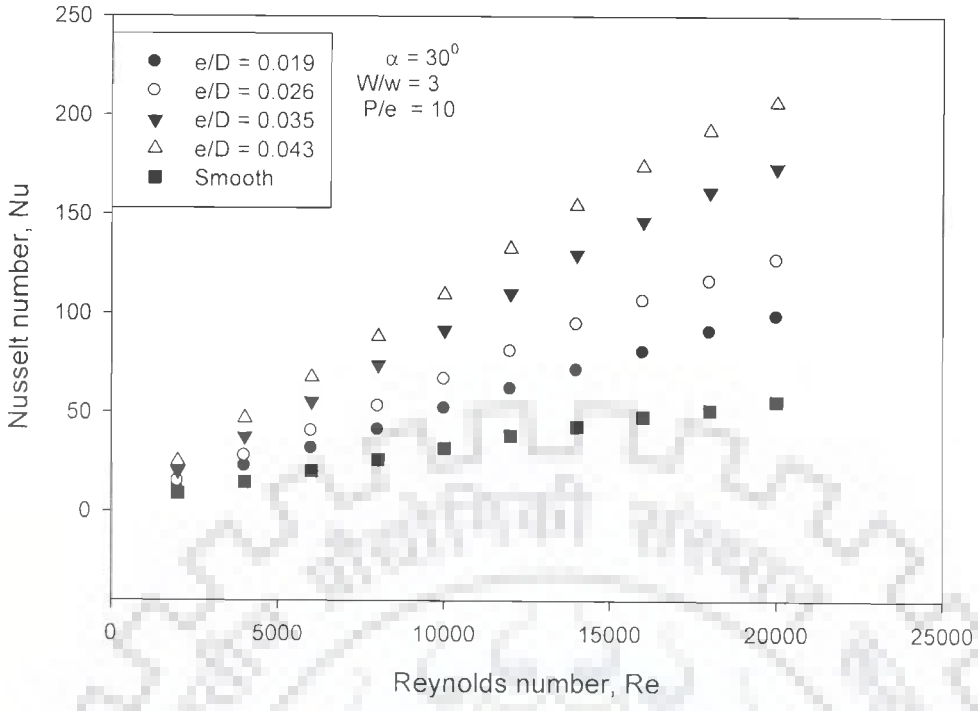

Fig.3.3 Effect of relative roughness height on Nusselt number for W/w = 3

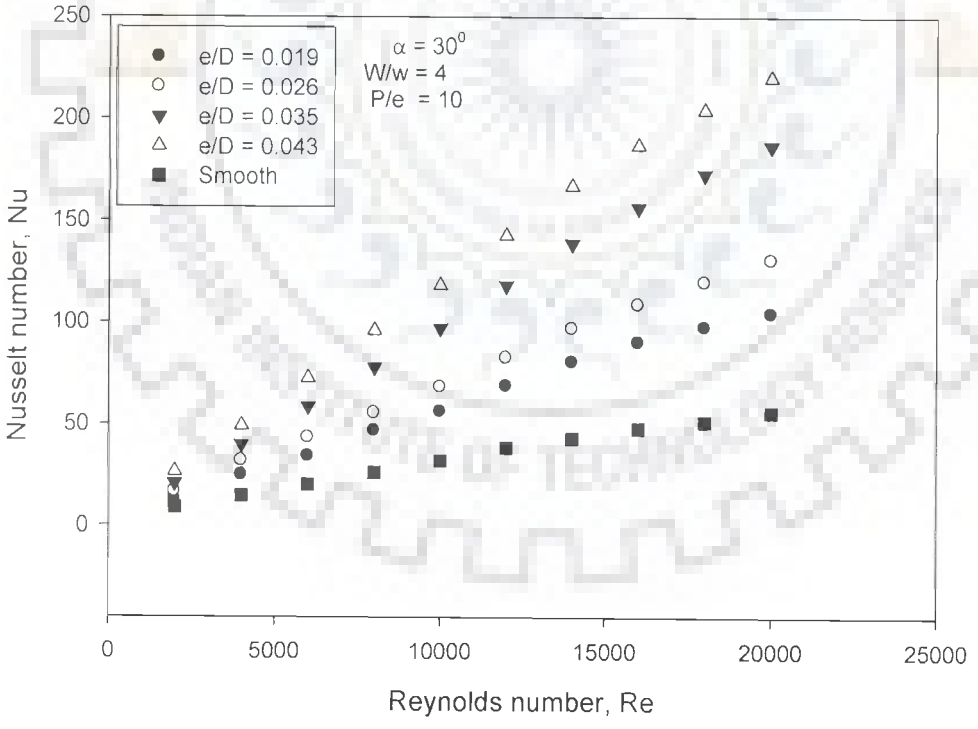

Fig.3.4 Effect of relative roughness height on Nusselt number for W/w = 4

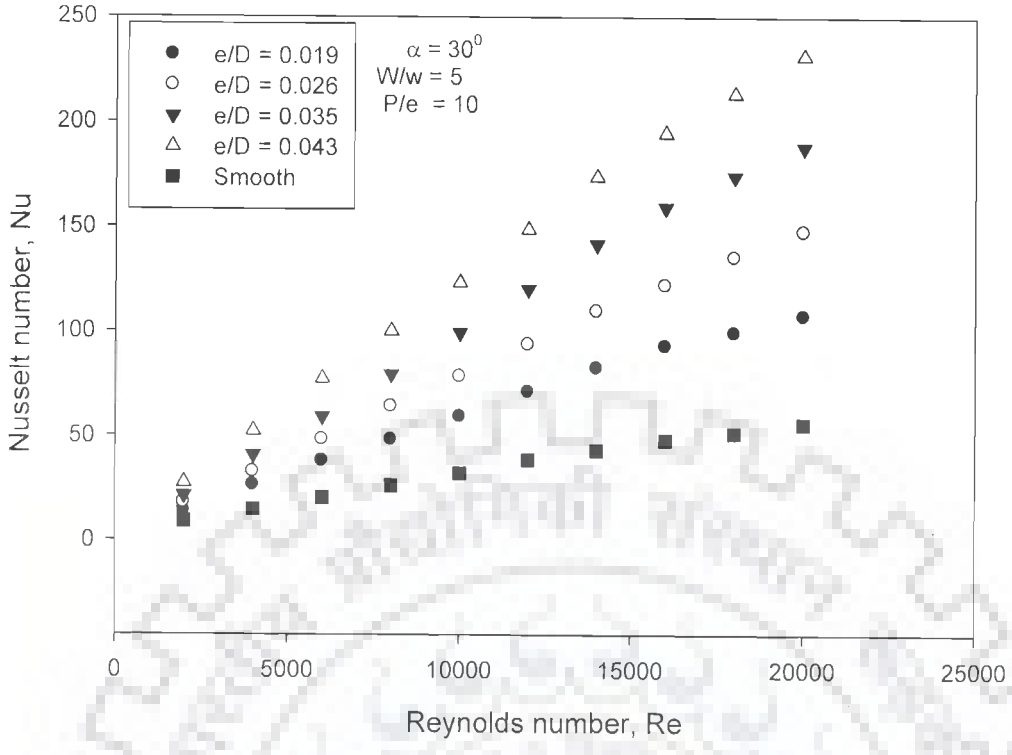

Fig.3.5 Effect of relative roughness height on Nusselt number for W/w = 5

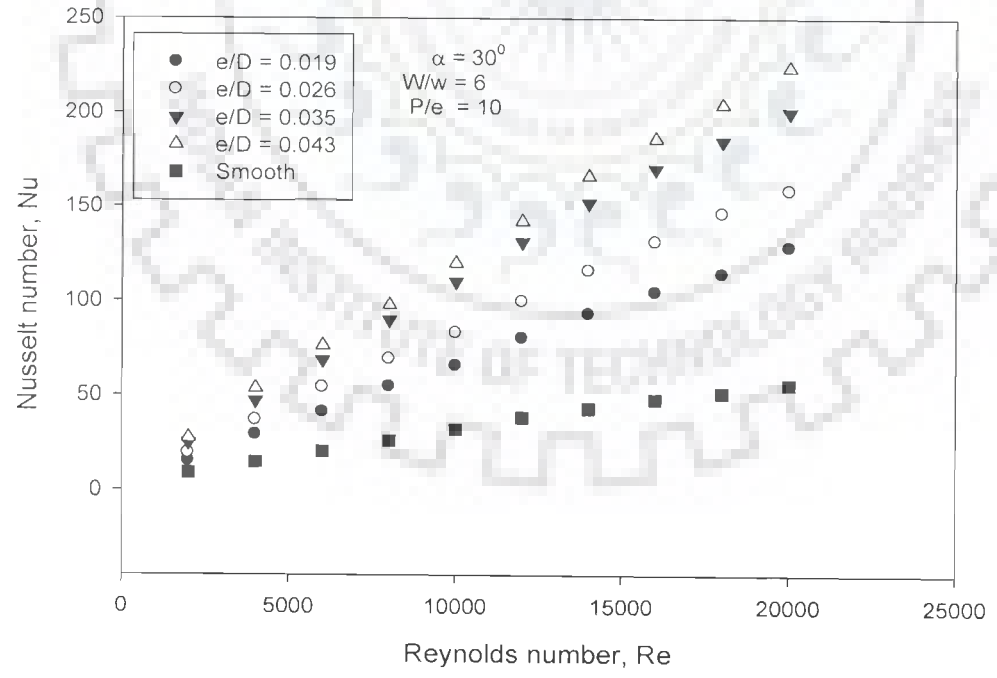

Fig.3.6 Effect of relative roughness height on Nusselt number for W/w = 6

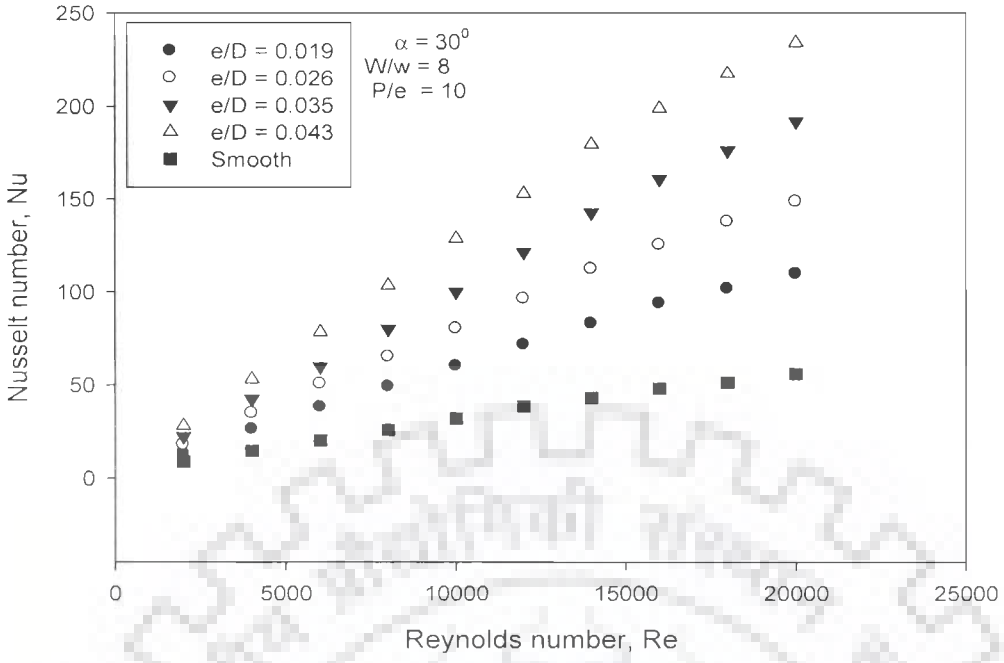

Fig.3.7 Effect of relative roughness height on Nusselt number for W/w = 8

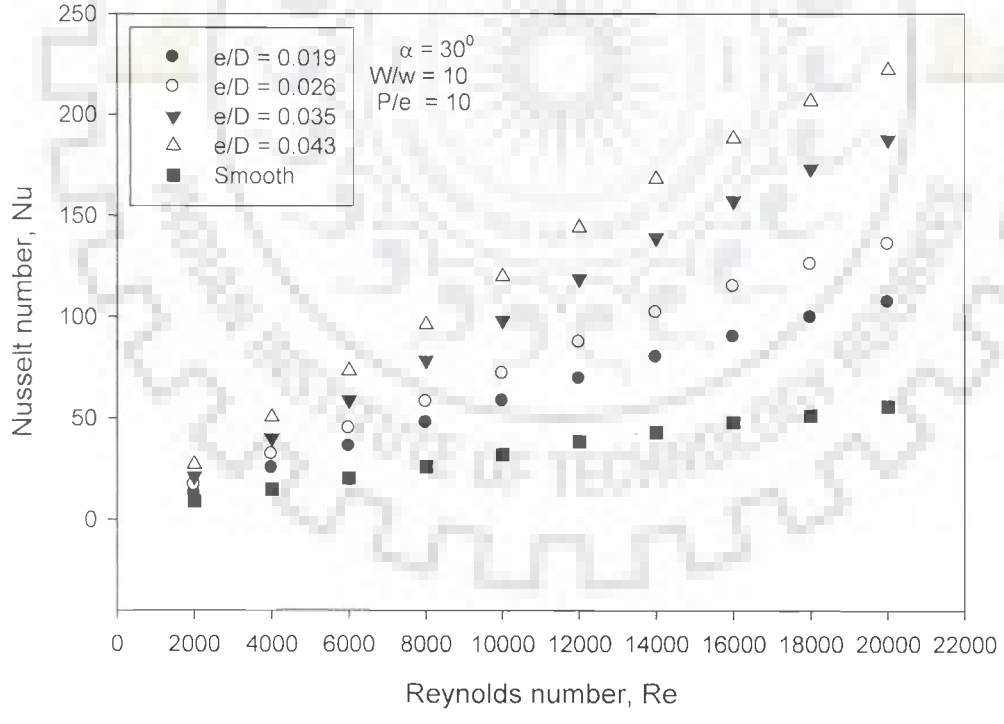

Fig.3.8 Effect of relative roughness height on Nusselt number for W/w = 10

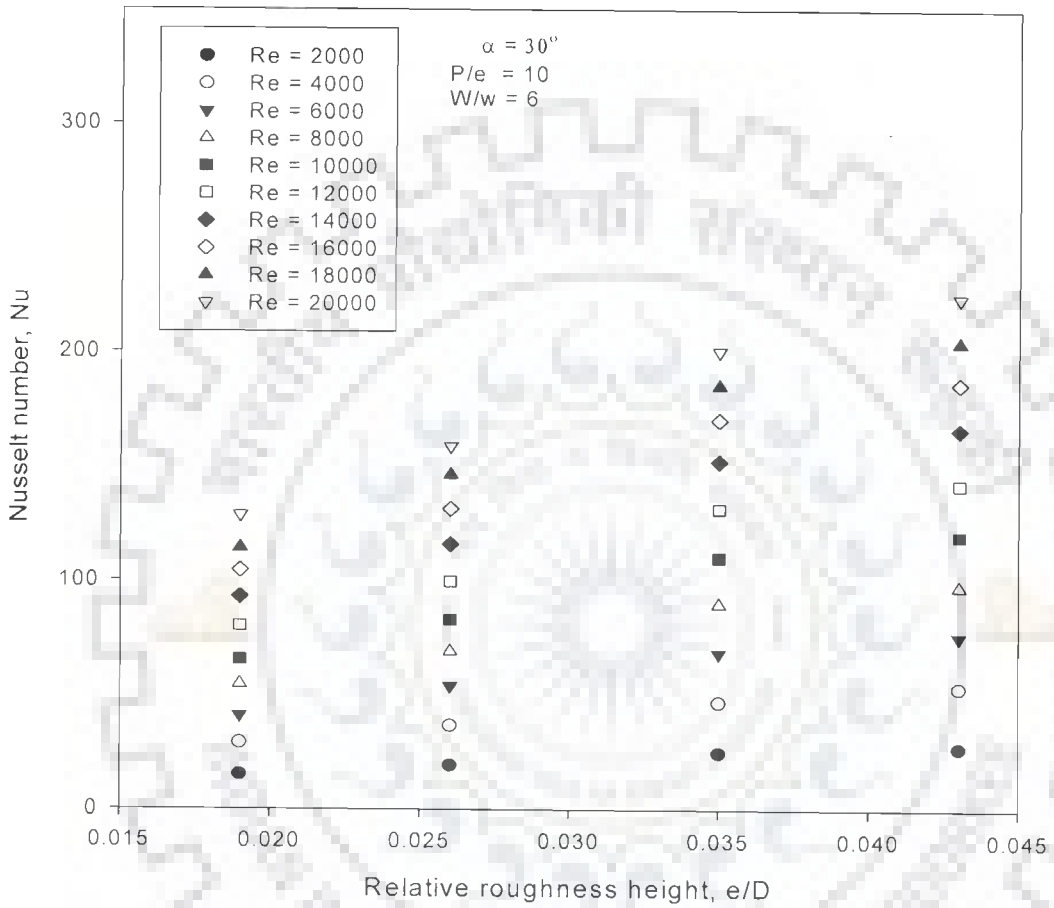

Fig.3.9 Effect of relative roughness height on Nusselt number for different values of Reynolds number

Table 3.1 Variation of Nusselt number with relative roughness height, e/D

Fixed roughness geometry parameters	Relative roughness height, e/D	Range of variation of Nusselt number (%)
P/e = 10 W/w = 6 $\alpha = 30^0$	0.019 to 0.026	23 to 31
	0.026 to 0.035	26 to 33
	0.035 to 0.043	8.2 to 14

3.2.2 Effect of Relative Roughness Width

Figs.3.10 to 3.13 show the effect of relative roughness width, W/w on Nusselt number as a function Reynolds number. These plots have been prepared for a given value of relative roughness height and fixed values of other roughness geometry parameters. It has been observed that for a given value of relative roughness width, Nusselt number increases with increase in Reynolds number. The experimental data presented in Fig.3.13 has been re-plotted in Fig.3.14 for different values of Reynolds number and fixed values of other roughness geometry parameters to bring out the effect of relative roughness width on Nusselt number. It has been observed that Nusselt number increases with increase in relative roughness width, W/w and attains a maximum value corresponding to relative roughness width value of 6 in the range of parameters considered. With further increase in the value of relative roughness width, Nusselt number decreases. This may be explained on account of the fact that shaping of a long, angled rib into v-shape helps in the formation of two leading ends (where heat transfer rate is high) and a single trailing end (where heat transfer is low) as well as two secondary flow cells which promote turbulence mixing and hence increased heat transfer in case of a single v-rib as shown in Fig.3.15 [79]. A single v-shaped rib placed along the width of duct has relative roughness width value of 1 and it brings about considerable improvement in heat transfer of the duct as compared to an angled rib [63].

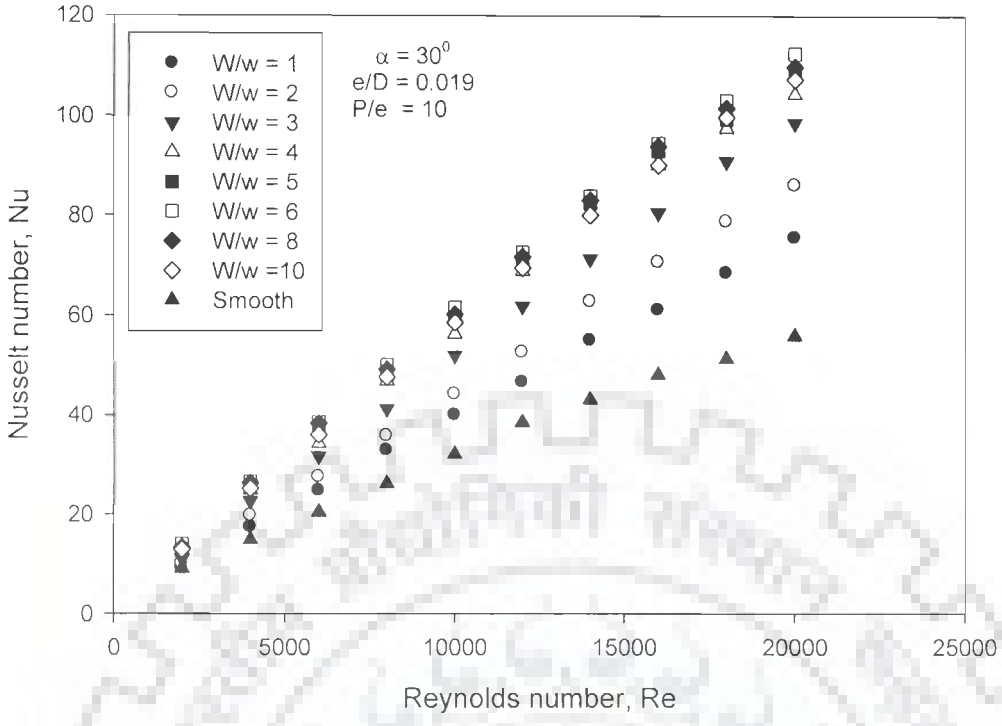

Fig.3.10 Effect of relative roughness width on Nusselt number for e/D = 0.019

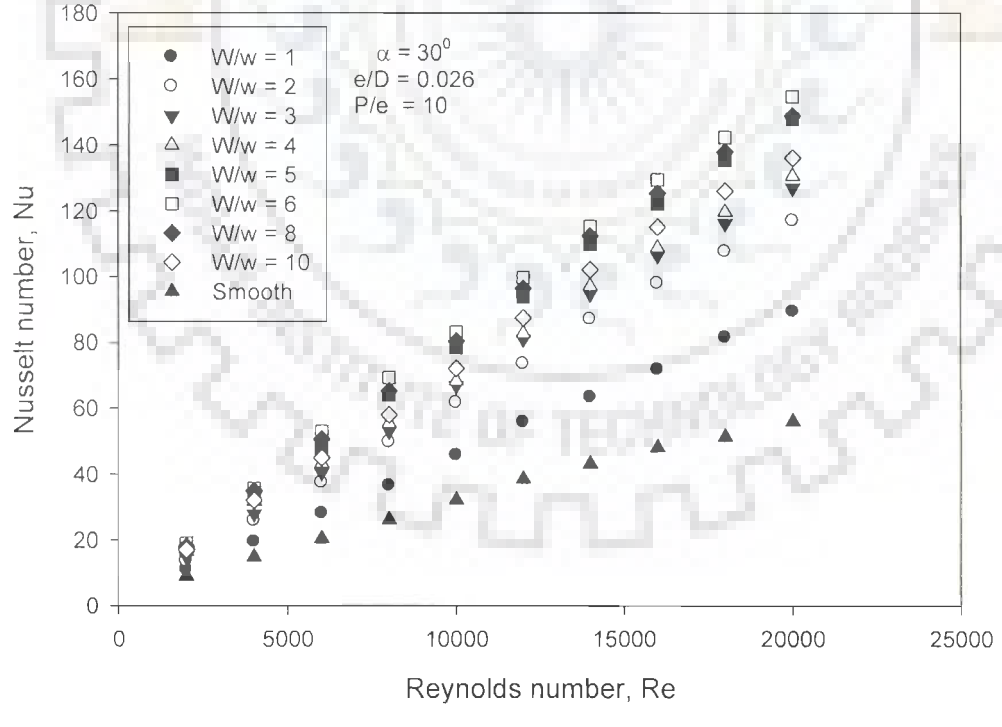

Fig.3.11 Effect of relative roughness width on Nusselt number for e/D = 0.026

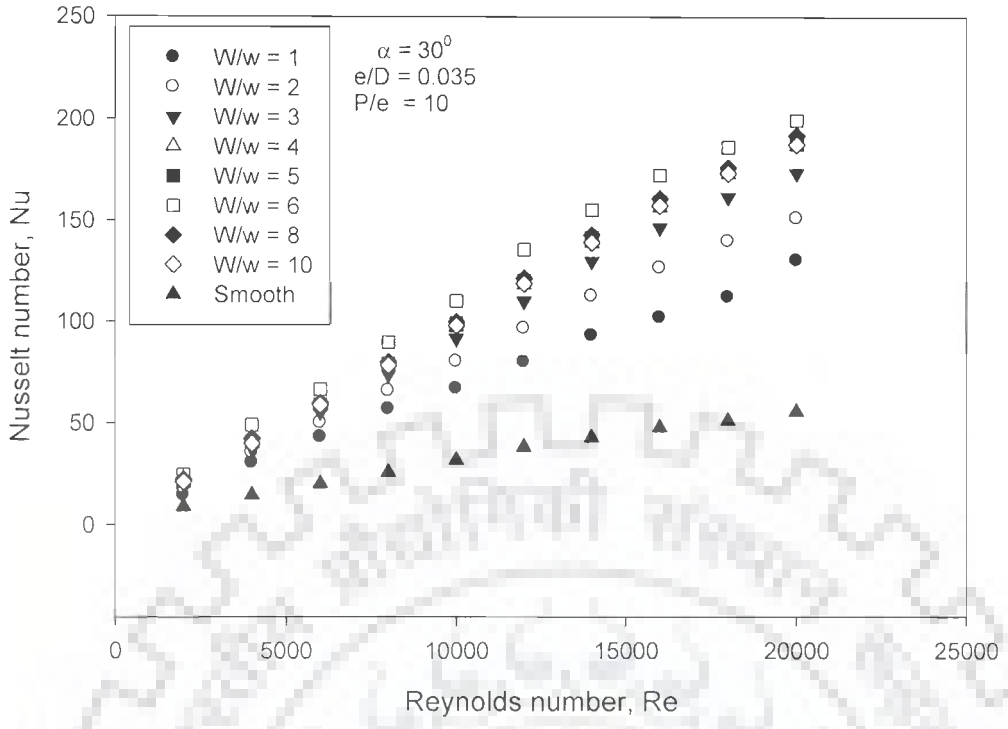

Fig.3.12 Effect of relative roughness width on Nusselt number for e/D = 0.035

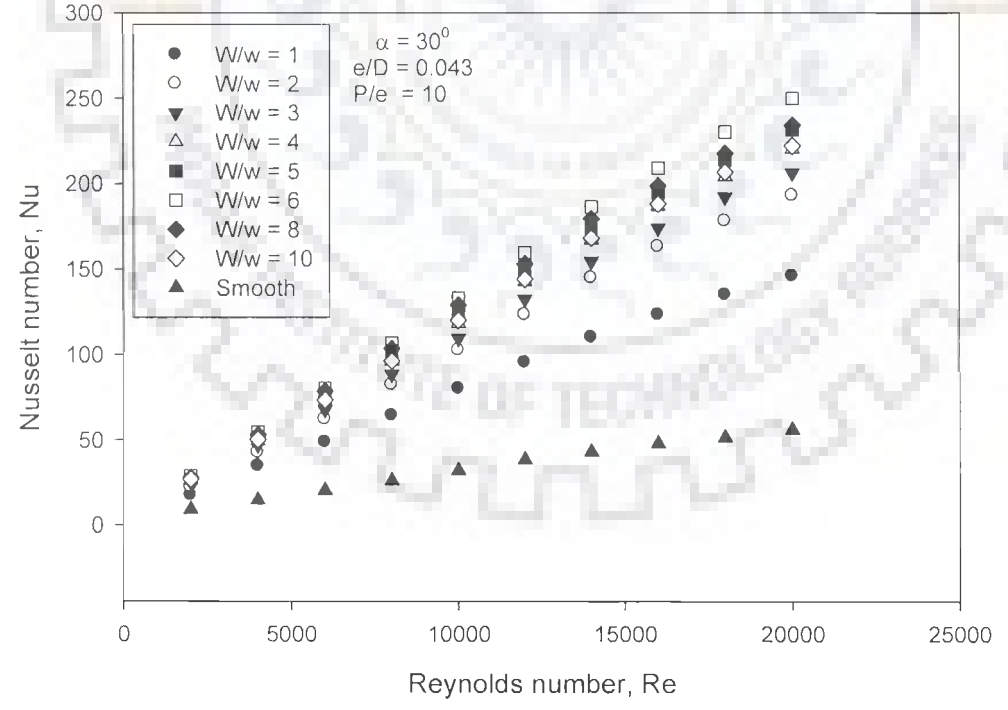

Fig.3.13 Effect of relative roughness width on Nusselt number for e/D = 0.043

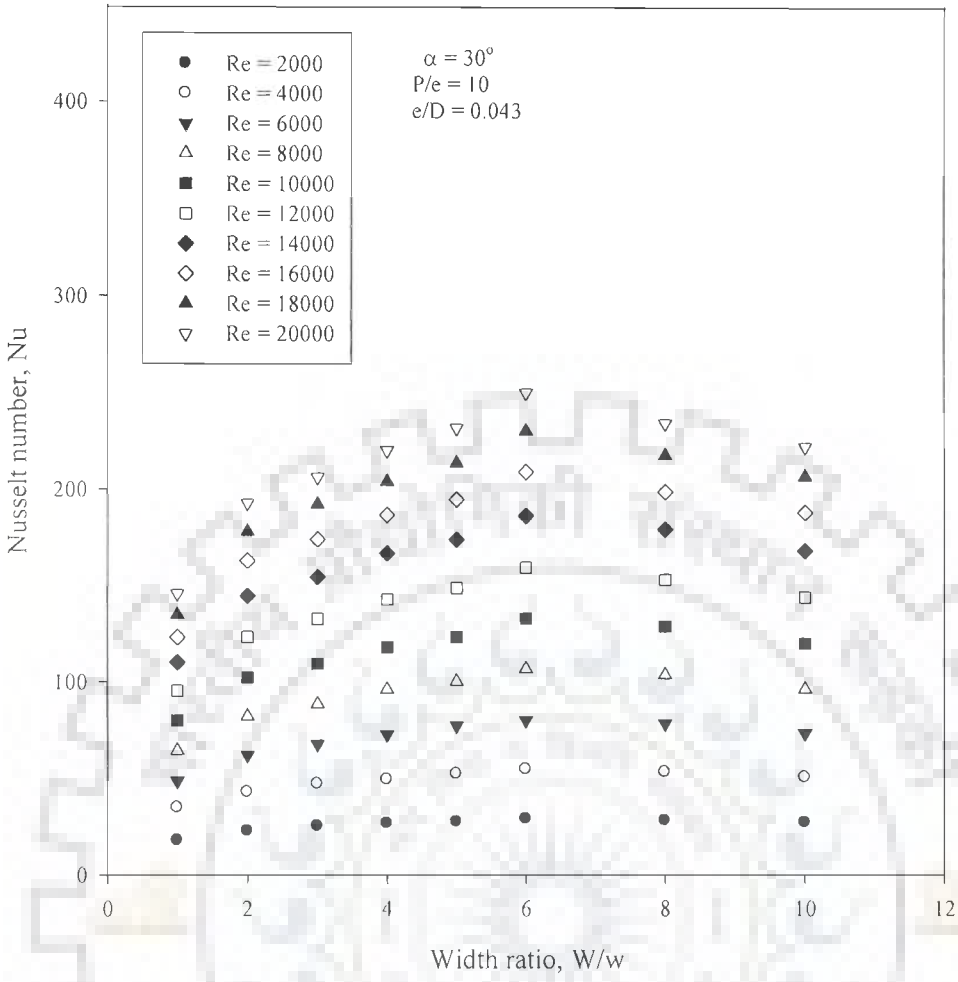

Fig.3.14 Effect of relative roughness width on Nusselt number for different values of Reynolds number

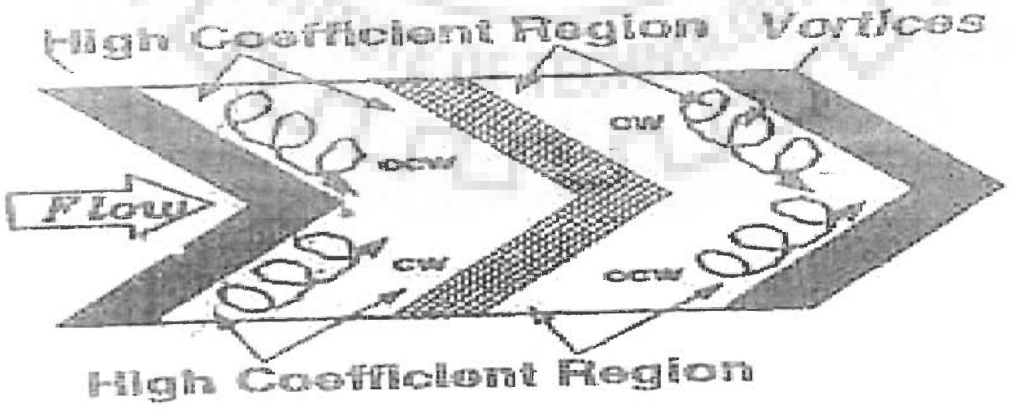

Fig.3.15 Effect of v-shaping of rib [79]

As shown in Figs.3.16 (a) and (b), increase in relative roughness width value to 2, doubles the number of leading ends and secondary flow cells, resulting in considerable enhancement in heat transfer. As the relative roughness width is further increased, heat transfer also increases on account of formation of higher number of leading ends and secondary flow cells as shown in Figs.3.16 (c) and (d). The increase in heat transfer coefficient with increase in relative roughness width continues up to relative roughness width value of 6 and beyond which heat transfer starts decreasing. It may be attributed to the fact that around relative roughness width value of 6, turbulence, resulting from the presence of multiple v-ribs, reaches its maximum value and with further increase in relative roughness width value appears to impede the development of secondary flow resulting in the reduction of heat transfer.

It has been observed from these plots that rate of increase of Nusselt number is quite high as relative roughness width increases from 1 to 2 and the rate of increase of Nusselt number decreases considerably with further increases in relative roughness width value. The rate of increase of Nusselt number becomes negative as relative roughness width value increases beyond 6.

Table 3.2 shows the percentage variation of Nusselt number with increase in relative roughness width.

Table 3.2 Variation of Nusselt number with relative roughness width, W/w

Fixed roughness geometry parameters	**Relative roughness width, W/w**	**Range of variation of Nusselt number (%)**
e/D = 0.043 P/e = 10 $\alpha = 30^0$	1 to 2	27.5 to 32
	2 to 3	7 to 11
	3 to 4	5 to 8
	4 to 5	4 to 7
	5 to 6	3.5 to 6
	6 to 8	-2.1 to -6.3
	8 to 10	-3.5 to -7.1

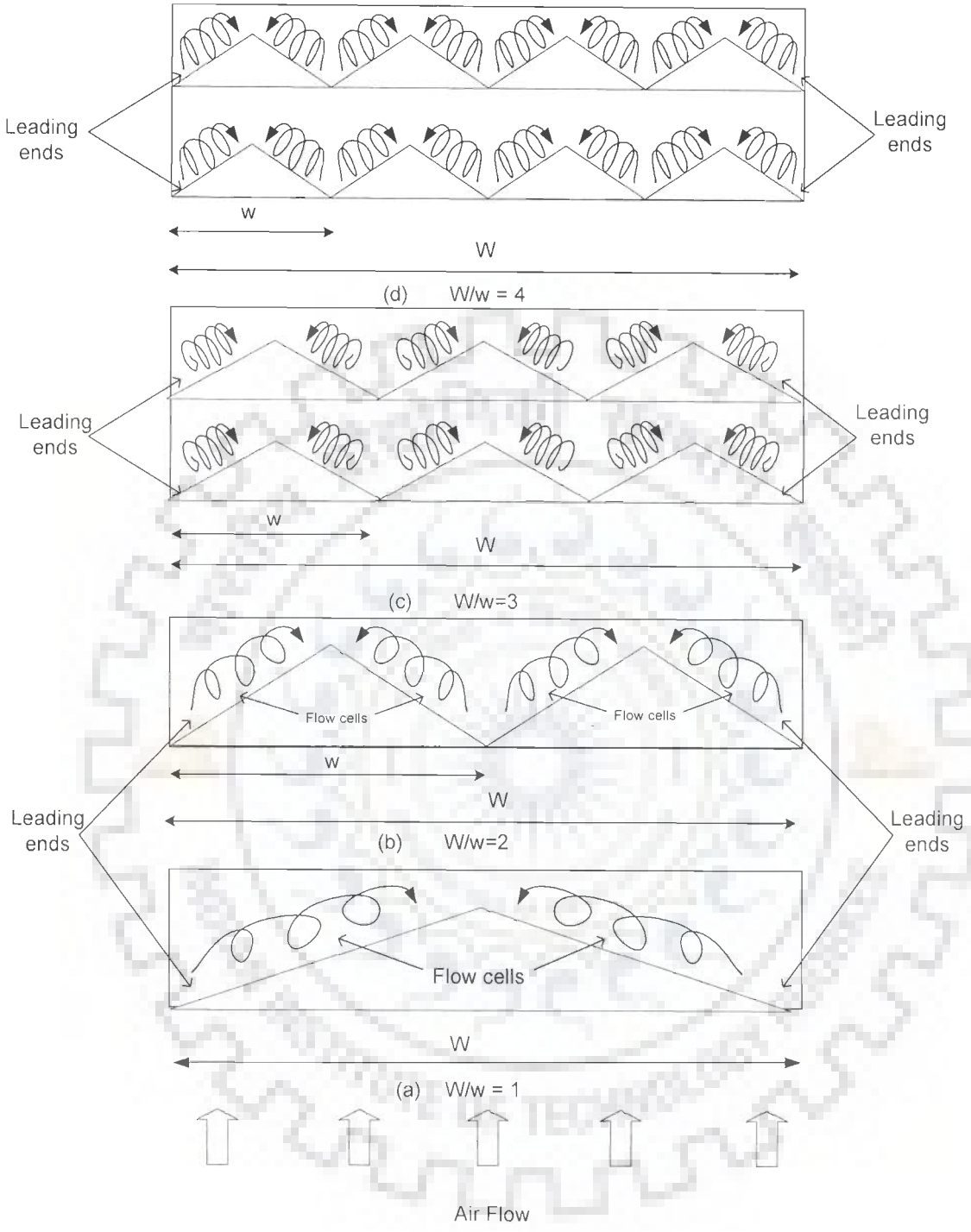

Fig.3.16 Formation of flow cells with increase in relative roughness width, W/w

3.2.3 Effect of Angle of Attack

Fig.3.17 shows the variation of Nusselt number as a function of angle of attack for various values of Reynolds number and fixed values of other roughness geometry parameters. It has been observed from Fig.3.17 that for a given value of angle of attack, Nusselt number increases monotonically with increase in Reynolds number.

In order to elaborate the effect of angle of attack on Nusselt number, the experimental data presented in Fig.3.17 has been re-plotted in Fig.3.18. In this plot, Nusselt number has been plotted as a function of angle of attack for different values of Reynolds number and fixed values of other roughness geometry parameters. Nusselt number increases with increase in angle of attack, attains a maximum value corresponding to angle of attack value of 60^0 and then decreases with further increases in the value of angle of attack. According to Momin et al. [69], the possible reason for Nusselt number attaining a maximum value corresponding to angle of attack value of 60^0 is separation of the secondary flow resulting from the presence of ribs and the movement of resulting vortices combining together to yield an optimum value of angle of attack. This observation is in general agreement with previous investigations [62, 74, 91, 92, 96, 102, and 122], involving inclined ribs, wire mesh roughness and single v-rib arrangements.

The rate of increase in Nusselt number is high as angle of attack increases from 30^0 to 45^0 and this rate of increase in Nusselt number decreases as angle of attack increases from 45^0 to 60^0. Table 3.3 shows the percentage variation in Nusselt number with increase in angle of attack.

Table 3.3 Variation of Nusselt number with angle of attack

Fixed roughness geometry parameters	Angle of attack, α	Range of variation of Nusselt number (%)
e/D = 0.043 P/e = 10 W/w = 6	30^0 to 45^0	16.5 to 33
	45^0 to 60^0	8 to 14
	60^0 to 75^0	-5 to -10

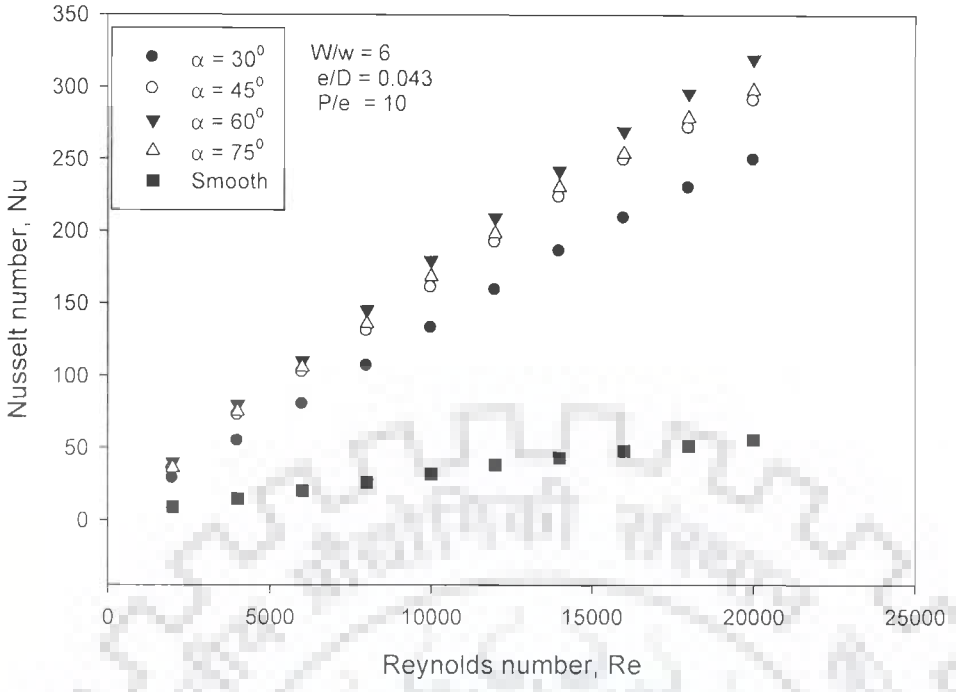

Fig.3.17 Effect of angle of attack on Nusselt number

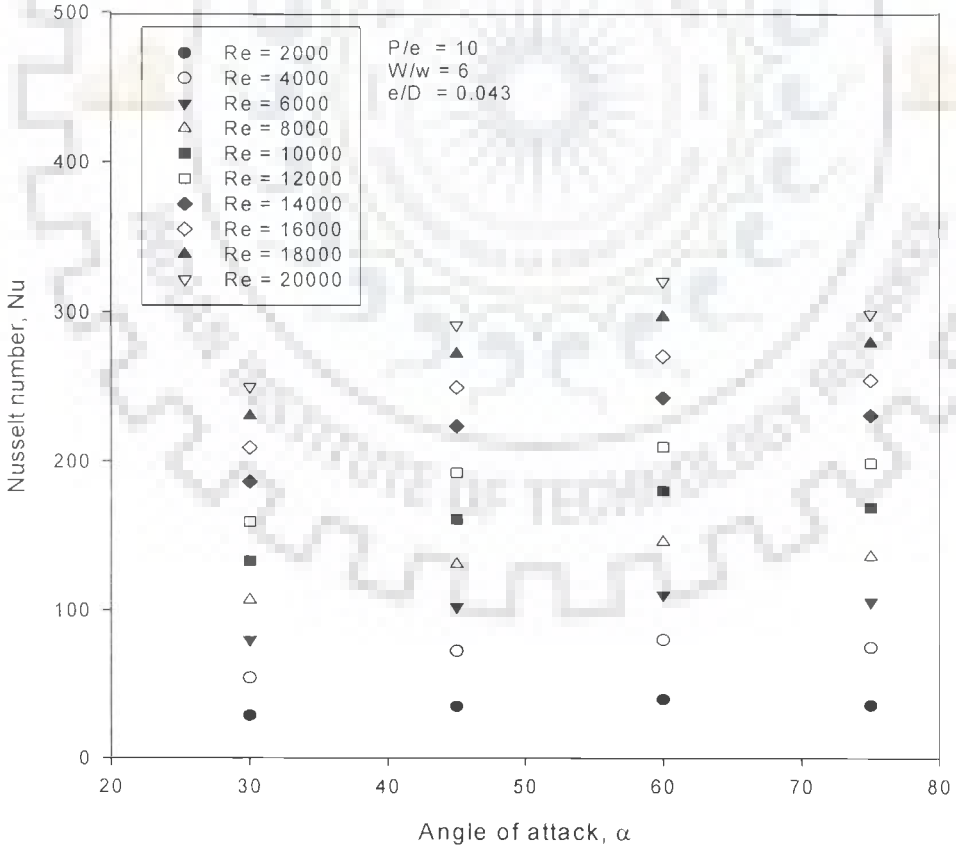

Fig.3.18 Effect of angle of attack on Nusselt number for different values of Reynolds number

3.2.4 Effect of Relative Roughness Pitch

Fig.3.19 shows the variation of Nusselt number as a function of Reynolds number for different values of relative roughness pitch and fixed values of other roughness geometry parameters. For all Reynolds numbers, the maximum value of Nusselt number has been observed corresponding to the relative roughness pitch value of 8, whereas the lowest value of Nusselt number has been found to occur at the relative roughness pitch value of 12 for the range of investigation. In order to bring out the effect of relative roughness pitch on Nusselt number, the results presented in Fig.3.19 are re-plotted in Fig.3.20 for different values of Reynolds number. It is observed that for all Reynolds numbers, Nusselt number increases as relative roughness pitch value increases from 6 to 8 and for relative roughness pitch values greater than 8, Nusselt number decreases. Han et al. [90] reported that the occurrence of the maximum value of Nusselt number at a certain relative roughness pitch value signifies the presence of the re-attachment point and this is the optimum pitch value. It is seen that the optimum relative roughness pitch value in the present case is 8.0. As the relative roughness pitch is reduced to a value below 8.0, the flow is not likely to reattach to the heat transferring surface before it reaches the successive rib. Therefore, the thermal performance of the duct deteriorates with decrease in the relative roughness pitch value below 8.0. On the other hand, as relative roughness pitch value increases above 8.0, the number of re-attachment points per unit length will reduce as compared to those with the relative roughness pitch of 8.0 which also results in the reduction of heat transfer coefficient and hence Nusselt number is lower for the relative roughness pitch values higher than 8.0. Han et al. [92] have also reported that the rib configuration with relative roughness pitch value of 7.5 yields higher enhancement in heat transfer as compared to the relative roughness pitch value of 10 or 5. Webb et al. [84] reported that the maximum heat transfer coefficient occurs at a value of relative roughness pitch value in the range of 6-8.

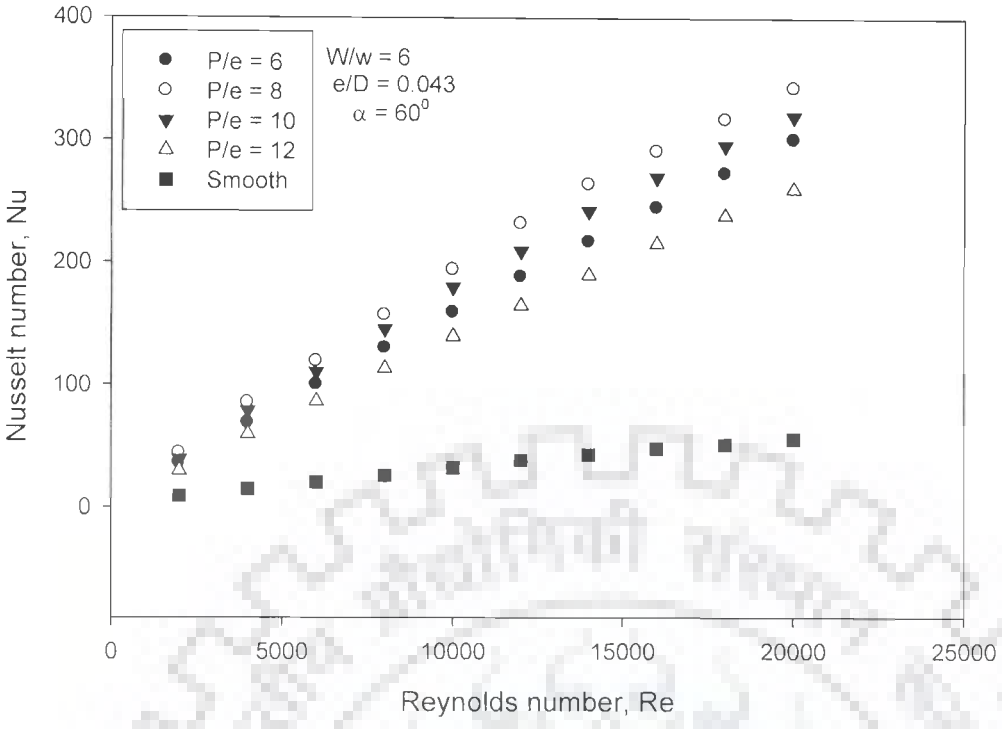

Fig.3.19 Effect of relative roughness pitch on Nusselt number

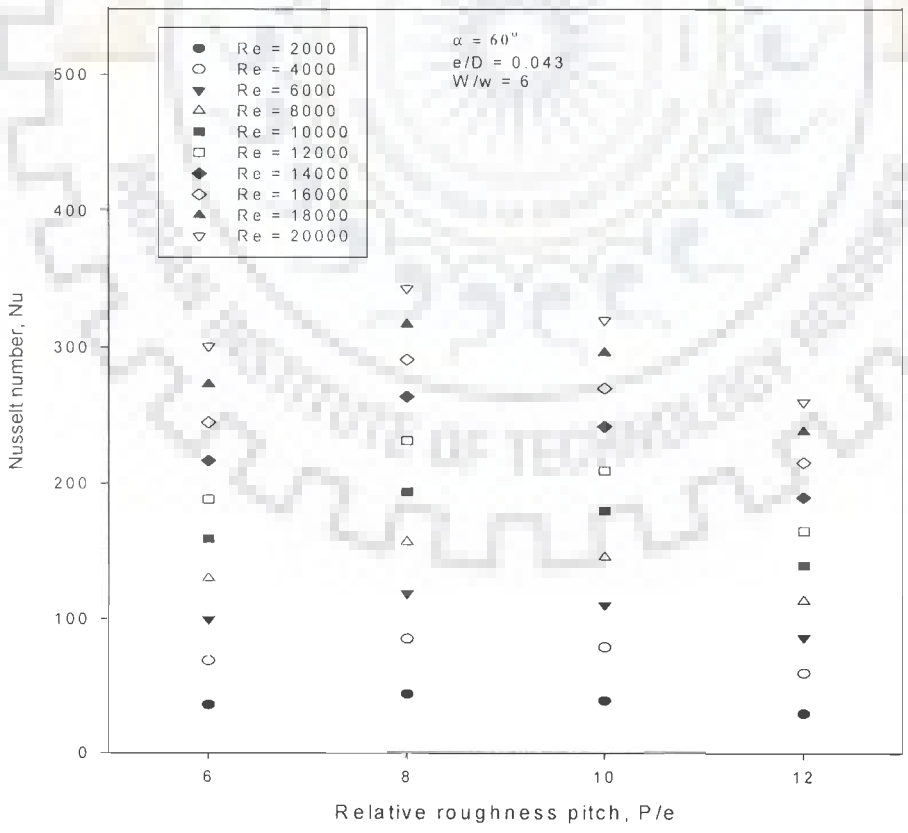

Fig.3.20 Effect of relative roughness pitch on Nusselt number for different values of Reynolds number

Table 3.4 shows the percentage variation of Nusselt number with relative roughness pitch.

Table 3.4 Variation of Nusselt number with relative roughness pitch, P/e

Roughness pitch, P/e	Fixed roughness geometry parameters	Range of variation of Nusselt number (%)
e/D = 0.043 W/w = 6 $\alpha = 60^0$	6 to 8	16 to 23.7
	8 to 10	-6.5 to -11.4
	10 to 12	-18.7 to -24.4

3.3 FRICTION CHARACTERISTICS

Invariably, use of artificial roughness geometry substantially enhances heat transfer from heated surface of rectangular ducts, however, there occurs a corresponding increase in frictional losses. In this experimental investigation, it has been found that the roughness geometry parameters associated with multiple v-rib type of roughness have a strong influence on friction factor of roughened surfaces. The results so obtained are discussed below.

3.3.1 Effect of Relative Roughness Height

The values of friction factor as function of Reynolds number for different values of relative roughness height have been plotted in Figs. 3.21 to 3.28. These plots have been prepared for a given value of relative roughness width, fixed values of angle of attack and relative roughness pitch. It has been observed from these plots that for a given relative roughness height value, friction factor decreases with increase in Reynolds number. The experimental data presented in Fig.3.26 has been re-plotted in Fig.3.29 for different values of Reynolds number in order to bring out the effect of relative roughness height on friction factor.

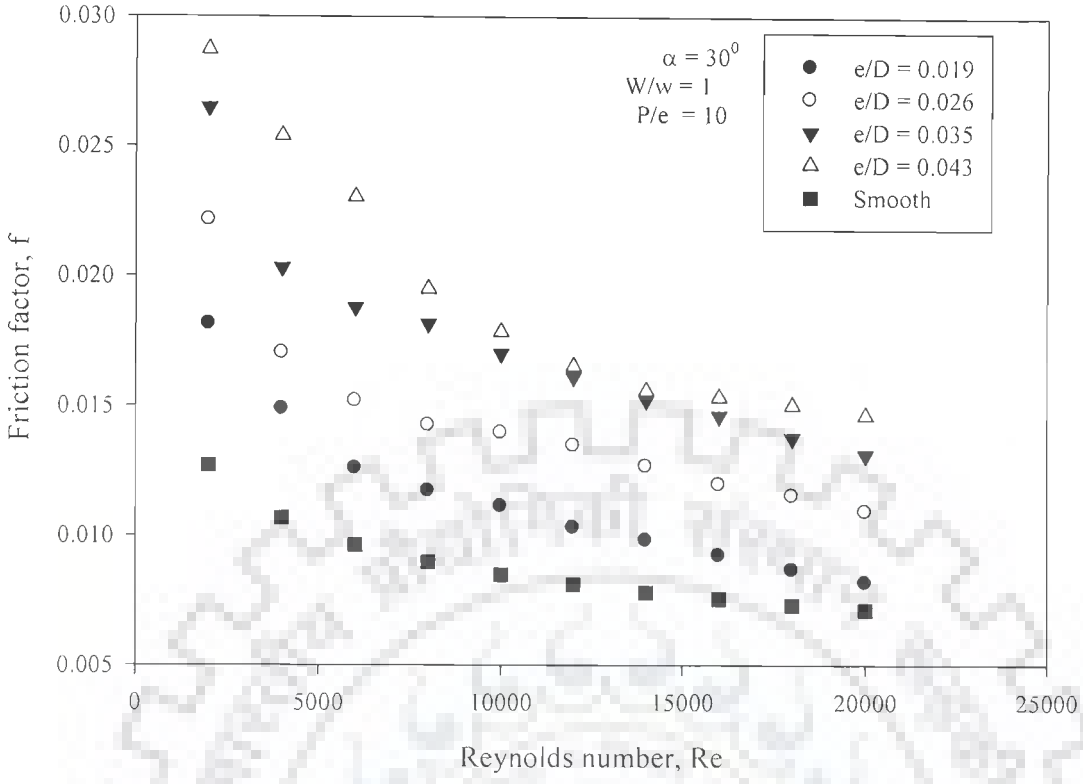

Fig.3.21 Effect of relative roughness height on friction factor for W/w = 1

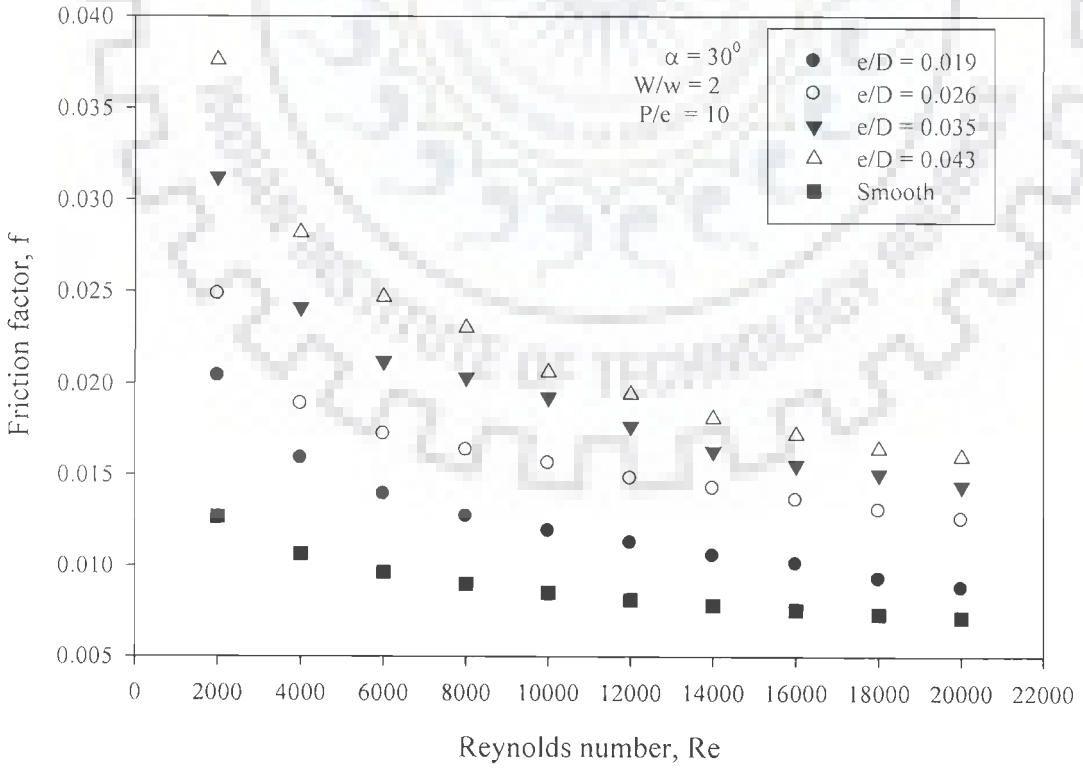

Fig.3.22 Effect of relative roughness height on friction factor for W/w = 2

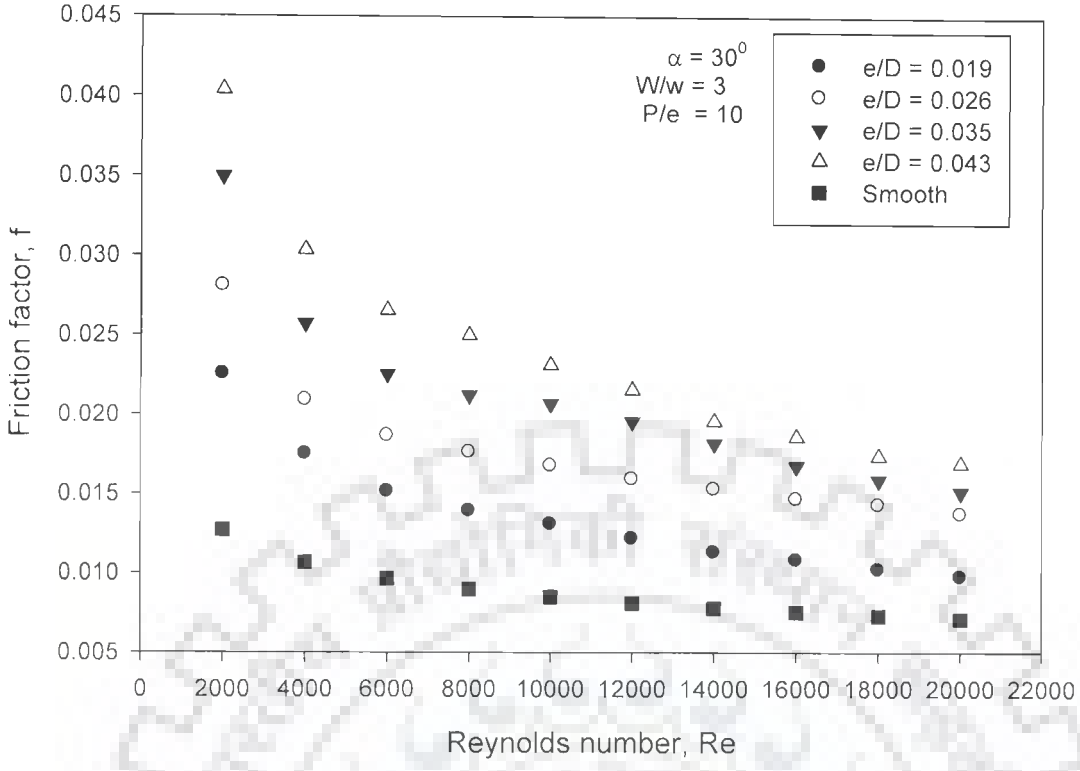

Fig.3.23 Effect of relative roughness height on friction factor for W/w = 3

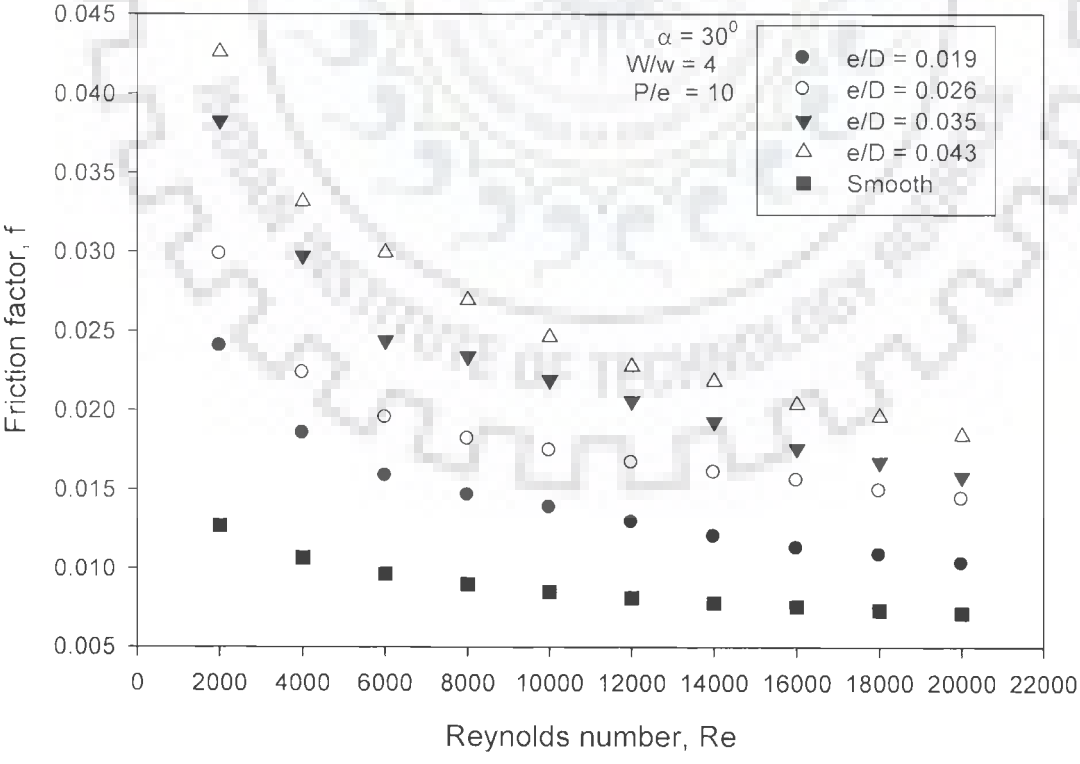

Fig.3.24 Effect of relative roughness height on friction factor for W/w = 4

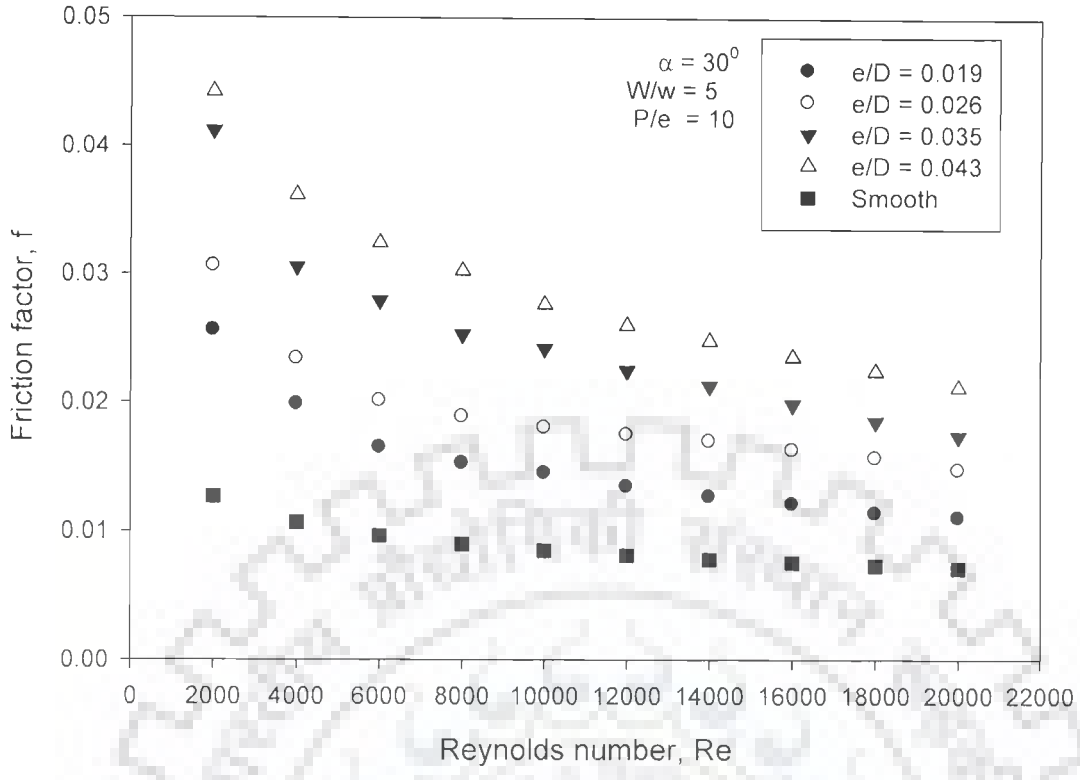

Fig.3.25 Effect of relative roughness height on friction factor for W/w = 5

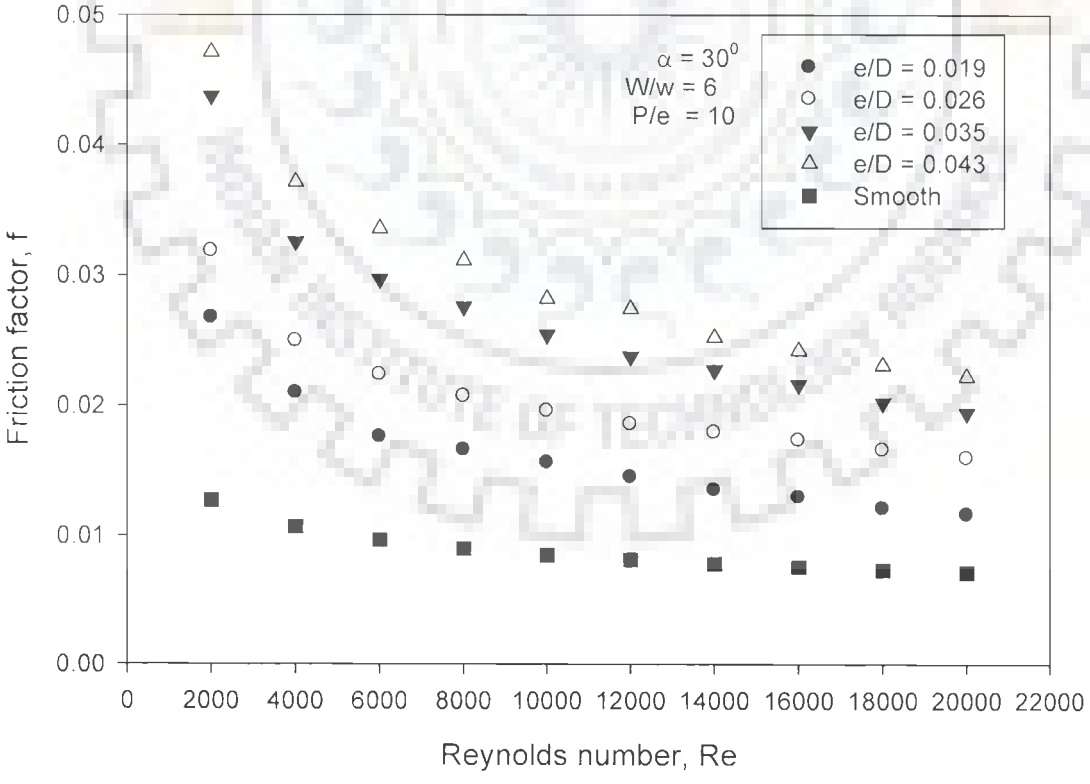

Fig.3.26 Effect of relative roughness height on friction factor for W/w = 6

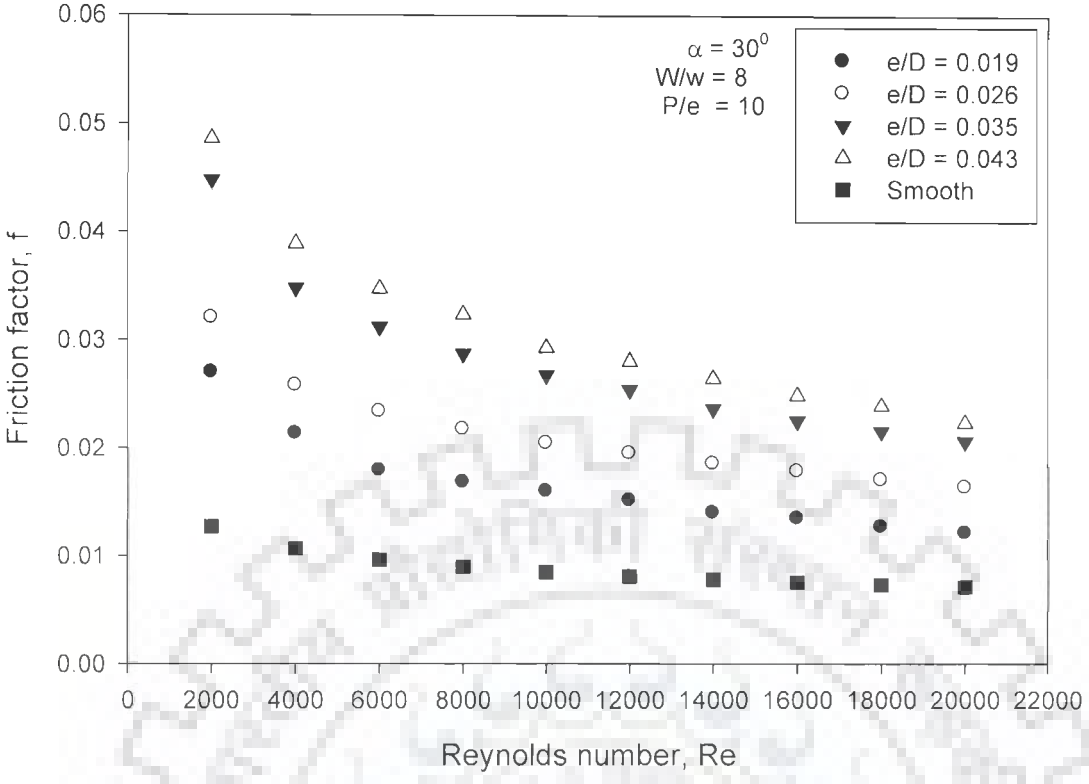

Fig.3.27 Effect of relative roughness height on friction factor for W/w = 8

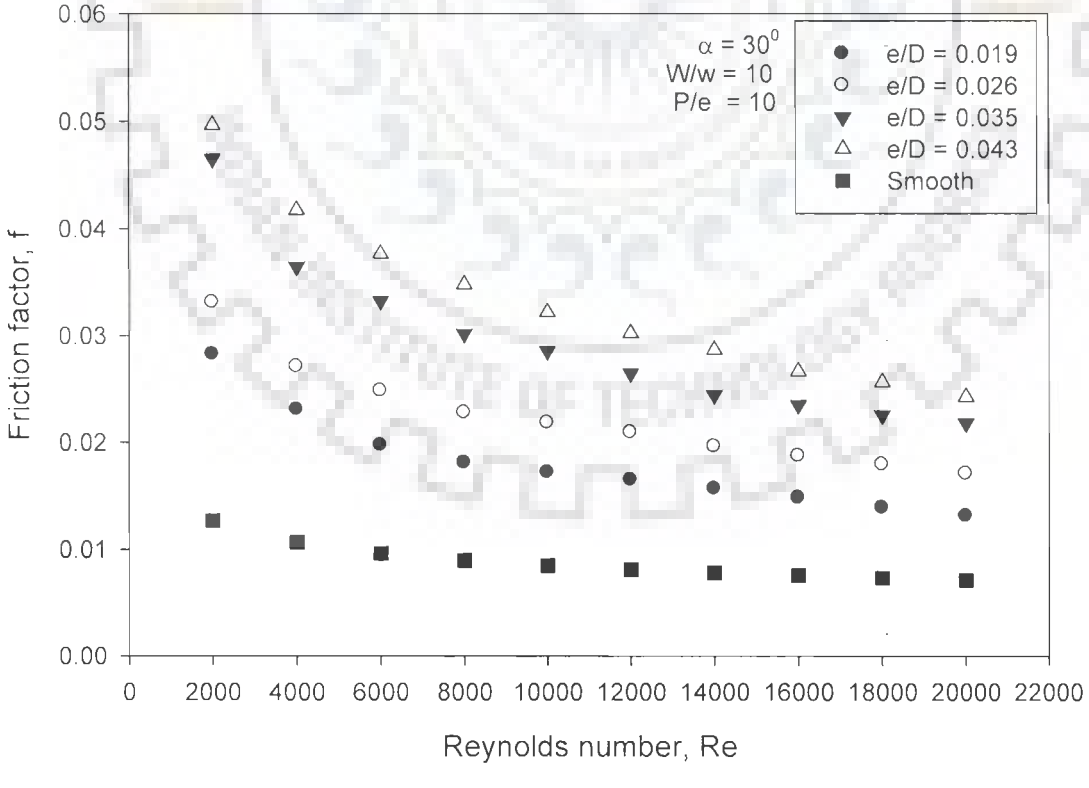

Fig.3.28 Effect of relative roughness height on friction factor for W/w = 10

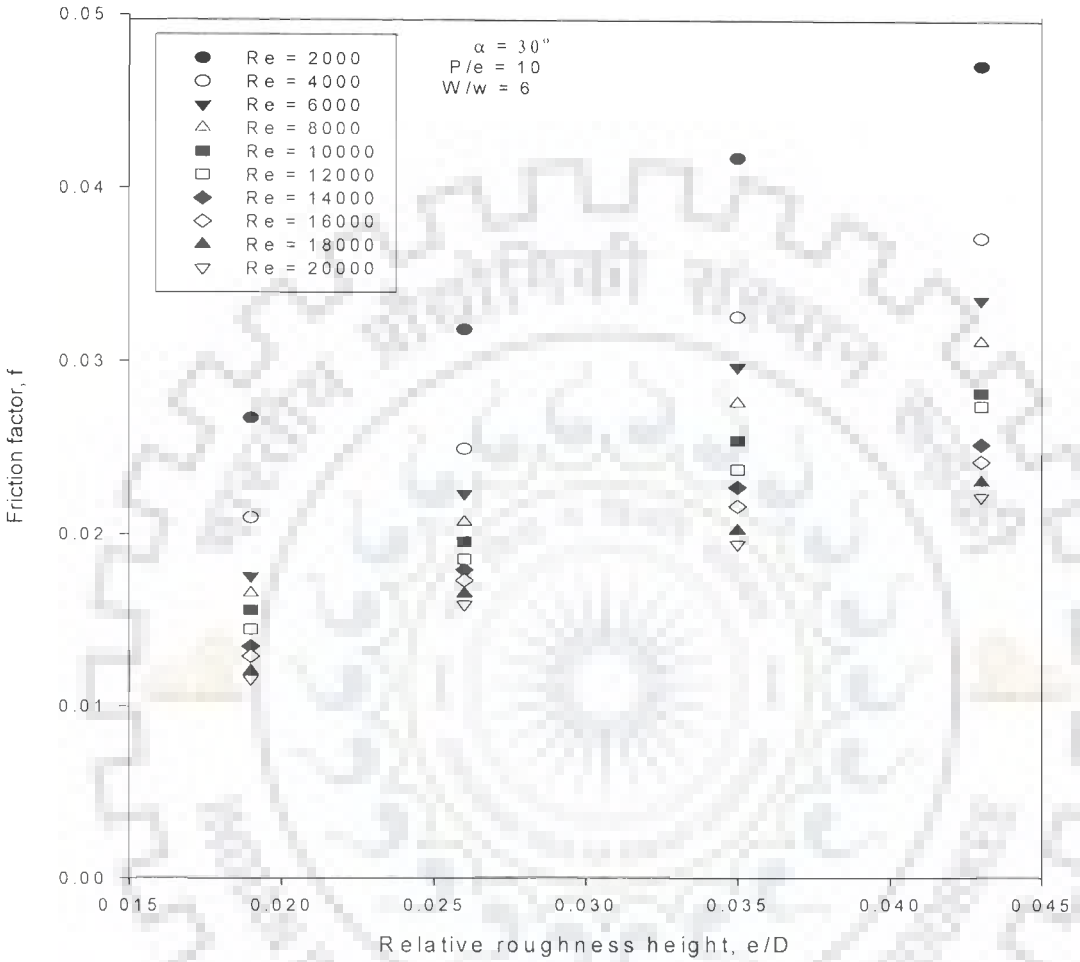

Fig.3.29 Effect of relative roughness height on friction factor for different values of Reynolds number

It has been observed from Fig.3.29 that friction factor increases monotonically with increase in relative roughness height and the maximum value of friction factor corresponds to relative roughness height value of 0.043. It is due to the fact that with the increase in relative roughness height value, ribs protrude more and more into the core flow resulting in increase in turbulence level as well as the pressure drop or friction factor. This is in agreement with the observations made by Webb et al [84], Prasad and Saini [73] and Bhagoria et al [125]. Table 3.5 presents the percentage variation of friction factor as relative roughness height increases.

Table 3.5 Variation of friction factor with relative roughness height, e/D

Fixed roughness geometry parameters	Relative roughness height, e/D	Range of variation of Nusselt number (%)
P/e = 10 W/w = 6 $\alpha = 30^0$	0.019 to 0.026	19 to 37.5
	0.026 to 0.035	22 to 37
	0.035 to 0.043	7.7 to 15.4

3.3.2 Effect of Relative Roughness Width

Figs.3.30 to 3.33 show the effect of relative roughness width on friction factor as a function of Reynolds number. These plots have been drawn for a given value of relative roughness height, fixed values of angle of attack and relative roughness pitch. It has been observed from these plots that for all the cases, friction factor decreases with increase in Reynolds number. The Fig.3.33 has been re-plotted as Fig.3.34 for different values of Reynolds number so that effect of relative roughness width on friction factor is clearly visible. It has been observed from Fig.3.34 that friction factor increases monotonically with increase in relative roughness width. The friction factor increases rapidly up to relative roughness width value of 6 and beyond this value, the rate of increases of friction factor decreases.

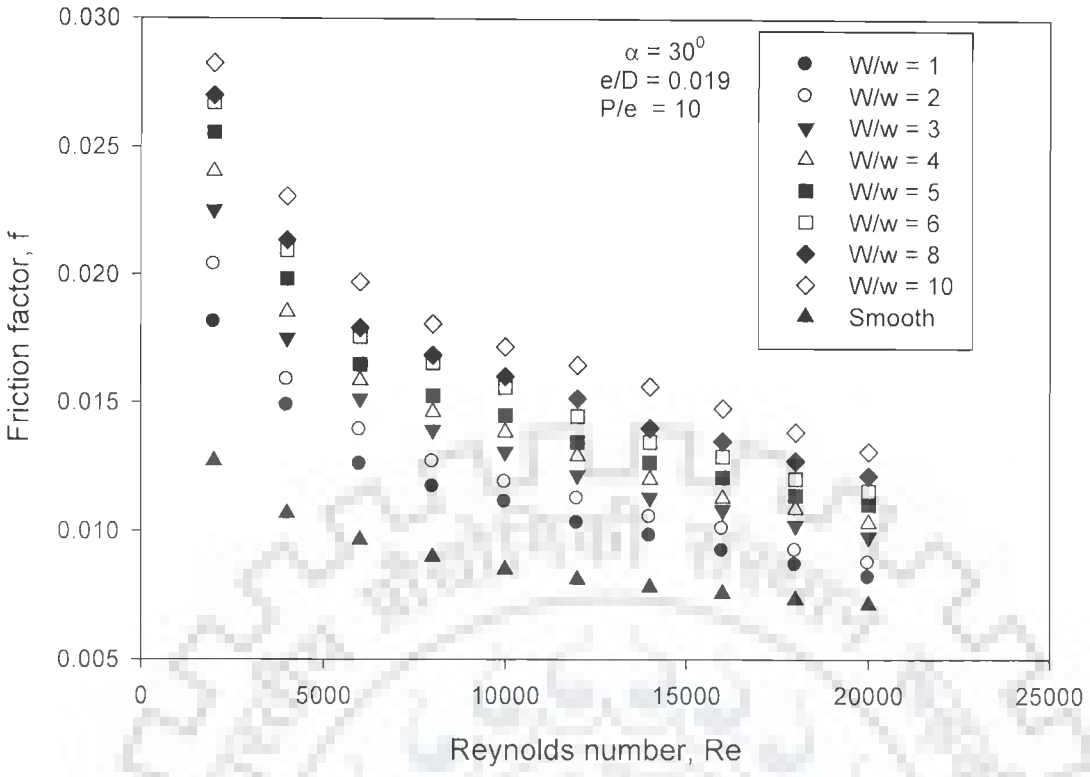

Fig.3.30 Effect of relative roughness width on friction factor for e/D = 0.019

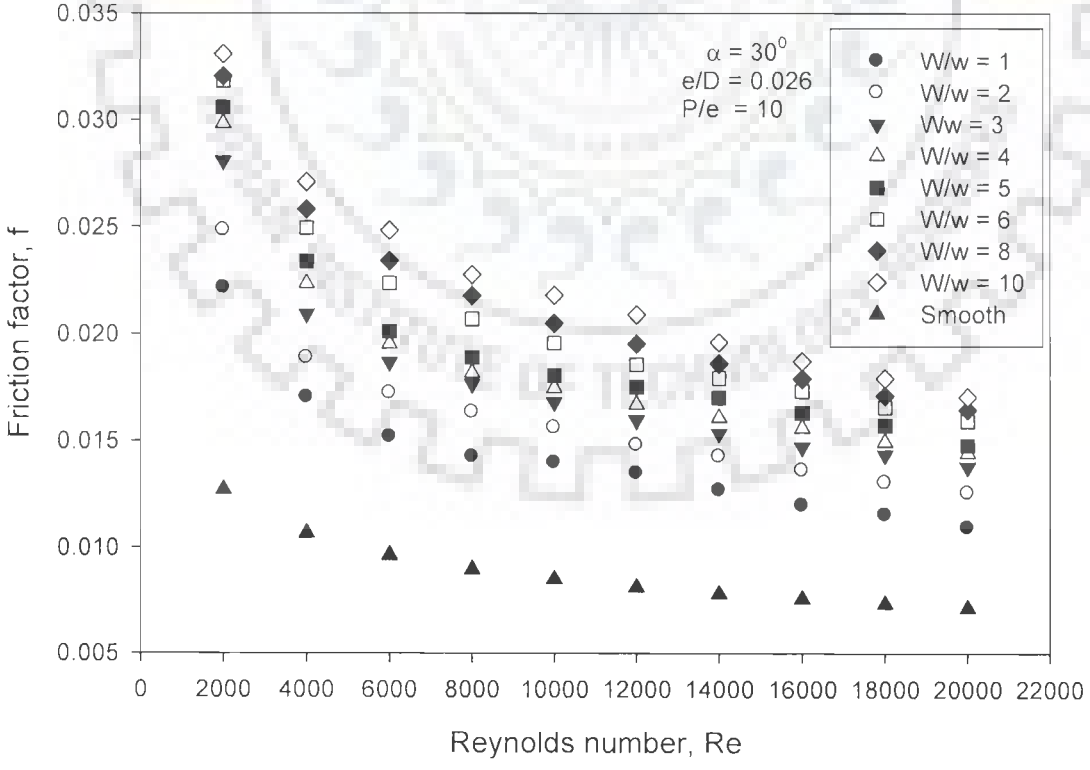

Fig.3.31 Effect of relative roughness width on friction factor for e/D = 0.026

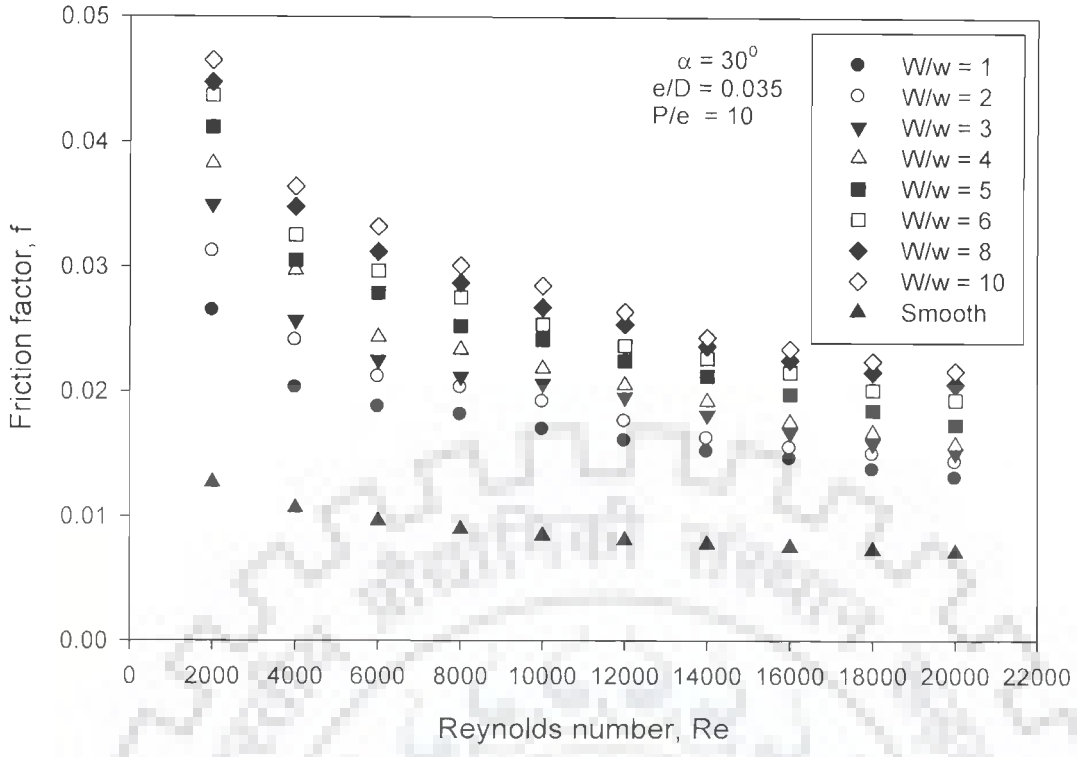

Fig.3.32 Effect of relative roughness width on friction factor for e/D = 0.035

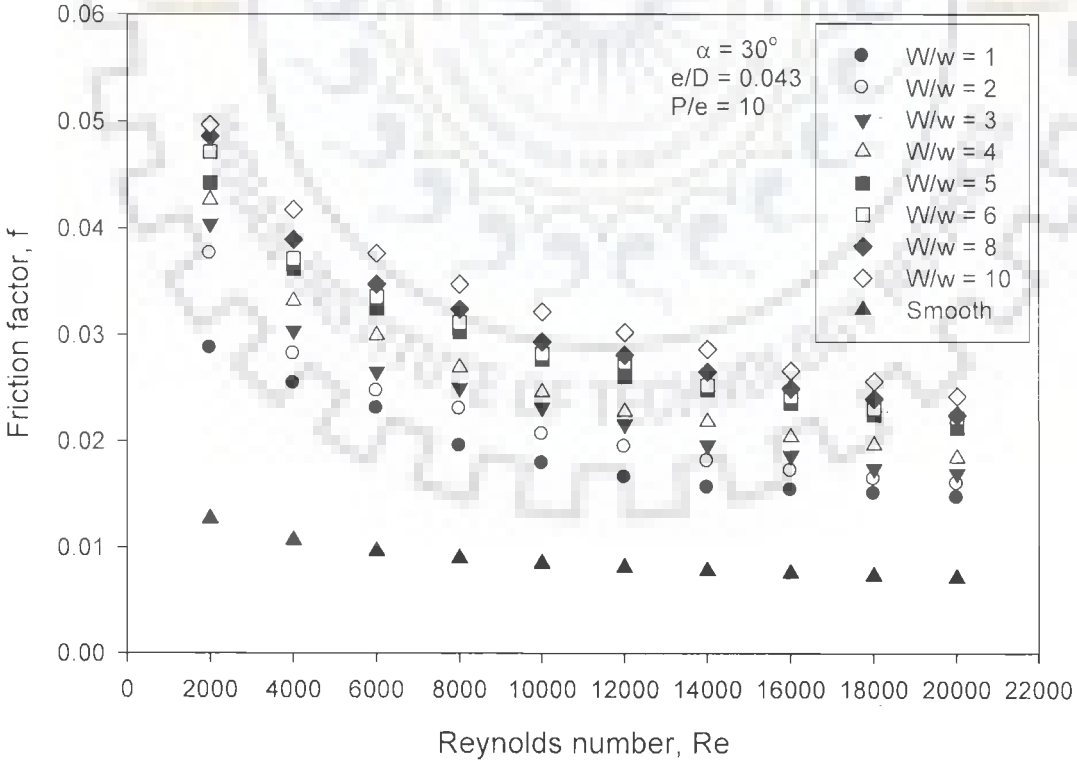

Fig.3.33 Effect of relative roughness width on friction factor for e/D = 0.043

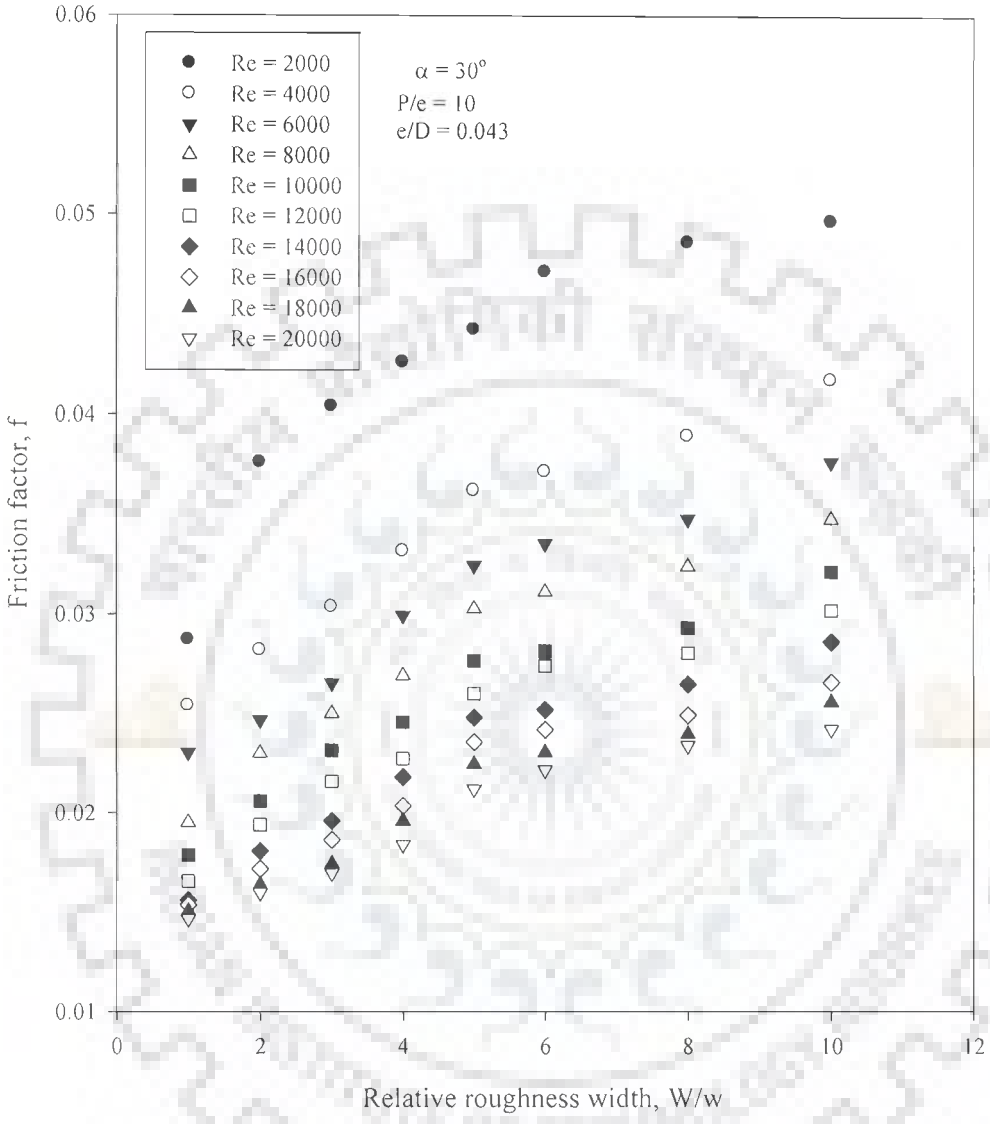

Fig.3.34 Effect of relative roughness width on friction factor for different values of Reynolds number

As already explained in Section 3.2.2 and shown in Fig.3.16, increase in relative roughness width results in increase in number of leading ends (high heat transfer region) and secondary flow cells, which increase the level of turbulence. This results in increase in heat transfer and friction factor. However, as the relative roughness width value, increases beyond 6, number of leading ends and secondary flow cells as well as friction factor continue to increase although the rate of increase of friction factor declines.

It may be attributed to the fact that around relative roughness width value of 6, turbulence, resulting from presence of multiple v-ribs, reaches its maximum value and further increase in relative roughness width value, may impede the development of secondary flow resulting in reduction in heat transfer, however friction factor goes on increasing on account of vortices formed.

Table 3.6 presents the percentage variation of friction factor as relative roughness width increases.

Table 3.6 Variation of friction factor with relative roughness width, W/w

Fixed roughness geometry parameters	**Relative roughness width, W/w**	**Range of variation of friction factor (%)**
e/D = 0.043 P/e = 10 $\alpha = 30^0$	1 to 2	7 to 31
	2 to 3	6.2 to 12.4
	3 to 4	5.4 to 12.7
	4 to 5	3.8 to 12.5
	5 to 6	1.5 to 6.5
	6 to 8	1.0 to 5.0
	8 to 10	2 to 7

3.3.3 Effect of Angle of Attack

The variation of friction factor as a function of Reynolds number for different values of angle of attack and fixed values of other roughness geometry parameters has been shown in Fig.3.35. It has been observed that for all the values of angle of attack, friction factor decreases with increase in Reynolds number.

In order to elaborate the effect of angle of attack on friction factor, Fig.3.35 has been re-plotted as Fig.3.36. Friction factor increases with increase in angle of attack, attains a maximum value corresponding to angle of attack value of 60^0 and decreases with further increase in angle of attack value. The least and maximum values of friction factor have been obtained corresponding to angle of attack values of 30^0 and 60^0 respectively. Similar observations have been reported by Han et al. [94] in an experimental study carried out for turbine blade cooling applications.

Table 3.7 presents percentage variation of friction factor as angle of attack value increases.

Table 3.7 Variation of friction factor with angle of attack, α

Angle of attack, α	Fixed roughness geometry parameters	Range of variation of friction factor (%)
e/D = 0.043	30^0 to 45^0	7.7 to 23.6
P/e = 10	45^0 to 60^0	6.4 to 11.4
W/w = 6	60^0 to 75^0	-3 to -6

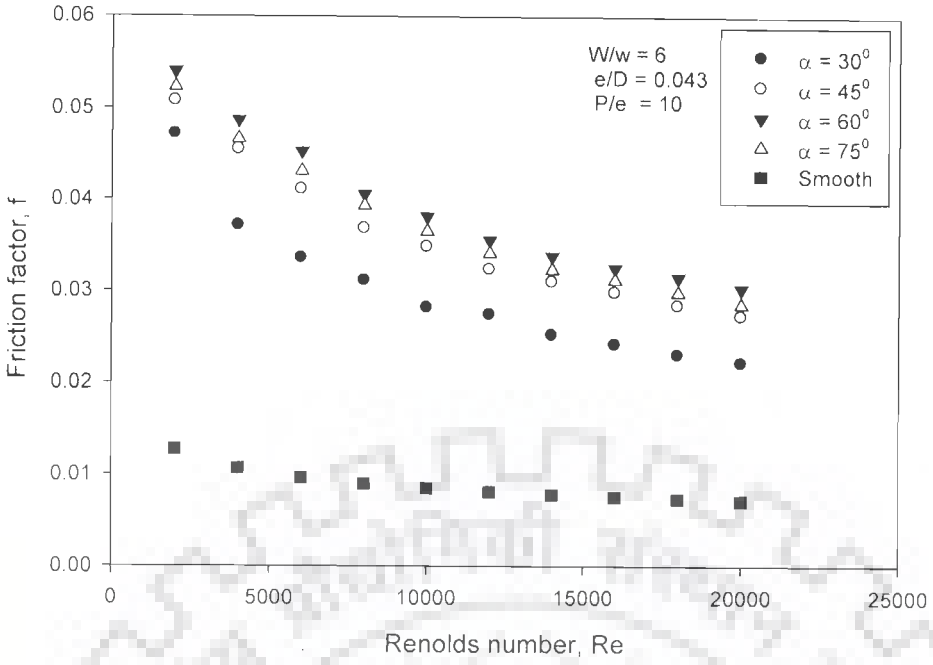

Fig.3.35 Effect of angle of attack on friction factor

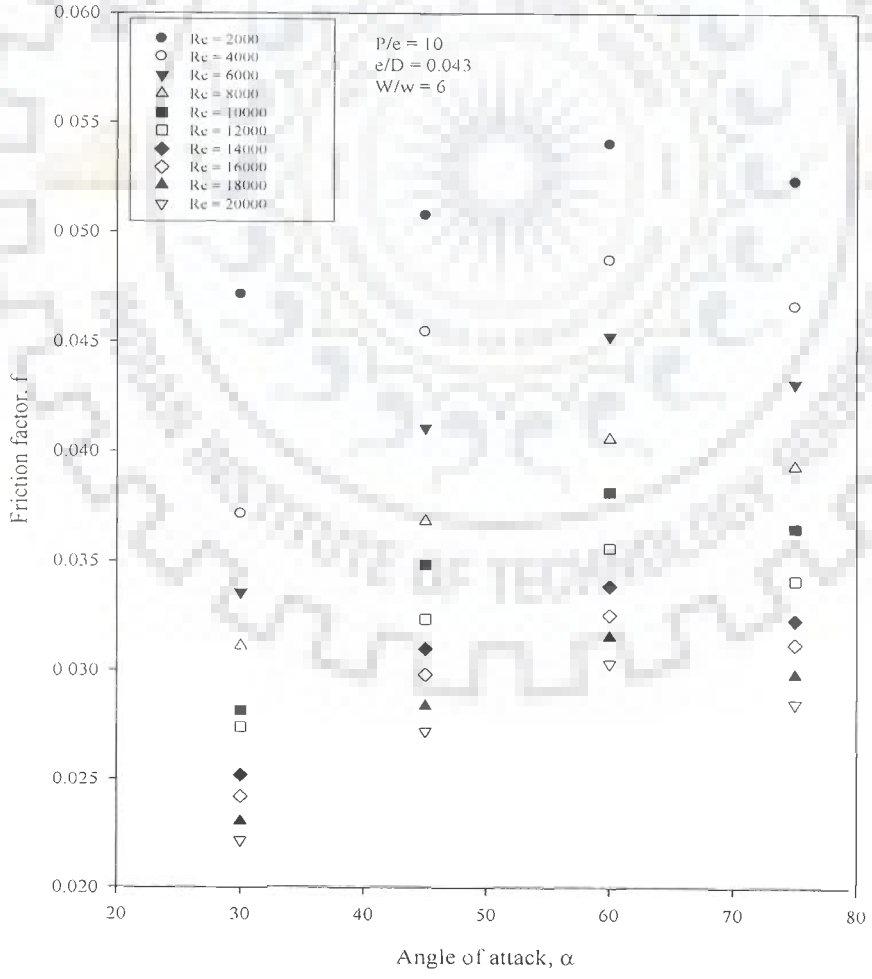

Fig.3.36 Effect of angle of attack on friction factor for different values of Reynolds number

3.3.4 Effect of Relative Roughness Pitch

Fig.3.37 depicts the variation of friction factor with Reynolds number for different values of relative roughness pitch and fixed values of other roughness geometry parameters. It has been observed from Fig.3.37 that for all values of relative roughness pitch, friction factor decreases with increase in Reynolds number. Relative roughness pitch values of 12 and 8 yield the least and maximum values of friction factor respectively. The experimental data presented in Fig.3.37 has been re-plotted in Fig.3.38 to clearly show the effect of relative roughness pitch on friction factor. It has been observed from Fig.3.38 that friction factor increases with increase in relative roughness pitch value up to 8 and then decreases with further increase in relative roughness pitch value. Table 3.8 presents the percentage variation of friction factor as relative roughness pitch increases.

Table 3.8 Variation of friction factor with relative roughness pitch, P/e

Roughness pitch, P/e	Fixed roughness geometry parameters	Range of variation of friction factor (%)
e/D = 0.043 W/w = 6 $\alpha = 60^0$	6 to 8	10.5 to 23.3
	8 to 10	-6.6 to –12
	10 to 12	-13 to -26

3.4 ENHANCEMENT OF HEAT TRANSFER AND FRICTION

The thermal performance of multiple v-rib roughened rectangular ducts has been analyzed and compared with that of smooth rectangular duct in terms of heat transfer under similar operating conditions. Considerable enhancement of heat transfer has been observed in case of roughened rectangular ducts. Heat transfer enhancement, due to the presence of multiple v-ribs on the under side of the heated surface of rectangular duct, has been represented by a term called enhancement ratio.

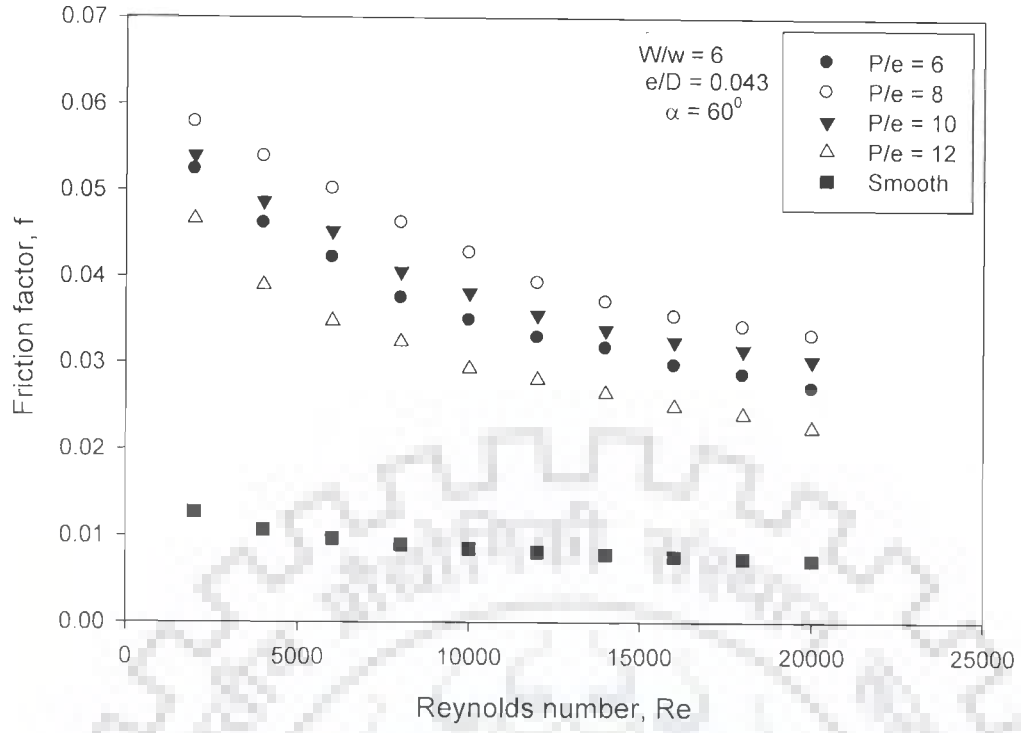

Fig.3.37 Effect of relative roughness pitch on friction factor

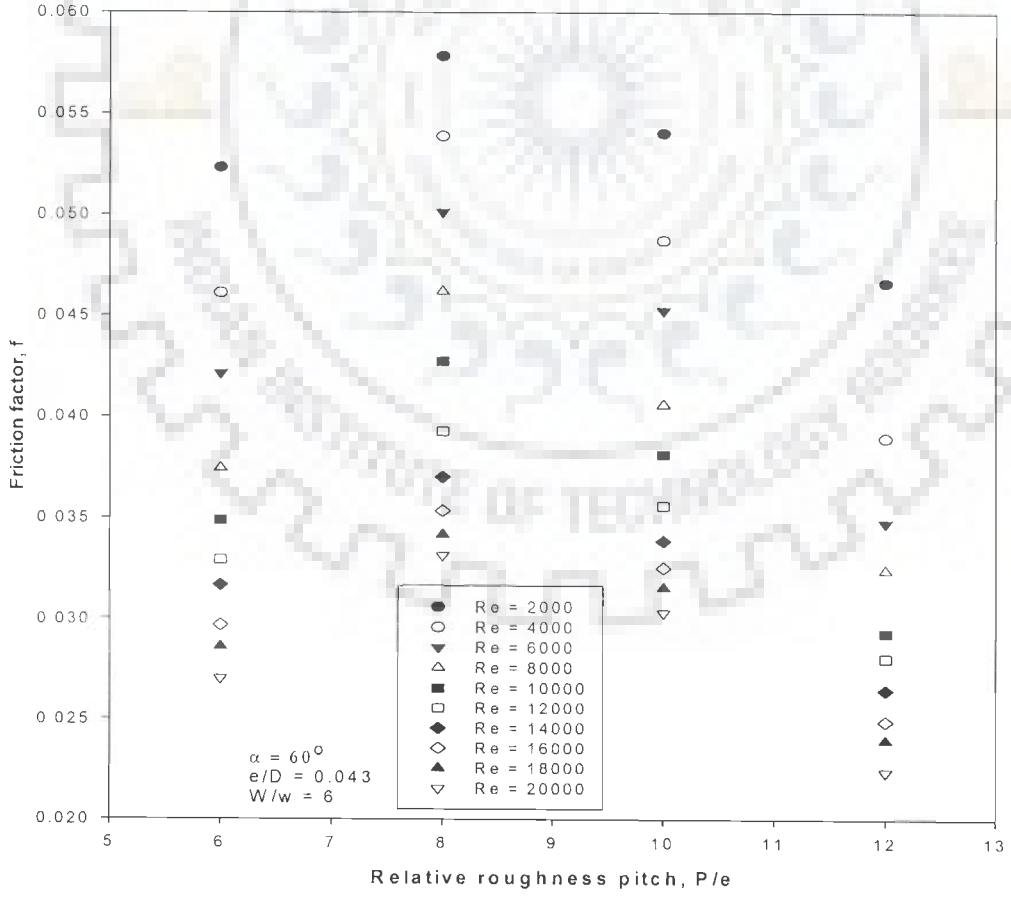

Fig.3.38 Effect of relative roughness pitch on friction factor for different values of Reynolds number

Enhancement ratio is defined as ratio of Nusselt number of roughened rectangular duct to that of smooth rectangular duct under similar flow conditions.

$$\text{Enhancement ratio} = Nu / Nu_s \qquad (3.1)$$

Figs.3.39 to 3.42 show the enhancement ratio, Nu/Nu_s, as function of Reynolds number and roughness geometry parameters. Table 3.9 presents the values of roughness geometry parameters for which the maximum value of enhancement ratio, Nu/Nu_s has been obtained. The maximum absolute value of enhancement ratio has been observed to be 6.18 corresponding to relative roughness height value of 0.043, relative roughness width value of 6, angle of attack value of 60^0 and relative roughness pitch value of 8.

Table 3.9 Roughness geometry parameter corresponding to maximum enhancement ratio, Nu/Nu_s

Roughness parameter	Fixed parameter	Value of Roughness parameter	Maximum value of enhancement ratio, Nu/Nu_s
Relative roughness height, e/D	P/e = 10 W/w = 6 $\alpha = 30^0$	0.043	4.0
Relative roughness width, W/w	e/D = 0.043 P/e = 10 $\alpha = 30^0$	6	4.80
Angle of attack, α	e/D = 0.043 P/e = 10 W/w = 6	60^0	5.70
Relative roughness pitch, P/e	e/D = 0.043 W/w = 6 $\alpha = 60^0$	8	6.18

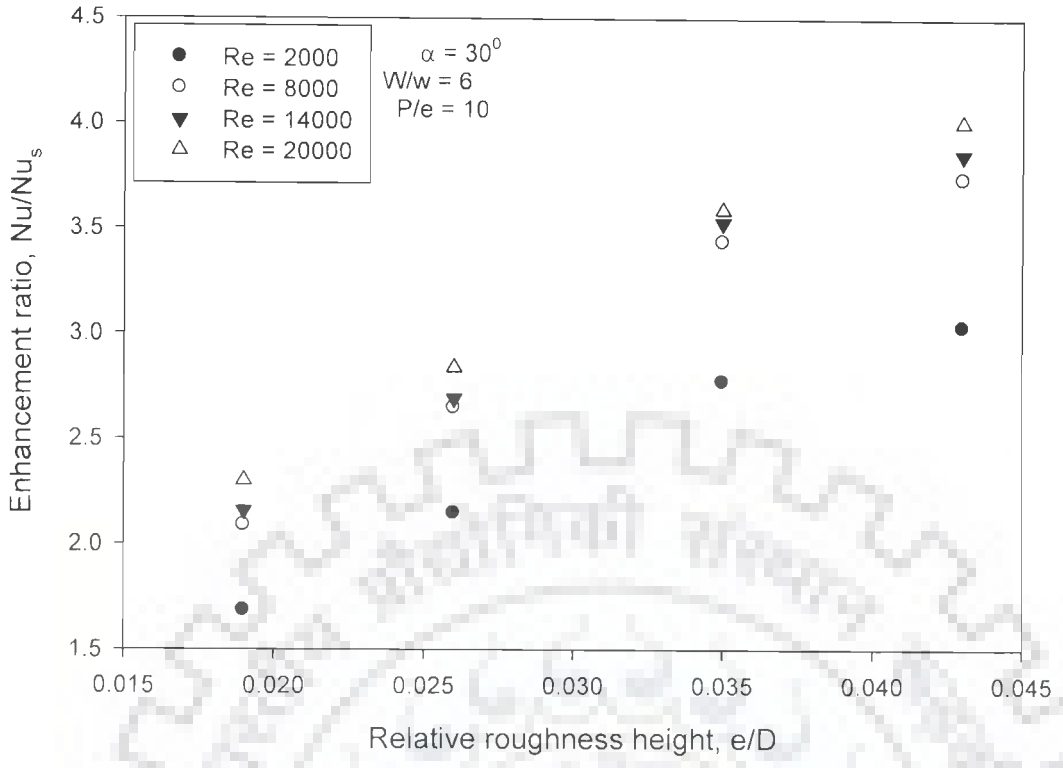

Fig.3.39 Effect of relative roughness height on enhancement ratio of Nusselt number

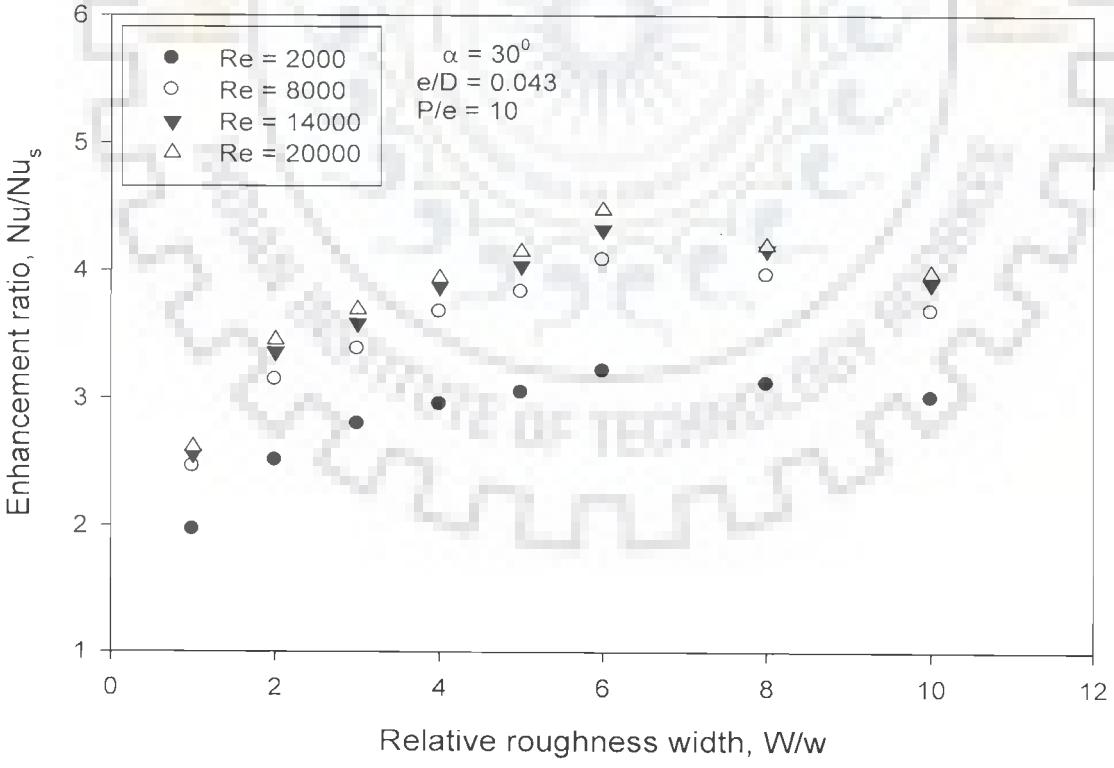

Fig.3.40 Effect of relative roughness width on enhancement ratio of Nusselt number

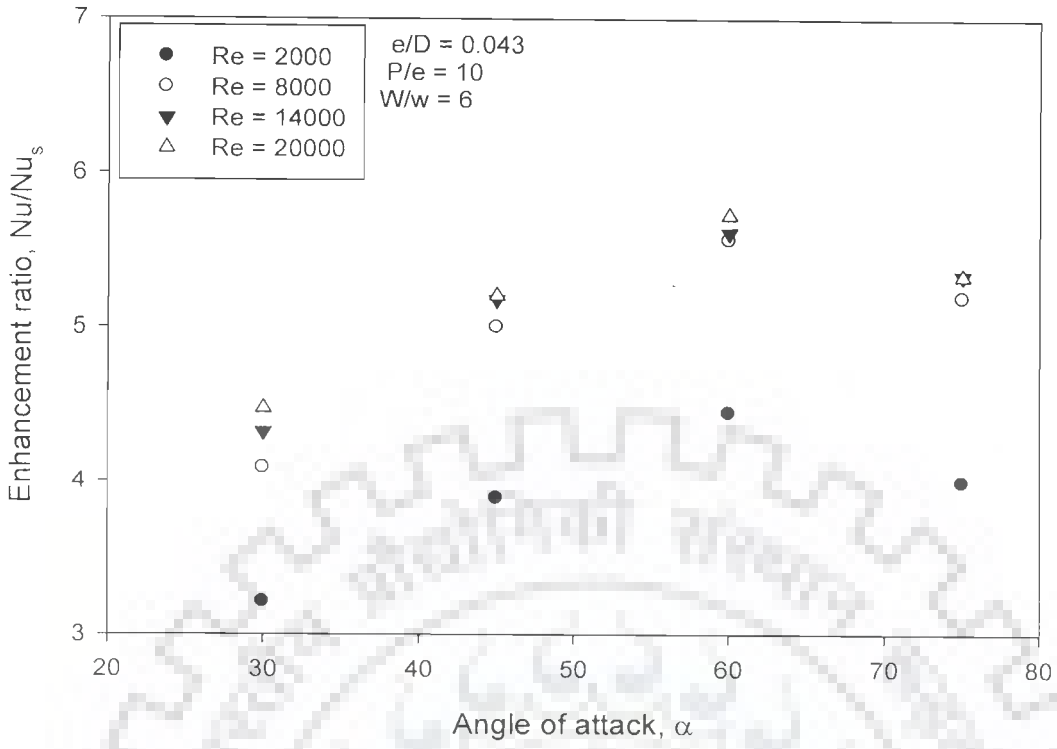

Fig.3.41 Effect of angle of attack on enhancement ratio of Nusselt number

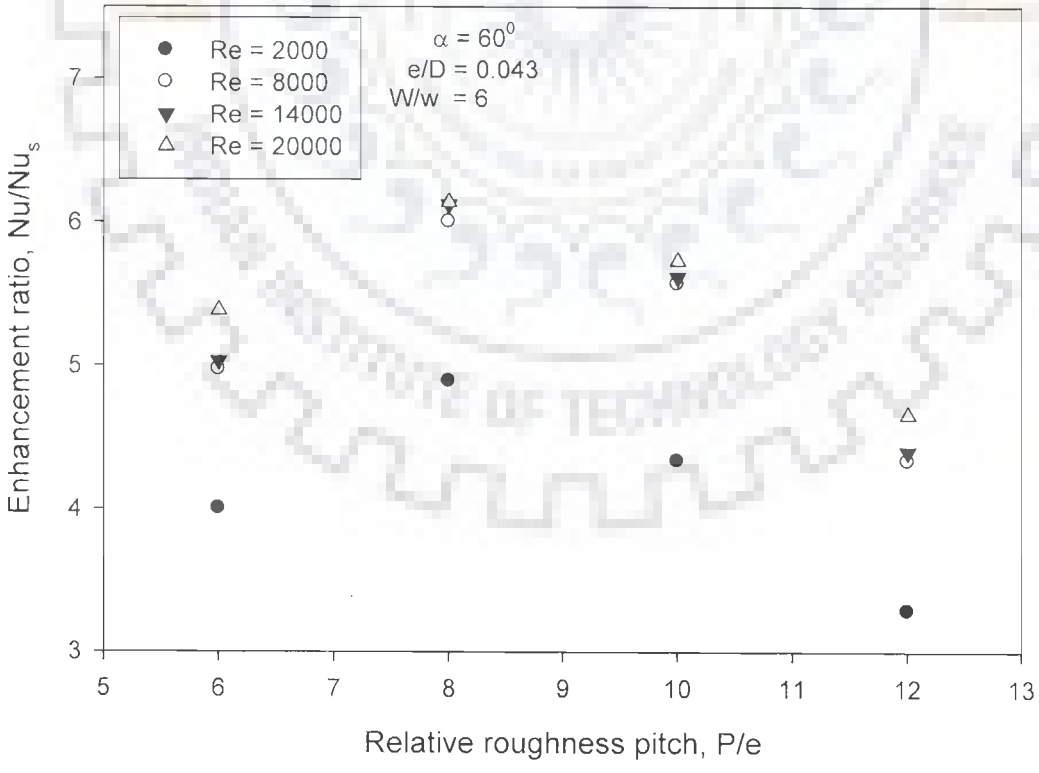

Fig.3.42 Effect of relative roughness pitch on Enhancement ratio of Nusselt number

The use of multiple v-rib type of artificial roughness in rectangular ducts results in enhancement of heat transfer along with increase in friction factor. Increase in friction has also been represented by a term called enhancement ratio which is defined as ratio of friction factor of roughened duct to that of smooth duct.

Enhancement ratio = f / f_s (3.2)

Figs.3.43 to 3.46 show the effect of roughness geometry parameters on enhancement ratio, f/f_s, as function of Reynolds number. In Table 3.10, those values of roughness geometry parameters have been presented for which enhancement ratio, f/f_s values have been found to be maximum. The maximum absolute value of enhancement ratio, f/f_s has been observed to be 5.2 corresponding to relative roughness height value of 0.043, relative roughness width value of 6, angle of attack value of 60^0 and relative roughness pitch value of 8.

Table 3.10 Roughness geometry parameter corresponding to maximum enhancement ratio, f/f_s

Roughness parameter	Fixed parameter	Value of Roughness parameter	Maximum value of enhancement ratio, f/f_s
Relative roughness height, e/D	P/e = 10 W/w = 6 $\alpha = 30^0$	0.043	3.7
Relative roughness width, W/w	e/D = 0.043 P/e = 10 $\alpha = 30^0$	10	3.90
Angle of attack, α	e/D = 0.043 P/e = 10 W/w = 6	60^0	4.70
Relative roughness pitch, P/e	e/D = .043 W/w = 6 $\alpha = 60^0$	8	5.20

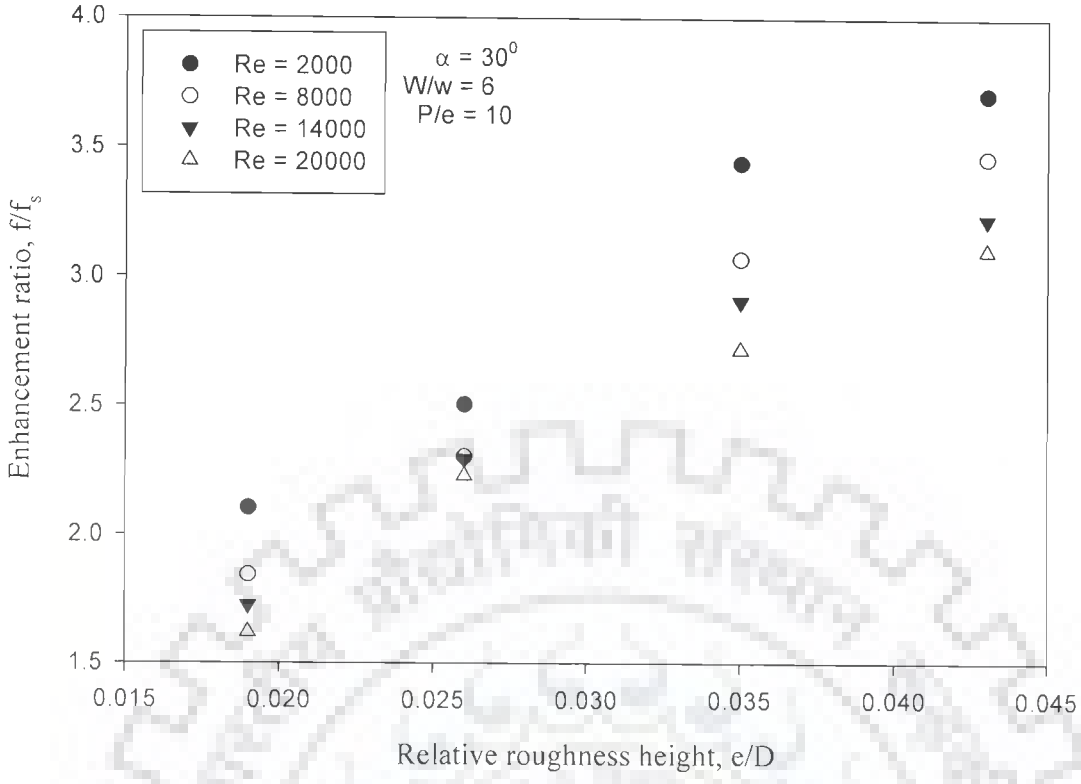

Fig.3.43 Effect of relative roughness height on enhancement ratio of friction factor

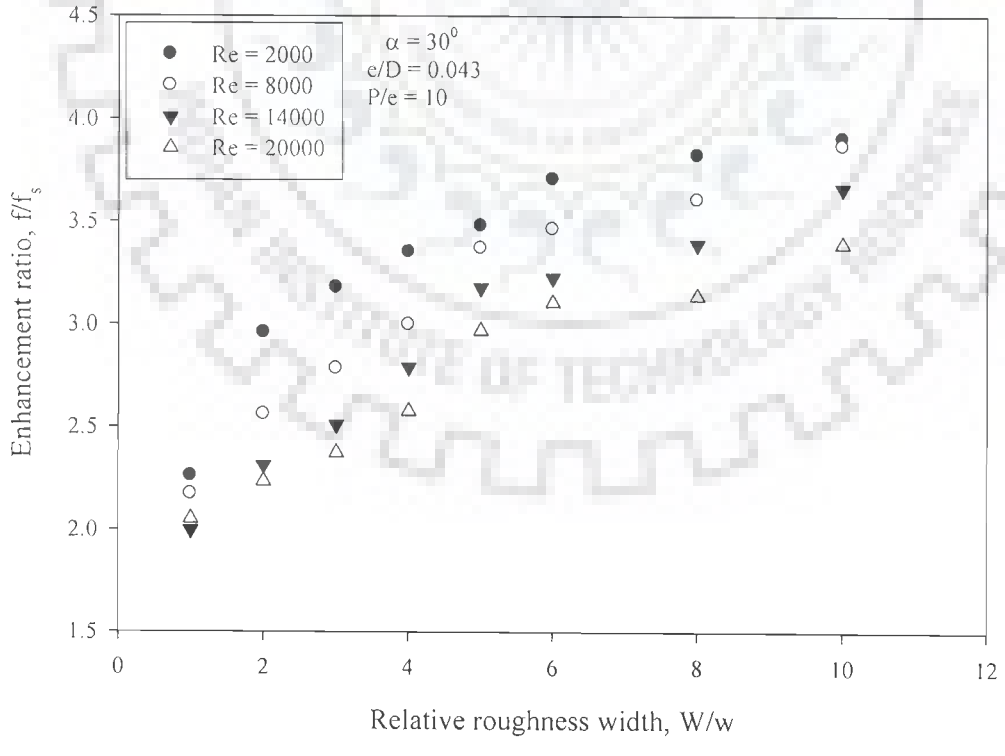

Fig.3.44 Effect of relative roughness width on enhancement ratio of friction factor

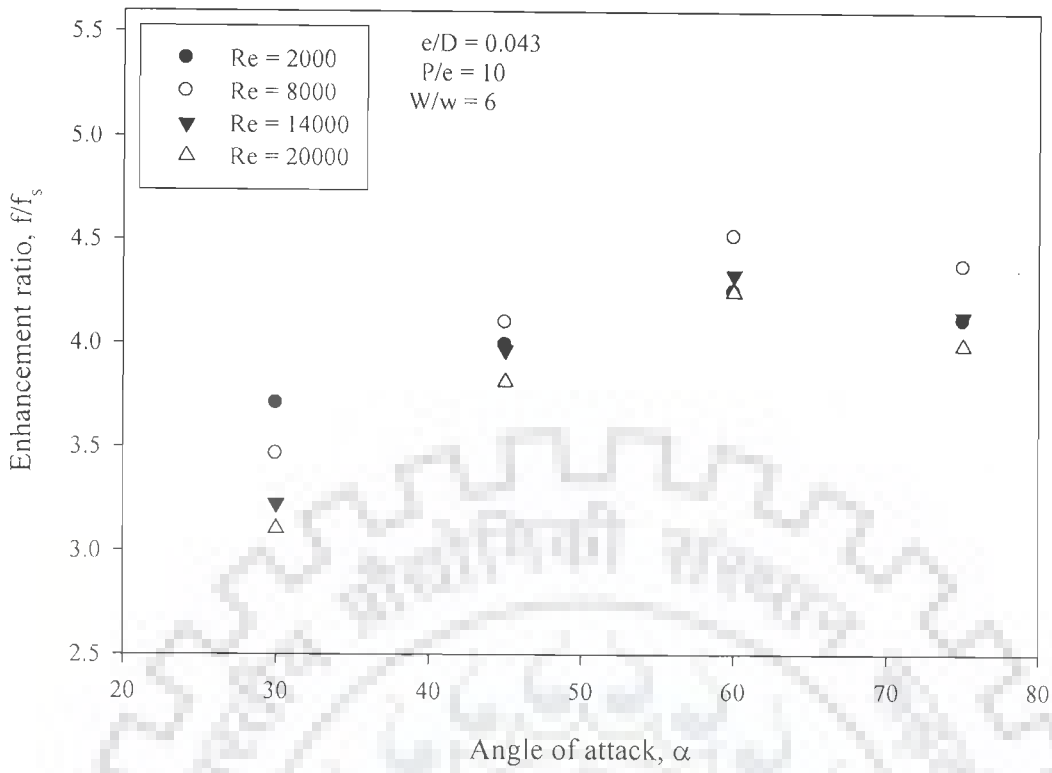

Fig.3.45 Effect of angle of attack on enhancement ratio of friction factor

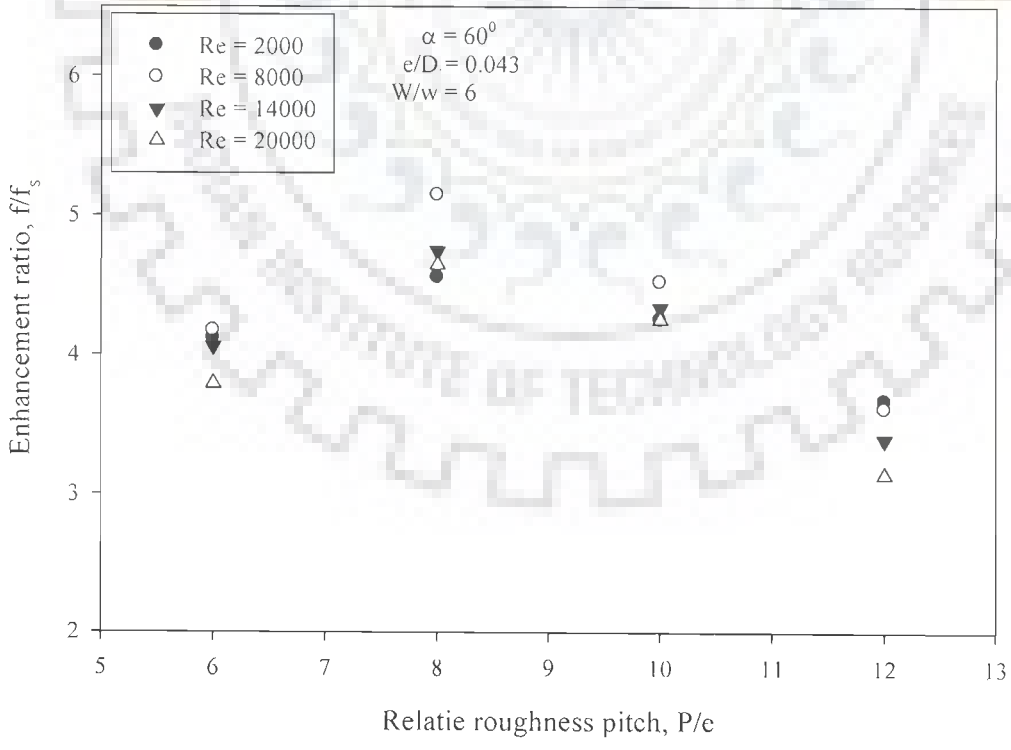

Fig.3.46 Effect of relative roughness pitch on Enhancement ratio of friction factor

CHAPTER-4

DEVELOPMENT OF CORRELATIONS FOR NUSSELT NUMBER AND FRICTION FACTOR

4.1 INTRODUCTION

Use of artificial roughness in solar air heaters results in creation of complex flow fields and turbulence that play a significant role in heat transfer enhancement as well as increase in friction. Due to lack of complete understanding of turbulent flows and complex nature of flow fields developed, analytical methods are not available for prediction of heat transfer coefficient and friction factor for artificially roughened solar air heaters. In such a scenario, for performance prediction of artificially roughened ducts of solar air heaters, designers have to make use of empirical or semi-empirical correlations developed on the basis of experimental data collected over range of roughness geometry configurations and flow parameters.

Correlations for friction in rough tubes are based on similarity considerations. Semi-empirical correlations have been derived by a large number of investigators, using the law of wall similarity and the heat-momentum transfer analogy for the flow over a rough surface. Some of these correlations were presented in Chapter 1.

In this chapter, correlations for Nusselt number (heat transfer coefficient) and friction factor have been developed for flow in the rectangular duct, in which one broad wall is artificially roughened with multiple v-ribs. These correlations may be helpful to the designers to predict heat transfer coefficient and friction factor of the roughened duct as a function of its geometrical parameters and operating conditions.

4.2 CHOICE OF CORRELATIONS

It has been observed in literature that for development of correlations, most of the investigators have, generally, used the following two methods;

(i) Heat-Momentum Transfer Analogy Method

(ii) Statistical Method

Investigators such as Karwa [65], Dippery and Sabersky [83], Webb et al. [84] and Han [89] used the law of wall similarity for computation of heat transfer coefficient and preferred Stanton number over Nusselt number because the expressions for the Stanton number turn out to be similar in form to those for friction factor and the two parameters are related through the Reynolds analogy and Dipprey and Sabersky's analogy. However, other investigators namely Gupta et al. [59], Momin et al. [69], Saini and Saini [75], Prasad and Mullick [120] and Ravigururajan and Bergles [158] used Nusselt number to develop heat transfer correlations instead of using the roughness functions for analysis of experimental results.

Webb et al. [84] pointed out that a correlation based on analogy method does not allow easy physical interpretation as it makes use of unconventional parameters like roughness Reynolds number [$e^+ = \frac{e}{D}\sqrt{\frac{f}{2}}\,\mathrm{Re}$] instead of flow Reynolds number. Momin et al. [69] and Saini and Saini [75] observed that correlations based on the analogy method are applicable because these represent a fundamental approach to the problem, however, requirement of a designer is that correlations must correlate the effects of all the geometrical parameters. Because of these shortcomings of the analogy-based correlations, statistical method based correlations are thought to be more useful.

Bergles [159] developed correlations based on statistical methods from large database for friction and heat transfer and statistical correlations developed for Nusselt number and friction factor were found to be more accurate in comparison to the correlations based on other methods. In view of the above, statistical method has been used in this chapter to formulate the correlations based on the experimental data given in Chapter 3 for rectangular ducts roughened with multiple v-ribs.

4.3 PARAMETERS AND THEIR RANGE

As mentioned earlier, multiple v-ribs have been used as artificial roughness elements in this study in order to enhance the heat transfer between air and the heated wall of a rectangular duct. The geometrical parameters of the roughness geometry have been expressed in terms of dimensionless parameters, such as relative roughness height, e/D, relative roughness width, W/w, angle of attack, α/90 and relative roughness pitch, P/e. In the previous chapter, the effect of these roughness geometry parameters and flow Reynolds number on heat transfer coefficient and friction factor have been presented and discussed. The range of parameters considered in this experimental study is given in Table 4.1.

Table 4.1 Range of roughness geometry and flow parameters

S. No.	Roughness geometry and flow parameters	Range of parameters
1	Relative roughness height, e/D	0.019 – 0.043
2	Relative roughness pitch, P/e	6 – 12
3	Relative roughness width, W/w	1 – 10
4	Angle of attack, α	30° – 75°
5	Reynolds number, Re	2000 – 20000

4.4 DEVELOPMENT OF CORRELATIONS FOR NUSSELT NUMBER AND FRICTION FACTOR

It has been observed that Nusselt number and friction factor are strong functions of roughness geometry and flow parameters namely, relative roughness height, e/D, relative roughness width, W/w, angle of attack, α, relative roughness pitch, P/e and flow Reynolds number, Re. The functional relationship for present correlation can be expressed as:

$$Nu = f_n (Re, e/D, W/w, \alpha, P/e) \quad (4.1)$$

$$f = f_n (Re, e/D, W/w, \alpha, P/e) \quad (4.2)$$

4.4.1 Development of Functional Relationships of Nusselt Number and Friction Factor with Roughness and Operating Parameters

The effect of roughness geometry and operating parameters on Nusselt number observed in Chapter 3 are summarized below:

i. Nusselt number increases monotonically with an increase in Reynolds number (Re)

ii. Nusselt number increases monotonically with increase in relative roughness height, e/D

iii Nusselt number attains a maximum value with change in relative roughness width, W/w and the maximum value corresponds to relative roughness width value of 6

iv. Nusselt number attains a maximum value with change in angle of attack, α and the maximum value corresponds to angle of attack value of 60^{o}

v. Nusselt number attains a maximum value with change in relative roughness pitch, P/e and the maximum value corresponds to the relative roughness pitch value of 8

It can be deduced from the above discussion that Nusselt number either increases monotonically (in case of Reynolds number and relative roughness height, e/D) or attains a maximum value (in case of relative roughness width, W/w, angle of attack, α and relative roughness pitch, P/e).

In order to determine the functional relationship between Nusselt number and Reynolds number, values of ln(Nu) were plotted against the values of ln(Re) for a set

of data points having different values of other parameters. It has been observed that the data yields straight lines with nearly same slope while the value of intercept of each line is different. This can be seen from Figs.4.1 and 4.2 where ln(Nu) has been plotted against ln(Re) for different sets of varying values of relative roughness, P/e and relative roughness height, e/D respectively. Therefore, the functional relationship between Nusselt number and Reynolds number can be expressed as;

$$\ln(Nu) = k_1 \ln(Re) + k_2 \quad (4.3)$$

where k_1 and k_2 are constants.

Eq. 4.3 can be written as;

$$Nu = k_o \, Re^{k_1} \quad (4.4)$$

where k_o is anti $\ln(k_2)$

A functional relationship between Nusselt number and relative roughness height, e/D has been established by plotting values of ln(Nu) against the values of ln(e/D) for different values of other parameters. It has been observed that the data yields straight lines with nearly same slope while the value of intercept of each line is different. This can be seen from a representative plot shown in Fig.4.3 where ln(Nu) has been plotted against ln(e/D) for different values of Reynolds number and fixed values of other parameters. Therefore, the functional relationship between Nusselt number and relative roughness height is governed by power law as given in Eq. 4.5.

$$Nu = J_o \, Re^{j} \quad (4.5)$$

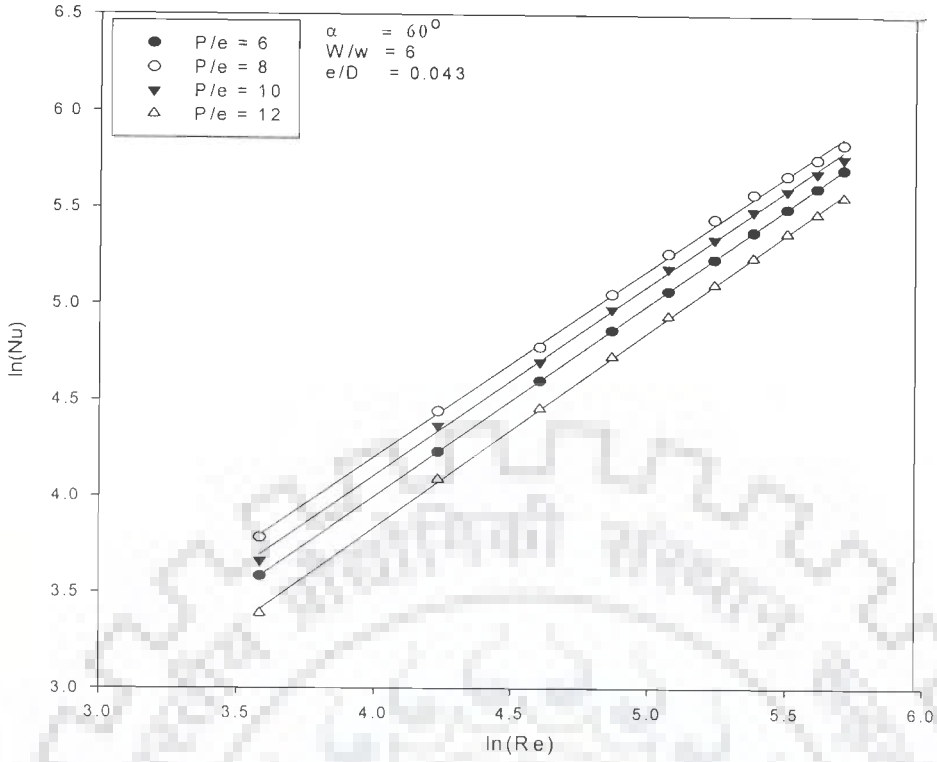

Fig.4.1 Nusselt number as a function of Reynolds number for different values of relative roughness pitch

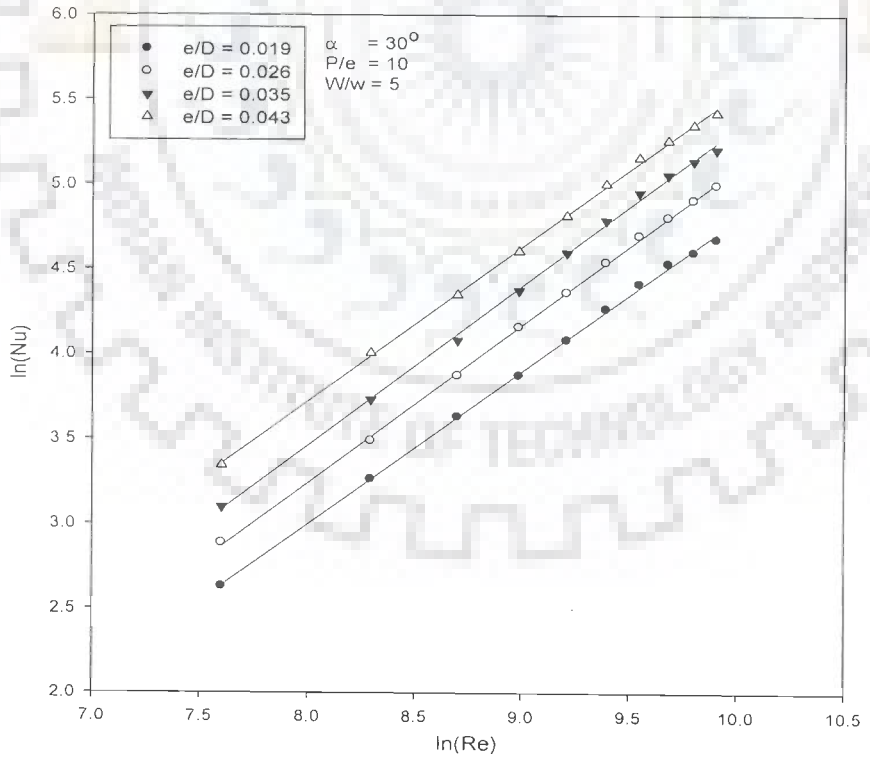

Fig.4.2 Nusselt number as a function of Reynolds number for different values of relative roughness height

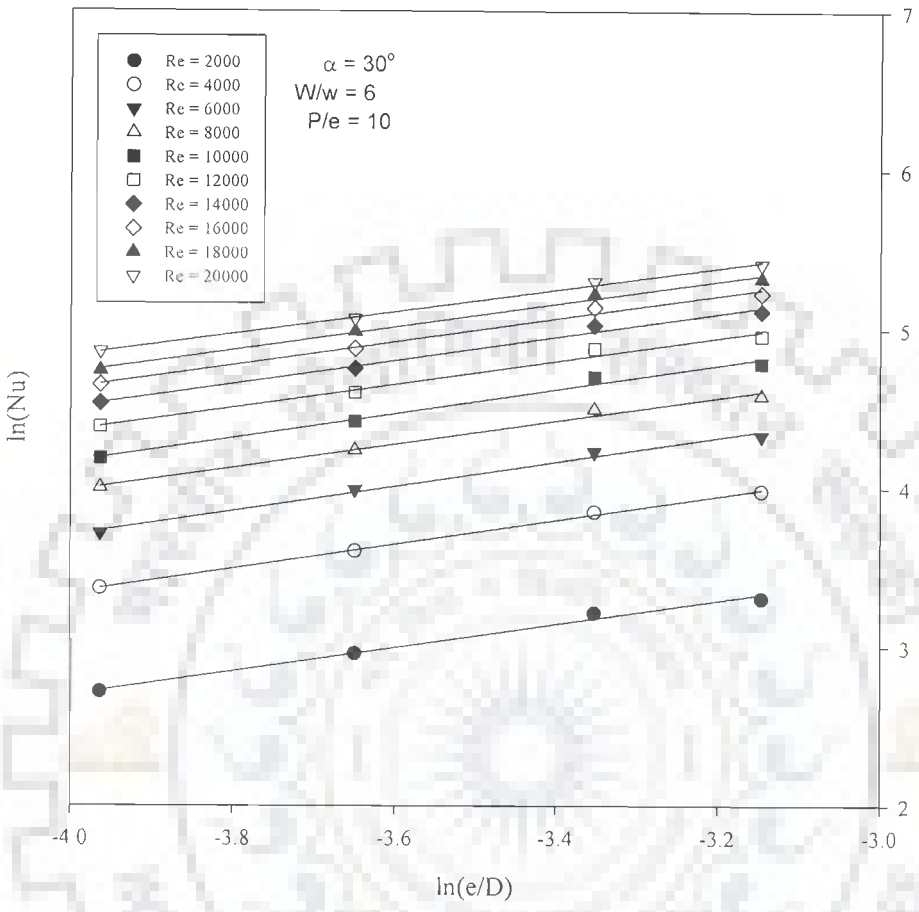

Fig.4.3 Nusselt number as a function of relative roughness height for different values of Reynolds number

In order to determine a functional relationship between Nusselt number and relative roughness width, W/w, values of ln(Nu) have been plotted against the values of ln(W/w) for different values of Reynolds number and fixed values of other roughness geometry parameters as shown in Fig.4.4. Similar plots of ln(Nu) and ln(W/w) had also been drawn for other sets of roughness geometry parameters. It can be observed that a polynomial functional relationship of the form given below exists between ln(Nu) and ln(W/w).

$$\ln(Nu)=\ln(m_1)+m_2\ln\left(\frac{W}{w}\right)+m_3\left(\ln\left(\frac{W}{w}\right)\right)^2 \qquad (4.6)$$

The values of coefficients m_1, m_2 and m_3 were determined for each plot and it was found that the coefficients m_2 and m_3 are nearly the same for all plots whereas m_1 has been seen to vary.

The above equation can be rearranged as,

$$Nu = m_0\left(\frac{W}{w}\right)^{m_2}\exp\left(m_3\ln\left(\frac{W}{w}\right)\right)^2 \qquad (4.7)$$

where m_0 is anti $\ln(m_1)$

Similarly, a quadratic functional relationship has been established between Nusselt number and angle of attack, α by plotting the values of ln(Nu) against $\ln(\alpha)$ for fixed values of other parameters as shown in Fig.4.5.

It has been observed that effect of relative roughness pitch, P/e on Nusselt number is similar to those of relative roughness width, W/w and angle of attack, α. Therefore, the functional relationship between Nusselt number and relative roughness pitch, P/e is also governed by a quadratic equation.

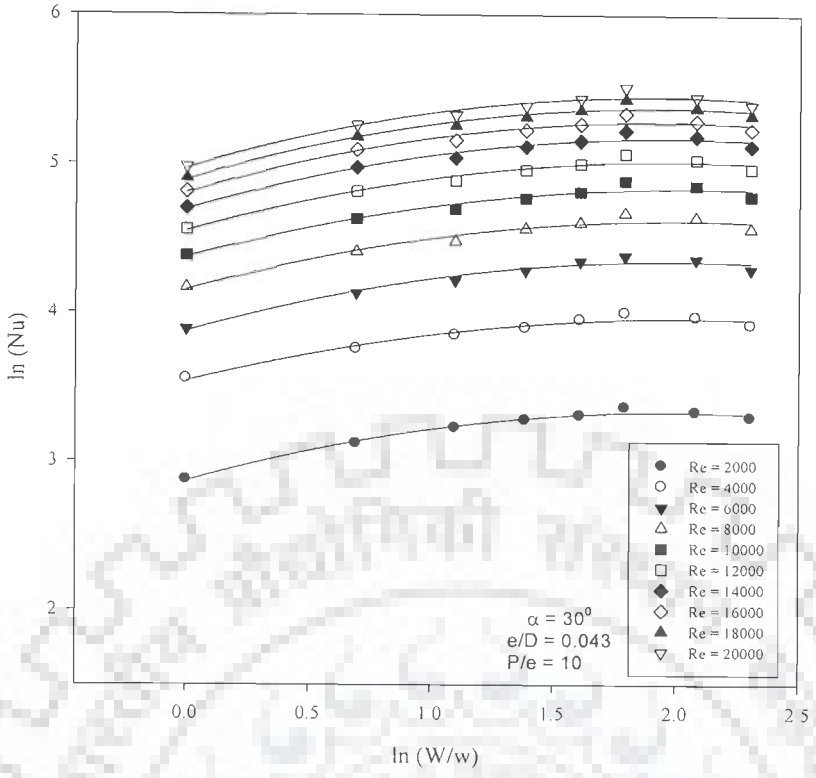

Fig.4.4 Nusselt number as function of relative roughness width for different values of other parameters

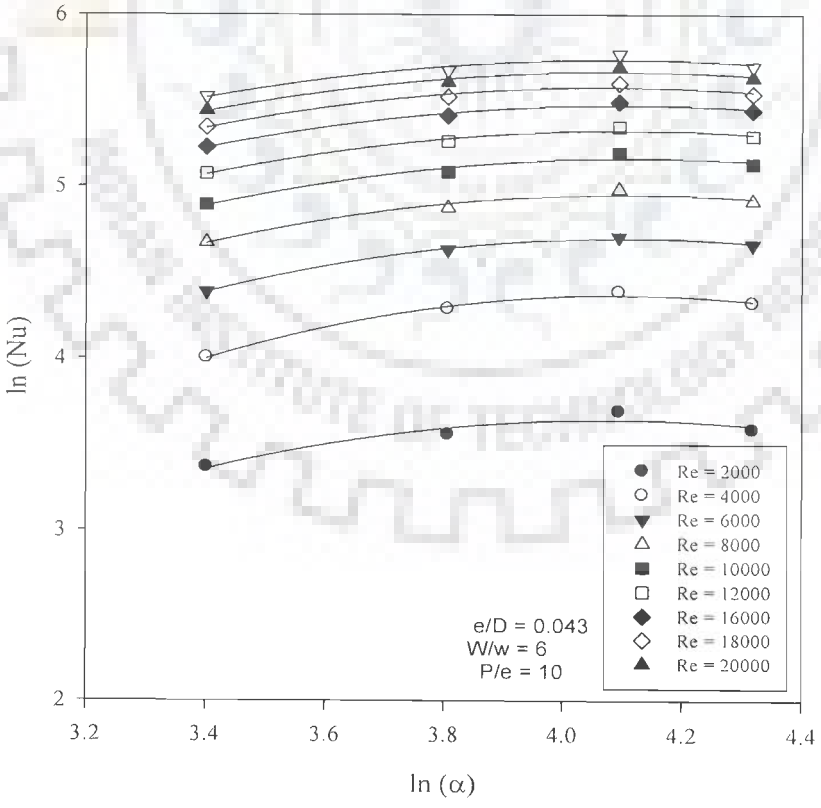

Fig.4.5 Nusselt number as a function of angle of attack for different values of other parameters

Similarly, the effect of roughness geometry and operating parameters on friction factor observed in Chapter 3 are also summarized below:

i. Friction factor decreases monotonically with an increase in Reynolds number, Re

ii. Friction factor increases monotonically with increase in relative roughness height, e/D

iii. Friction factor increases monotonically with increase in relative roughness width, W/w

iv. Friction factor attains a maximum value with change in angle of attack, α and the maximum value corresponds to angle of attack value of 60^{0}

v. Friction factor attains a maximum value with change in relative roughness pitch, P/e and the maximum value corresponds to relative roughness pitch of 8

From above discussion, it can be concluded that friction factor either increases or decreases monotonically (in case of relative roughness height, e/D and Reynolds number respectively) or attains a maxima (in case of angle of attack, α and relative roughness pitch, P/e).

The functional relationships of friction factor with roughness geometry and operating parameters were established by following a similar procedure as adopted for establishing the functional relationships of Nusselt number with roughness and operating parameters. The functional relationship of friction factor with Reynolds number, Re, relative roughness height, e/D and relative roughness width, W/w has been found to be governed by power law. The functional relationship of friction factor with angle of attack, α and relative roughness pitch, P/e has been found to be governed by a quadratic equation.

4.4.2 Development of Correlation for Nusselt Number

A correlation for Nusselt number has been developed by regression analysis of the experimental data presented in the previous chapter. The functional relationships of Nusselt number with roughness geometry and operating parameters have been discussed in Section 4.4.1.

Nusselt number increases with increase in Reynolds number and the functional relationship between the two is governed by the power law as established in Section 4.41. Fig.4.6 shows a plot of ln(Nu) as a function of ln(Re) for the entire data corresponding to all thirty eight multiple v-rib roughened plates. A regression analysis to fit a straight line through all the scattered data points yields the following equation;

$$Nu = A_0 (Re)^{0.92} \tag{4.8}$$

The value of A_0 in Eq.4.8 is a function of other roughness geometry parameters such as relative roughness height, e/D, relative roughness width, W/w, angle of attack, α and relative roughness pitch, P/e. In order to incorporate the effect of relative roughness height, e/D, the values of $\ln(A_0)$ are plotted against the values of ln(e/D) as shown in Fig.4.7. The least square method is used to fit a straight line through all the scattered data points as shown in Fig.4.7 and the following equation is obtained;

$$\frac{Nu}{Re^{0.92}} = B_0 \left(e / D\right)^{0.77} \tag{4.9}$$

where B_0 is anti $\ln(B_1)$

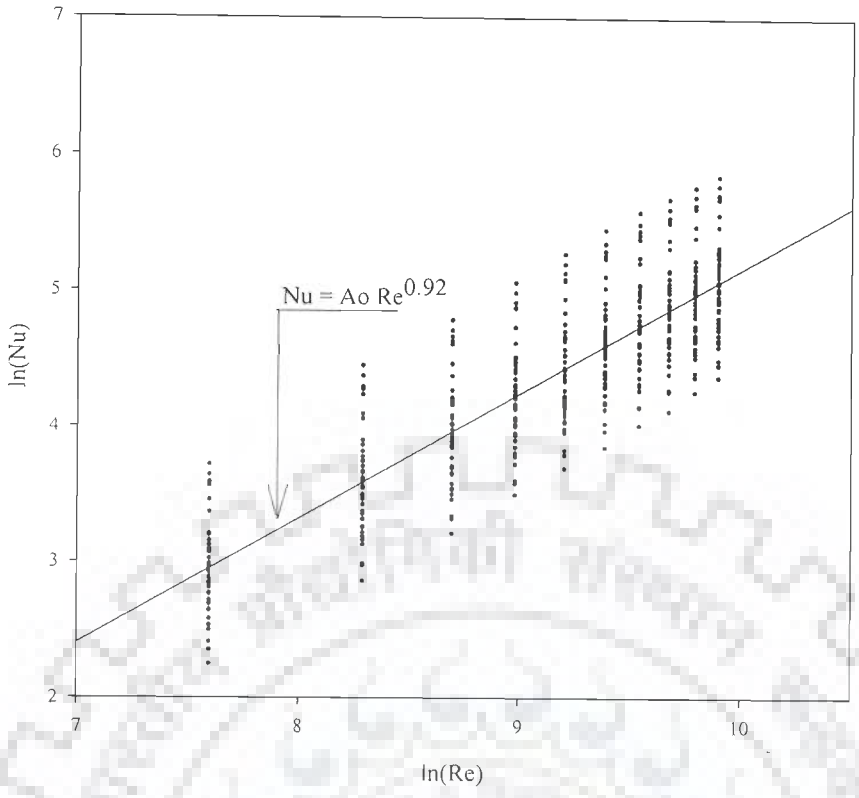

Fig.4.6 Plot of ln(Nu) as a function of ln(Re) for entire range of experimental data

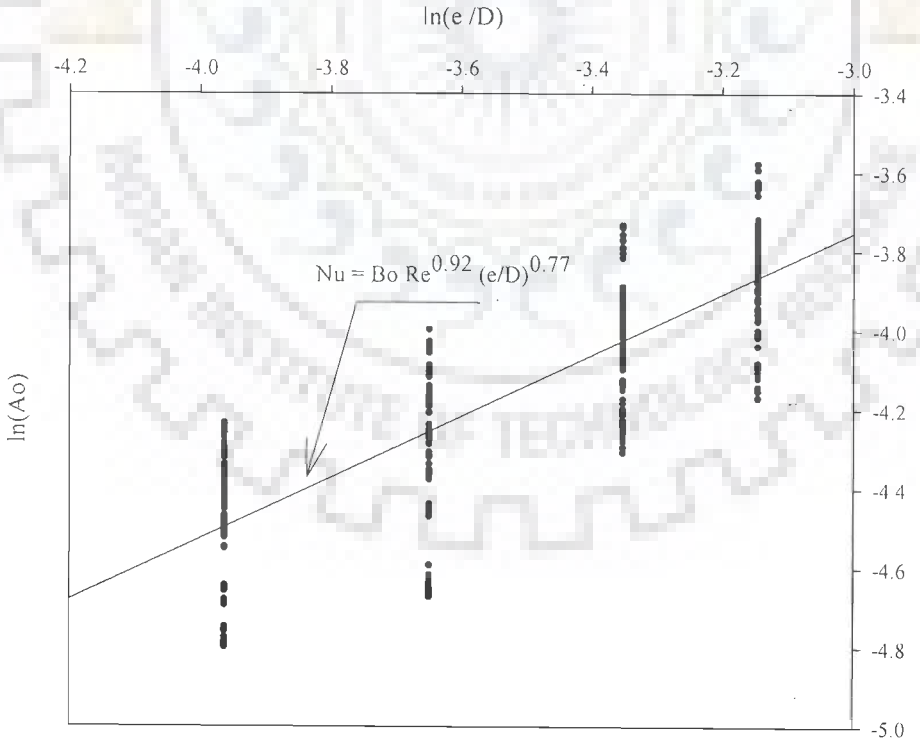

Fig.4.7 Plot on ln[Nu / Re $^{0.92}$] as a function of ln(e /D)

The value of B_o in Eq. 4.9 is a function of relative roughness width, W/w, angle of attack (α) and relative roughness pitch, P/e. In order to incorporate the effect of relative roughness width, W/w in the correlation of Nusselt number, values of $\ln(B_o)$ have been plotted against the values of $\ln(W/w)$ as shown in Fig.4.8. As discussed earlier in Section 4.4.1 that the relationship between Nusselt number and relative roughness width, W/w is governed by a quadratic equation, the least square method is used to fit a quadratic equation through all the scattered data points which yields the following equation;

$$\left[\frac{Nu}{Re^{0.92}\left(\frac{e}{D}\right)^{0.77}}\right] = C_0\left(\frac{W}{w}\right)^{0.43} \exp\left(-0.1177 \ln\left(\frac{W}{w}\right)\right)^2 \qquad (4.10)$$

where C_o is anti $\ln(C_1)$

The value of C_o in Eq. 4.10 is dependent on other roughness geometry parameters namely; angle of attack, α and relative roughness pitch, P/e. Therefore, in order to incorporate the effect of angle of attack, α in the correlation of Nusselt number, values of $\ln(C_o)$ have been plotted as a function of $\ln(\alpha/90)$ as shown in Fig.4.9. As discussed earlier in Section 4.4.1 that the relationship between Nusselt number and angle of attack, α is governed by a quadratic equation, therefore, the least square method is used to fit a quadratic equation through all the scattered data points which yields the following equation;

$$\left[\frac{Nu}{Re^{0.92}\left(\frac{e}{D}\right)^{0.77}\left(\frac{W}{w}\right)^{0.43}\exp\left[-0.1177(\ln(W/w))^2\right]}\right] = D_o \ln\left(\frac{\alpha}{90}\right)^{-0.49} \exp\left[-0.61\,(\ln(\alpha/90))^2\right] \qquad (4.11)$$

where D_0 is anti $\ln(D_1)$

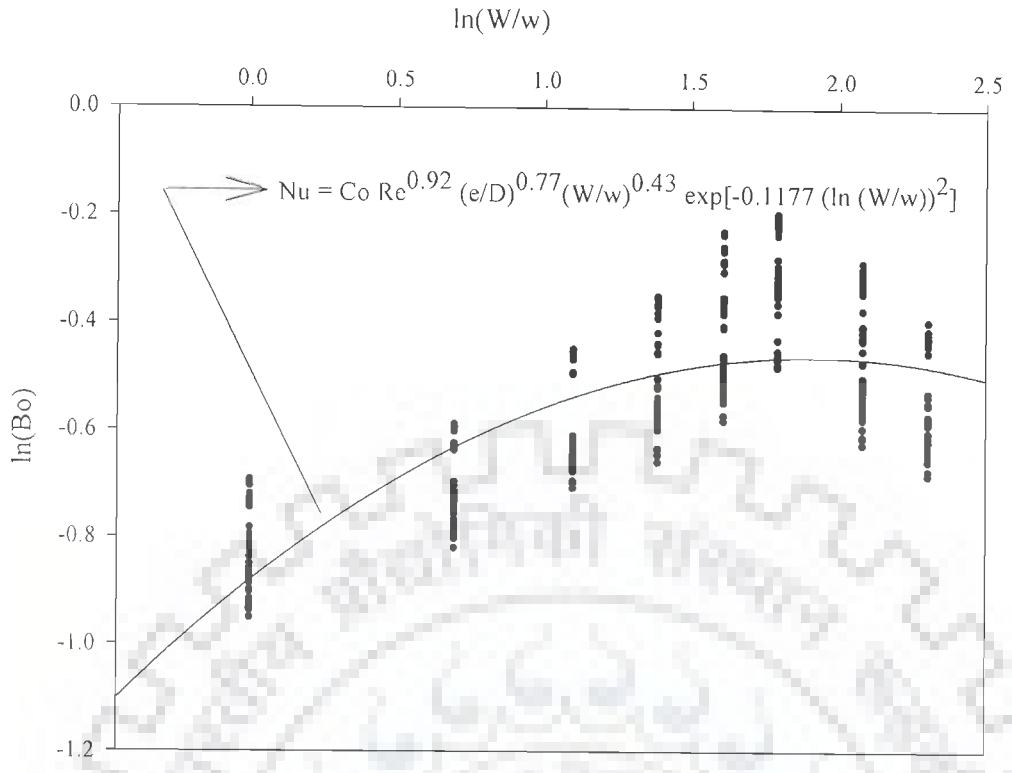

Fig.4.8 Plot of ln {Nu / [$Re^{0.92}$ $(e/D)^{0.77}$]} as a function of ln(W/w)

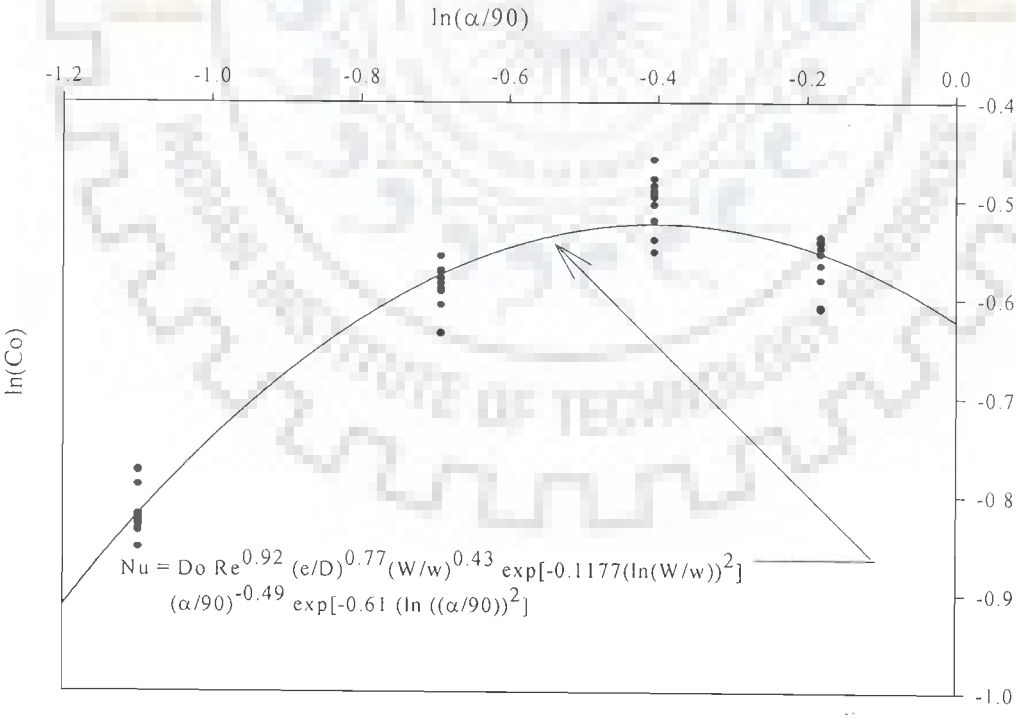

Fig.4.9 Plot of ln{Nu/[$Re^{0.92}$ $(e/D)^{0.77}$ $(W/w)^{0.43}$ exp (-0.1177 (ln $(W/w))^2$)]} as a function of ln(α/90)

The value of D_o in Eq. 4.11 is dependent on relative roughness pitch, P/e and therefore, in order to incorporate the effect of relative roughness pitch, P/e in the correlation of Nusselt number, values of $\ln(D_o)$ have been plotted as a function of $\ln(P/e)$ as shown in Fig.4.10. As discussed earlier in Section 4.4.1 that the relationship between Nusselt number and relative roughness pitch, P/e is governed by a quadratic equation, therefore, the least square method is used to fit a quadratic equation through all the scattered data points which yields the following equation;

$$\left[\frac{Nu}{Re^{0.92}\left(\frac{e}{D}\right)^{0.77}\left(\frac{W}{w}\right)^{0.43}\left(\frac{\alpha}{90}\right)^{-0.49}\exp\left[-0.1177(\ln(W/w))^2\right]\exp\left[-0.61(\ln(\alpha/90))^2\right]}\right] = E_o\left(\frac{P}{e}\right)^{8.54}\exp\left[-2.0407\,(\ln(P/e))^2\right] \quad (4.12)$$

where E_o is anti $\ln(E_1)$

The rearrangement of Eq. 4.12 yields the final correlation for Nusselt number;

$$Nu = 3.35\times10^{-5}\,Re^{0.92}\left(\frac{e}{D}\right)^{0.77}\left(\frac{W}{w}\right)^{0.43}\left(\frac{\alpha}{90}\right)^{-0.49}\exp\left[-0.1177(\ln(W/w))^2\right]\exp\left[-0.61(\ln(\alpha/90))^2\right] \times\left(\frac{P}{e}\right)^{8.54}\exp\left[-2.0407(\ln(P/e))^2\right] \quad (4.13)$$

Fig.4.11 shows the comparison between the experimental values of Nusselt number and those predicted by the correlating Eq. 4.13. About ninety five percent (95%) of the predicted values of the data lie with in ±10% (360 out of 380) of experimentally observed data values. Thus, the heat transfer correlation can predict the values of the heat transfer function quite satisfactorily in the range of parameters investigated in the present work. The regression of data for the correlation is found to have:

(i) Regression coefficient value of 0.98

(ii) Average absolute deviation of 4.45%

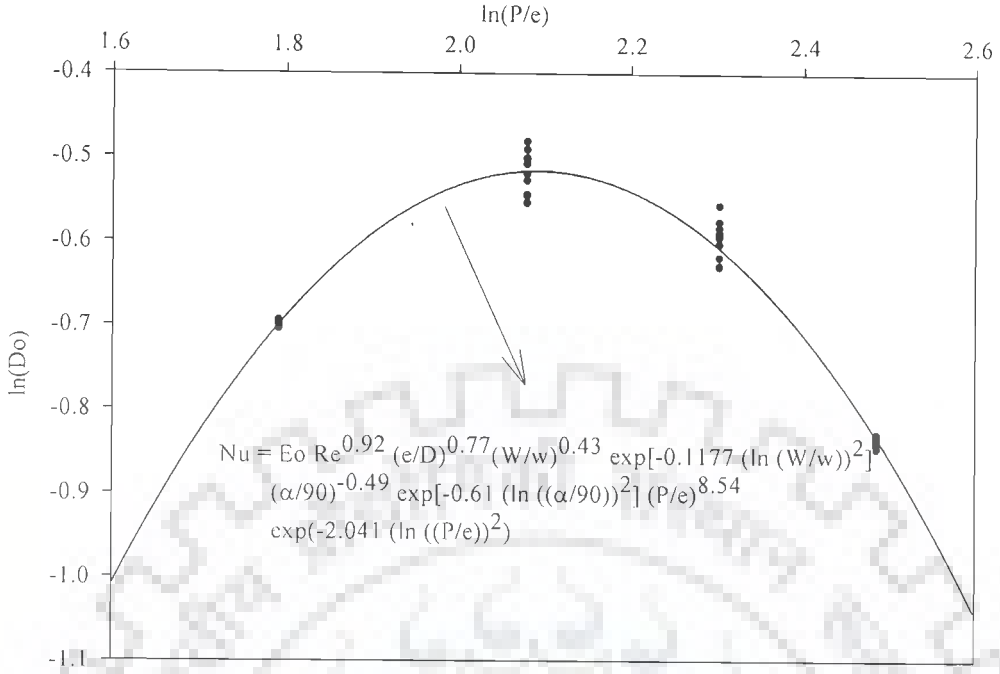

Fig.4.10 Plot of ln{ Nu/[$Re^{0.92}$ $(e/D)^{0.77}$ $(W/w)^{0.43}$ exp(-0.1177(ln $(W/w))^2$) $(\alpha/90)^{-0.49}$ exp (-0.61 (ln $(\alpha/90))^2$)]} as a function of ln (P/e)

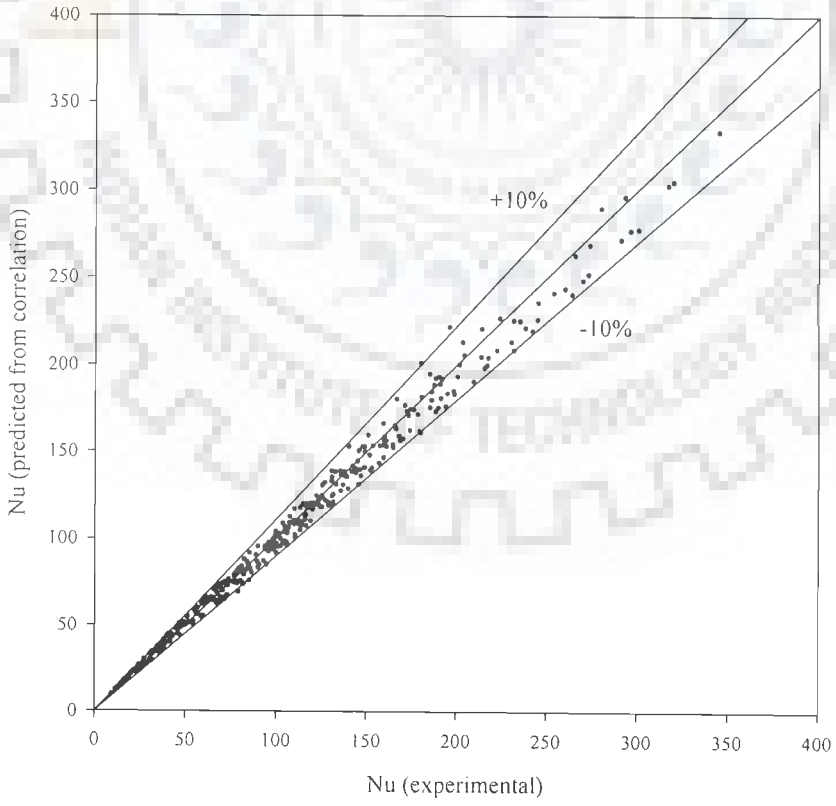

Fig.4.11 Comparison of experimental and predicted values of Nusselt number

4.4.3 Development of Correlation for Friction Factor

Friction factor has also been found to be a strong function of roughness geometry and flow parameters. The effect of roughness geometry parameters namely, relative roughness height, e/D, relative roughness width, W/w, angle of attack, α, relative roughness pitch, P/e and flow Reynolds number, Re on friction factor have been discussed in detail in Chapter 3.

As observed in Chapter 3, friction factor decreases with increase in Reynolds number and the functional relationship between the two is governed by a power equation as established in Section 4.41. Fig.4.12 shows a plot of ln(f) as a function of ln(Re) for the entire data corresponding to all thirty eight multiple v-rib roughened plates. A regression analysis to fit a straight line through all the scattered data points yields the following equation;

$$f = a_0 (Re)^{-0.318} \tag{4.14}$$

The value of a_0 in Eq. 4.14 is function of other roughness geometry parameters such as relative roughness height, e/D, relative roughness width, W/w, angle of attack, α and relative roughness pitch, P/e. In order to incorporate the effect of relative roughness height, e/D in the correlation of friction factor, the values of $\ln(a_0)$ are plotted against the values of ln(e/D) for the entire data as shown in Fig.4.13. A regression analysis to fit a straight line through all the scattered data points yields the following equation;

$$\frac{f}{Re^{-0.318}} = b_o \left(\frac{e}{D}\right)^{0.73} \tag{4.15}$$

where b_o is anti $\ln(b_1)$

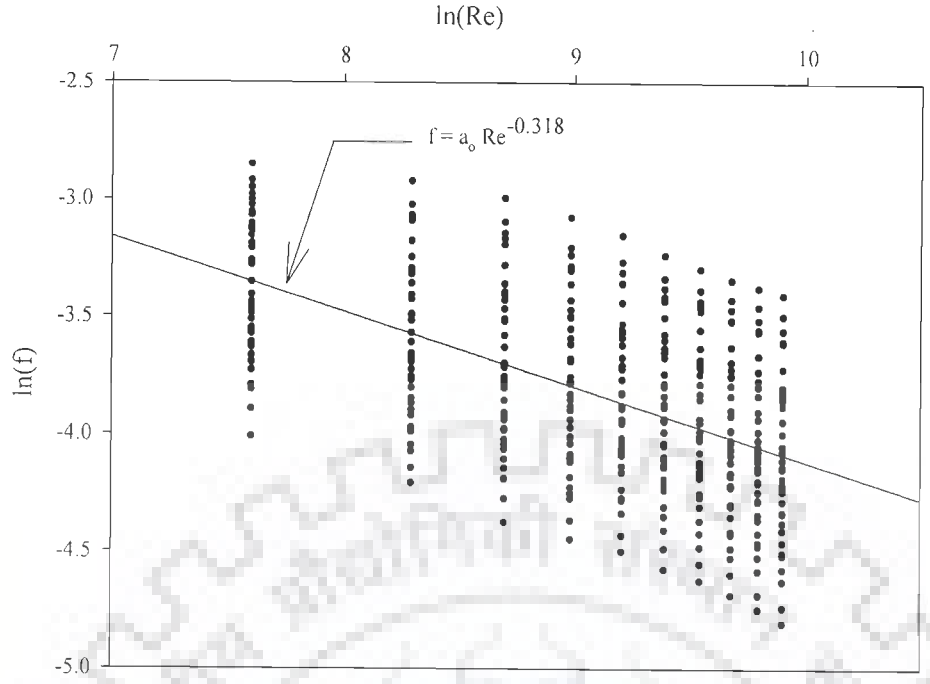

Fig.4.12 Plot of ln(f) as a function of ln(Re) for entire range of experimental data

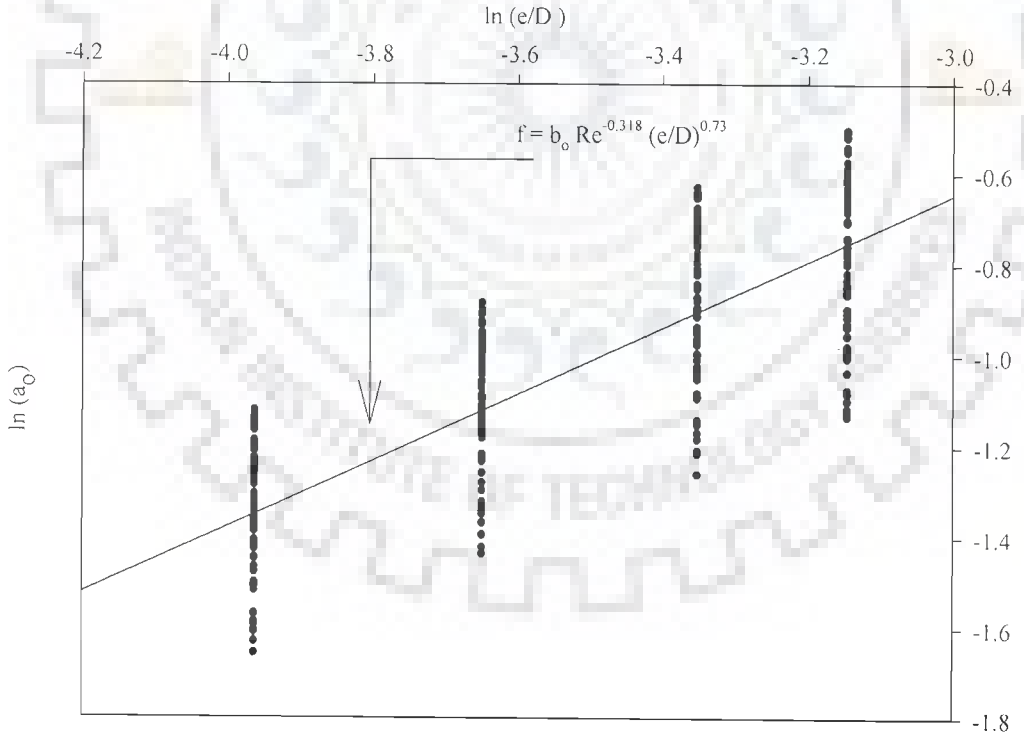

Fig.4.13 Plot of ln(f / $Re^{-0.318}$) as a function of ln(e/D)

The value of b_o in Eq. 4.15 is function of other influencing parameters namely, relative roughness width, W/w, angle of attack, α and relative roughness pitch, P/e. Therefore, in order to incorporate the effect of relative roughness width, W/w in the correlation of friction factor, values of $\ln(b_o)$ have been plotted against values of ln(W/w) as shown in Fig.4.14. Friction factor increases monotonically with increase in relative roughness width, W/w and the relationship between the two is governed by a linear equation as explained in Section 4.4.1. Therefore, the least square method is used to fit a straight line through all the scattered data points to obtain the following equation:

$$\ln\left[\frac{f}{Re^{-0.318}\,(e/D)^{0.73}}\right] = \ln(c_1) + c_2 \ln\left(\frac{W}{w}\right) \qquad (4.16)$$

The least square method is used to fit the best curve through all the scattered data points as shown in Fig.4.14 and the following equation is obtained;

$$\left[\frac{f}{Re^{-0.318}\,(e/D)^{0.73}}\right] = c_0\left(\frac{W}{w}\right)^{0.22} \qquad (4.17)$$

where c_o is anti $\ln(c_1)$

The value of c_o in Eq. 4.17 is dependent on other roughness geometry parameters namely, angle of attack, α and relative roughness pitch, P/e. Therefore, in order to incorporate the effect of angle of attack, α in the correlation of fiction factor, the values of $\ln(c_o)$ have been plotted as a function of ln(α/90) as shown in Fig.4.14. The functional relationship between $\ln(c_o)$ and ln (α/90) represented by the following equation;

$$ln\left[\frac{f}{Re^{-0.318}\left(\frac{e}{D}\right)^{0.73}\left(\frac{W}{w}\right)^{0.22}}\right] = ln(d_1) + d_2 ln\left(\frac{\alpha}{90}\right) + d_3\left(ln\left(\frac{\alpha}{90}\right)\right)^2 \qquad (4.18)$$

The least square method has been used to fit the best curve through all the scattered data points as shown in Fig.4.14 and the following equation is obtained;

$$\left[\frac{f}{Re^{-0.318}\left(\frac{e}{D}\right)^{0.73}\left(\frac{W}{w}\right)^{0.22}}\right]=d_o\left(\frac{\alpha}{90}\right)^{-0.39}\exp\left[-0.52(\ln(\alpha/90))^2\right] \qquad (4.19)$$

where d_0 is anti $\ln(d_1)$

The value of d_o in Eq. 4.19 is dependent on relative roughness pitch, P/e and in order to incorporate the effect of relative roughness pitch in the correlation of friction factor, the values of $\ln(d_o)$ have been plotted as a function of $\ln(P/e)$ as shown in Fig.4.15. The functional relationship between $\ln(d_o)$ and $\ln(P/e)$, is represented by the following equation;

$$\ln\left[\frac{f}{Re^{-0.318}\left(\frac{e}{D}\right)^{0.73}\left(\frac{W}{w}\right)^{0.22}\left(\frac{\alpha}{90}\right)^{-0.39}\exp\left[-0.52(\ln(\alpha/90))^2\right]}\right]=\ln(e_1)+e_2\ln\left(\frac{P}{e}\right)+e_3\left(\ln\left(\frac{P}{e}\right)\right)^2 \qquad (4.20)$$

The least square method is used to fit the best curve through all the scattered data points as shown in Fig.4.15 and the following equation is obtained;

$$\left[\frac{f}{Re^{-0.318}\left(\frac{e}{D}\right)^{0.73}\left(\frac{W}{w}\right)^{0.22}\left(\frac{\alpha}{90}\right)^{-0.39}\exp\left[-0.52(\ln(\alpha/90))^2\right]}\right]=e_o\left(\frac{P}{e}\right)^{8.9}\exp\left[-2.133(\ln(P/e))^2\right] \qquad (4.21)$$

where e_o is anti $\ln(e_1)$

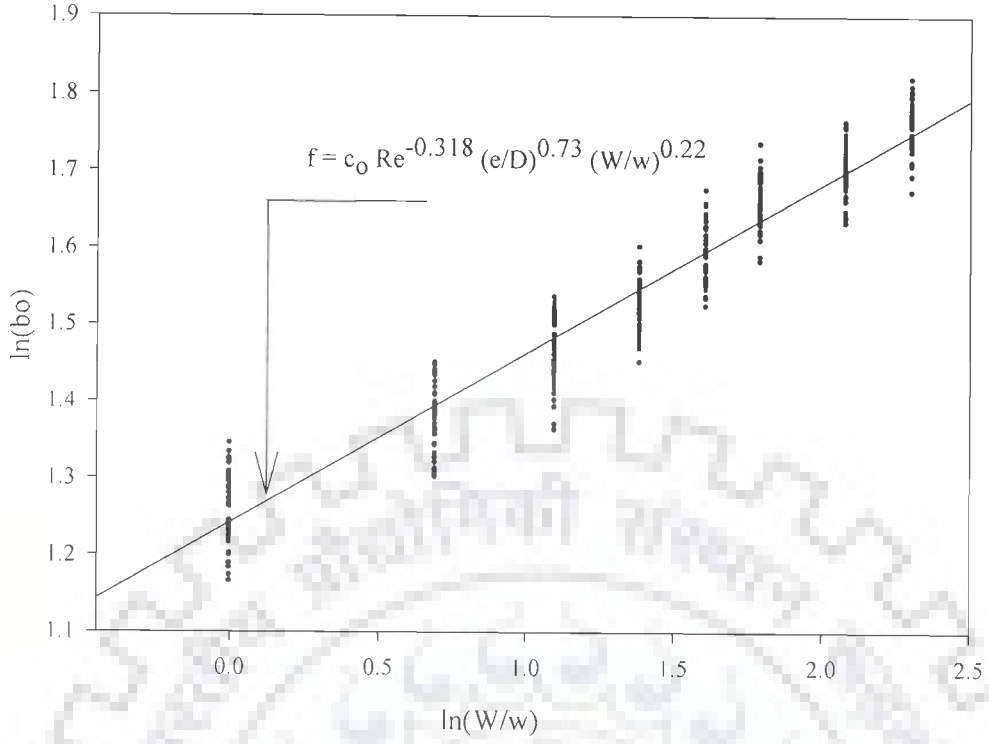

Fig.4.14 Plot of ln{f / [$Re^{-0.318}$ $(e/D)^{0.73}$]} as a function of ln(W/w)

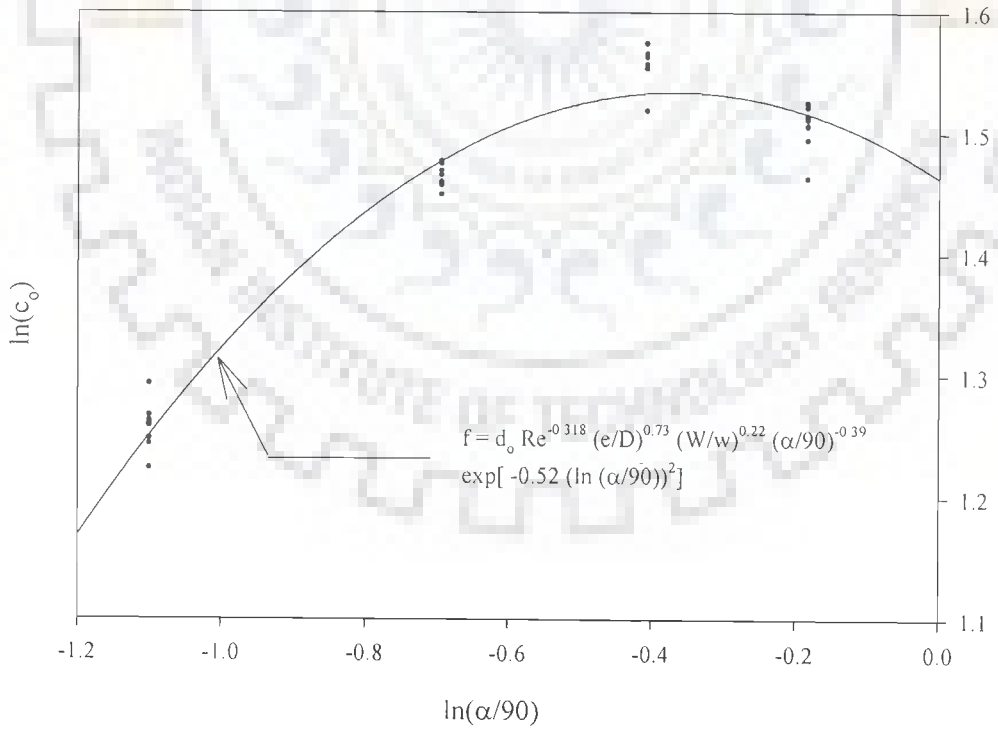

Fig.4.15 Plot of ln{f/[$Re^{-0.318}$ $(e/D)^{0.73}$ $(W/w)^{0.22}$]} as a function of ln(α/90)

The Eq.4.21 can be rearranged to obtain the final correlation for friction factor;

$$f = 4.47 \times 10^{-4} Re^{-0.318} \left(\frac{e}{D}\right)^{0.73} \left(\frac{W}{w}\right)^{0.22} \left(\frac{\alpha}{90}\right)^{-0.39} exp\left[-0.52(ln(\alpha/90))^2\right] \left(\frac{P}{e}\right)^{8.9} exp\left[-2.133\,(ln(P/e))^2\right] \quad (4.22)$$

Fig.4.16 shows the comparison between the experimental values of friction factor and those predicted by the correlating Eq. 4.22. About ninety six percent (96%) of the predicted values of the data lie with in ±10% (364 out of 380) of experimentally observed data values. Thus, the friction factor correlation can predict the values of the heat transfer function quite satisfactorily in the range of parameters investigated in the present work. The regression of data for the correlation is having

(i) Regression coefficient value of 0.98

(ii) Average absolute deviation of 4.0%

It can be, therefore, concluded that the correlations developed as Eqs. 4.13 and 4.22 can be used for the prediction of Nusselt number and friction factor respectively, as a function of roughness and flow parameters of a multiple v-rib roughened rectangular duct with reasonable accuracy.

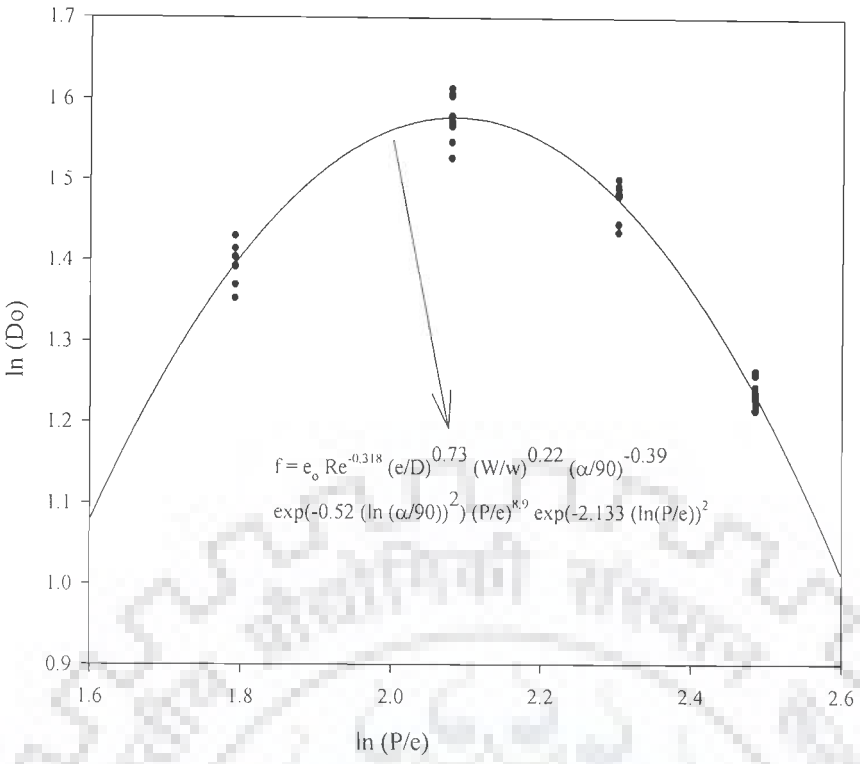

Fig.4.16 Plot of ln{f/[$Re^{-0.318}$ $(e/D)^{0.73}(W/w)^{0.22}$ $(\alpha/90)^{-0.39}$exp (-0.52 (ln $(\alpha/90))^2$)]} as a function of ln (P/e)

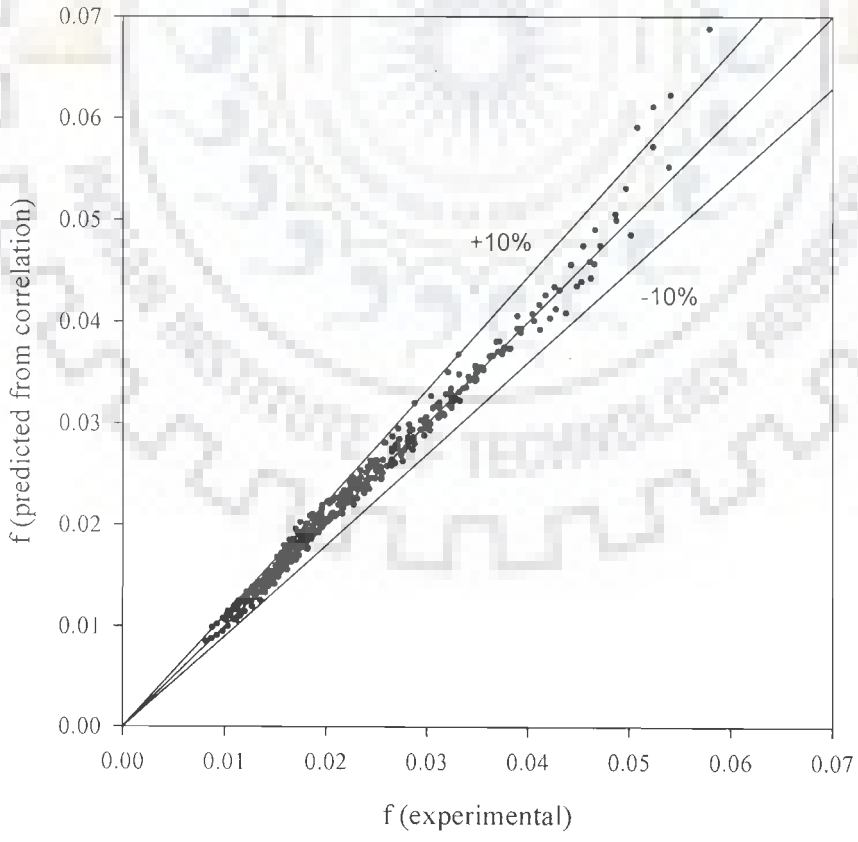

Fig.4.17 Comparison of experimental and predicted values of friction factor

CHAPTER-5

PREDICITON OF THERMAL PERFORMANCE OF COLLECTORS

5.1 GENERAL

It has been concluded from the experimental investigation carried out and as discussed in Chapter 3 that the use of artificial roughness, in the form of repeated multiple v-ribs, on the underside of absorber plate of a collector brings about considerable enhancement in heat transfer from the absorber plate to air along with increase in frictional losses. The effect of roughness geometry and operating parameters such as relative roughness height, e/D, relative roughness width, W/w, angle of attack, α, relative roughness pitch, P/e and Reynolds number, Re on heat transfer coefficient and friction factor have been investigated and discussed in Chapter 3. The correlations for Nusselt number and friction factor have been developed in terms of the roughness geometry and operating parameters as discussed in Chapter 4.

In this chapter, a computer program has been developed to predict the thermal performance of roughened collectors in terms of plate efficiency factor, F', heat removal factor, F_o and thermal efficiency, η_{Th} on the basis of the correlations developed in Chapter 4 for Nusselt number and friction factor. The effect of roughness geometry and operating parameters on the thermal performance has been investigated and thermal performance of roughened and smooth collectors has been compared in order to determine the enhancement of thermal performance on account of use of multiple v-rib type of roughness geometry.

5.2 REPRESENTATION OF THERMAL PERFORMANCE OF SOLAR AIR HEATER

In this chapter, recommendations of American Society of Heating and Air Conditioning Engineering (ASHRAE Standard 93–77) [151] have been followed for thermal performance prediction of collectors roughened with multiple v-ribs. A number of expressions used in this section to describe thermal performance of collectors have also been given in Chapter 1. However, for the purpose of clarity and better understanding, the relevant expressions have been given in this chapter again.

Thermal efficiency, η_{Th} is a measure of collector performance and as per ASHRAE recommendation [151], it is defined as ratio of the useful heat energy gain to rate of total incident solar energy and is expressed as;

$$\eta_{Th} = \frac{m \times C_p \times (T_o - T_i)}{A_p \times I} \tag{5.1}$$

The instantaneous rate of useful energy collection is the difference between the energy of incident solar radiations absorbed by the absorber plate and the rate at which the energy is lost due to the difference in absorber plate and ambient temperatures. The useful energy collected can be expressed mathematically [2, 20] as:

$$Q_u = A_p [I(\tau\alpha) - U_L (T_p - T_a)] \tag{5.2}$$

To overcome the difficulty of determining the average plate temperature, T_p, a parameter called plate efficiency or collector efficiency factor, F' is introduced and is defined as:

$$F' = \frac{\text{Actual useful energy collected}}{\text{Useful energy collected if entire collector surface were maintained at average fluid temperature}} \tag{5.3}$$

Introduction of plate efficiency factor, F' makes it convenient to express Eq.5.2 in terms of inlet or average fluid temperatures as given below;

$$Q_u = F' A_P \left[I(\tau\alpha) - U_L (T_{f'} - T_a) \right] \tag{5.4}$$

where, $T_{f'} = \frac{(T_o + T_i)}{2}$

For collectors operating in open loop system, $T_a = T_i$, Eq.5.4 reduces to;

$$Q_u = F' A_P \left[I(\tau\alpha) - U_L (T_o - T_i)/2 \right] \tag{5.5}$$

The rate of useful energy collected can also be expressed by considering increase in enthalpy of air flowing through collector, as;

$$Q_u = m C_P (T_o - T_i) \tag{5.6}$$

Then, thermal efficiency of collector can be alternatively expressed as;

$$\eta_{Th} = F' A_P \left[I(\tau\alpha) - U_L (T_o - T_i)/2I \right] \tag{5.7}$$

$$\eta_{Th} = F' A_P \left[I(\tau\alpha) - U_L (T_o - T_a)/2I \right] \tag{5.8}$$

$$\eta_{Th} = m C_P (T_o - T_i) / A_c I \tag{5.9}$$

The thermal efficiency of a collector can also be expressed in terms of another factor called heat removal factor, F_o as given below;

$$\eta_{Th} = F_o \left[(\tau\alpha) - U_L \left(\frac{T_i - T_a}{I} \right) \right] \tag{5.10}$$

where, F_o is the heat removal factor of collector and is defined as ratio of actual heat transfer to the maximum possible rate of heat transfer when absorber plate is

maintained at inlet fluid temperature. Heat removal factor, F_o is equivalent to the effectiveness of a conventional heat exchanger. The actual useful energy gain can be expressed as;

$$Q_u = F_0 A_P \left[I(\tau\alpha) - U_L (T_i - T_a) \right] \tag{5.11}$$

In a specific case of a solar air heater where air is not recirculated, inlet air temperature remains same as the ambient temperature (i.e., $T_i = T_a$). The Eq.5.10 reduces to;

$$\eta = F_o (\tau\alpha) \tag{5.12}$$

This expression of efficiency does not permit the real operative temperature to be shown. In context of these limitations, Biondi et al. [17] proposed the following equation for thermal efficiency of a collector to overcome these limitations.

$$\eta = F_o \left[(\tau\alpha) - U_L \left(\frac{T_o - T_i}{I} \right) \right] \tag{5.13}$$

where F_o is the heat removal factor related to outlet temperature and can be expressed as;

$$F_o = \frac{mC_P}{A_P U_L} \left[\exp \left\{ \frac{F' U_L A_P}{mC_P} \right\} - 1 \right] \tag{5.14}$$

5.3 THERMAL PERFORMANCE PREDICTION

The performance of a solar collector can be predicted on the basis of detailed consideration of heat transfer and fluid flow processes in the system. The performance parameters, namely overall heat loss coefficient, heat removal factor and thermal efficiency can be evaluated analytically. For this purpose, a computer program has been developed and step-by-step procedure followed is discussed below;

5.3.1 Prediction Procedure

A computer program has been developed in C^{++} language for computing thermal performance of roughened collectors in terms of plate efficiency factor, F', heat removal factor, F_o and thermal efficiency, η_{Th}. The flow diagram of the computer program is shown in Fig.5.1. The important steps of the iterative procedure are given below:

(i) Area of the absorber plate is calculated as;

$A_p = W \times L$

where

W - width of the collector

L - length of the collector

(ii) Hydraulic diameter of the duct is calculated as;

$D = 2 (W \times H) / (W+H)$

where H - height or depth of the duct

(iii) Fixed system parameters such as;

Thickness of insulation, t_i

Thermal conductivity of insulation, k_i

Transmittance–absorptance product, $(\tau\alpha)$

Emissivity of the absorber plate, ε_p

Emissivity of the glass cover, ε_g

Fixed operating parameters such as;

Atmospheric air velocity, V_w and atmospheric temperature, T_a are selected.

(iv) A set of system roughness geometry parameters such as relative roughness height, e/D, relative roughness width, W/w, angle of attack, α and relative roughness pitch, P/e are selected.

(v) A set of values of design parameters namely temperature rise parameter, $[(T_o - T_i)/I]$ and insolation, I are selected.

(vi) The rise of temperature of air across the duct and outlet temperature are calculated as;

$$\Delta T = (\Delta T/I) \times I$$

$$T_o = T_i + \Delta T$$

(vii) Approximate initial mean plate temperature is assumed to be as;

$$T_p = \frac{T_o + T_i}{2} + 10^\circ C$$

(viii) Using the value of mean plate temperature, T_P value of the top loss coefficient, U_t is computed by using equation proposed by Akhtar and Mullick [26];

$$U_t^{-1} = \left[\frac{\sigma\left(T_p^2 + T_g^2\right)\left(T_p + T_g\right)}{\left(\frac{1}{\varepsilon_p} + \frac{1}{\varepsilon_g} - 1\right)} + \left(\frac{k_a Nu}{L_g}\right) \right]^{-1} + \left[\sigma\,\varepsilon_g\left(T_g^2 + T_a^2\right)\left(T_g + T_a\right) + h_w\right]^{-1} + \frac{t_g}{k_g}$$

where, $$T_g = \left(\frac{F_1 T_p + c\,T_a}{1 + F_1}\right)$$

where, $$F_1 = \frac{\left[12\times10^{-8}\left(T_a + 0.2T_p\right)^3 + h_w\right]^{-1} + 0.3t_g}{\left[6\times10^{-8}\left(\varepsilon_p + 0.028\right)\left(T_p + 0.5T_a\right)^3 + 0.6L_g^{-0.2}\left\{\left(T_p - T_a\right)\cos\beta\right\}^{0.25}\right]^{-1}}$$

and $$c = \left(\frac{(T_s/T_a) + (h_w/3.5)}{(1 + (h_w/3.5))}\right)$$

$$T_s = 0.0522\left(T_a\right)^{1.5}$$

$$Nu = 1 + 1.44\left[1 - 1708/Ra\cos\beta\right]^{+}\left\{1 - 1708\left(\sin 1.8\beta\right)^{1.6}/Ra\cos\beta\right\} + \left[\left(Ra\cos\beta/5830\right)^{0.33} - 1\right]^{+}$$

where, $$Ra = Gr \times Pr$$

$$Gr = \frac{g\beta'\left(T_p - T_g\right)L_g^3}{\nu^2}$$

$$\beta' = \frac{1}{\left[\left(T_o + T_i\right)/2\right]}$$

$$Pr = \frac{\mu C_p}{k_a}$$

Back loss coefficient U_b is expressed as;

$$U_b = k_i / t_i$$

The edge loss coefficient, based on the collector area A_P is given as;

$$U_e = \frac{(L+W)\, t_e k_i}{LW t_i}$$

$$U_L = U_t + U_b + U_e$$

(ix) Useful energy gain rate is calculated as;

$$Q_{u_1} = \left[I(\tau\alpha) - U_L\right]\left(T_P - T_a\right) A_P$$

(x) Mass flow rate is determined from the expression given as;

$$m = \frac{Q_{u_1}}{C_p \Delta T}$$

(xi) Reynolds number of flow of air in the duct is computed as;

$$Re = GD/\mu$$

where, G is the mass velocity of air through the collector

$$G = m / (WH)$$

(xii) Nusselt number is calculated using the correlation developed in Chapter 4 and reproduced below.

$$Nu = 3.35 \times 10^{-5} \times Re^{0.92} \left(\frac{e}{D}\right)^{0.77} \left(\frac{W}{w}\right)^{0.43} \left(\frac{\alpha}{90}\right)^{-0.49} \exp(-0.1177\ (ln(W/w))^2)$$

$$\times \exp(-0.61\ (ln(\alpha/90))^2) \left(\frac{P}{e}\right)^{8.54} \exp(-2.0407\ (ln(P/e))^2)$$

Convective heat transfer coefficient is computed as;

$$h = \frac{Nu\ k}{D}$$

(xiii) The plate efficiency factor is then computed as;

$$F' = \frac{h}{h + U_L}$$

(xiv) The heat removal factor, F_o based on outlet temperature is calculated as;

$$F_o = \frac{\dot{m}C_P}{A_P U_L}\left[\exp\left\{\frac{F'U_L A_P}{\dot{m}C_P}\right\} - 1\right]$$

(xv) New value of useful heat gain is calculated as;

$$Q_{u2} = A_P F_o \left[I(\tau\alpha) - U_L (T_o - T_i)\right]$$

(xvi) The values of Q_{u1} and Q_{u2} are compared; if the difference is found to be more than the 0.1 % of Q_{u1}, then the new value of mean plate temperature is calculated as;

$$T_p = T_a + [(I(\tau\alpha) - Q_{u2}/A_p)/U_L]$$

Using this new value of plate temperature, steps from 8 to 16 are repeated till the difference between Q_{u1} and Q_{u2} lies within the target value. Consequently

$$Q_u = Q_{u1} = Q_{u2}$$

(xvii) Thermal efficiency is calculated as;

$$\eta_{Th} = F_o\left[(\tau\alpha) - \frac{U_L (T_o - T_i)}{I}\right]$$

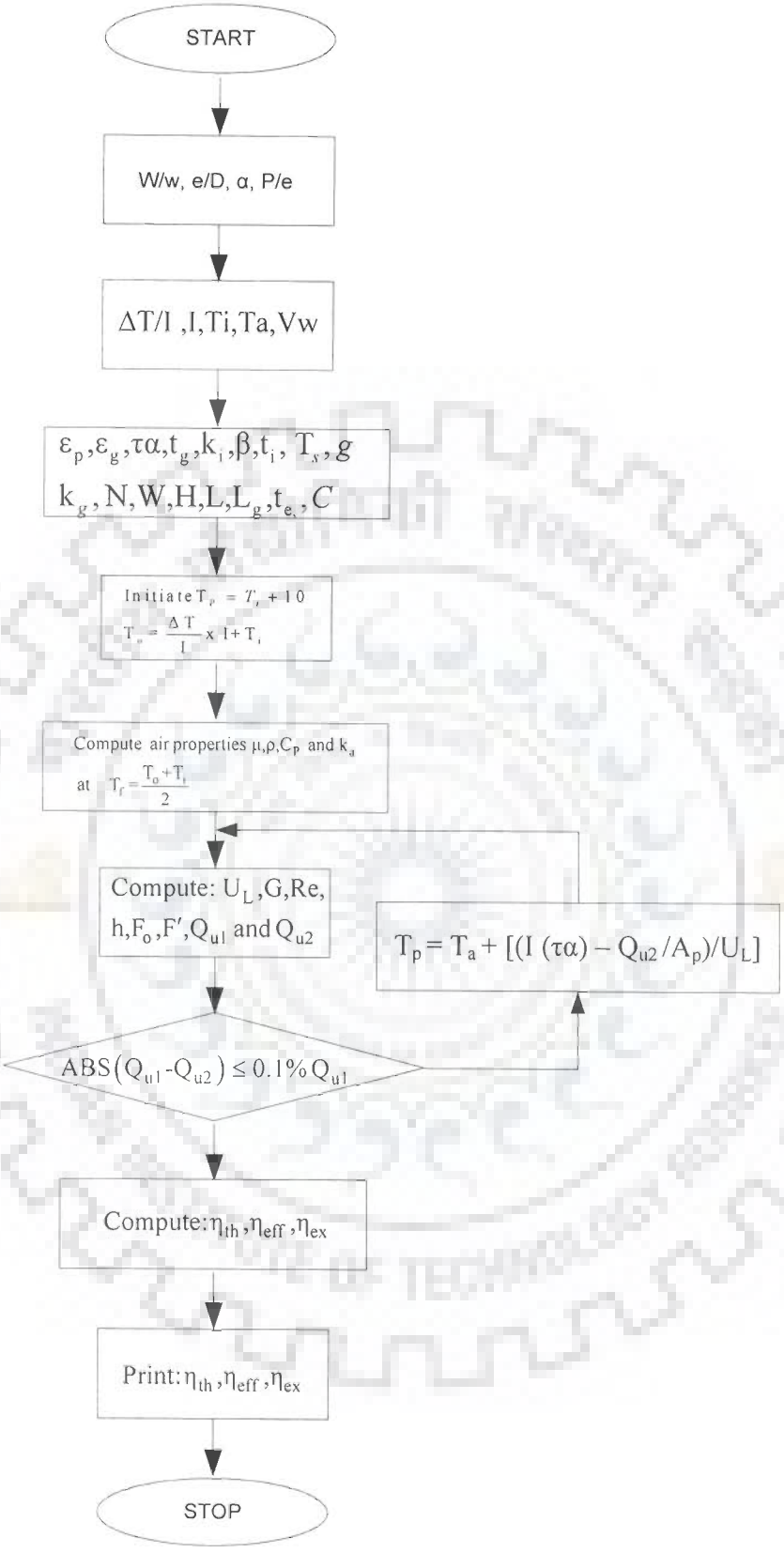

Fig.5.1 Flow diagram of computer program

5.3.2 Range of Parameters

The thermal performance of roughened collector has been computed for the range of roughness geometry and operating parameters given below:

5.3.2.1 Roughness geometry parameters

(i) Relative roughness height, e/D : $0.019 \leq e/D \leq 0.043$

(ii) Relative roughness width, W/w : $1 \leq W/w \leq 10$

(iii) Angle of attack, α : $30^{\circ} \leq \alpha \leq 75^{\circ}$

(iv) Relative roughness height, P/e : $6 \leq P/e \leq 12$

5.3.2.2 Operating parameters

(i) Reynolds number, Re : $2000 \leq Re \leq 20000$

(ii) Intensity of solar radiations, I : $1000\ W/m^2$

(iii) Temperature rise parameter, $(T_o-T_i)/I$: $0.003 \leq (T_o-T_i)/I \leq 0.027$

The thermo physical properties are determined by using following equations;

$$\mu = 1.81 \times 10^{-5} \left(\frac{T_{fm}}{293} \right)^{0.735} \quad N\text{-}s/m^2$$

$$C_p = 1006 \left(\frac{T_{fm}}{293} \right)^{0.0155} \quad J/kg\text{-}K$$

$$K = 0.0275 \left(\frac{T_{fm}}{293} \right)^{0.086} \quad W/m\text{-}K$$

$$\rho = \frac{P_{atm}}{R\ T_{fm}} \quad kg/m^3$$

The values of other system parameters related to collector are given in Table 5.1

Table 5.1 System parameters

S. No.	Description of system parameters	Parameter	Value/range
1.	Collector length, m	L	1
2.	Collector width, m	W	0.3
3.	Duct depth, m	H	0.025
4.	Number of glass covers	N	1
5.	Thermal conductivity of insulation, W/m K	K_i	0.037
6.	Thickness of insulation, m	t_i	0.05
7.	Transmittance–absorptance product	$(\tau\alpha)$	0.8
8.	Emissivity of the absorber plate	ε_P	0.9
9.	Emissivity of the glass cover	ε_g	0.88
10.	Thickness of glass cover, m	t_g	0.002
11.	Air gap between absorber plate and glass cover, m	L_g	0.025
12.	Thickness of collector edge, m	t_e	0.016

5.4 RESULTS AND DISCUSSION

In order to discuss the effect of roughness geometry parameters (relative roughness height, e/D, relative roughness width, W/w, angle of attack, α and relative roughness pitch, P/e) and operating parameters (Reynolds number, Re) on thermal performance parameters (collector efficiency factor, F', heat removal factor, F_o and thermal efficiency, η_{Th}), various plots have been prepared and discussed as:

5.4.1 Effect of Roughness Geometry and Operating Parameters on Plate Efficiency Factor

Figs.5.2 to 5.5 show the variation of plate efficiency factor F' with respect to Reynolds number for different values of roughness geometry parameters. Plate efficiency factor F' computed for the collectors roughened with multiple v-ribs has been compared with that of smooth collector.

It has been observed from these plots that plate efficiency factor, F' increases with increase in Reynolds number and increase in plate efficiency factor is rapid up to

Reynolds number value of about 9000 and beyond this value of Reynolds number, the rate of increase of efficiency factor decreases corresponding to all values of roughness geometry parameters. The plate efficiency factor of roughened collector is found to be higher in comparison to that of smooth collector for the range of parameters investigated.

Fig.5.2 shows the effect of relative roughness height, e/D on plate efficiency factor as a function of Reynolds number for the fixed values of other roughness geometry parameters such as relative roughness width, W/w, angle of attack, α and relative roughness Pitch, P/e.

It has been observed from these plots that plate efficiency factor increases with increase in the value of relative roughness height and minimum and maximum values have been obtained corresponding to relative roughness height values of 0.019 and 0.043 respectively for the range of parameters investigated. For a fixed value of relative roughness height rate of increase of plate efficiency factor is high in the Reynolds number range of about 2000 to 9000 and beyond this range of Reynolds number, rate of increase of plate efficiency factor decreases.

Fig.5.3 shows the effect of relative roughness width, W/w on plate efficiency factor as a function of Reynolds number for fixed values of relative roughness height, e/D, angle of attack, α and relative roughness pitch, P/e. It has been observed from the Fig.5.3 that plate efficiency factor increases with increase in relative roughness width, W/w and attains a maximum value corresponding to relative roughness width, W/w value of 6 in the range of parameters investigated. With further increase in relative roughness width, W/w, a decrease in the plate efficiency factor has been observed. For a particular value of relative roughness width, W/w plate efficiency factor increases with increase in Reynolds number.

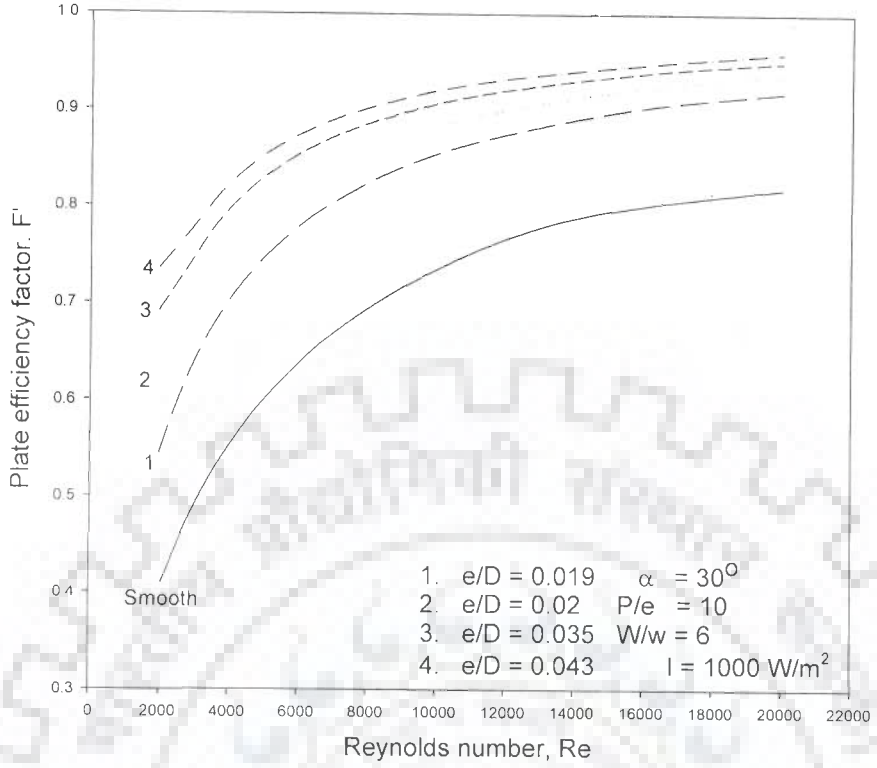

Fig.5.2 Effect of relative roughness height on plate efficiency factor as a function of Reynolds number

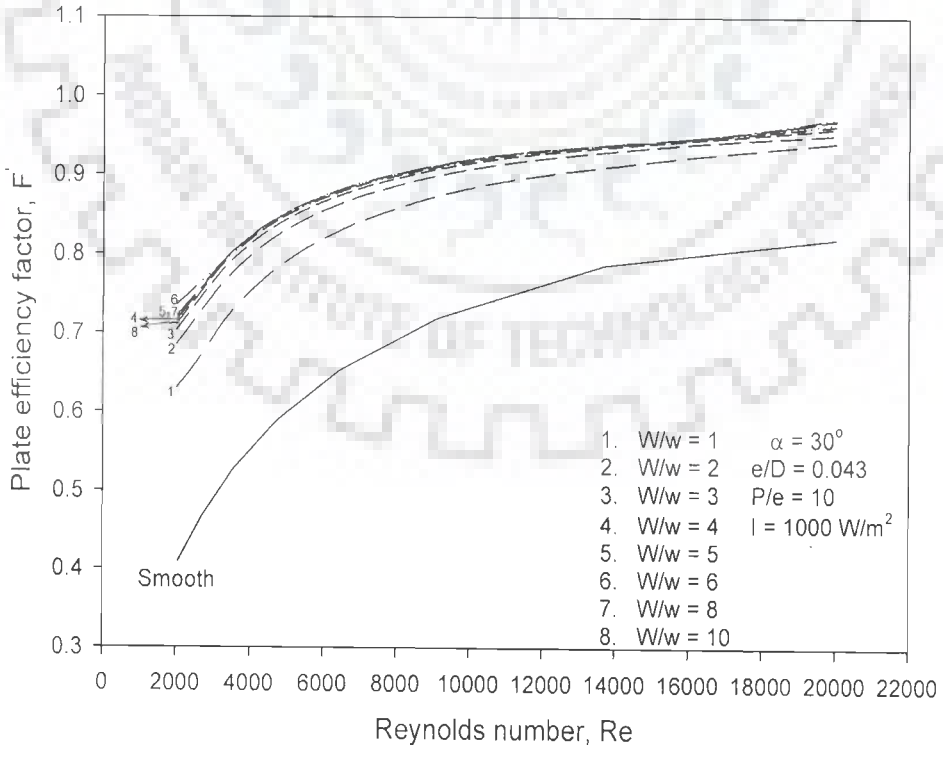

Fig.5.3 Effect of relative roughness width on plate efficiency factor as a function of Reynolds number

Fig.5.4 has been drawn to bring out the effect of angle of attack, α on plate efficiency factor, F' as a function of Reynolds number for fixed values of relative roughness height, e/D, relative roughness width, W/w and relative roughness pitch, P/e. Plate efficiency factor increases with increase in angle of attack and attains a maximum value corresponding to angle of attack, α value of 60° for the range of parameters investigated. With further increase in angle of attack, α, plate efficiency factor decreases. For a fixed value of angle of attack, plate efficiency factor increases with increase in Reynolds number.

Fig.5.5 shows the effect of relative roughness pitch, P/e on plate efficiency factor, F' as a function of Reynolds number for fixed values of relative roughness height, e/D, relative roughness width, W/w and angle of attack, α. Plate efficiency factor increases with increase in the value of relative roughness pitch and attains a maximum value corresponding to relative roughness pitch value of 8 for the range of parameters investigated. For a fixed value of relative roughness pitch, P/e plate efficiency factor increases with increase in Reynolds number.

5.4.2 Effect of Roughness Geometry and Operating Parameters on Heat Removal Factor

Figs.5.6 to 5.9 show the effect of roughness geometry and operating parameters on heat removal factor, F_o and heat removal factor of roughened collectors has been compared with that of conventional smooth collectors. The roughness geometry and operating parameters have similar effect on heat removal factor, F_o as in case of plate efficiency factor, F'.

Fig.5.6 has been drawn to illustrate the effect of relative roughness height, e/D on heat removal factor, F_o. These plots have been prepared for relative roughness height, e/D values of 0.019, 0.026, 0.035 and 0.043 with values of other roughness geometry parameters such as relative roughness width, W/w, angle of attack, α and relative roughness pitch, P/e remaining constant.

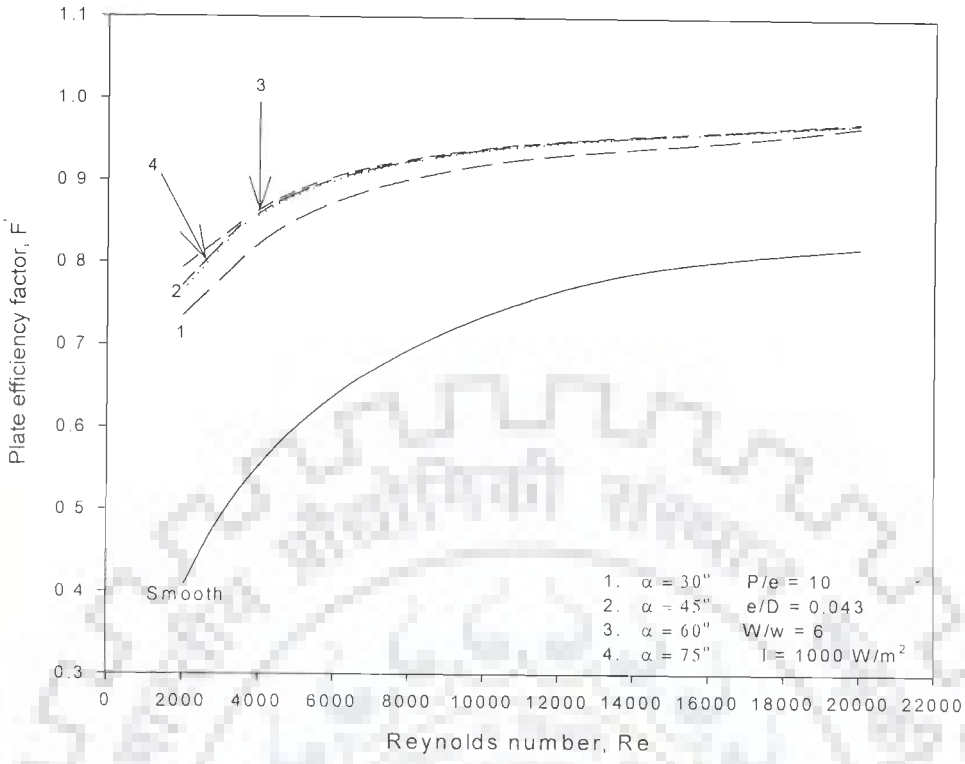

Fig.5.4 Effect of angle of attack on plate efficiency factor as a function of Reynolds number

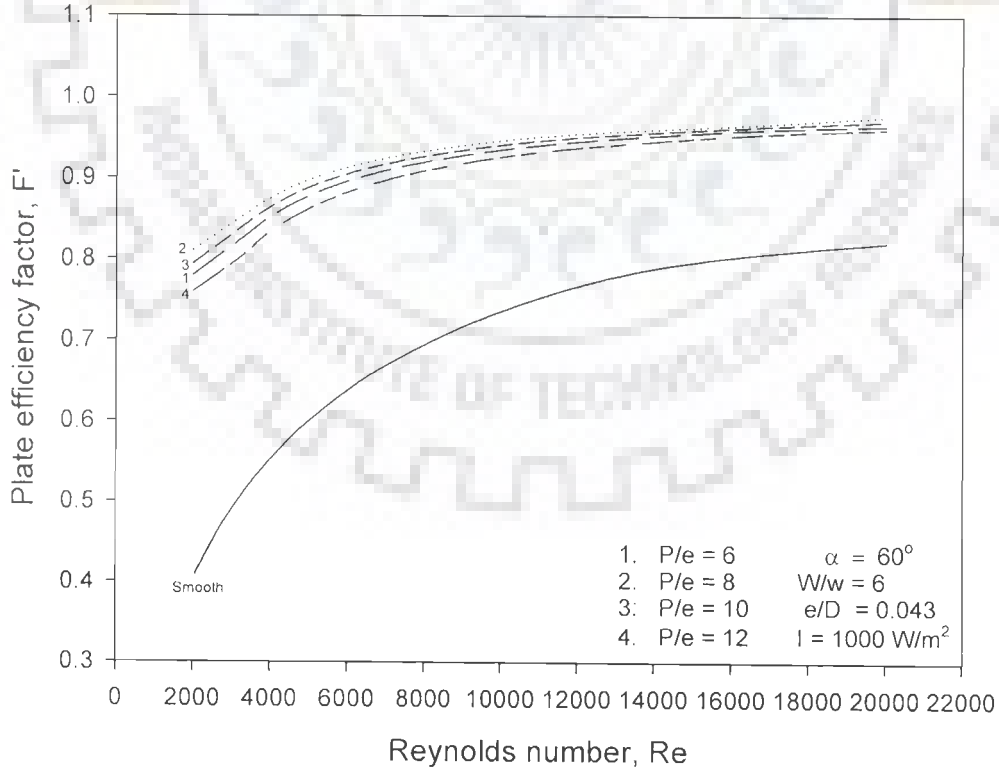

Fig.5.5 Effect of relative roughness pitch on plate efficiency factor as a function of Reynolds number

It has been observed from this plot that heat removal factor, F_0 increases with increase in relative roughness height, e/D for entire range of Reynolds number. For a fixed value of relative roughness height, heat removal factor increases with increase in Reynolds number.

Fig.5.7 shows the variation of heat removal factor with relative roughness width, W/w as a function of Reynolds number while the other roughness geometry parameters such as relative roughness height, e/D, angle of attack, α and relative roughness pitch, P/e remaining constant. It has been observed from the Fig.5.7 that heat removal factor increases with increase in relative roughness width and attains a maximum value corresponding to relative roughness width value of 6 in the range of parameters investigated. With further increase in relative roughness width, a decrease in the value of heat removal factor has been observed. For a particular value of relative roughness width, heat removal factor increases with increase in Reynolds number.

Fig.5.8 illustrates the effect of angle of attack, α, on heat removal factor, F_0 as a function of Reynolds number for fixed values of relative roughness height, e/D, relative roughness width, W/w and relative roughness pitch, P/e. Heat removal factor increases with increase in angle of attack and attains a maximum value corresponding to angle of attack value of 60° for the range of parameters investigated. With further increase in angle of attack value, heat removal factor decreases. For a fixed value of angle of attack, heat removal factor increases rapidly with increase in Reynolds number up to a value of about 9000 and beyond this value of Reynolds number, a decrease in the rate of increase in heat removal factor has been observed.

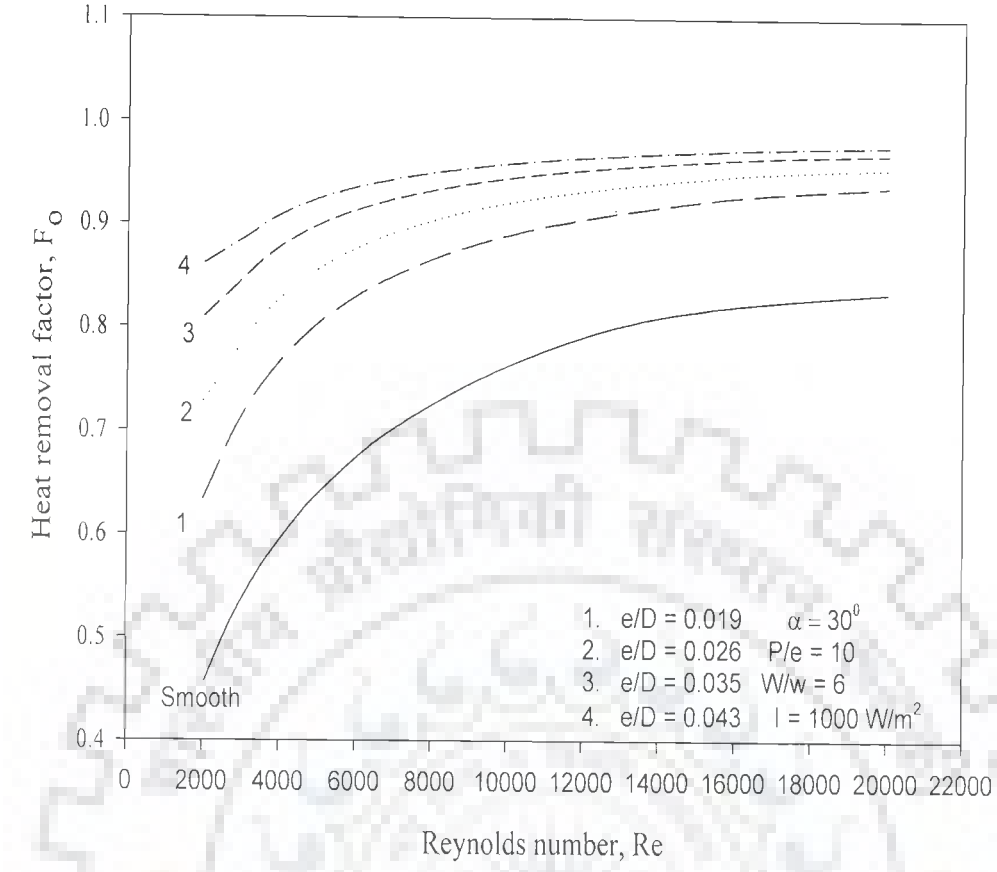

Fig.5.6 Effect of relative roughness height on heat removal factor as a function of Reynolds number

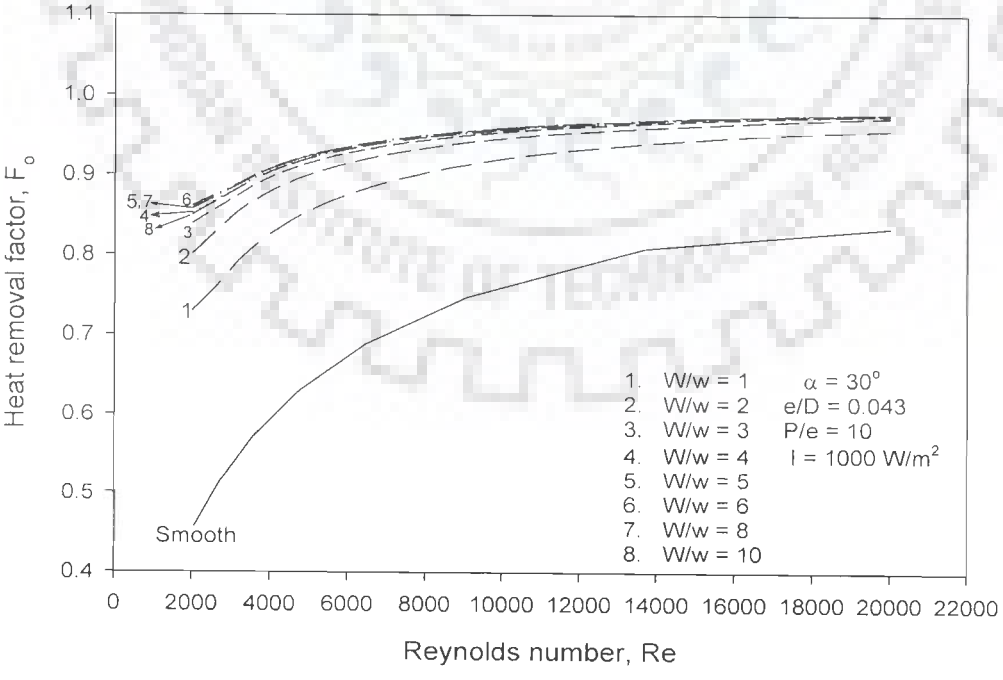

Fig.5.7 Effect of relative roughness width on heat removal factor as a function of Reynolds number

Fig.5.9 shows the variation of heat removal factor, F_o with relative roughness pitch, P/e as a function of Reynolds number and fixed values of relative roughness height, e/D, relative roughness width, W/w and angle of attack, α. The effect of relative roughness pitch on heat removal factor is similar to those of relative roughness width and angle of attack. Heat removal factor increases with increase in relative roughness pitch value and attains a maximum value corresponding to relative roughness pitch value of 8 and then decreases with further increase in the value of relative roughness pitch for the range of parameters investigated. For a fixed value of relative roughness pitch, heat removal factor increases with increase in Reynolds number.

5.4.3 Effect of Roughness Geometry and Operating Parameters on Thermal Efficiency

Thermal efficiency of collectors roughened with multiple v-ribs has been computed using correlations developed in Chapter 4. Performance plots have been prepared to illustrate the effect of roughness geometry and operating parameters on thermal efficiency as a function of Reynolds number and temperature rise parameter. Thermal efficiency of roughened collectors has also been compared with that of conventional smooth collector.

5.4.3.1 Effect of Reynolds number

Fig.5.10 shows the effect of Reynolds number on thermal efficiency, η_{Th} of collectors roughened with multiple v-ribs for given values of roughness geometry parameters. Fig.5.10 has been drawn to illustrate the variation of thermal efficiency, η_{Th} with respect to Reynolds number for relative roughness height, e/D value of 0.043, relative roughness width, W/w value of 6, angle of attack, α value of 60^0 and relative roughness pitch, P/e value of 8. Variation of thermal efficiency, η_{Ths} of smooth collector with respect to Reynolds number has also been plotted to show the enhancement in thermal efficiency due to presence of roughness geometry.

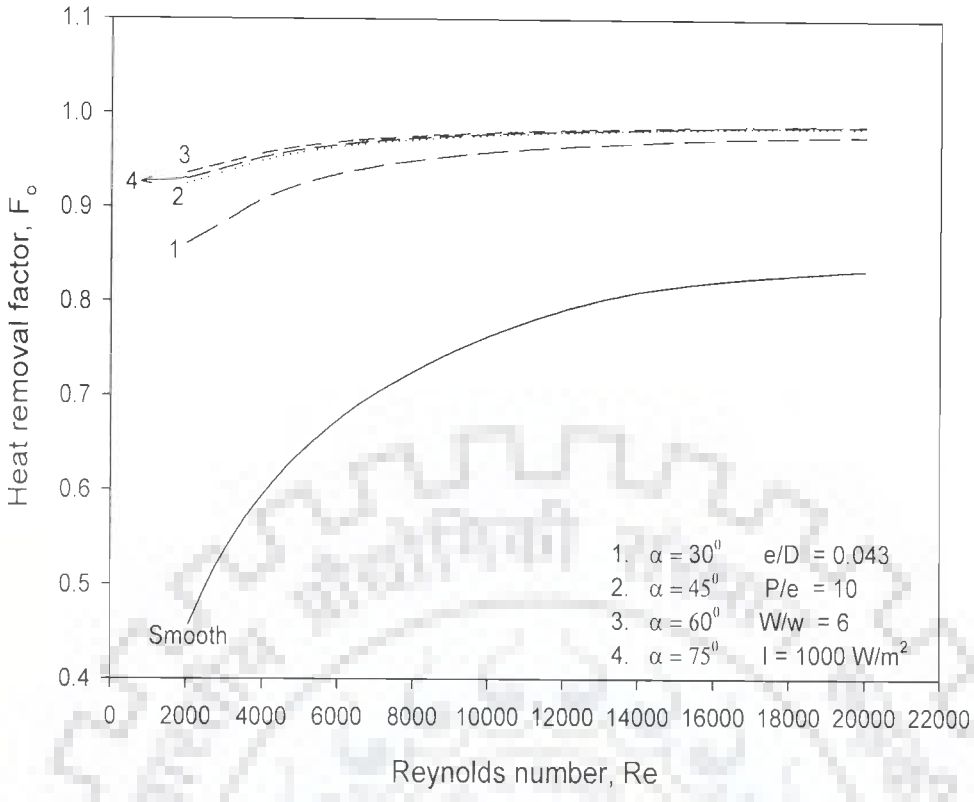

Fig.5.8 Effect of angle of attack on heat removal factor as a function of Reynolds number

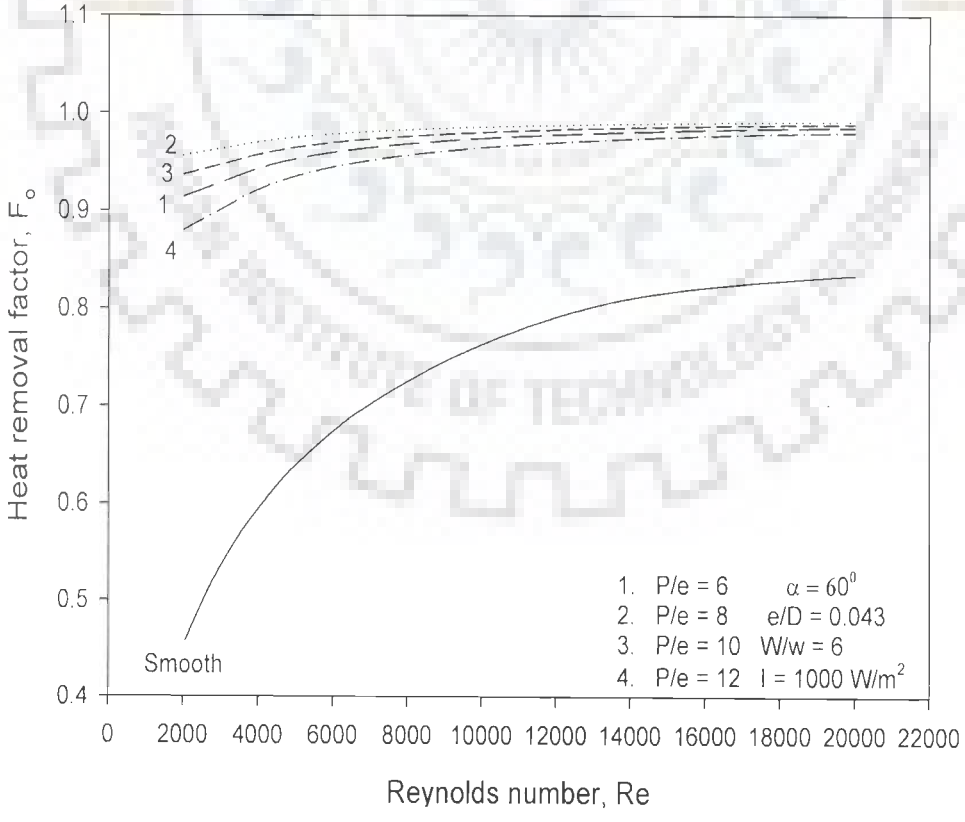

Fig.5.9 Effect of relative roughness pitch on heat removal factor as a function of Reynolds number

It has been observed from the Fig.5.10 that thermal efficiency, η_{Th} of roughened collector is higher in comparison with that of smooth collector. Thermal efficiency of roughened collector has been found to increase from 0.51 to 0.71 with an increase in Reynolds number from 2000 to 10000 and an increase in Reynolds number from 10000 to 20000 yielded increase in thermal efficiency from 0.71 to abut 0.77. For conventional collector having smooth duct, increase in thermal efficiency, η_{Th} for corresponding values of Reynolds number has been found to be 0.29 to 0.58 and 0.58 to 0.65 respectively.

5.4.3.2 Effect of relative roughness height

Fig.5.11 has been drawn to bring out the effect of relative roughness height, e/D on thermal efficiency as a function of temperature rise parameter $[(T_o - Ti)/I]$, for fixed values of other roughness geometry parameters. From this plot, an increase in the value of thermal efficiency has been observed as relative roughness height value increases. A maximum value of 0.76 of thermal efficiency has been obtained corresponding to relative roughness height value of 0.043, relative roughness width value of 6, angle of attack value of 30^o, relative roughness pitch, value of 10 and temperature rise parameter value of 0.0045.

It has been observed that for a fixed value of relative roughness height, e/D, thermal efficiency decreases with increase in temperature rise parameter and thermal efficiency of roughened collector is higher in comparison to that of conventional collector having smooth duct for the entire range of parameters investigated.

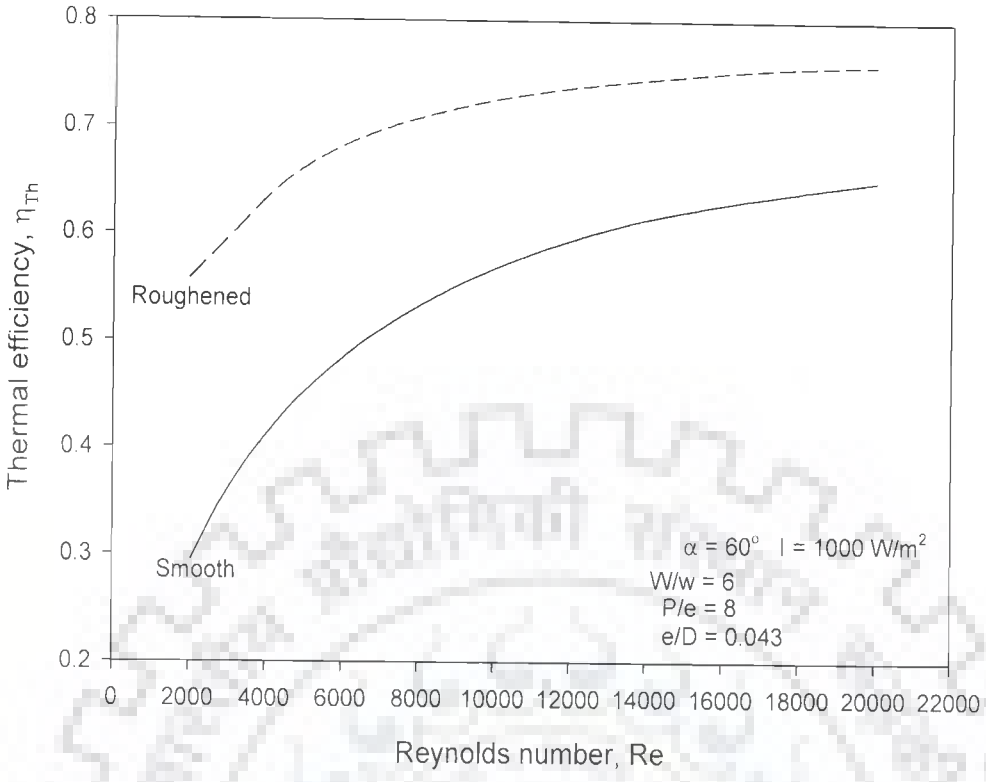

Fig.5.10 Variation of thermal efficiency as a function of Reynolds number

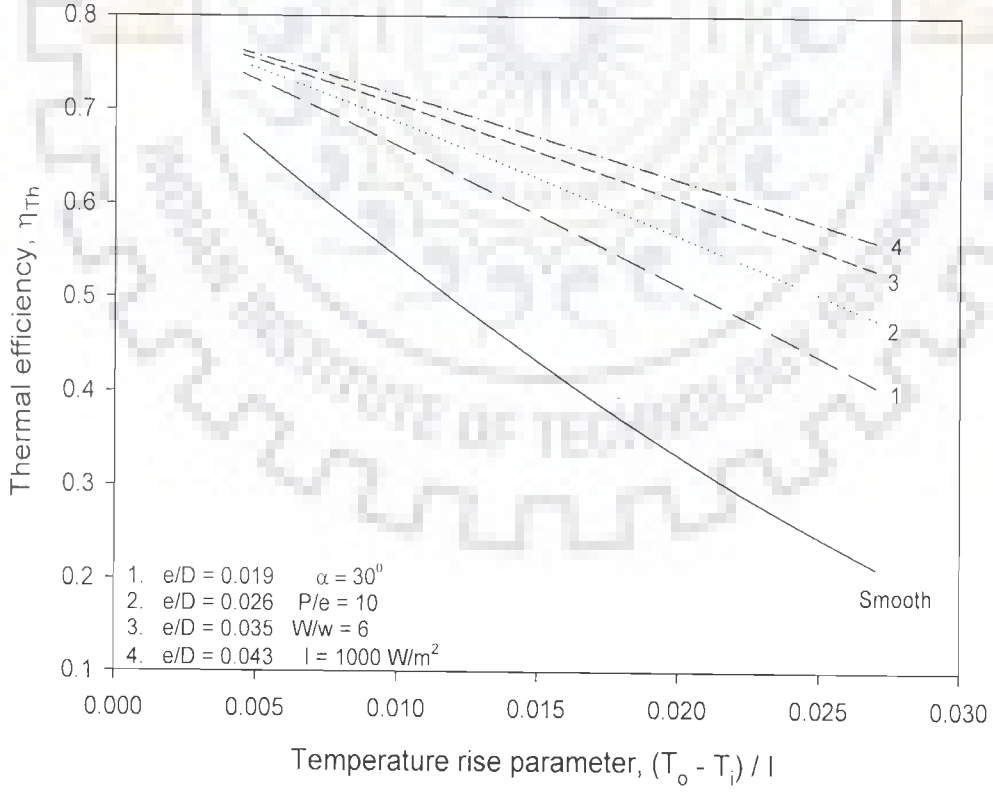

Fig.5.11 Effect of relative roughness height on thermal efficiency as a function of temperature rise parameter

5.4.3.3 Effect of relative roughness width

The effect of relative roughness width, W/w on thermal efficiency, η_{Th} has been shown in Fig.5.12 as a function of temperature rise parameter for fixed values of relative roughness height, e/D, angle of attack, α and relative roughness pitch, P/e. In order to determine the enhancement of thermal performance, thermal efficiency of roughened and conventional smooth collectors has been compared.

It has been observed that thermal efficiency increases with increase in relative roughness width value and attains a maxima corresponding to relative roughness width value of 6 and further increase in relative roughness width brings a decrease in the value of thermal efficiency. For a given value of relative roughness width, thermal efficiency decreases with increase in temperature rise parameter.

5.4.3.4 Effect of angle of attack

The variation of thermal efficiency, η_{Th} as a function of temperature rise parameter for different values of angles of attack has been plotted in Fig.5.13 for fixed values of other roughness geometry parameters. The thermal efficiency of roughened collector has also been compared with that of conventional smooth collector in order to determine the enhancement obtained as result of roughness geometry. The thermal efficiency value increase with increase in value of angle of attack and attains a maxima corresponding to angle of attack value of 60° and with further increase in the value of angle of attack, thermal efficiency decreases. For a given value of angle of attack, thermal efficiency decreases with increase in temperature rise parameter.

5.4.3.5 Effect of relative roughness pitch

Fig.5.14 demonstrates the variation of thermal efficiency, η_{Th} as a function of temperature rise parameter for different values of relative roughness pitch, P/e and fixed values of other roughness geometry parameters.

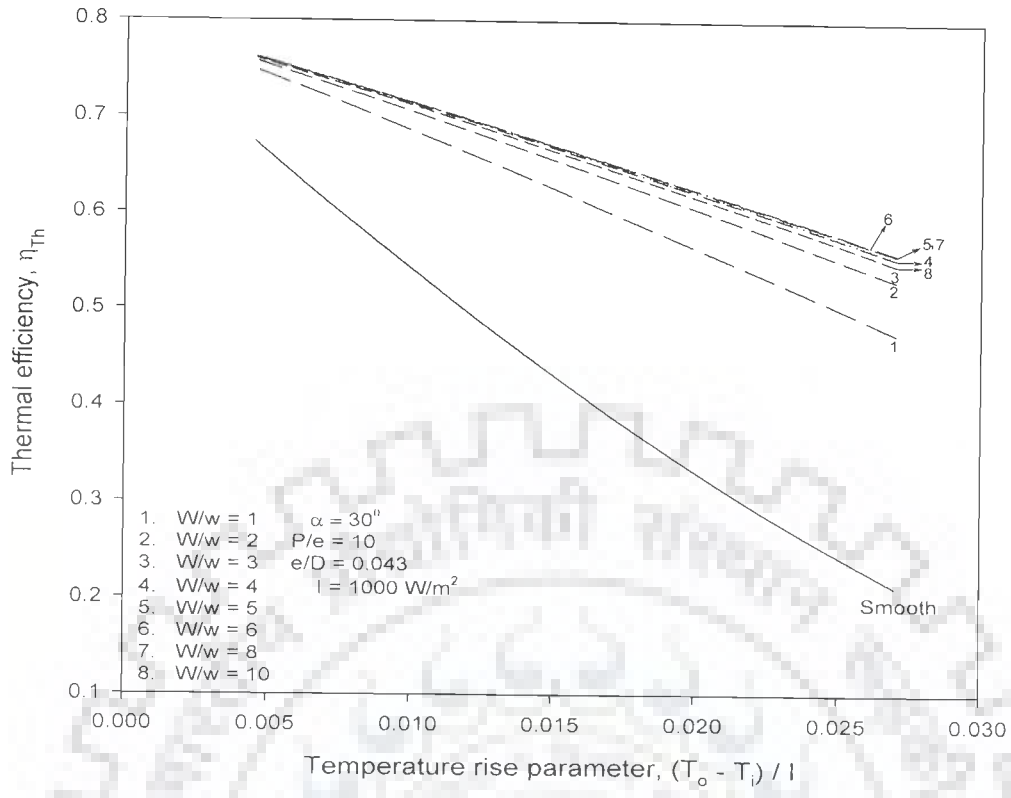

Fig.5.12 Effect of relative roughness width on thermal efficiency as a function of temperature rise parameter

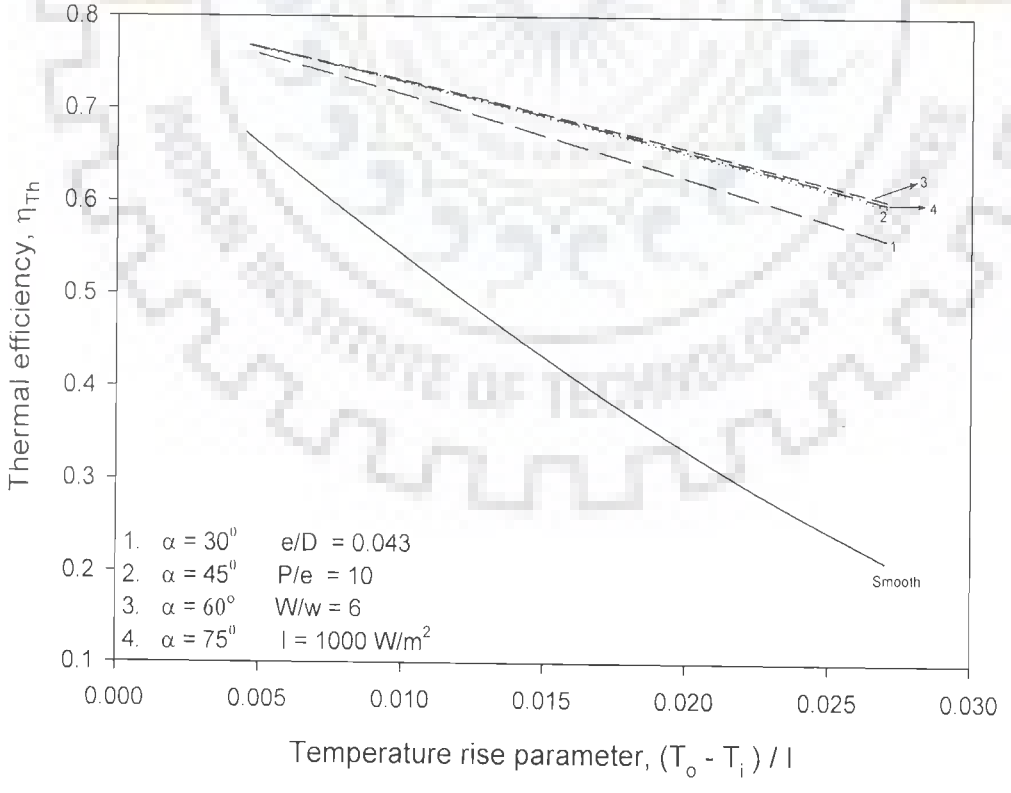

Fig.5.13 Effect of angle of attack on thermal efficiency as a function of temperature rise parameter

The effect of relative roughness pitch, P/e on thermal efficiency has been found to be similar in nature as those of relative roughness width and angle of attack. Thermal efficiency, increases with increase in value of relative roughness pitch, P/e and attains a maxima corresponding to relative roughness pitch value of 8 and further increase in relative roughness pitch value brings a decrease in the value of thermal efficiency. Thermal efficiency decreases with increase in temperature rise parameter for a given value of relative roughness pitch value.

5.4.4 Enhancement of Thermal Efficiency

Figs.5.11 to 5.14 represent the performance curves of collectors roughened with multiple v-ribs along with those of conventional smooth collectors. These plots reveal that thermal efficiency of roughened as well as smooth collectors increases with increase in Reynolds number and decrease in temperature rise parameter. Comparison of results of roughened collectors with that of conventional smooth collector, show that a considerable enhancement in thermal efficiency occurs as a result of use of artificial roughness in collectors. Enhancement in thermal efficiency has been represented in terms of enhancement factor, EF that is defined as the ratio of thermal efficiency of roughened collector to that of conventional smooth collector for the same operating conditions.

$$EF = \eta_{Th} / \eta_{Ths} \qquad (5.16)$$

The values of enhancement factor, EF as a function of temperature rise parameters for various roughness geometry parameters have been presented in Figs. 5.15 to 5.18. Fig.5.15 depicts the effect of relative roughness height, e/D on enhancement factor, EF for fixed relative roughness width value of 6, angle of attack value of 30°, relative roughness pitch value of 10 and insolation value of 1000 W/m^2.

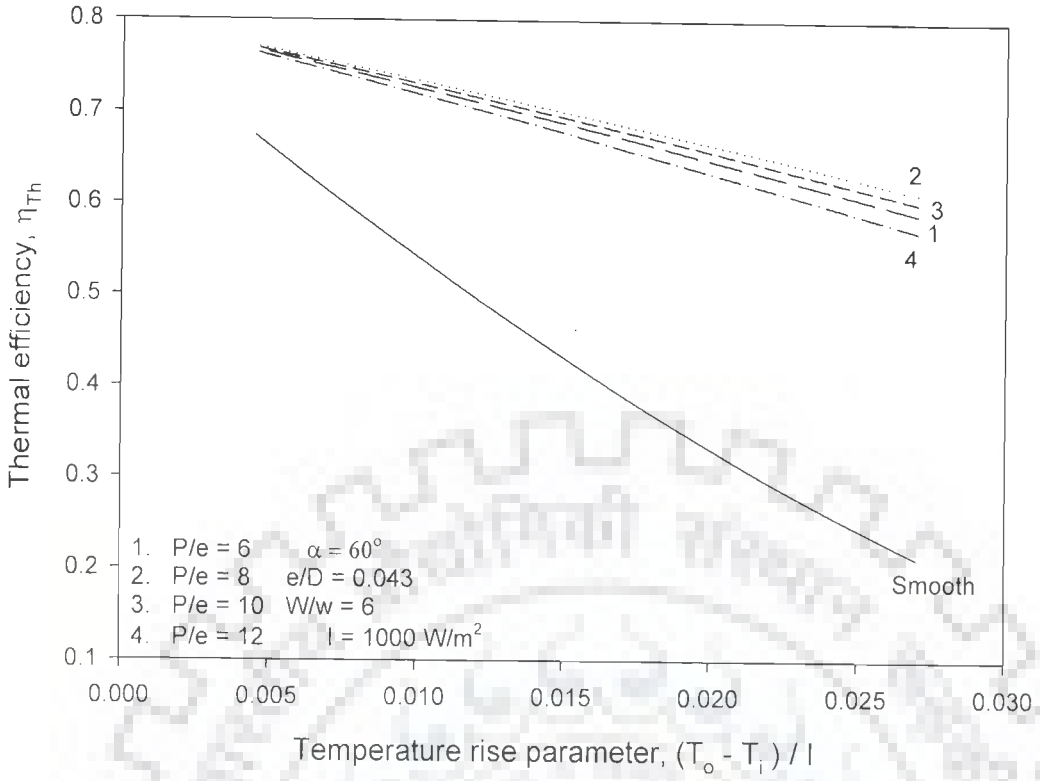

Fig.5.14 Effect of relative roughness pitch on thermal efficiency as a function of temperature rise parameter

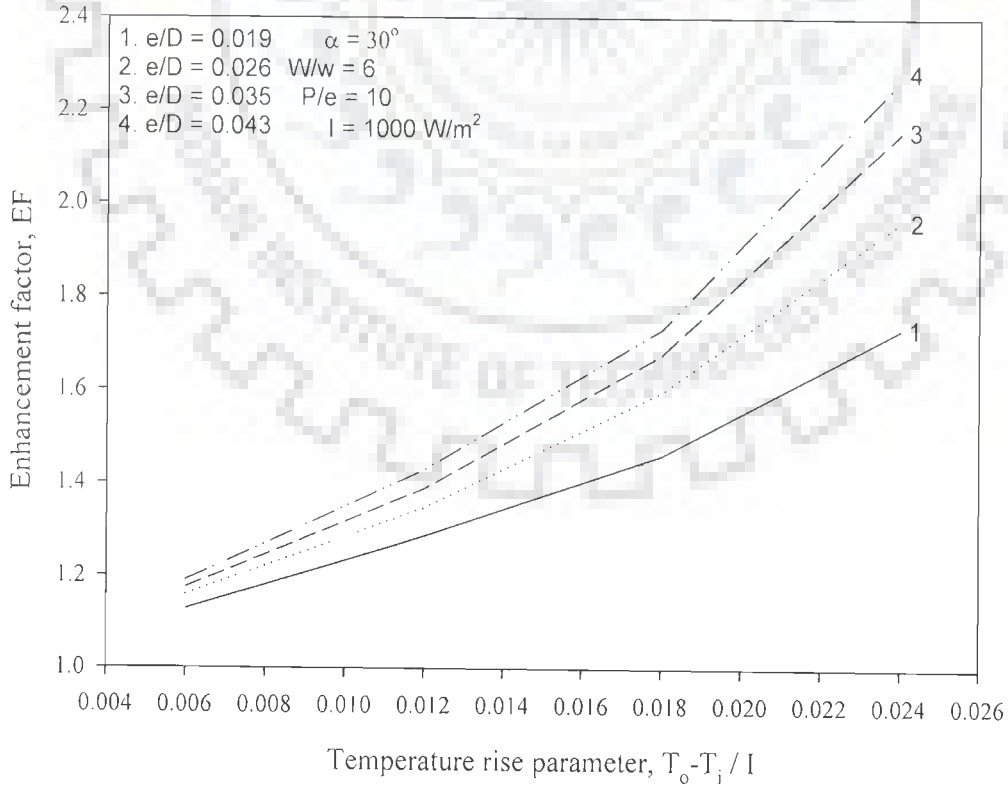

Fig.5.15 Effect of relative roughness height on enhancement factor as a function of temperature rise parameter

It has been observed that collector with relative roughness height value of 0.043 performs better and maximum value of 2.2692 of enhancement factor, EF has been obtained for the highest value of temperature rise parameter considered. The thermal efficiency of roughened collector has been observed to be about 19% higher than that of conventional smooth collector for temperature rise parameter value of 0.006 $(K\text{-}m^2)/W$ and for temperature rise parameter value of 0.024 $(K\text{-}m^2)/W$, it is about 127%. Table 5.2 presents the values of enhancement factor for different values of relative roughness height as a function of temperature rise parameter.

Table 5.2 Enhancement factor, EF, as a function of relative roughness height, e/D

Temperature rise parameter, $(K\text{-}m^2)/W$	Enhancement factor, EF, for relative roughness height, e/D			
	0.019	**0.026**	**0.035**	**0.043**
0.006	1.1269	1.1587	1.1746	1.1904
0.012	1.2857	1.3469	1.3877	1.4285
0.018	1.4594	1.5945	1.6756	1.7297
0.024	1.7307	1.9615	2.1538	2.2692

It has been observed from Fig.5.16 that the enhancement factor, EF of a roughened collector attains highest value for the relative roughness width value of 6 while the lowest value of enhancement factor is obtained corresponding to relative roughness width value of 1. Table 5.3 presents the values of enhancement factor for different values of relative roughness width as a function of temperature rise parameter.

The effect of angle of attack, α on the enhancement factor, EF of a roughened collector has been presented in Fig.5.17 for fixed values of other roughness geometry parameters and insolation. The highest value of enhancement factor has been obtained for angle of attack value of 60° while angle of attack value of 30° yields the least performance.

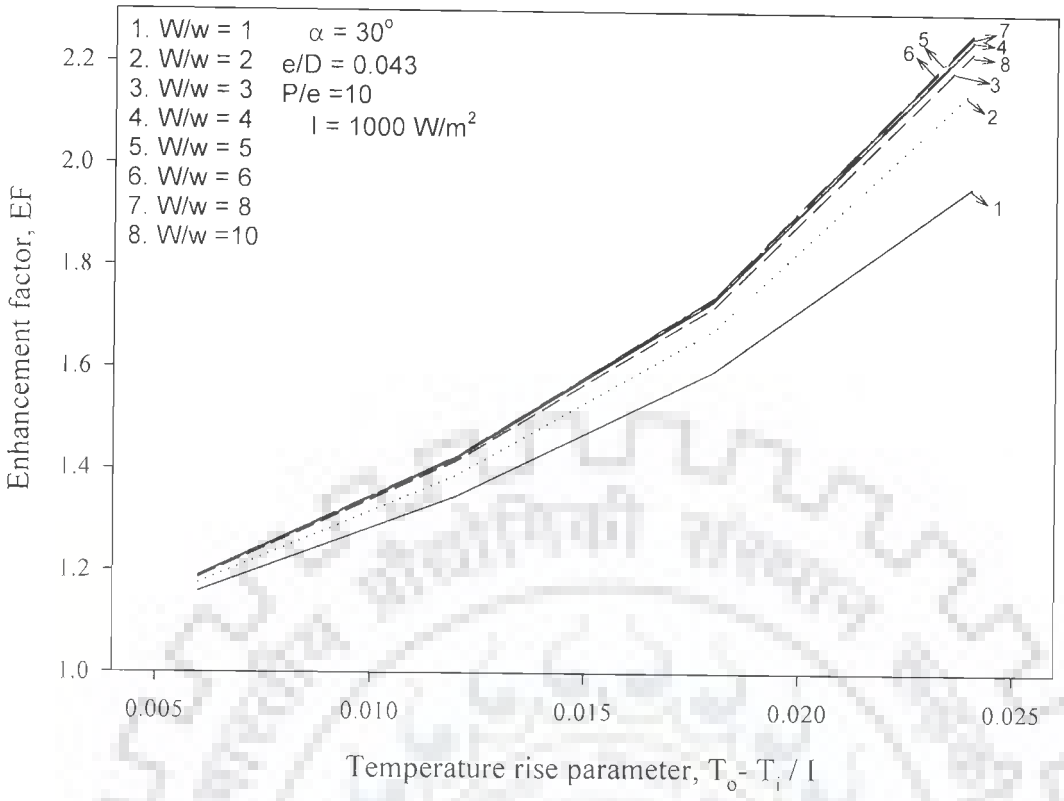

Fig.5.16 Effect of relative roughness width on enhancement factor as a function of temperature rise parameter

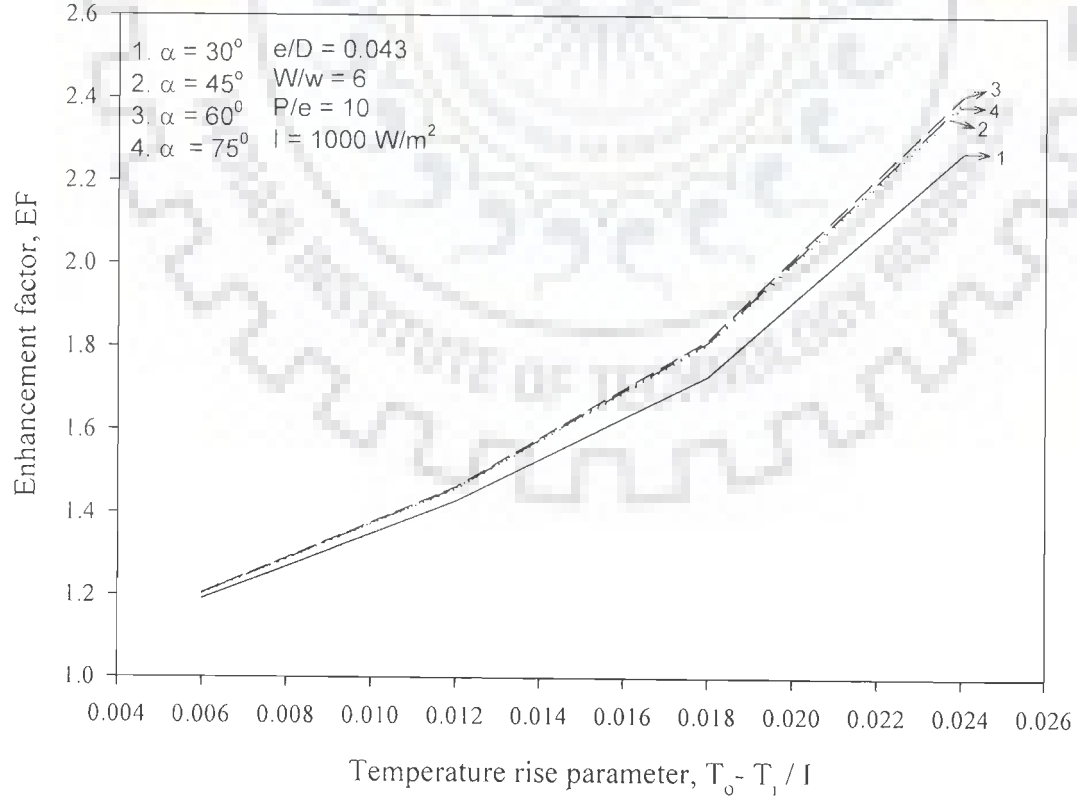

Fig.5.17 Effect of angle of attack on enhancement factor as a function of temperature rise parameter

Table 5.3 Enhancement factor, EF as a function of relative roughness width, W/w

Temperature rise parameter, $(K\text{-}m^2)/W$	Enhancement factor, EF for relative roughness width, W/w							
	1	2	3	4	5	6	8	10
0.006	1.1587	1.1746	1.1863	1.1887	1.1897	1.1901	1.1896	1.1885
0.012	1.3469	1.3877	1.4161	1.4220	1.4245	1.4253	1.4242	1.4214
0.018	1.5945	1.6756	1.7212	1.7336	1.7388	1.7404	1.7382	1.7324
0.024	1.9615	2.1538	2.2260	2.2495	2.2594	2.2625	2.2583	2.2472

Table 5.4 presents the values of enhancement factor for different values of angle of attack as a function of temperature rise parameter.

Table 5.4 Enhancement factor, EF as a function of angle of attack, α

Temperature rise parameter, $(K\text{-}m^2)/W$	Enhancement factor, EF for angle of attack, α			
	30°	45°	60°	75°
0.006	1.1904	1.2027	1.2050	1.2037
0.012	1.4285	1.4565	1.4623	1.4590
0.018	1.7297	1.8067	1.8178	1.8116
0.024	2.2692	2.3857	2.4081	2.3956

Fig.5.18 depicts the effect of relative roughness pitch, P/e on the enhancement factor, EF and it has been observed that the best and the least performances have been observed corresponding to relative roughness pitch values of 8 and 12 respectively. Table 5.5 presents the values of enhancement factor for different values of relative roughness pitch as a function of temperature rise parameter.

Table 5.5 Enhancement factor, EF as a function of relative roughness pitch, P/e

Temperature rise parameter, (K-m^2)/ W	Enhancement factor, EF for relative roughness pitch, P/e			
	6	8	10	12
0.006	1.2007	1.2087	1.2050	1.1941
0.012	1.4516	1.4716	1.4623	1.4352
0.018	1.7949	1.8360	1.8178	1.7612
0.024	2.3664	2.4470	2.4081	2.3021

5.4.5 Effect of Intensity of Radiation on Enhancement Factor

The effect of intensity of radiations on the enhancement factor as a function of temperature rise parameter has been shown in Fig.5.19 for a given set of roughness geometry parameters. It has been observed from Fig.5.19 that enhancement factor increases with increase in intensity of radiation and the maximum and the minimum values of enhancement factor corresponds to intensity of radiation values of 1000 W/m^2 and 500 W/m^2 respectively. For a given value of intensity of radiation, enhancement factor increases with increase in temperature rise parameter value.

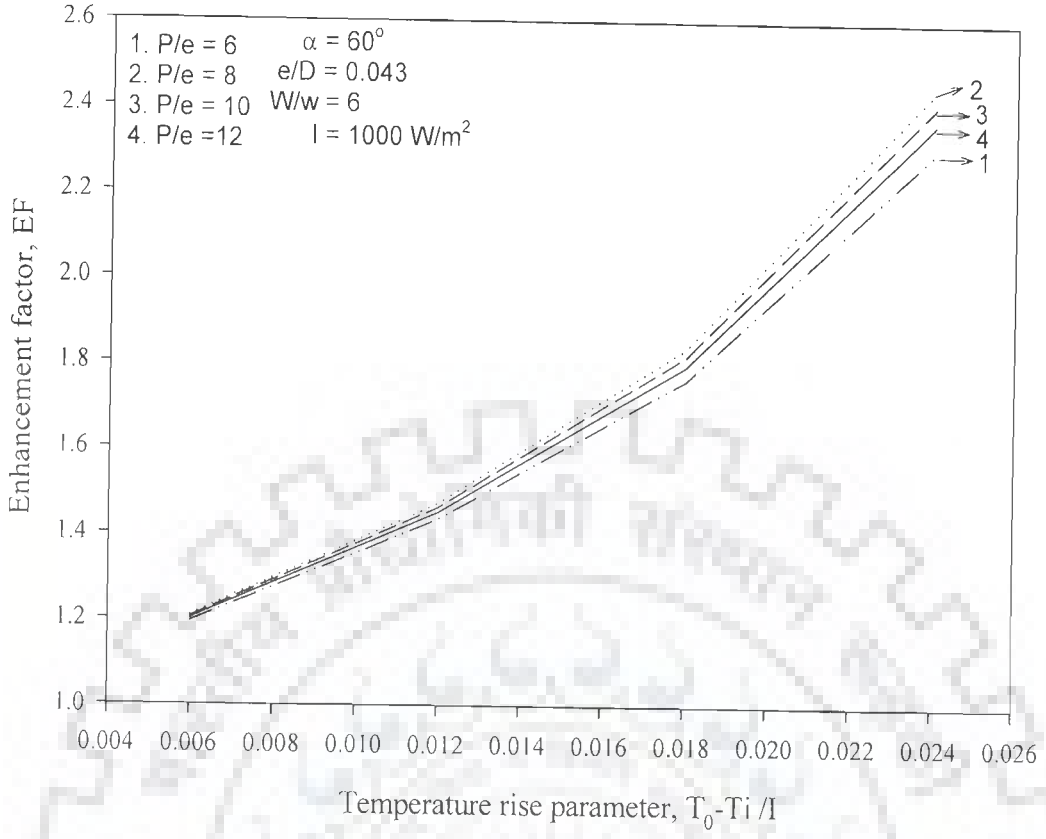

Fig.5.18 Effect of relative roughness pitch on enhancement factor as a function of temperature rise parameter

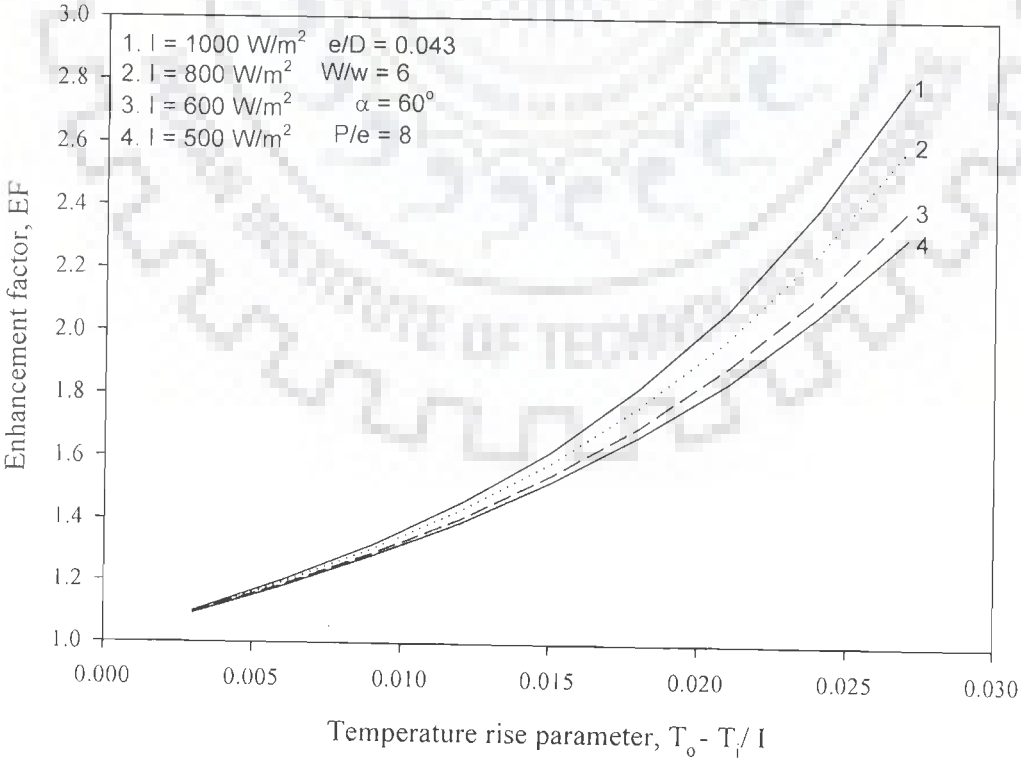

Fig.5.19 Effect of intensity of radiation on enhancement factor

CHAPTER-6

THERMOHYDRAULIC PERFORMANCE OF SOLAR AIR HEATER

6.1 INTRODUCTION

As discussed earlier, thermal performance of a solar air heater having roughened absorber plate has been found to be better in comparison to that of a solar air heater having smooth absorber plate. The use of artificial roughness on the underside of the absorber plate creates turbulence resulting in enhancement of heat transfer between the absorber plate and air. However, inclusion of roughness elements increases the friction, which in turn, increases the pumping power requirements to propel air through the solar air heater duct. Both, the heat transfer coefficient and friction factor have been found to be strong functions of roughness geometry and flow parameters. It, therefore, becomes imperative to determine the values of roughness geometry parameters that result in maximization of heat transfer with minimum increase in friction factor. The selection of optimal values of roughness geometry parameters involves comparison of enhancement of thermal performance and frictional losses of a roughened collector system with that of a smooth collector system. A number of investigators such as Lewis [137], Cortes and Piacentini [139] and Altfeld et al. [147] have worked in the area of optimization of such systems. It has been proposed that comparison of the performance can be made on the basis of thermal and thermohydraulic performance.

In this chapter, thermal and thermohydraulic performance of a solar air heater, having absorber plate roughened with multiple v-ribs, have been discussed in order to determine the values of roughness geometry and flow parameters that yield the optimum performance. The concept, method of predicting thermohydraulic performance and the results of optimization based on the best thermohydraulic

performance of roughened solar air heaters have been presented and discussed in this chapter.

6.2 OPTIMIZATION CRITERIA

The use of artificial roughness in solar air heaters improves the thermal performance considerably by breaking the laminar sub layer formed on the absorber plate. However, this improvement in thermal performance is accompanied by increased frictional losses resulting in an increase in pumping power requirement to overcome the friction. Therefore, it becomes necessary to evaluate the effectiveness of roughness geometry in order to obtain maximum possible enhancement of heat transfer while keeping the hydraulic (pumping) losses to the minimum. This will help in designing a compact and efficient solar air heater.

The following three criteria have been proposed for optimization of roughness geometry parameters of a roughened solar air heater.

(i) Thermal efficiency, η_{th}

(ii) Effective efficiency, η_{eff}

(iii) Exergetic efficiency, η_{exg}

All the above mentioned optimization criteria are explained in brief.

6.2.1 Thermal Efficiency

The thermal performance of a solar air heater is evaluated in terms of thermal efficiency and as per the recommendations of ASHRAE [151], the instantaneous thermal efficiency is defined as the ratio of rate of useful thermal energy gain to the rate of incident solar energy. It is expressed as:

$$\eta_{th} = \frac{Q_u}{A_p I} \qquad (6.1)$$

6.2.2 Effective Efficiency

Cortes and Piacentini [139] have suggested that the pumping power (P_m) cannot be simply subtracted from the thermal output (Q_u) of the collectors while determining the net gain when both useful collector gain (Q_u) and pumping power (P_m) get enhanced by using artificial roughness. It is due to the fact that the pumping power (P_m) is produced by conversion of thermal energy to work and then to electrical energy in a power plant and then transmitted, losing a considerable part of the energy in conversion and transmission. In order to evaluate the real performance of the collector, the following expression for effective efficiency has been used in the present analysis based on the net thermal energy gain obtained by subtracting the equivalent thermal energy required to overcome the friction, from the collector useful heat gain as proposed by Cortes and Piacentini [139]. The effective efficiency is expressed as follows:

$$\eta_{eff} = \frac{Q_u - \frac{P_m}{C}}{IA_p} \qquad (6.2)$$

where, 'C' (= $\eta_f \eta_m \eta_{tr} \eta_{th}$) is the conversion factor accounting for net conversion efficiency from primary thermal energy to mechanical energy of pumping power.

η_f : efficiency of the fan,

η_m : efficiency of the electric motor,

η_{tr} : efficiency of electrical transmission from the power plant, and

η_{th} : efficiency of thermal conversion of the power plant.

The value of 'C' as recommended by Cortes and Piacentini [139] is 0.18 (typical values of efficiency factors being: $\eta_F = 0.65$, $\eta_m = 0.88$, $\eta_{tr} = 0.925$ and $\eta_{th} = 0.344$).

6.2.3 Exergetic Efficiency

Altfeld et al. [147] proposed a method based on the second law of thermodynamics to determine the optimum values of roughness geometry parameters. All energy flows are evaluated in terms of exergy. Exergetic efficiency, defined as a ratio of net exergy flow to exergy flow associated with solar irradiation on collector surface, can be expressed as:

$$\eta_{exg} = \frac{E_n}{E_s} \tag{6.3}$$

where E_n is net exergy flow rate and is expressed as:

$$E_n = IA_p\eta_{th}\eta_c - P_m(1-\eta_c)$$

I is the global irradiation (W/m^2)

P_m is pumping power

η_c is the Carnot efficiency $[= (1 - T_a/T_f)]$

E_s is the exergy associated with solar irradiation on collector surface and is given as:

$$E_s = I\left(1 - \frac{T_a}{T_{sun}}\right)$$

T_{sun} is the equivalent temperature of the Sun as a blackbody ($\approx$ 5762 K)

6.3 SYSTEM AND OPERATING PARAMETRS

In order to investigate the performance of an artificially roughened solar air heater and subsequently to evaluate the values of roughness geometry parameters which yield the optimum thermohydraulic performance for a given set of system and operating parameters, it is necessary to fix the appropriate values or the range of values of system and operating parameters.

The system parameters include the values of collector dimensions; namely collector length, L, collector width, W, duct depth, H, number of glass covers, N, spacing between glass covers, thermal and radiation properties of the components and roughness geometry parameters namely; relative roughness height, e/D, relative roughness width, W/w, angle of attack, α and relative roughness pitch, P/e.

The operating parameters include ambient air inlet temperature, T_a, thermo physical properties of air (μ, Cp, k, ρ), wind velocity, V_w, temperature rise parameter $(T_o - T_i)/ I$ or $(\Delta T/I)$ and solar radiation intensity, I.

The range of design parameters representing roughness geometry has been selected on the basis of experimental results, the temperature rise parameter decided on the basis of range of application of solar air heater and insolation as the average value at a given location for a period of application. The list of values of system and operating parameters are given in Table 6.1.

The thermo physical properties are determined from the readily available as;

$$\mu = 1.81 \times 10^{-5} \left(\frac{T_f}{293} \right)^{0.735} \quad \text{N-s/m}^2$$

$$C_p = 1006 \left(\frac{T_f}{293} \right)^{0.0155} \quad \text{J/kg-K}$$

$$K = 0.0275 \left(\frac{T_f}{293} \right)^{0.086} \quad \text{W/m-K}$$

$$\rho = \frac{P_{atm}}{R \; T_f} \quad \text{kg/m}^3$$

Table 6.1 System and operating parameters.

		Description	Parameter	Value/range
System parameters	Fixed	Collector length, m	L	1
		Collector width, m	W	0.3
		Duct depth, m	H	0.025
		Number of glass covers	N	1
		Thermal conductivity of insulation, W/m K	K_i	0.037
		Thickness of insulation, m	t_i	0.05
		Transmittance–absorptance product	$(\tau\alpha)$	0.8
		Emissivity of the absorber plate	ε_P	0.9
		Emissivity of the glass cover	ε_g	0.88
		Thickness of glass cover, m	t_g	0.002
		Air gap between absorber plate and glass cover, m	L_g	0.025
		Thickness of collector edge, m	t_e	0.016
	Variable	Relative roughness pitch	P/e	6-12
		Relative roughness width	W/w	1-10
		Angle of attack, degree	α	30 - 75
		Relative roughness height	e/D	0.019-0.043
Operating parameters	Fixed	Ambient temperature, K	T_a	300
		Wind velocity, m/s	V_w	1.0
	Variable	Temperature rise parameter, $K\text{-}m^2/W$	$\Delta T/I$	0.003-0.027
		Solar radiation intensity, W/m^2	I	500-1000

6.4 PROCEDURE FOR PREDICTION OF PERFORMANCE

The performance of a solar air heater can be predicted on the basis of detailed consideration of heat transfer and fluid flow processes in the system. The performance parameters, namely overall heat loss coefficient, heat removal factor and other relevant factors and subsequently thermal, thermohydraulic and exergetic efficiency can be evaluated. For this purpose a step-by-step procedure has to be followed. The salient features of the procedure are discussed below.

One of the objectives of this work is to present a methodology for optimal design of a solar air heater. Results need to be presented in terms of two basic collector operating parameters namely;

- Temperature rise parameter, $\Delta T/I$ (ratio of air temperature rise across the duct, (To −Ti) to the average intensity of insolation)
- Insolation, I

The calculation proceeds as follows:

(i). Area of the plate is calculated as;

$$A_p = W \times L$$

where W and L are the width and the length of the collector, respectively

(ii). Hydraulic diameter of the duct is calculated as;

$$D = \frac{2\,WH}{(W+H)}$$

where, H is the duct depth

(iii). Fixed system parameters such as;

Thickness of insulation, t_i

Thermal conductivity of insulation, k_i

Transmittance–absorptance product, $\tau\alpha$

Emissivity of absorber plate, ε_p

Emissivity of glass cover, ε_g

Fixed operating parameters such as;

Atmospheric air velocity of air, V_w and atmospheric temperature, T_a are selected.

(iv). A set of system roughness parameters such as relative roughness pitch, P/e, relative roughness width, W/w, angle of attack, α and relative roughness height, e/D is selected.

(v). A set of values of design parameters namely temperature rise parameter, ($\Delta T/I$) and insolation, I is selected.

(vi). The temperature rise of air across the duct and the outlet temperature are calculated as;

$$\Delta T = \frac{\Delta T}{I} I$$

$$T_o = T_i + \Delta T$$

(vii). Approximate initial mean plate temperature is assumed as;

$$T_p = \frac{T_o + T_i}{2} + 10^\circ C$$

(viii). Using the value of mean plate temperature, T_p, the value of the top loss coefficient, U_t, is computed using the equation given by Akhtar and Mullick et al. [26];

$$U_t^{-1} = \left[\frac{\sigma\left(T_p^2 + T_g^2\right)\left(T_p + T_g\right)}{\left(\frac{1}{\varepsilon_p} + \frac{1}{\varepsilon_g} - 1\right)} + \left(\frac{k_a Nu}{L_g}\right) \right]^{-1} + \left[\sigma\varepsilon_g\left(T_g^2 + T_a^2\right)\left(T_g + T_a\right) + h_w\right]^{-1} + \frac{t_g}{k_g}$$

where

$$T_g = \left(\frac{F_1 T_p + c T_a}{1 + F_1} \right)$$

where $$F_1 = \frac{\left[12x10^{-8} \left(T_a + 0.2T_p \right)^3 + h_w \right]^{-1} + 0.3t_g}{\left[6x10^{-8} \left(\varepsilon_p + 0.028 \right) \left(T_p + 0.5T_a \right)^3 + 0.6L_g^{-0.2} \left\{ \left(T_p - T_a \right) \cos\beta \right\}^{0.25} \right]^{-1}}$$

and $$c = \left(\frac{(T_S / T_a) + (h_w / 3.5)}{(1 + (h_w / 3.5)} \right)$$

$$T_s = 0.0522 \left(T_a \right)^{1.5}$$

$$Nu = 1 + 1.44 \left[1 - 1708 / Ra \cos\beta \right]^{+} \left\{ 1 - 1708 \left(\sin 1.8\beta \right)^{1.6} / Ra \cos\beta \right\} + \left[\left(Ra \cos\beta / 5830 \right)^{0.33} - 1 \right]^{+}$$

$$Ra = Gr \times Pr$$

$$Gr = \frac{g\beta' \left(T_p - T_g \right) L_g^3}{\nu^2}$$

$$\beta' = \frac{1}{\left[\left(T_o + T_i \right) / 2 \right]}$$

$$P_r = \frac{\mu C_p}{k_a}$$

Back loss coefficient, U_b is expressed as; $U_b = ki/t_i$

The edge loss coefficient, based on the collector area A_p is given as;

$$U_e = \frac{(L+W) t_e k_i}{L W t_i}$$

$$U_L = U_t + U_b + U_e$$

(ix). Useful energy gain rate is calculated as;

$$Q_{ul} = [I(\tau\alpha) - U_L \left(T_p - T_a \right)] A_p$$

(x). Mass flow rate is determined from;

$$m = \frac{Q_{u1}}{C_p \Delta T}$$

(xi). Reynolds number of flow of air in the duct is computed as;

$Re = G D/\mu$

where G is the mass velocity of air through the collector

$G = m / WH$

(xii). The Nusselt number is calculated using the correlation developed in chapter 4 and reproduced below;

$$Nu = 3.35\times10^{-5}\, Re^{0.92} \left(\frac{e}{D}\right)^{0.77} \left(\frac{W}{w}\right)^{0.43} \left(\frac{\alpha}{90}\right)^{-0.49} \exp[-0.1177\,(ln(W/w))^2]$$
$$\times \exp[-0.61\,(ln(\alpha/90))^2] \left(\frac{P}{e}\right)^{8.54} \exp[-2.0407\,(ln(P/e))^2]$$

Convective heat transfer coefficient is computed as;

$$h = \frac{Nu\, k}{D}$$

(xiii). The plate efficiency factor is then computed as;

$$F' = \frac{h}{h + U_L}$$

(xiv). The heat removal factor based on outlet temperature, F_o is calculated as;

$$F_o = \frac{mC_p}{A_p U_L}\left[\exp\left\{\frac{F' U_L A_p}{\dot{m} C_p}\right\} - 1\right]$$

(xv). New value of useful heat gain is calculated as;

$$Q_{u2} = A_p F_o \left[I(\tau\alpha) - U_L (T_o - T_i)\right]$$

(xvi). The values of Q_{u1} and Q_{u2} are compared; if the difference is found to be more than 0.1 % of Q_{u1}, then the new value of mean plate temperature is calculated as;

$$T_p = T_a + [(I(\tau\alpha) - Q_{u2}/A_p)/U_L]$$

Using this new value of plate temperature, steps from 8 to 16 are repeated till the difference between Q_{u1} and Q_{u2} lies within the target value. Consequently

$$Q_u = Q_{u1} = Q_{u2}$$

(xvii). The friction factor value is calculated from the correlation developed in Chapter 4 and reproduced below;

$$f = 4.47\times10^{-4}\,\mathrm{Re}^{-0.318}\left(\frac{e}{D}\right)^{0.73}\left(\frac{W}{w}\right)^{0.22}\left(\frac{\alpha}{90}\right)^{-0.39}\exp\left(-0.52(\ln(\alpha/90))^2\right)\left(\frac{P}{e}\right)^{8.9}$$
$$\times\exp\left(-2.133\,(ln(P/e))^2\right)$$

(xviii). Using this value of friction factor, pressure drop across the duct is calculated as;

$$(\Delta P)_d = \frac{4fL\rho_a V^2}{2D}$$

and the mechanical power required to drive the air through collector is calculated as;

$$P_m = \frac{m(\Delta P)_d}{\rho}$$

(xix). The thermal efficiency is calculated as;

$$\eta_{Th} = F_o\left[(\tau\alpha) - \frac{U_L(T_o - T_i)}{I}\right]$$

(xx). The effective efficiency is calculated as;

$$\eta_{eff} = \frac{Q_u - \frac{P_m}{C}}{IA_p}$$

(xxi). Logarithmic mean fluid temperature is calculated as;

$$T_m = \frac{(T_o - T_i)}{Ln\left(\frac{T_o}{T_i}\right)}$$

(xxii). Carnot efficiency based on logarithmic mean air temperature is calculated as;

$$\eta_c = 1 - \left(\frac{T_a}{T_m}\right)$$

(xxiii). The net exergy flow to the air is calculated as;

$$E_n = IA_p\eta_{th}\eta_c - P_m(1-\eta_c)$$

(xxiv). Exergy input is calculated as;

$$E_s = I\left(1 - \frac{T_a}{T_{sun}}\right)$$

(xv). Exergetic efficiency is calculated as;

$$\eta_{exg} = \frac{E_n}{E_s}$$

(xvi). Next set of values of temperature rise parameter and insolation is selected and steps from 5 to 25 are repeated to cover the entire range of temperature rise parameter and insolation.

(xvii). Next set of roughness geometry parameters such as relative roughness height, e/D, relative roughness width, W/w, angle of attack, α and relative roughness pitch, P/e is selected and the steps from 4 to 26 are repeated.

A computer program has been developed in C^{++} language for this purpose and the flow diagram for the program is shown in Fig.6.1.

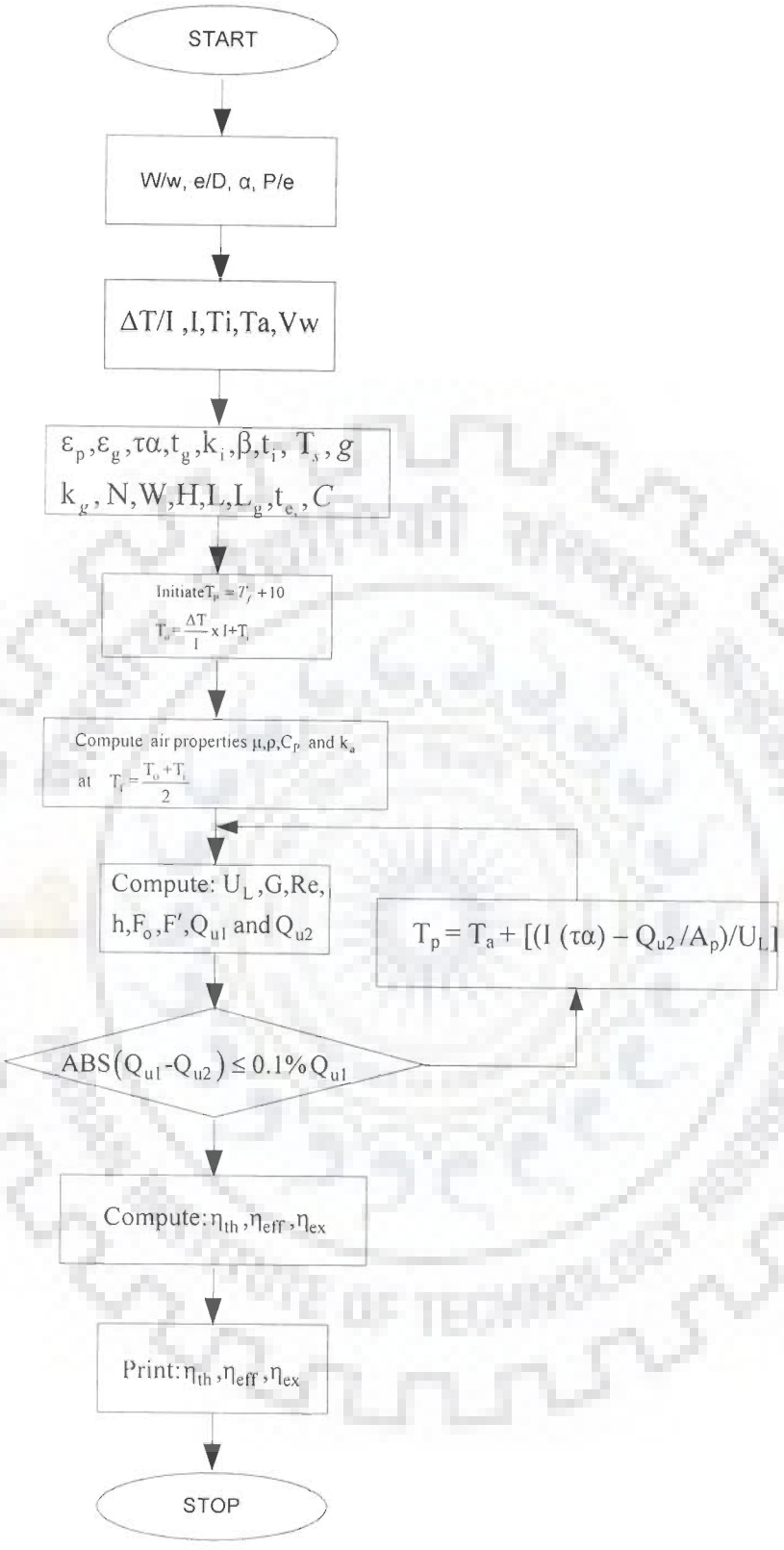

Fig.6.1 Flow diagram of computer program

6.5 RESULTS AND DISCUSSION

As per the calculation procedure described in Section 6.4, thermal, effective and exergetic efficiencies have been calculated as a function of temperature rise parameter and intensity of solar radiation.

6.5.1 Thermal Efficiency

The plots of variation of thermal efficiency, as a function of operating parameters for different roughness geometry parameters such as relative roughness height, relative roughness width, angle of attack and relative roughness pitch, have been presented and discussed in detail in Chapter 5. Enhancement in the values of thermal efficiency as result of using artificial roughness has also been determined.

In order to obtain the optimum values of roughness geometry parameters on the basis of thermal efficiency, values of thermal efficiency have been calculated as per the procedure described in Section 6.4 for different combination of roughness geometry parameters for the range given in Table 6.1. For a given set of values of temperature rise parameter, $\Delta T/I$ and solar radiation intensity, I, thermal efficiency values were calculated for a set of roughness geometry parameters such as relative roughness height, e/D, relative roughness width, W/w, angle of attack, α and relative roughness pitch, P/e. A total of 512 values of thermal efficiency were obtained for different sets of roughness geometry parameters corresponding to 4 values of relative roughness height, e/D, 8 values of relative roughness width, W/w, 4 values of angle of attack, α and 4 values of relative roughness pitch, P/e. These 512 values of thermal efficiency were compared to obtain a set of values of roughness geometry parameters (relative roughness height, e/D, relative roughness width, W/w, angle of attack, α and relative roughness pitch, P/e) corresponding to which thermal efficiency attains the maximum value for the specified values of temperature rise parameter, $\Delta T/I$ and solar radiation intensity, I. Similar computational procedure was repeated for the next set

of values of temperature rise parameter, ΔT/I and solar radiation intensity, I, to obtain a set of optimum values of relative roughness geometry parameters. For the entire range of temperature rise parameter, ΔT/I and solar radiation intensity, I, considered in this experimental investigation, 18,432 values of thermal efficiency were obtained.

The optimum values of roughness geometry parameters (relative roughness height, e/D, relative roughness width, W/w, angle of attack, α and relative roughness pitch, P/e) obtained on the basis of thermal efficiency have been given in Table 6.2.

Table 6.2 Temperature rise parameter range corresponding to maximum thermal efficiency

Roughness geometry parameter	Temperature rise parameter range $K\text{-}m^2/W$	Value of roughness geometry parameter
Relative roughness height ,e/D	0.003 – 0.027	0.043
Relative roughness width, W/w	0.003 – 0.027	6
Angle of attack, α	0.003 – 0.027	60^o
Relative roughness pitch, P/e	0.003 – 0.027	8

6.5.2 Effective Efficiency

Figs.6.2 and 6.3 show the variation of effective efficiency of an artificially roughened solar air heater as a function of Reynolds number and temperature rise parameter respectively. The plots of effective efficiency have been drawn for relative roughness width value of 6, angle of attack value of 30^0, relative roughness pitch value of 10, insolation value of 1000 W/m^2 and different values of relative roughness height, e/D.

It has been observed from Fig.6.2 that for Reynolds number value up to about 21000, the maximum value of effective efficiency has been obtained for relative roughness height value of 0.043 where as beyond Reynolds number value of about 42000, the maximum value of effective efficiency is found to correspond to smooth collector.

Fig.6.3 shows that for temperature rise parameter value higher than 0.0055 K-m^2/W, relative roughness height value of 0.0043 yields the maximum value of effective efficiency whereas, for temperature rise parameter value less than 0.003 K-m^2/W, smooth collectors perform better in comparison with artificially roughened collectors. For temperature rise parameter value between 0.003 and 0.00425 K-m^2/W, the maximum value of effective efficiency has been obtained corresponding to relative roughness height value of 0.019 while for temperature rise parameter value between 0.00425 and 0.0045 K-m^2/W, relative roughness height value of 0.026 provides the maximum value of effective efficiency. Relative roughness height value of 0.035 has the best performance among the other values of relative roughness height for temperature rise parameter range between 0.0045 and 0.0055 K-m^2/W. For a fixed value of relative roughness height, value of effective efficiency increases with increase in temperature rise parameter, attains a maximum value and then starts decreasing with further increase in value of temperature rise parameter.

Figs.6.4 and 6.5 show the effect of relative roughness width on effective efficiency as a function of Reynolds number and temperature rise parameter respectively for fixed values of other roughness geometry parameters. The plots have been drawn for relative roughness height value of 0.043, angle of attack value of 30^0, relative roughness pitch value of 10, insolation value of 1000 W/m^2 and different values of relative roughness width.

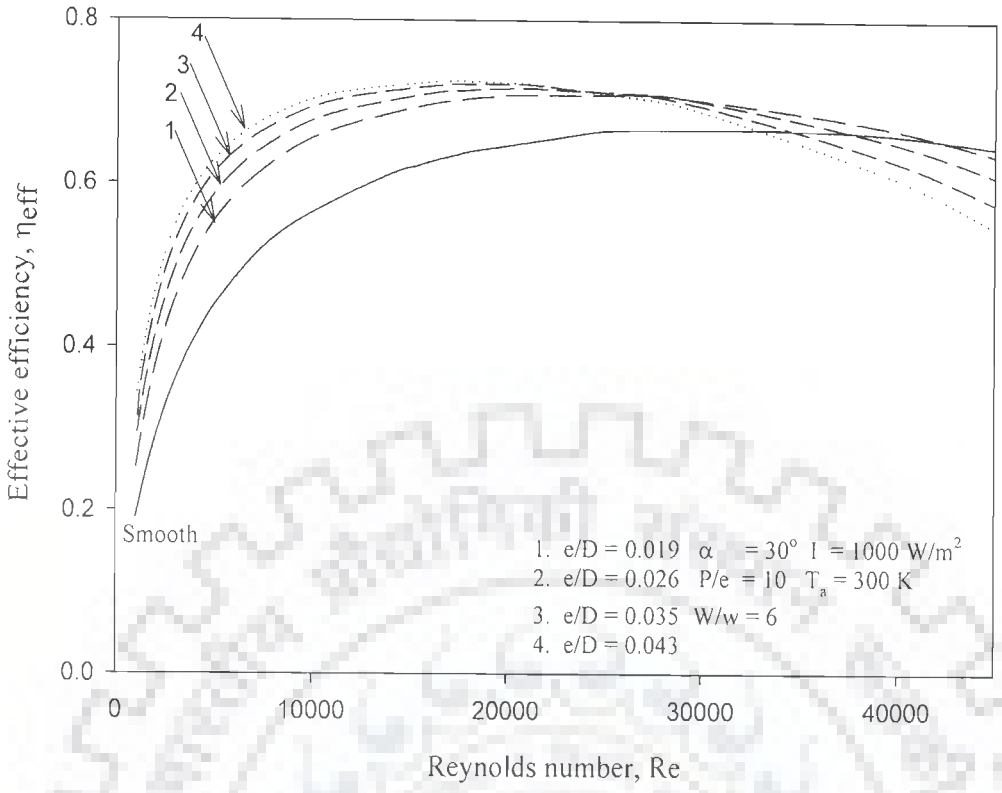

Fig.6.2 Effective efficiency as a function of Reynolds number for different values of relative roughness height

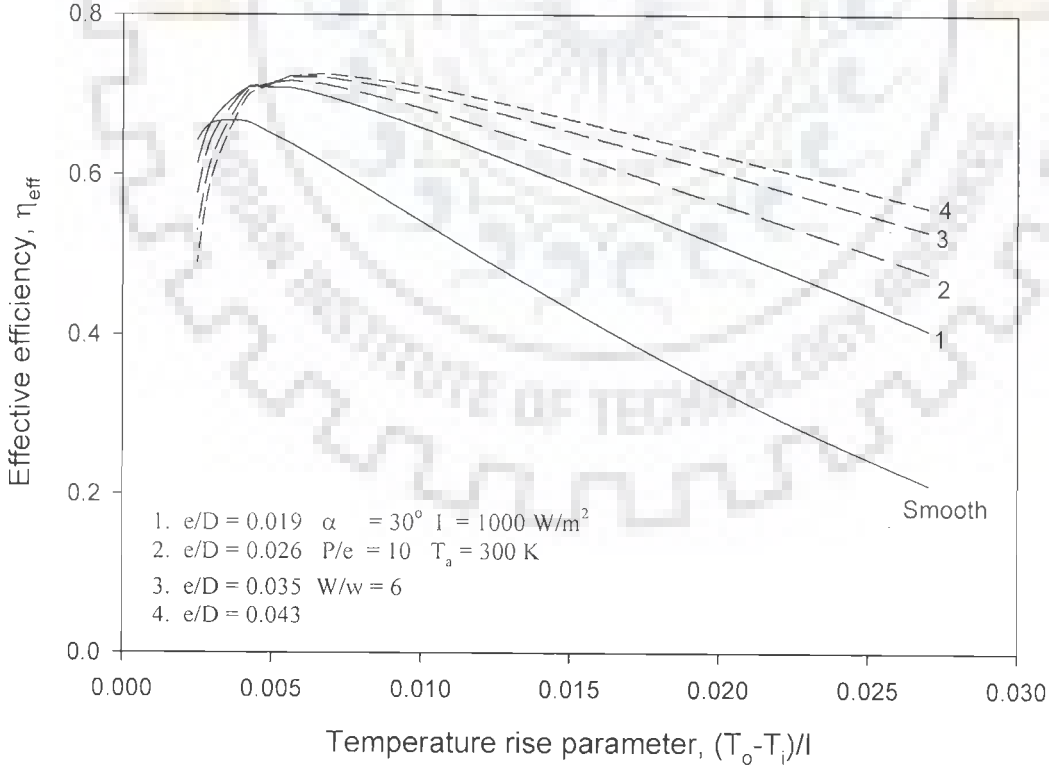

Fig.6.3 Effective efficiency as a function of temperature rise parameter for different values of relative roughness height

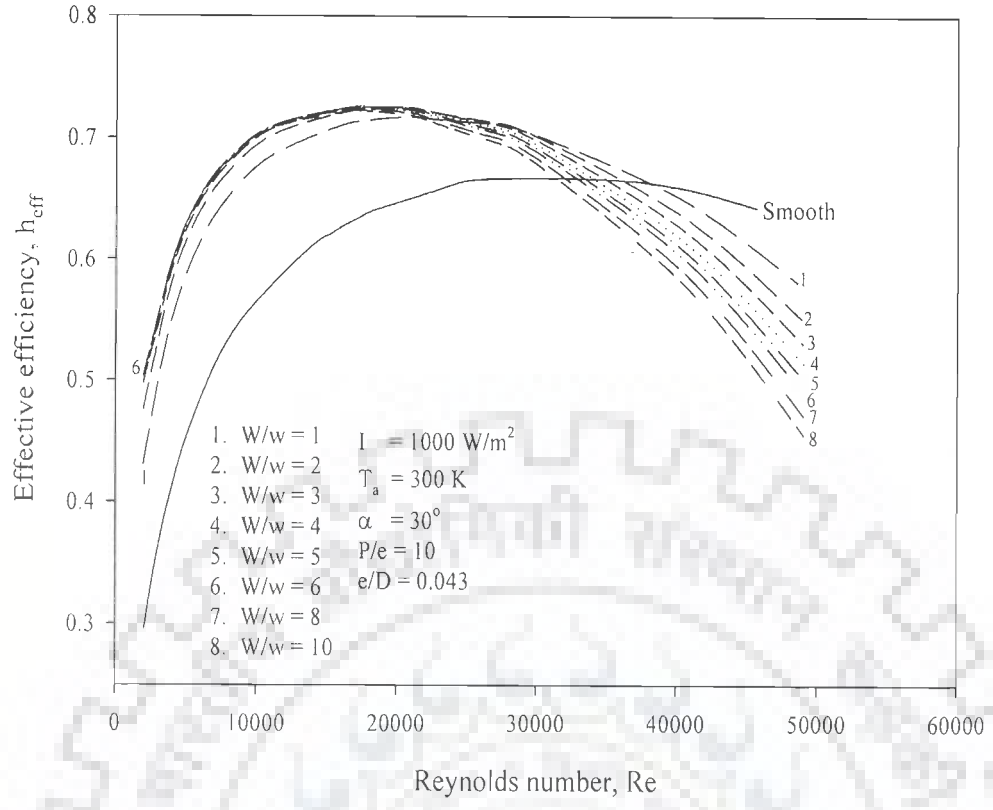

Fig.6.4 Effective efficiency as a function of Reynolds number for different values of relative roughness width

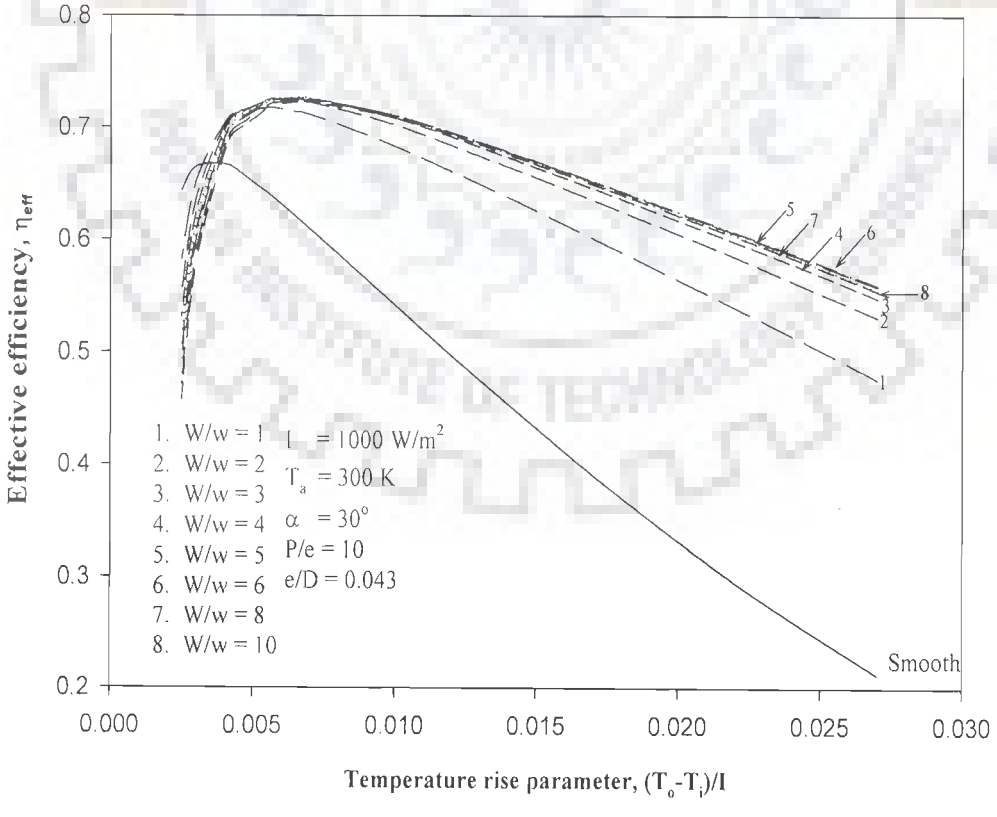

Fig.6.5 Effective efficiency as a function of temperature rise parameter for different values of relative roughness width

It can be observed from Fig.6.4 that for Reynolds number value up to about 12000, value of effective efficiency increases with increase in relative roughness width and attains a maximum value corresponding to relative roughness width value of 6. For Reynolds number range of 12000 to 17000, performance of roughness geometry with relative roughness width value of 5 is better as compared to other values of relative roughness width. For Reynolds number range of 17000 to 20000, the maximum value of effective efficiency has been obtained corresponding to relative roughness width value of 4 and beyond this range of Reynolds number, relative roughness width value of 3 exhibits better performance. For Reynolds number range of 26500 to 29000, relative roughness width value of 2 yields the maximum value of effective efficiency. For Reynolds number range of 29000 to 39000, relative roughness width value of 1 outperforms other values of relative roughness width and beyond this range of Reynolds number; smooth solar collector has the maximum value of effective efficiency. It may be due to the fact that as the value of relative roughness width increases, heat transfer and friction factor also increase on account of formation of more number of secondary flow cells resulting in increase in turbulence. For relative roughness width values less than 6, increase in heat transfer enhancement factor dominates over the increase in friction factor whereas, for relative roughness width values higher than 6, increase in friction factors dominates over the heat transfer enhancement thereby, resulting in lower values of effective efficiency.

It has been observed from Fig.6.4 that for a given value of relative roughness width, effective efficiency increases with increase in Reynolds number and attains a maximum value and then decreases with further increase in Reynolds number.

Fig.6.5 shows the effect of relative roughness width on effective efficiency as temperature rise parameter is varied for constant values of other roughness geometry parameters. It has been observed from Fig.6.5 that for value of temperature rise parameter greater than 0.009 K-m^2/W, the maximum value of effective efficiency is obtained for relative roughness width value of 6 whereas for temperature rise

parameter value less than 0.003 K-m^2/W, smooth solar air heater performs better in comparison with roughened solar air heaters. For temperature rise parameter value between 0.003 and 0.0042 K-m^2/W, the maximum value of effective efficiency has been observed for relative roughness width value of 1. For temperature rise parameter values between 0.0042 and 0.009, the maximum values of effective efficiencies correspond to relative roughness width values in the range 2 – 5.

It has been observed that for a given value of relative roughness width, effective efficiency increases with increase in temperature rise parameter and attains a maximum value and then decreases with further increase in temperature rise parameter value.

Fig.6.6 shows the effect of angle of attack on effective efficiency of a roughened solar collector. The plot has been drawn for different values of angle of attack and for fixed values of other roughness geometry parameters. It has been observed from the Fig.6.6 that for Reynolds number value less than 18000, the maximum value of effective efficiency has been observed for angle of attack value of 60^0 and for Reynolds number value in the range of 18000 and 20500, value of effective efficiency has been found to be maximum corresponding to angle of attack value of 45^0. For Reynolds number range between 20500 and 33500, angle of attack value of 30^0 yields the maximum value of effective efficiency and beyond this range of Reynolds number, smooth solar collector performs better from effective efficiency point of view.

It has been observed from Fig.6.6 that for a given value of angle of attack, effective efficiency increases with increase in Reynolds number, attains a maximum value and then decreases with further increase in Reynolds number value.

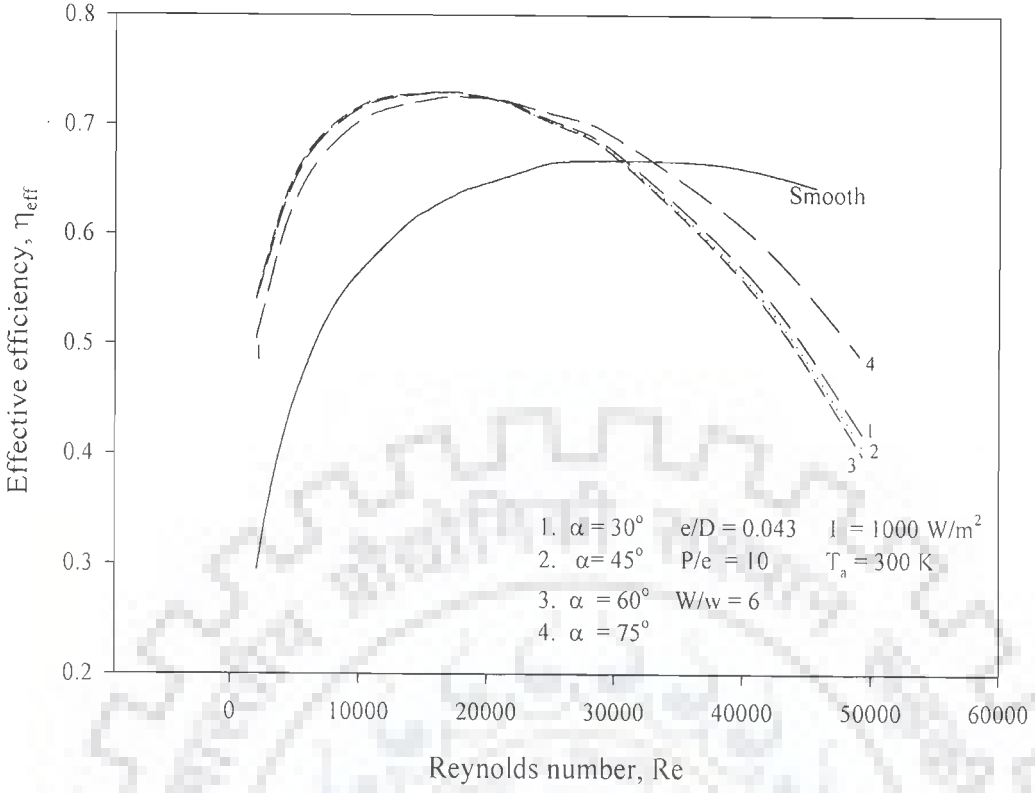

Fig.6.6 Effective efficiency as a function of Reynolds number for different values of angle of attack

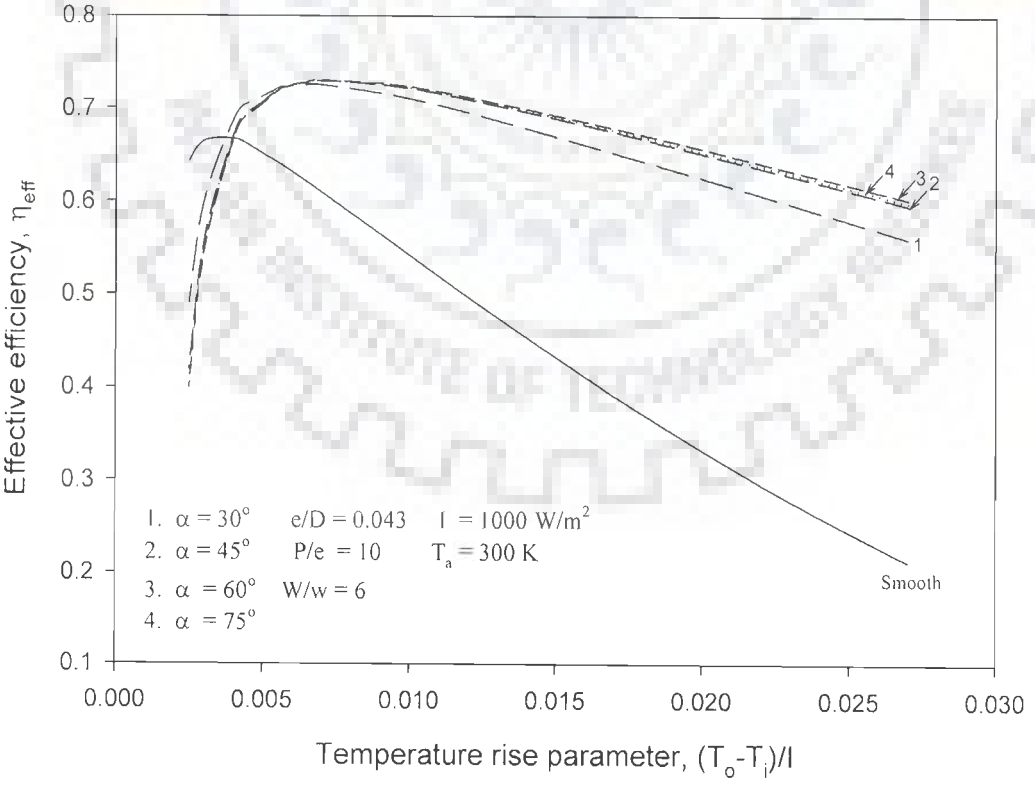

Fig.6.7 Effective efficiency as a function of temperature rise parameter for different values of angle of attack

Fig.6.7 shows the effect of angle of attack on effective efficiency as a function of temperature rise parameter. For temperature rise parameter value less than 0.0036 K-m^2/W, smooth collector outperforms the roughened collectors and the maximum value of effective efficiency correspond to an angle of attack value of 30^0 for temperature rise parameter range of 0.0036 to 0.006 K-m^2/W. For temperature rise parameter value between 0.006 and 0.0065 K-m^2/W, the maximum value of effective efficiency occurs at an angle of attack value of 45^0 and for temperature rise parameter value greater than 0.0065 K-m^2/W, angle of attack value of 60^0 yields the maximum value of effective efficiency.

From Fig.6.7, it is clear that for a given value of angle of attack, effective efficiency increase with increase in temperature rise parameter, attains a maximum value and then decreases with further increase in temperature rise parameter value.

Fig.6.8 shows the variation of effective efficiency as a function of Reynolds number for different values of relative roughness pitch and for fixed values of other roughness parameters. It has been observed that for Reynolds number value less than about 17000, relative roughness pitch value of 8 yields the maximum value of effective efficiency and for Reynolds number range of 17000 to19000, the maximum value of effective efficiency has been observed for relative roughness pitch value of 10. For the Reynolds number range of 19000 to 33000, relative roughness pitch value of 12 has the maximum value of effective efficiency and for Reynolds number value beyond this range, smooth solar collector has the best performance for the range of parameters considered.

It has been observed from Fig.6.8 that for a given value of relative roughness pitch, effective efficiency increases with increase in Reynolds number, attains a maximum value and then decreases with further increase in Reynolds number.

Fig.6.9 shows the effect of relative roughness pitch on effective efficiency as a function of temperature rise parameter. For temperature rise parameter value greater than 0.00690 K-m^2/W, relative roughness pitch value of 8 has the best performance and for temperature rise parameter values less than 0.003 K-m^2/W, smooth collector has the best performance from effective efficiency point of view. Relative roughness pitch value of 12 gives the maximum values of effective efficiency for temperature rise parameter range of 0.003 to 0.00625 K-m^2/W and for temperature rise parameter value between 0.00625 to 0.00690 K-m^2/W, the maximum values of effective efficiency are corresponding to relative roughness pitch value of 10.

It is clear from Fig.6.9 that for a given value of relative roughness pitch, effective efficiency increases with increase in temperature rise parameter, attains a maximum value and then decreases with further increase in temperature rise parameter value.

The values of roughness geometry parameters that result in the maximization of effective efficiency have been listed in Tables 6.3 and 6.4 for different ranges of Reynolds number and temperature rise parameter respectively. It can be concluded that no single value or single set of roughness geometry parameters yield the maximum value of effective efficiency for the entire range of Reynolds number or temperature rise parameter.

In order to obtain the optimum values of roughness geometry parameters on the basis of effective efficiency, a similar procedure has been followed as described in Section 6.5.1.

Figs. 6.10 to 6.13 show the plots of optimum values of relative roughness height, relative roughness width, angle of attack and relative roughness pitch that correspond to maximum effective efficiency for a given value of temperature rise parameter.

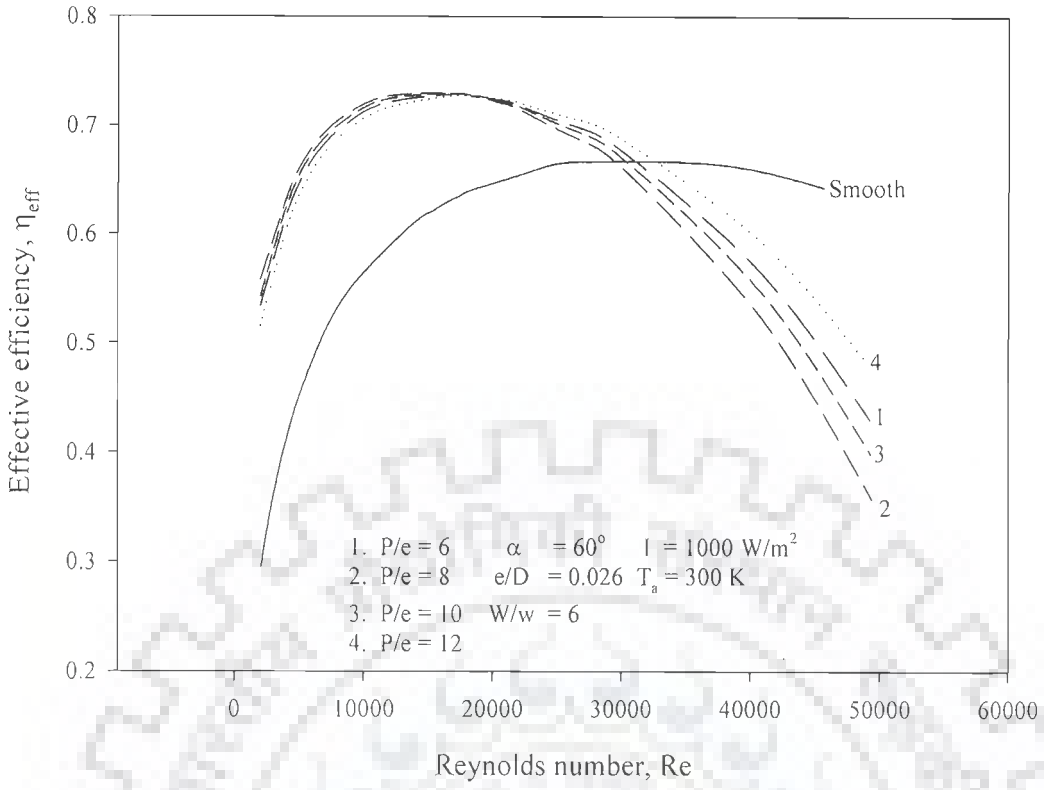

Fig.6.8 Effective efficiency as a function of Reynolds number for different values of relative roughness pitch

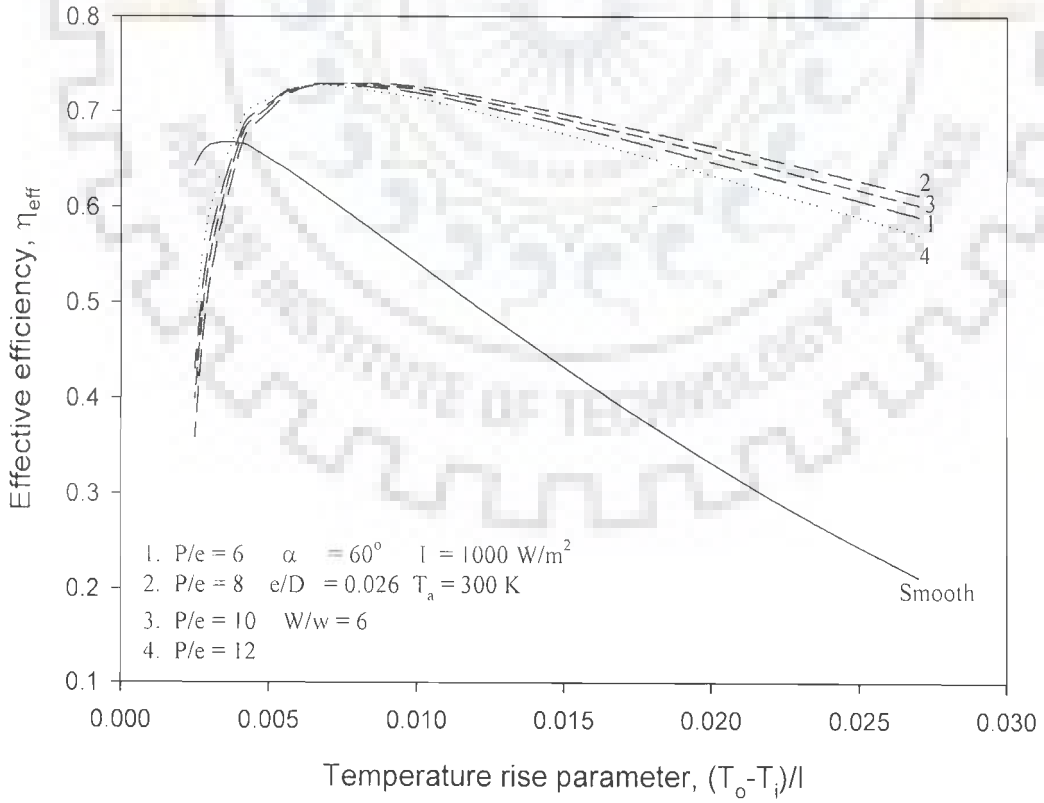

Fig.6.9 Effective efficiency as a function of temperature rise parameter for different values of relative roughness pitch

Table 6.3 Reynolds number range corresponding to maximum effective efficiency (I = 1000 W/m^2)

Roughness parameter	Fixed parameter	Reynolds number range	Value of Roughness parameter
Relative roughness height, e/D	P/e = 10 W/w = 6 $\alpha = 30^0$	Re < 21000	0.043
		21000 < Re > 26000	0.035
		26000 < Re > 29300	0.026
		29300 < Re > 42000	0.019
		Re > 42000	Smooth
Relative roughness width, W/w	e/D = 0.043 P/e = 10 $\alpha = 30^0$	Re < 12000	6
		12000>Re > 17000	5
		17000>Re>20000	4
		20000>Re>26500	3
		26500>Re>29000	2
		29000>Re > 39000	1
		Re>39000	Smooth
Angle of attack, α	e/D = 0.043 P/e = 10 W/w = 6	Re < 18000	60^0
		18000<Re < 20500	45^0
		20500<Re<33500	30^0
		Re > 33500	Smooth
Relative roughness Pitch, P/e	e/D = 0.043 W/w = 6 $\alpha = 60^0$	Re < 17000	8
		17000<Re< 19000	10
		19000<Re<33000	12
		Re > 33000	Smooth

Table 6.4 Temperature rise parameter range corresponding to maximum effective efficiency (I=1000 W/m^2)

Roughness parameter	Fixed parameter	Temperature rise parameter range (Km^2 /W)	Value of Roughness parameter
Relative roughness height, e/D	P/e = 10 W/w = 6 α = 30^0	$\Delta T/I < 0.003$	Smooth
		$0.003 < \Delta T/I < 0.00425$	0.019
		$0.00425 < \Delta T/I < 0.0045$	0.026
		$0.0045 < \Delta T/I < 0.0055$	0.035
		$\Delta T/I > 0.0055$	0.043
Relative roughness width, W/w	e/D = 0.043 P/e = 10 α = 30^0	$\Delta T/I < 0.003$	Smooth
		$0.003 < \Delta T/I < 0.0042$	1
		$0.0042 < \Delta T/I < 0.0045$	2
		$0.0045 < \Delta T/I < 0.006$	3
		$0.006 < \Delta T/I < 0.007$	4
		$0.007 < \Delta T/I < 0.009$	5
		$\Delta T/I > 0.009$	6
Angle of attack, α	e/D = 0.043 P/e = 10 W/w = 6	$\Delta T/I < 0.0036$	Smooth
		$0.0036 < \Delta T/I < 0.006$	30^0
		$0.006 < \Delta T/I < 0.0065$	45^0
		$\Delta T/I > 0.0065$	60^0
Relative roughness pitch, P/e	e/D = .043 W/w = 6 α = 60^0	$\Delta T/I < 0.003$	Smooth
		$0.003 < \Delta T/I < 0.00625$	12
		$0.00625 < \Delta T/I < 0.00690$	10
		$\Delta T/I > 0.00690$	8

Fig.6.10 shows the optimum values of relative roughness height as a function of temperature rise parameter for various values of insolation. For temperature rise parameter value lower than 0.00375 K-m^2/W, the relative roughness height value of 0.019 represents the optimum conditions for all values of insolation and for values of temperature rise parameter higher than 0.006 K-m^2/W; the relative roughness height value of 0.043 represents the optimum conditions for all the values of insolation. However, for temperature rise parameter range between 0.00375 and 0.006 K-m^2/W, the optimum value of relative roughness height is a function of insolation.

Fig.6.11 shows the optimum values of relative roughness width as a function of temperature rise parameter for various values of insolation. For temperature rise parameter value higher than 0.01375 K-m^2/W, the relative roughness width value of 6 represents the optimum conditions for all the values of insolation. However, for temperature rise parameter range less than 0.003 K-m^2/W, relative roughness width value of 1 yields optimum performance from effective efficiency point of view. For temperature rise parameter range between 0.003 and 0.01375 K-m^2/W, the optimum value of relative roughness width is a function of insolation.

Fig.6.12 shows the optimum values of angle of attack as a function of temperature rise parameter for various values of insolation. For temperature rise parameter value lower than 0.00325 K-m^2/W, the angle of attack value of 30^0 represents the optimum condition for all values of insolation and for values of temperature rise parameter higher than 0.00675 K-m^2/W, the angle of attack value of 60^0 represents the optimum conditions for all the values of insolation. However, for temperature rise parameter range between 0.00325 and 0.00675 K-m^2/W, the optimum value of relative roughness height is a function of insolation.

Fig.6.13 shows the optimum values of relative roughness pitch with temperature rise parameter for various values of insolation. For temperature rise parameter value lower than 0.00575 K-m^2/W, the relative roughness pitch value of 12 represents the optimum condition for all values of insolation and for values of

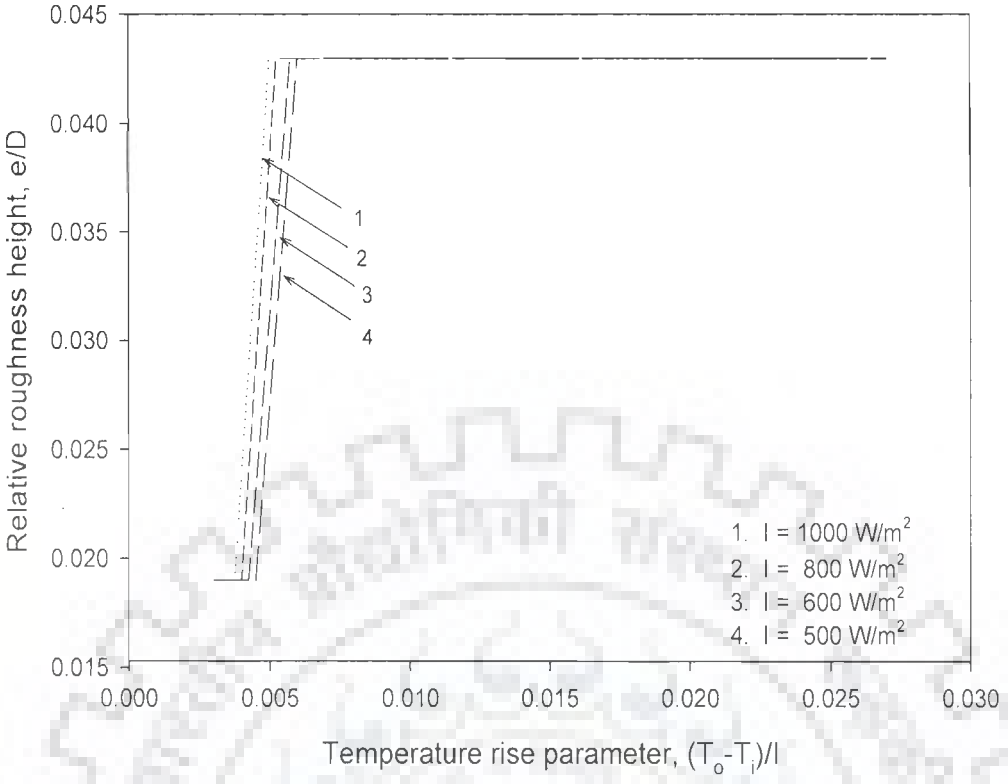

Fig.6.10 Optimum values of relative roughness height on the basis of effective efficiency criterion

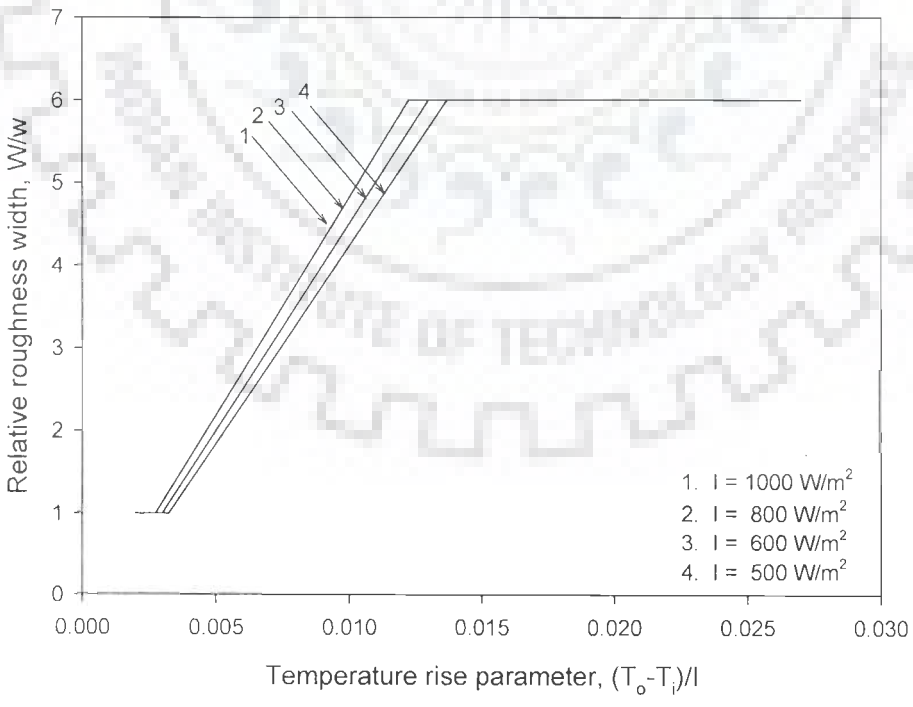

Fig.6.11 Optimum values of relative roughness width on the basis of effective efficiency criterion

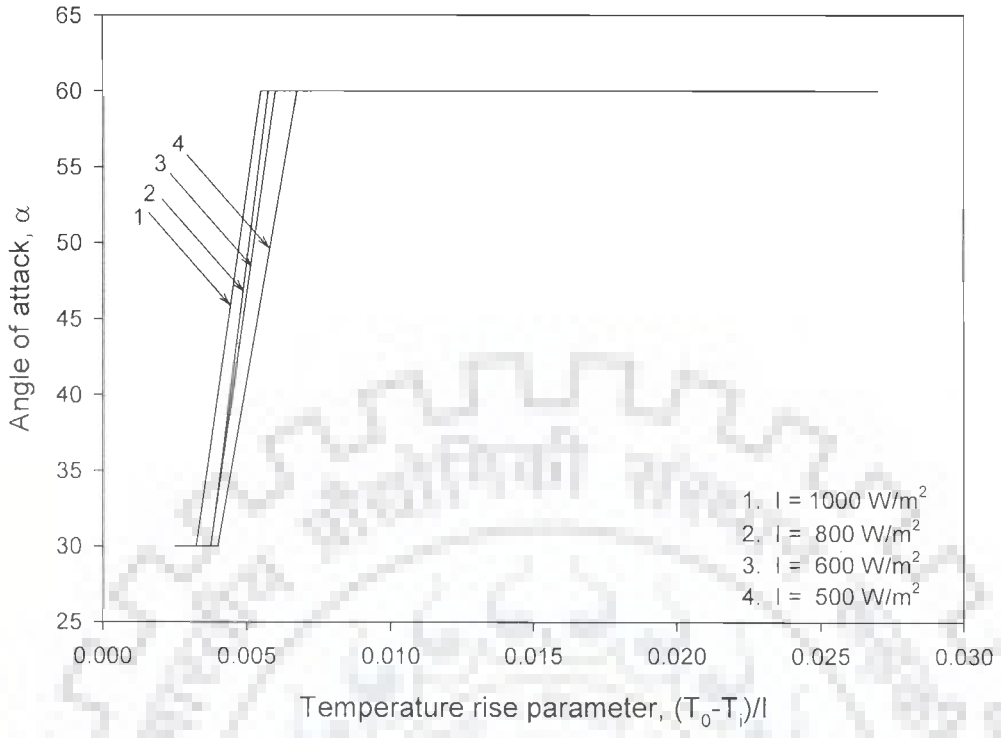

Fig.6.12 Optimum values of angle of attack on the basis of effective efficiency criterion

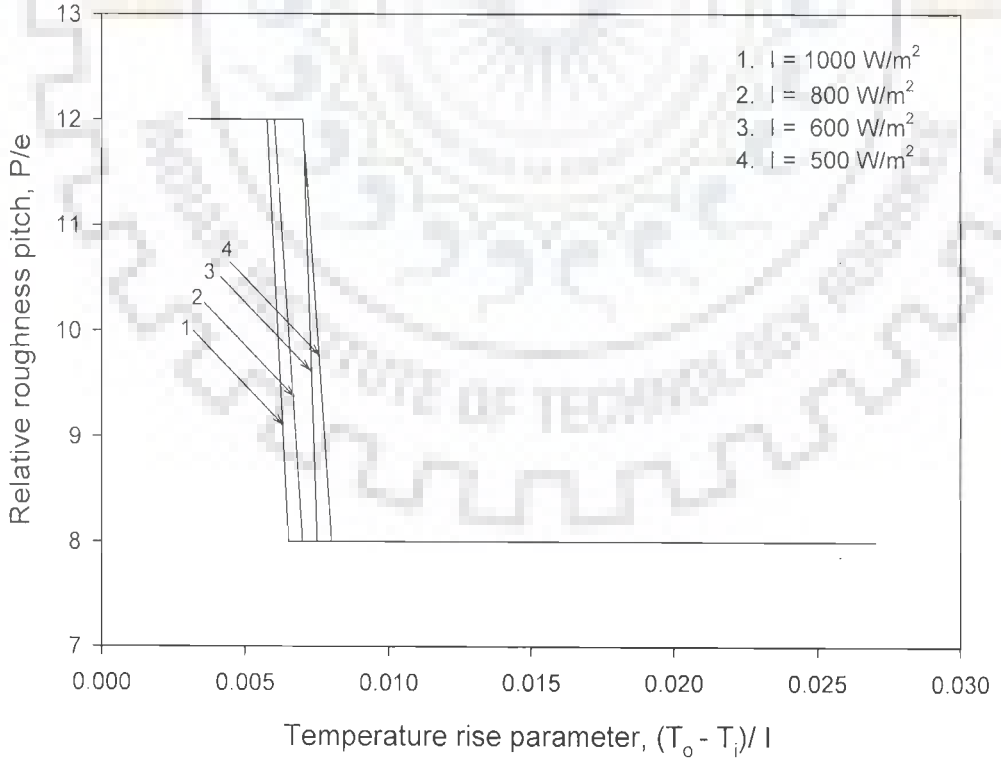

Fig.6.13 Optimum values of relative roughness pitch on the basis of effective efficiency criterion

temperature rise parameter higher than 0.008 Km^2/W, the relative roughness pitch value of 8 represents the optimum conditions for all the values of insolation. However, for temperature rise parameter range between 0.00575 and 0.008 Km^2/W, the optimum value of relative roughness pitch is a function of insolation. The summary of the results has been presented in Table 6.5.

It can be concluded from the above discussion that the maximum value of effective efficiency correspond to a set of roughness geometry parameters relative roughness height, e/D, relative roughness width, W/w, angle of attack, α, and relative roughness pitch, P/e. The optimum values of roughness geometry parameters depend on the operating parameters, i.e., temperature rise parameter and insolation. A set of roughness geometry parameters can be directly determined from Figs. 6.10 to 6.13 corresponding to given values of temperature rise parameter and insolation. For example, the typical optimum sets of roughness geometry parameters for three typical design conditions are given in Table 6. 6.

6.5.3 Exergetic Efficiency

In Figs. 6.14 to 6.21, the values of exergetic efficiency have been plotted as functions of Reynolds number and temperature rise parameter for different values of roughness geometry parameters, relative roughness height, e/D, relative roughness width, W/w, angle of attack, α and relative roughness pitch, P/e. These plots have been prepared to discuss the effect of roughness parameters on the value of exergetic efficiency for given operating parameters of the multi v-rib roughened solar air heater. These plots also include the values of exergetic efficiency for conventional smooth solar air heater for the purpose of comparison.

Table 6.5 Optimum values of roughness parameters on the basis of effective efficiency

Roughness parameter	Temperature rise parameter range ($K\text{-}m^2 / W$)	Value of roughness parameter
Relative roughness height, e/D	$\Delta T/I < 0.00375$	0.019
	$0.00375 < \Delta T/I < 0.006$	Function of insolation and temperature rise parameter
	$\Delta T/I > 0.006$	0.043
Relative roughness width, W/w	$\Delta T/I < 0.003$	1
	$0.003 < \Delta T/I < 0.01375$	Function of insolation & temperature rise parameter
	$\Delta T/I > 0.01375$	6
Angle of attack, α	$\Delta T/I < 0.00325$	30^0
	$0.00325 < \Delta T/I < 0.00675$	Function of insolation and temperature rise parameter
	$\Delta T/I > 0.00675$	60^0
Relative roughness pitch, P/e	$\Delta T/I < 0.00575$	12
	$0.00575 < \Delta T/I < 0.008$	Function of insolation and temperature rise parameter
	$\Delta T/I > 0.008$	8

Table 6.6 Optimum values of roughness geometry parameters corresponding to different values of temperature rise parameter on the basis of effective efficiency criterion

Solar radiation intensity, I, W/m^2	Temperature rise parameter, $\Delta T/I$	Relative roughness height, e/D	Relative roughness width, W/w	Angle of attack, α	Relative roughness pitch, P/e	Effective efficiency
800	0.004	0.019	3	45	12	0.7024
800	0.006	0.043	3	60	12	0.7228
800	0.015	0.043	6	60	8	0.699

Fig.6.14 shows the effect of relative roughness height on exergetic efficiency for fixed values of other roughness geometry parameters and insolation value of 1000 W/m^2. It can be observed that for Reynolds number value up to about 11000, value of exergetic efficiency increases with increase in relative roughness height value and the maximum value of exergetic efficiency corresponds to relative roughness height value of 0.043. Beyond this value of Reynolds number, the trend is reversed. For a given value of relative roughness height, exergetic efficiency increases with increase in Reynolds number, attains a maximum value and then decreases with further increase in Reynolds number value.

Fig.6.15 shows the above mentioned data of exergetic efficiency plotted as a function for temperature rise parameter It can be observed that for temperature rise parameter value higher than 0.011 $K\text{-}m^2/W$, exergetic efficiency increases with increase in relative roughness height and this trend is reversed for temperature rise parameter value below 0.011$K\text{-}m^2/W$. For temperature rise parameter value below 0.00625 $K\text{-}m^2/W$, performance of smooth conventional air heater is better as compared to roughened solar air heaters and for temperature rise parameter value in the range of 0.00625 to 0.008 $K\text{-}m^2/W$, relative roughness height value of 0.019 yields the maximum value of exergetic efficiency. For temperature rise parameter value between 0.008 to 0.0095 $K\text{-}m^2/W$, the maximum value of exergetic efficiency is obtained for relative roughness height value of 0.026 and for temperature rise parameter value between 0.0095 to 0.011 $K\text{-}m^2/W$, the maximum value of exergetic efficiency has been obtained for relative roughness height value of 0.035 and beyond this range of temperature rise parameter, relative roughness height value of 0.043 yields the maximum value of exergetic efficiency.

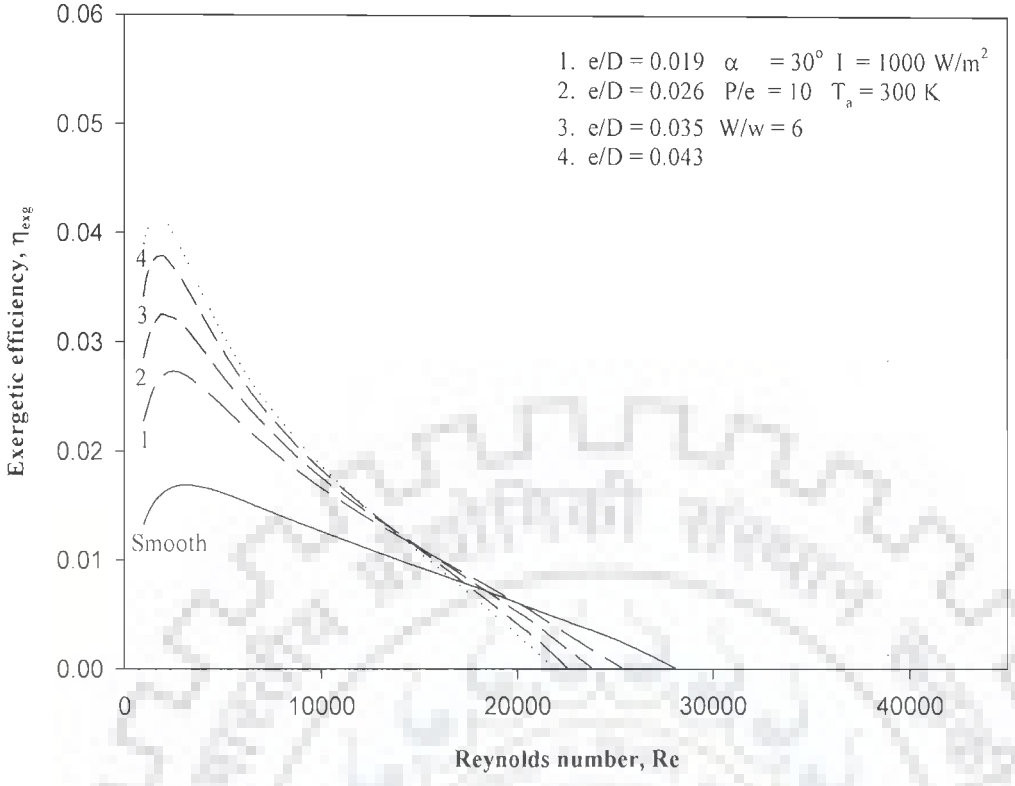

Fig.6.14 Exergetic efficiency as a function of Reynolds number for different values of relative roughness height

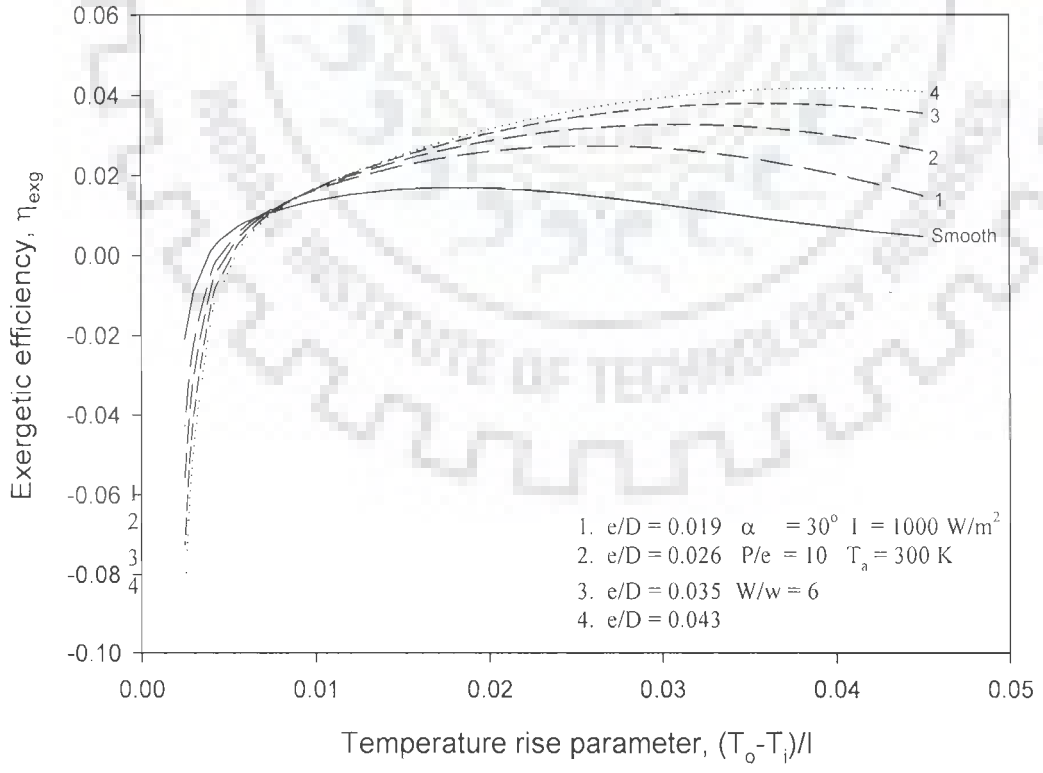

Fig.6.15 Exergetic efficiency as a function of temperature rise parameter for different values of relative roughness height

It can also be observed that for a given value of relative roughness height, exergetic efficiency increases with increase in temperature rise parameter value, attains a maxima and then decreases with further increase in temperature rise parameter value.

Fig.6.16 shows the effect of relative roughness width on exergetic efficiency for fixed values of other roughness geometry parameters and an insolation value of 1000 W/m^2. Performance of smooth conventional solar air heater has been found to be better as compared to roughened solar air heater for Reynolds number value higher than 18500. For Reynolds number value less than 6650, relative roughness width value of 6 yields the maximum value of exergetic efficiency and for Reynolds number value in the range of 11500 to 18500 the maximum efficiency is obtained for relative roughness width value of 1. The maximum value of exergetic efficiency corresponds to relative roughness width values in the range of 2-5 for Reynolds number range of 6650 to 11500. For a given value of relative roughness width, exergetic efficiency increases with increases in Reynolds number, attains a maximum value and then decreases with further increase in Reynolds number.

These values of effective efficiency have been replotted in Fig.6.17 as a function of temperature rise parameter. For temperature rise parameter value less than 0.00725 $K\text{-}m^2/W$, smooth conventional solar air heaters perform better as compared to roughened solar air heaters and for temperature rise parameter value greater than 0.0155 $K\text{-}m^2/W$, relative roughness width value of 6 yields the maximum value of exergetic efficiency. For temperature rise parameter value in the range of 0.00725 to 0.0155 $K\text{-}m^2/W$, the maximum values of exergetic efficiency correspond to relative roughness width values in the range of 2 to 5.

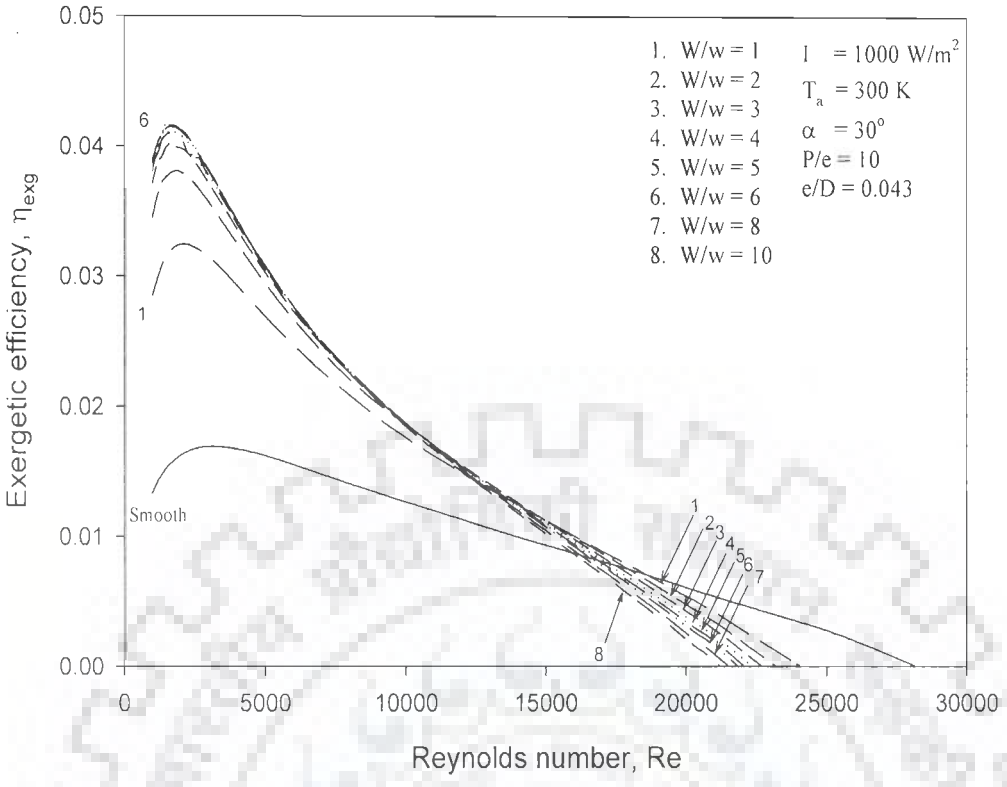

Fig.6.16 Exergetic efficiency as a function of Reynolds number for different values of relative roughness width

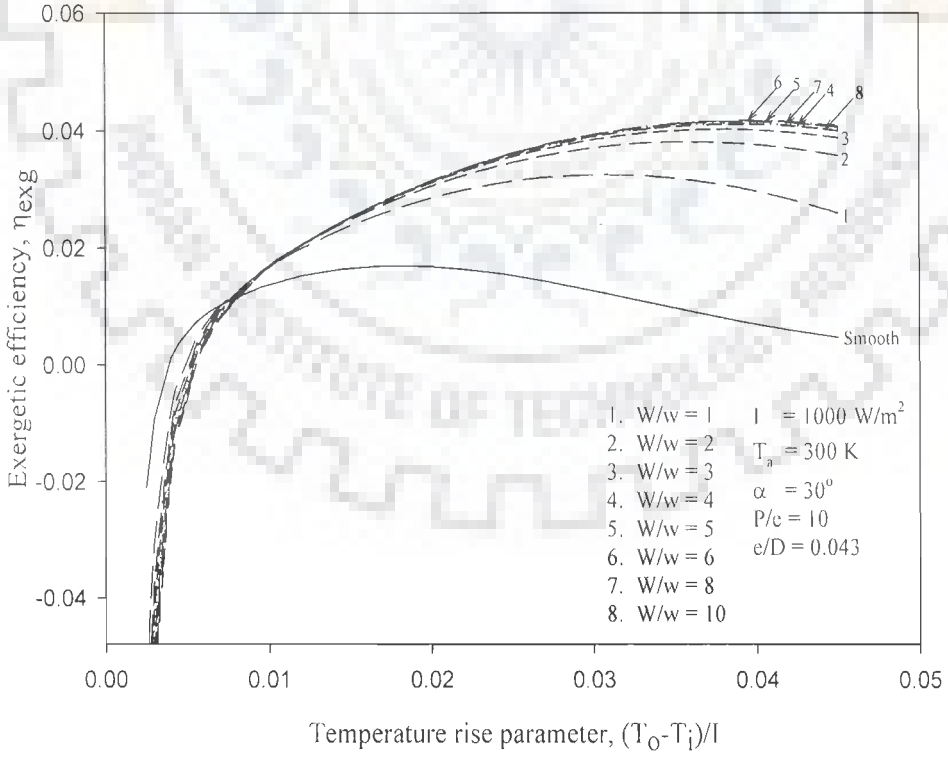

Fig.6.17 Exergetic efficiency as a function of temperature rise parameter for different values of relative roughness width

Fig.6.18 shows the effect of angle of attack on exergetic efficiency for fixed values of other roughness geometry parameters and an insolation value of 1000 W/m^2. For Reynolds number value less than 9950, angle of attack value of 60^o yields the maximum value of exergetic efficiency and for Reynolds number in the range of 9950 to 14300, angle of attack value of 45^0 yields the maximum value of exergetic efficiency. Exergetic efficiency value attains the maximum value corresponding to angle of attack value of 30^o for Reynolds number in the range of 14300 to 17000 and for Reynolds number value greater than 17000, the maximum value of exergetic efficiency correspond to smooth solar air heater. For a given value of angle of attack, exergetic efficiency increases with increase in Reynolds number, attains a maximum value and then decreases with further increase in Reynolds number value.

Fig.6.19 shows the same data of exergetic efficiency replotted as a function of temperature rise parameter. For the temperature rise parameter value lower than 0.008 K-m^2/W, smooth solar air heaters out perform the roughened solar air heaters and for temperature rise parameter value greater than 0.012 K-m^2/W, angle of attack value of 60^o has the best performance as compared to other values of angle of attack. For temperature rise parameter value in the range of 0.008 to 0.01125 K-m^2/W, angle of attack value of 30^o yields the maximum value of exergetic efficiency and for temperature rise parameter value in the range of 0.01125 to 0.012 K-m^2/W, the maximum value of exergetic efficiency corresponds to angle of attack value of 45^o.

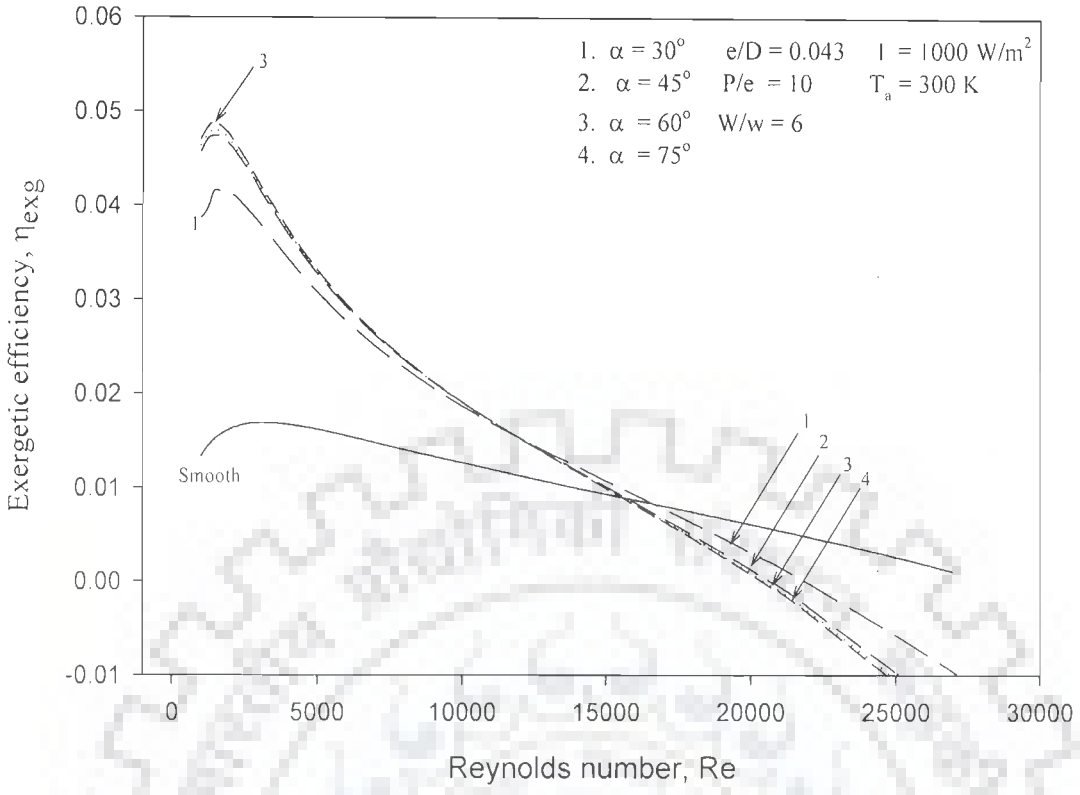

Fig.6.18 Exergetic efficiency as a function of Reynolds number for different values of angle of attack

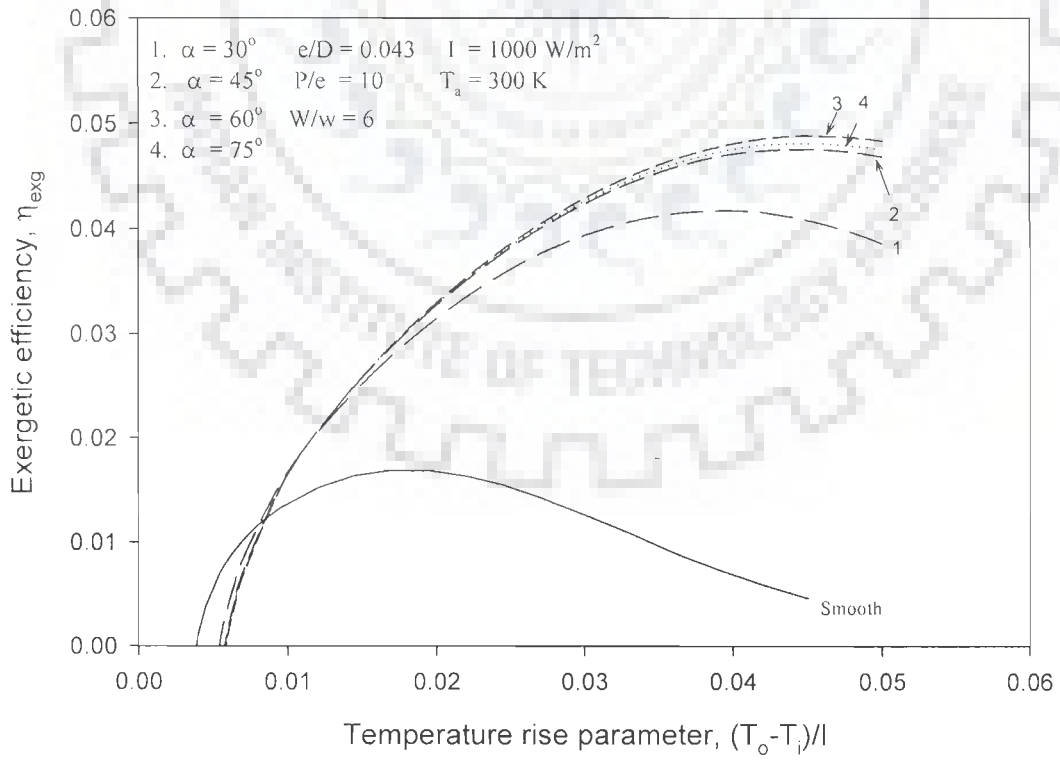

Fig.6.19 Exergetic efficiency as a function of temperature rise parameter for different values of angle of attack

Fig.6.20 shows the effect of relative roughness pitch on exergetic efficiency for fixed values of other roughness geometry parameters and an insolation value of 1000 W/m^2. For Reynolds number value greater than 15000, smooth solar air heaters have the maximum value of exergetic efficiency and for Reynolds number value less than 8700, relative roughness pitch value of 8 yields the maximum value of exergetic efficiency. For Reynolds number ranges of 8700 to 9300 and 9300 to 15000, the maximum values of exergetic efficiency are obtained corresponding to relative roughness pitch values 10 and 12 respectively.

Fig.6.21 shows the above value of exergetic efficiency replotted as a function of temperature rise parameter. It can be observed that for temperature rise parameter value less than 0.00775 K-m^2/W, smooth solar air heaters perform better in comparison to roughened solar air heaters and for temperature rise parameter value greater than 0.012 K-m^2/W, relative roughness pitch value of 8 yield the maximum value of exergetic efficiency. For temperature rise parameter value in the range of 0.00775 to 0.01125 K-m^2/W, the maximum value of exergetic efficiency is obtained for relative roughness pitch value of 12 and for temperature rise parameter value in the range of 0.01125 to 0.012 K-m^2/W, relative roughness pitch value of 10 yields the maximum value. For a given value of relative roughness pitch, exergetic efficiency increases with increase in temperature rise parameter, attains a maximum value and then decreases with further increase in temperature rise parameter.

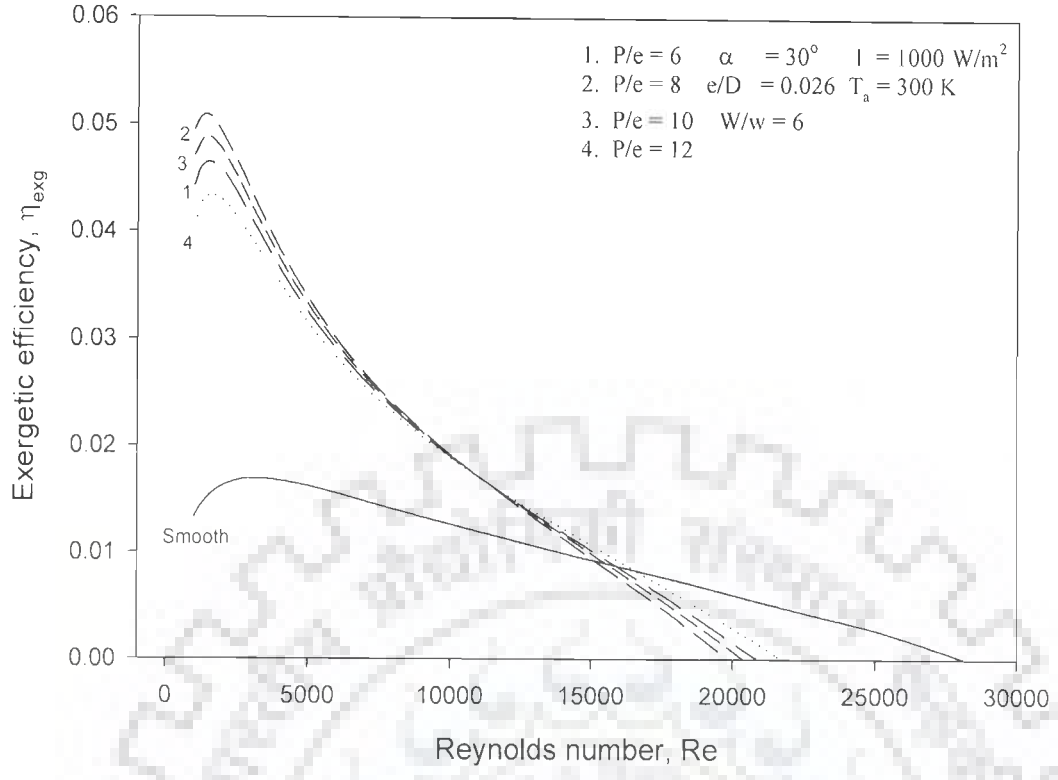

Fig.6.20 Exergetic efficiency as a function of Reynolds number for different values of relative roughness pitch

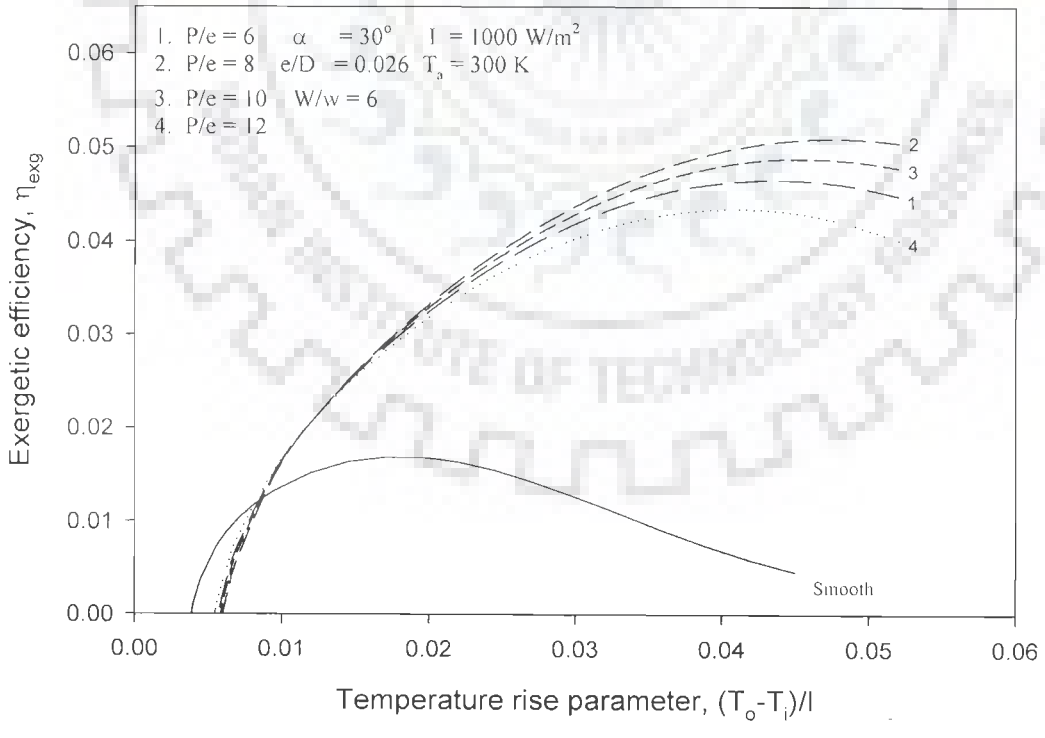

Fig.6.21 Exergetic efficiency as a function of temperature rise parameter for different values of relative roughness pitch

The values of roughness geometry parameters that result in the maximum value of exergetic efficiency have been listed in Tables 6.7 and 6.8 for different ranges of Reynolds number and temperature rise parameter respectively corresponding to insolation value of 1000 W/m^2. It can be concluded that no single value or single set of roughness geometry parameters yield the maximum exergetic efficiency for the entire range of Reynolds number or temperature rise parameter.

In order to obtain the optimum values of roughness geometry parameters on the basis of exergetic efficiency, a similar procedure has been followed as described in Section 6.5.1.

Figs.6.22 to 6.25 show the plots of optimum values of relative roughness height, relative roughness width, angle of attack and relative roughness pitch that correspond to maximum exergetic efficiency for a given value of temperature rise parameter. Fig.6.22 shows the optimum values of relative roughness height as a function of temperature rise parameter for various values of insolation. For temperature rise parameter value lower than 0.008 K-m^2/W, the relative roughness height value of 0.019 represents the optimum condition for all values of insolation and for values of temperature rise parameter higher than 0.013 K-m^2/W, the relative roughness height value of 0.043 represents the optimum conditions for all the values of insolation. However, for temperature rise parameter range between 0.008 and 0.013 K-m^2/W, the optimum value of relative roughness height is a function of insolation.

Fig.6.23 shows the optimum values of relative roughness width as a function of temperature rise parameter for various values of insolation. For temperature rise parameter value lower than 0.006 K-m^2/W, the relative roughness width value of 1 represents the optimum condition for all values of insolation and for values of temperature rise parameter higher than 0.02425 K-m^2/W, the relative roughness width value of 6 represents the optimum conditions for all the values of insolation. However, for temperature rise parameter range between 0.006 and 0.02425 K-m^2/W, the optimum value of relative roughness width is a function of insolation.

Table 6.7 Reynolds number range corresponding to maximum exergetic efficiency (I=1000 W/m^2)

Roughness parameter	Fixed parameter	Reynolds number range	Value of roughness parameter
Relative roughness height, e/D	P/e = 10 W/w = 6 $\alpha = 30^0$	Re < 11000	0.043
		11000<Re<12000	0.035
		12000<Re<16000	0.026
		16000<Re <20000	0.019
		Re > 20000	Smooth
Relative roughness width, W/w	e/D = 0.043 P/e = 10 $\alpha = 30^0$	Re < 6600	6
		6600<Rc <8200	5
		8200<Re <9900	4
		9900<Re <10700	3
		10700<Re <11350	2
		11500<Re < 18500	1
		Re > 18500	Smooth
Angle of attack, α	e/D = 0.043 P/e = 10 W/w = 6	Re <9950	60^0
		9950<Re < 14300	45^0
		14300<Re < 17000	30^0
		Re > 17000	Smooth
Relative roughness Pitch, P/e	e/D = 0.043 W/w = 6 $\alpha = 60^0$	Re < 8700	8
		8700 < Re < 9300	10
		9300 < Re < 15000	12
		Re > 15000	Smooth

Table 6.8 Temperature rise parameter range corresponding to maximum exergetic efficiency (I=1000 W/m^2)

Roughness parameter	Fixed parameter	Temperature rise parameter range (K-m^2 / W)	Value of roughness parameter
Relative roughness height, e/D	P/e = 10 W/w = 6 α = 30^0	$\Delta T/I < 0.00625$	Smooth
		$0.00625 < \Delta T/I < 0.008$	0.019
		$0.008 < \Delta T/I < 0.0095$	0.026
		$0.0095 < \Delta T/I < 0.011$	0.035
		$\Delta T/I > 0.011$	0.043
Relative roughness width, W/w	e/D = 0.043 P/e = 10 α = 30^0	$\Delta T/I < 0.00725$	Smooth
		$0.007 < \Delta T/I < 0.00875$	1
		$0.00875 < \Delta T/I < 0.01025$	2
		$0.01025 < \Delta T/I < 0.011$	3
		$0.011 < \Delta T/I < 0.014$	4
		$0.014 < \Delta T/I < 0.0155$	5
		$\Delta T/I > 0.0155$	6
Angle of attack, α	e/D = 0.043 P/e = 10 W/w = 6	$\Delta T/I < 0.008$	Smooth
		$0.008 < \Delta T/I < 0.01125$	30^0
		$0.01125 < \Delta T/I < 0.012$	45^0
		$\Delta T/I > 0.012$	60^0
Relative roughness pitch, P/e	e/D = .043 W/w = 6 α = 60^0	$\Delta T/I < 0.00775$	Smooth
		$0.00775 < \Delta T/I < 0.01125$	12
		$0.01125 < \Delta T/I < 0.012$	10
		$\Delta T/I > 0.012$	8

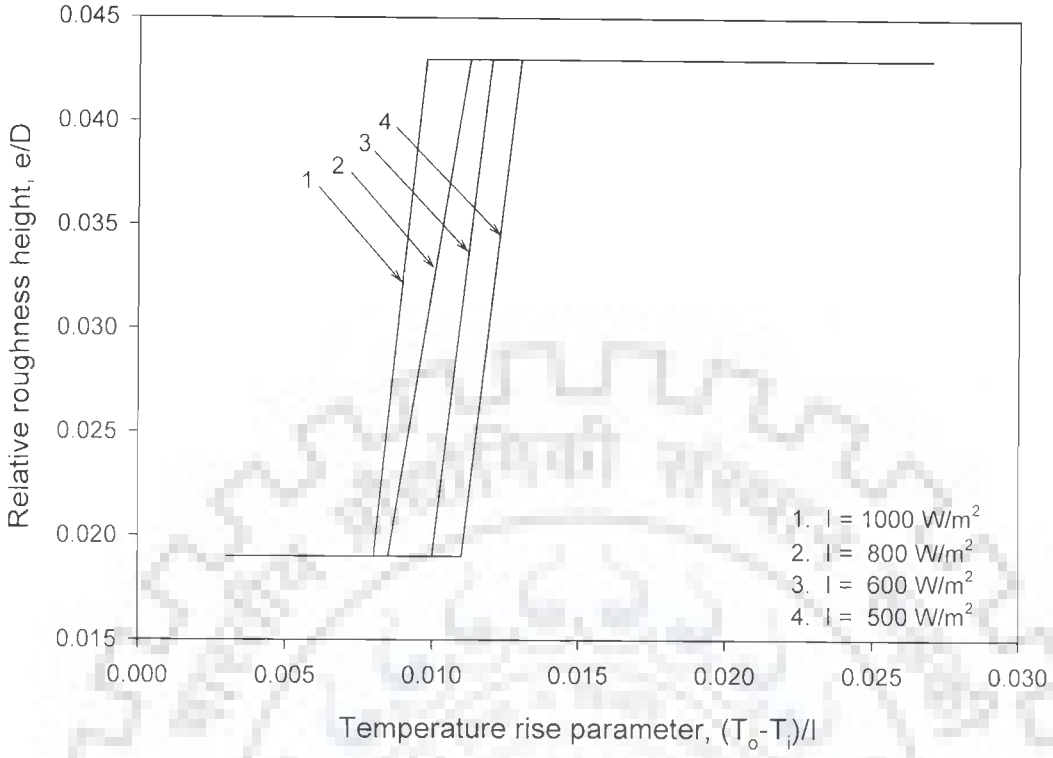

Fig.6.22 Optimum values of relative roughness height on the basis of exergetic efficiency

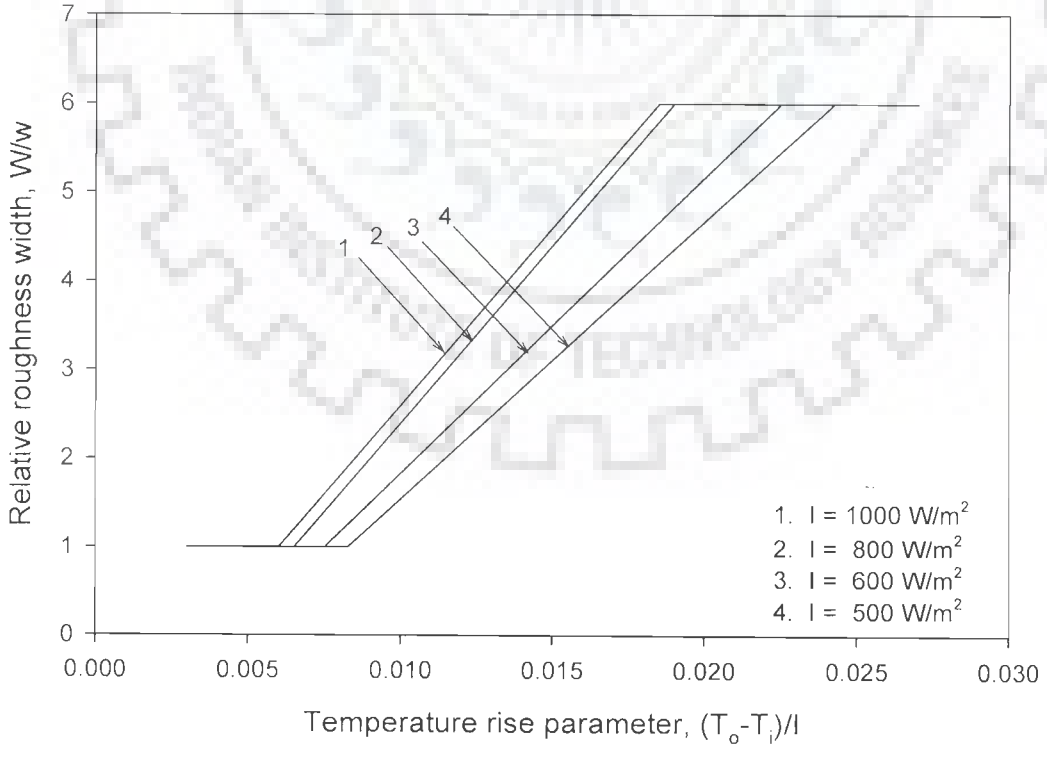

Fig.6.23 Optimum values of relative roughness width on the basis of exergetic efficiency

Fig.6.24 shows the optimum values of angle of attack as a function of temperature rise parameter for various values of insolation. For temperature rise parameter value lower than 0.007 K-m^2/W, the angle of attack value of 30^0 represents the optimum condition for all values of insolation and for values of temperature rise parameter higher than 0.01575 K-m^2/W, the angle of attack value of 60^0 represents the optimum conditions for all the values of insolation. However, for temperature rise parameter range between 0.007 and 0.01575 K-m^2/W, the optimum value of relative roughness height is a function of insolation.

Fig.6.25 shows the optimum values of relative roughness pitch as a function of temperature rise parameter for various values of insolation. For temperature rise parameter value lower than 0.011 K-m^2/W, relative roughness pitch value of 12 represents the optimum condition for all values of insolation and for values of temperature rise parameter higher than 0.01625 K-m^2/W, relative roughness pitch value of 0.043 represents the optimum conditions for all the values of insolation. However, for temperature rise parameter range between 0.011 and 0.01625 K-m^2/W, the optimum value of relative roughness pitch is a function of insolation. The summary of the results has been presented in Table 6.9.

It can be concluded from the above discussion that the maximum value of exergetic efficiency correspond to a set of roughness geometry parameters, i.e., relative roughness height, e/D, relative roughness width, W/w, angle of attack, α and relative roughness pitch, P/e. The optimum values of roughness geometry parameters depend on the operating parameters, temperature rise parameter and insolation. A set of roughness geometry parameters can be directly determined from Figs. 6.22 to 6.25 corresponding to given values of temperature rise parameter and insolation. For example, the typical optimum sets of roughness geometry parameters for three typical design conditions are given in Table 6.10.

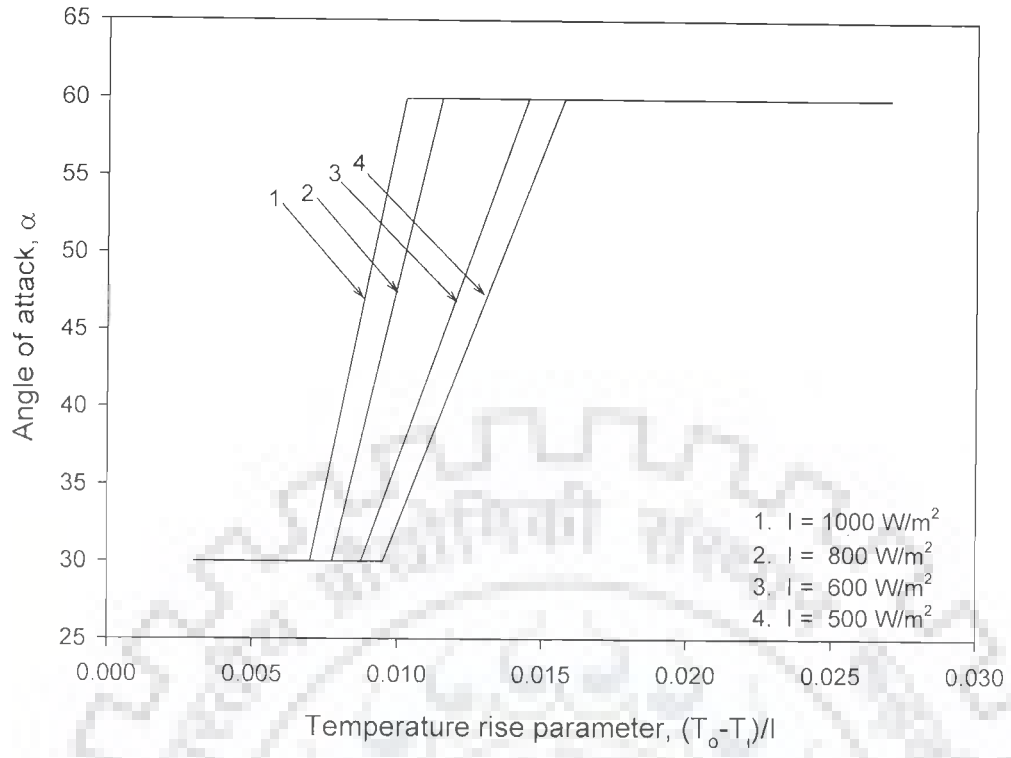

Fig.6.24 Optimum values of angle of attack on the basis of exergetic efficiency

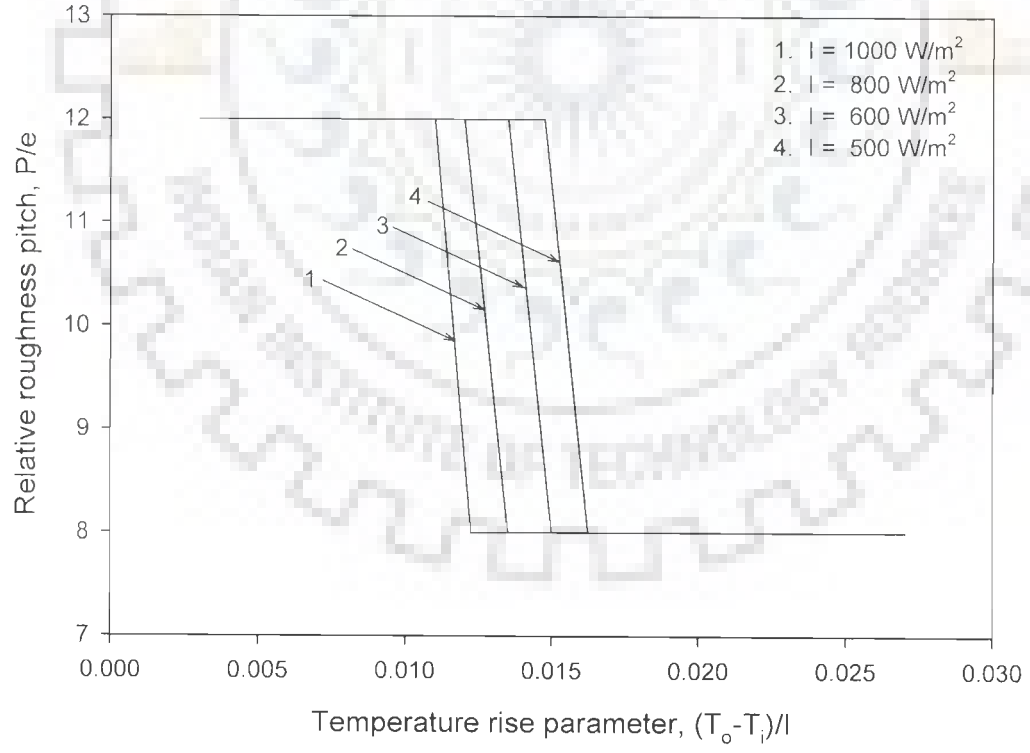

Fig.6.25 Optimum values of relative roughness pitch on the basis of exergetic efficiency

Table 6.9 Optimum values of roughness parameter on the basis of exergetic efficiency

Roughness parameter	Temperature rise parameter range (Km^2 / W)	Value of roughness parameter
Relative roughness height, e/D	$\Delta T/I < 0.008$	0.019
	$0.008 < \Delta T/I < 0.013$	Function of insolation and temperature rise parameter
	$\Delta T/I > 0.013$	0.043
Relative roughness width, W/w	$\Delta T/I < 0.006$	1
	$0.006 < \Delta T/I < 0.02425$	Function of insolation and temperature rise parameter
	$\Delta T/I > 0.02425$	6
Angle of attack, α	$\Delta T/I < 0.007$	30^0
	$0.007 < \Delta T/I < 0.01575$	Function of insolation and temperature rise parameter
	$\Delta T/I > 0.01575$	60^0
Relative roughness pitch, P/e	$\Delta T/I < 0.011$	12
	$0.011 < \Delta T/I < 0.01625$	Function of insolation and temperature rise parameter
	$\Delta T/I > 0.01625$	8

Table 6.10 Optimum values of roughness geometry parameters corresponding to different values of temperature rise parameter on the basis of exergetic efficiency criterion

Solar radiation intensity, I, W/m^2	Temperature rise parameter, $\Delta T/I$	Relative roughness height, e/D	Relative roughness width, W/w	Angle of attack, α	Relative roughness pitch, P/e	Exergetic efficiency
800	0.004	0.019	1	30	12	-0.0013
800	0.006	0.019	1	30	12	0.0062
800	0.015	0.043	4	60	8	0.0207

6.6 COMPARISON OF OPTIMIZATION CRITERIA

In order to compare the optimum values of roughness parameters obtained from various optimization criteria, plots have been prepared for a fixed insolation value of 1000 W/m^2 as shown in Figs.6.26 to 6.29. It can be observed from these plots that on the basis of thermal efficiency criterion, the optimum values of relative roughness height, relative roughness width, angle of attack and relative roughness pitch obtained are 0.043, 6, 60^0 and 8 respectively for the entire range of temperature rise parameter. Hence, a set of roughness parameters, comprising of a single value of each roughness parameter, has been obtained on the basis of thermal efficiency criterion, which represents the optimal artificial roughness geometry for a solar air heater. It can also be seen that no single set represents the optimal values of roughness parameters for the entire range of temperature rise parameter in the case of effective efficiency and exergetic efficiency criteria. The optimum values of roughness parameters have been found to be dependent on temperature rise parameter.

Table 6.11 shows the range of temperature rise parameter for which the optimum values of roughness geometry parameters are same as per the effective efficiency and exergetic efficiency criteria for insolation value of 1000 W/m^2. A similar comparative evaluation for other values of insolation revealed that the temperature rise parameter range, for which the optimum values of roughness geometry parameters are same, is a function of insolation. In Table 6.12, range of temperature rise parameter, for which the optimum values of roughness geometry parameters are different as per effective efficiency and exergetic efficiency criteria, has been presented for all the values of insolation.

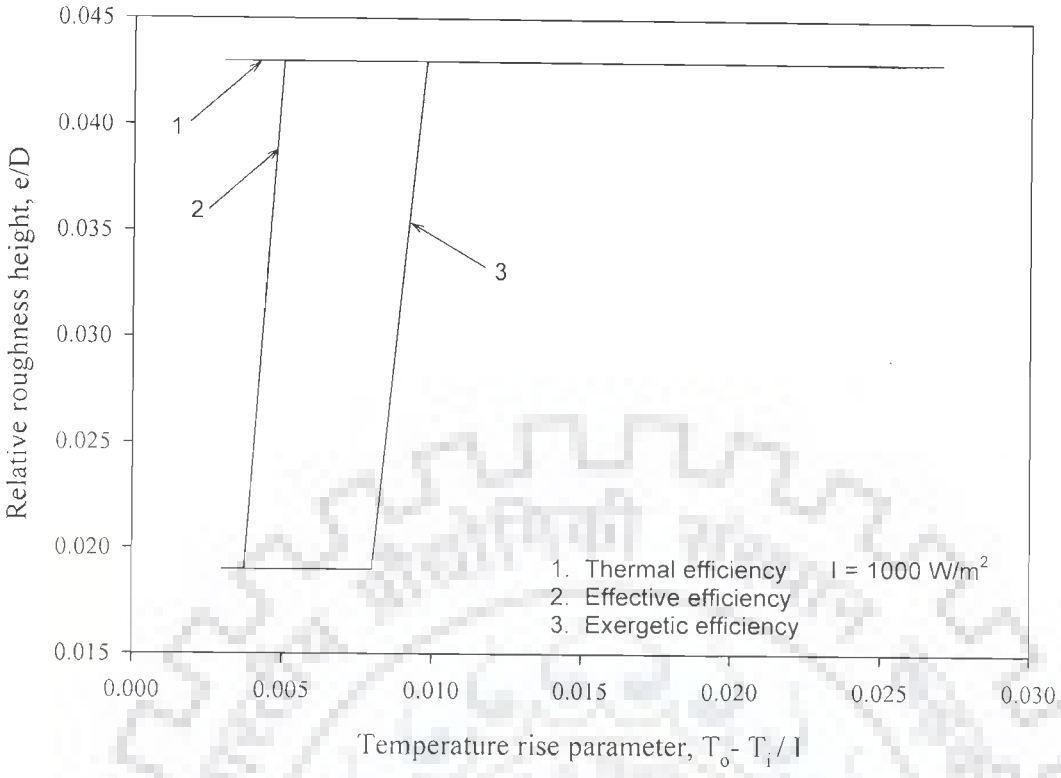

Fig.6.26 Comparison of optimum values of relative roughness height

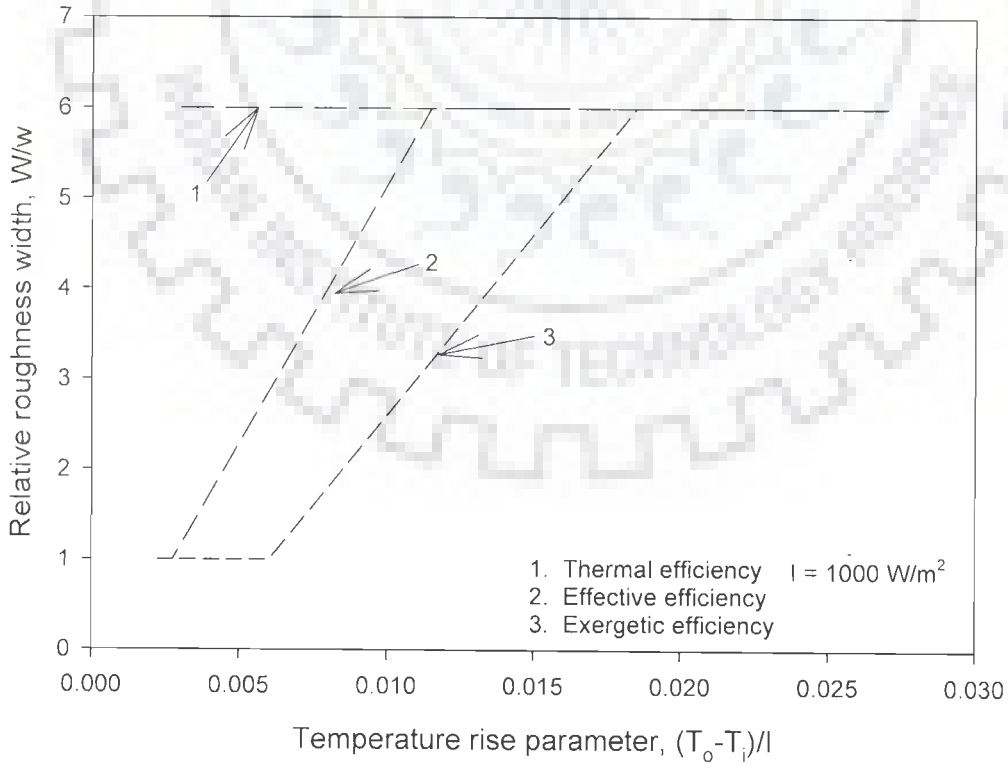

Fig.6.27 Comparison of optimum values of relative roughness width

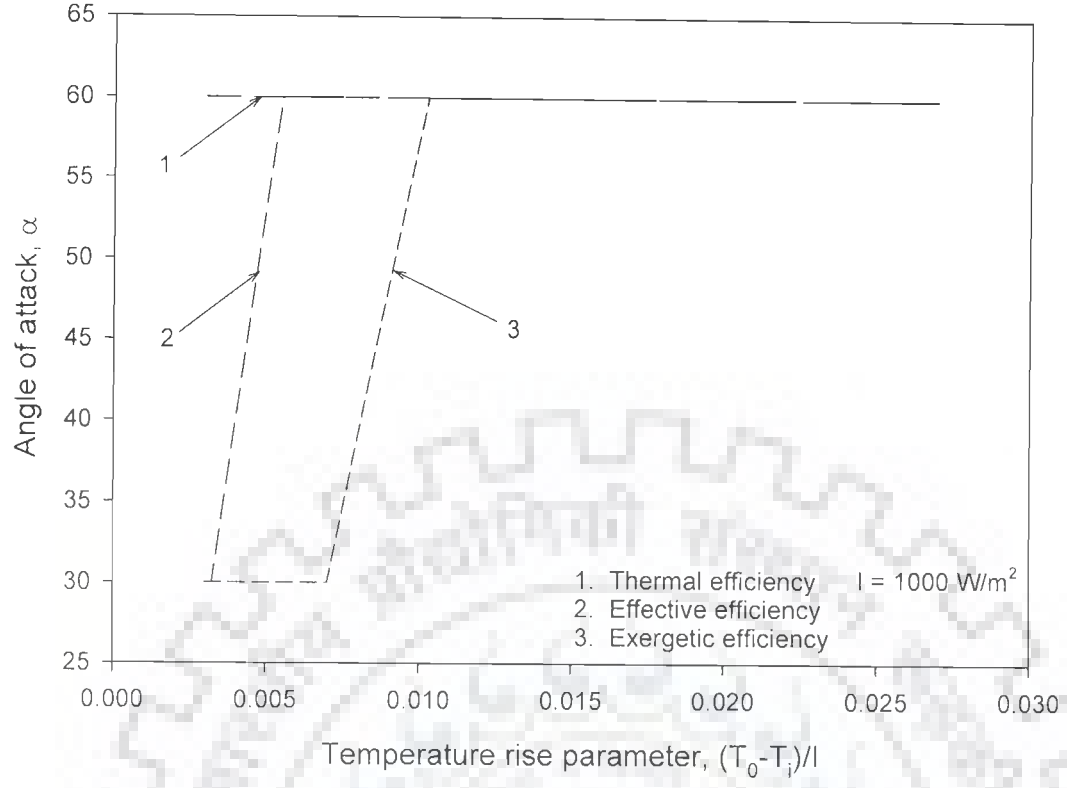

Fig.6.28 Comparison of optimum values of angle of attack

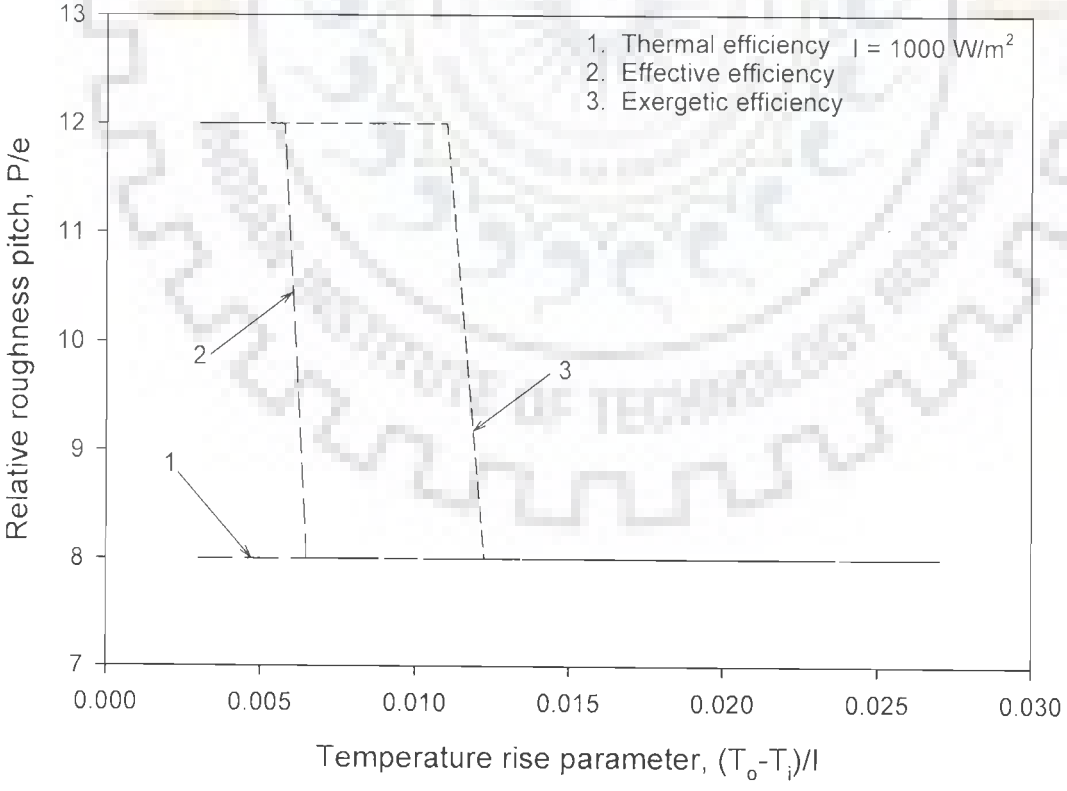

Fig.6.29 Comparison of optimum values of relative roughness pitch

Table 6.11 Temperature rise parameter range having same values of optimum roughness parameters as per effective efficiency and exergetic efficiency criterion ($I = 1000\ W/m^2$)

Roughness parameter	Temperature rise parameter range (Km^2/W)	Value of optimum roughness parameter
Relative roughness height, e/D	$\Delta T/I < 0.00375$	0.019
	$\Delta T/I > 0.00975$	0.043
Relative roughness width, W/w	$\Delta T/I < 0.003$	1
	$\Delta T/I > 0.0185$	6
Angle of attack, α	$\Delta T/I < 0.00325$	30^0
	$\Delta T/I > 0.01025$	60^0
Relative roughness pitch, P/e	$\Delta T/I < 0.00575$	12
	$\Delta T/I > 0.01225$	8

Table 6.12 Range of temperature rise parameter for which optimum roughness parameter values are different as per effective efficiency and exergetic efficiency criteria for different insolation

Insolation (W/m^2)	Roughness parameter	Range of $\Delta T/I$ for which the values are different
1000	Relative roughness height (e/D)	$0.00375 < \Delta T/I < 0.00975$
	Relative roughness width (W/w)	$\Delta T/I < 0.0185$
	Angle of attack (α)	$0.00325 < \Delta T/I < 0.01025$
	Relative roughness pitch (P/e)	$0.00575 < \Delta T/I < 0.01225$
800	Relative roughness height (e/D)	$0.004 < \Delta T/I < 0.001125$
	Relative roughness width (W/w)	$\Delta T/I < 0.019$
	Angle of attack (α)	$0.0035 < \Delta T/I < 0.0115$
	Relative roughness pitch (P/e)	$0.006 < \Delta T/I < 0.0135$
600	Relative roughness height (e/D)	$0.00425 < \Delta T/I < 0.012$
	Relative roughness width (W/w)	$0.003 < \Delta T/I < 0.0225$
	Angle of attack (α)	$0.00375 < \Delta T/I < 0.0145$
	Relative roughness pitch (P/e)	$0.00675 < \Delta T/I < 0.015$
500	Relative roughness height (e/D)	$0.0045 < \Delta T/I < 0.013$
	Relative roughness width (W/w)	$0.00325 < \Delta T/I < 0.02425$
	Angle of attack (α)	$0.004 < \Delta T/I < 0.01575$
	Relative roughness pitch (P/e)	$0.007 < \Delta T/I < 0.01625$

The optimization of performance of solar air heater has been carried out on the basis of thermal performance i.e. thermal efficiency and thermo hydraulic considerations i.e. effective efficiency and exergetic efficiency. It is clear from the above discussion that the different criteria, used for optimization, yield different optimum values of roughness geometry parameters depending on the range of temperature rise parameter. Therefore, it becomes imperative to select the criterion to be used for optimization. Thermal efficiency criterion considers only the useful heat gain without taking into account the pumping power required to propel air through the duct. In roughened solar air heaters, pumping power required to overcome the frictional losses dilutes the benefits of enhancement of heat transfer obtained by using artificial roughness. Therefore, the optimization of performance of solar air heaters should be carried out on the basis of thermo hydraulic considerations namely effective efficiency and exergetic efficiency as it take into account the thermal as well as hydraulic (friction) performance.

It may be noted that optimization based on exergetic efficiency is suitable when a thermodynamic conversion of heat into work is involved and use of solar air heater for work production is not economically viable because of its low temperature range of operation [142, 160]. Exergetic considerations are more relevant for power generation applications where mean temperature is quite high and in low temperature applications net exergy flow is seen to be even negative under certain conditions [61]. On the other hand, thermo hydraulic performance in terms of effective efficiency takes into account the useful thermal gain reduced by equivalent thermal energy required to generate power needed to overcome friction. Hence, effective efficiency criterion has been proposed for thermohydraulic optimization of artificially roughened solar air heaters.

The set of optimum values of roughness geometry parameters determined on the basis of effective efficiency criterion have been used to compute the values of

thermal efficiency of solar air heater with optimum roughness geometry and the plot of thermal efficiency, as shown in Fig.6.30, has been prepared. These plots may be used to determine the thermal efficiency of optimally roughened solar air heater for given values of operating parameters such as temperature rise parameter and insolation.

In context of the above discussion, it may be concluded that it is not always beneficial to operate the system with roughness geometry parameters yielding maximum heat transfer because mechanical energy required for pumping purposes will offset a part of the heat transfer enhancement obtained. Therefore, values of roughness parameters should be so chosen that may yield maximum thermohydraulic benefit.

6.7 DESIGN PROCEDURE

It is clear from the above discussions that there exists a set of roughness geometry parameters that optimizes the performance of a roughened solar air heater and this set comprising of relative roughness height, relative roughness width, angle of attack and relative roughness pitch is a strong function of operating parameters namely temperature rise parameter and insolation. The set of these roughness geometry parameters (based on effective efficiency criterion) can be determined from Figs. 6.10 to 6.13. Fig.6.30 can be used to determine the thermal efficiency of a collector using roughness elements represented by set of optimal roughness geometry parameters. This value of thermal efficiency can be used to determine the optimum area of collector for a given requirement of energy collection rate.

The following example explains the simple optimum design methodology for the solar air heater having absorber plate roughened with repeated multiple v-ribs.

Assuming that a roughened solar air heater is desired for a temperature rise of 20^0C for a place having insolation of 1000 W/m^2, the values of design parameters work out to be as:

Temperature rise parameter, $\Delta T/I$: 0.020

Insolation, I : 1000 W/m^2

The optimum values of roughness geometry parameters have been determined from Figs. 6.10 to 6.13 and are presented in Table 6.13.

Fig.6.30 has been used to obtain the value of thermal efficiency for the roughened solar collector with optimum roughness geometry and this works out to be 0.65. In order to determine the enhancement in performance as a result of providing optimum artificial roughness, the corresponding thermal efficiency for a conventional smooth solar air heater operating under similar conditions has been determined and it works out to be 0.33. Therefore, a solar air heater roughened with multiple v-ribs enhances the thermal efficiency by 97%.

Table 6.13 Optimum values of roughness geometry parameters on the basis of effective efficiency criterion corresponding to given operating conditions

S. No.	Roughness geometry parameter	Optimum value
1.	Relative roughness height, e/D	0.043
2.	Relative roughness width, W/w	6
3.	Angle of attack, α	60^0
4.	Relative roughness pitch, P/e	8

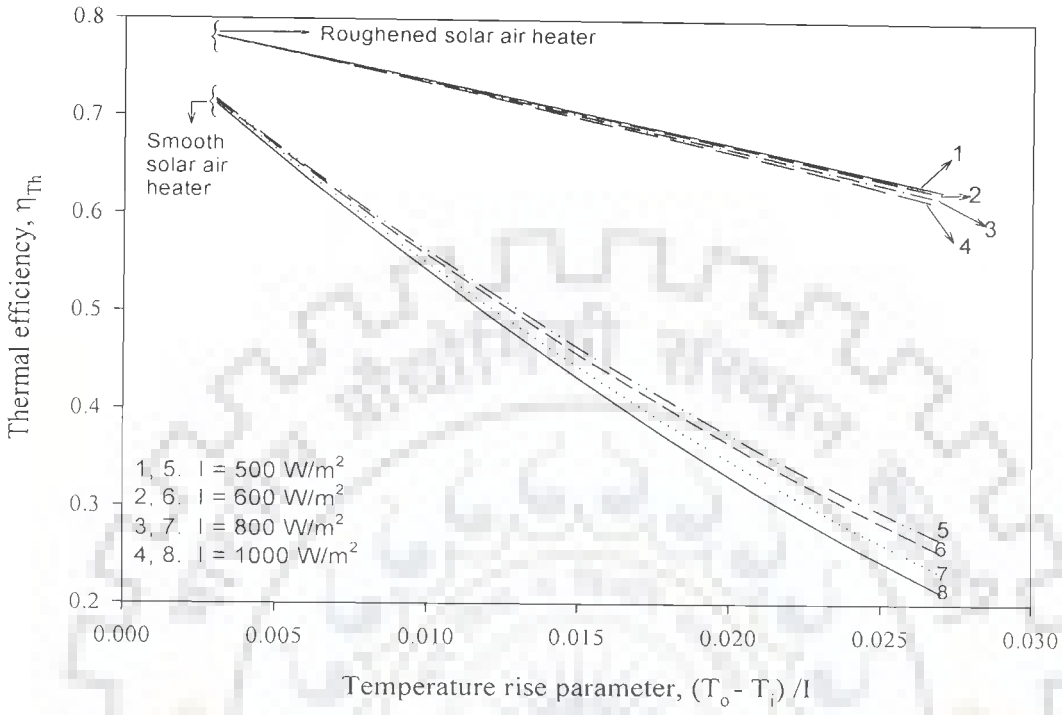

Fig.6.30 Thermal efficiency as a function of temperature rise parameter and insolation for optimum roughness geometry parameters

CHAPTER-7

CONCLUSIONS

An experimental investigation on heat transfer and friction characteristics of airflow in rectangular duct having multiple v-rib roughness geometry on one broad heated wall has been carried out. An experimental set-up comprising rectangular duct having one broad wall heated and roughened with multiple v-rib type of roughness geometry and equipped with control and measuring instruments has been designed and fabricated. The experimental set-up has been used for extensive data collection with respect to data on heat transfer and friction characteristics of flow of air as function of roughness geometry and flow parameters. Data are collected on temperature rise of air in the duct, temperature of the plate and pressure drop across the duct as function of roughness geometry parameters and flow Reynolds number. The range of parameters for investigation was decided on the basis of practical considerations of system and operating conditions for solar air heater. The range of parameters covered in this investigation is given below:

Roughness and flow parameters	**Range of parameters**
Relative roughness height, e/D	0.019 – 0.043 (4 values)
Relative roughness width, W/w	1 – 10 (8 values)
Angle of attack, α	30° – 75° (4 values)
Relative roughness pitch, P/e	6 – 12 (4 values)
Reynolds number, Re	2000 – 20000 (10 values)

Experimentation was carried out on 38 sets of roughened surfaces having different values of roughness geometry parameters to collect heat transfer and friction data. In addition to these, a smooth surface has also been tested with the objective of

comparison to determine the enhancement in Nusselt number and friction factor as a result of providing multiple v-rib roughness. The data has been presented in terms of Nusselt number and friction factor as function of roughness geometry and flow parameters to bring out the effect of these parameters on the enhancement of heat transfer coefficient and friction factor as a result of providing artificial roughness. The experimental data have also been used to develop correlations for Nusselt number and friction factor in terms of roughness geometry parameters and Reynolds number. These correlations have been used to predict the performance of solar air heaters employing artificial roughness in the form of multiple v-ribs. Optimum values of roughness geometry parameters as a function of operating conditions of solar air heater have been determined on the basis of '*thermal efficiency*', '*effective efficiency*' and '*exergetic efficiency*' criteria. Design plots have been prepared for obtaining values of optimum roughness geometry parameters to yield the best thermohydraulic performance.

The following conclusions have been drawn on the basis of the present experimental investigation:

1. Experimental set-up has been validated by collecting data for obtaining values of Nusselt number and friction factor for conventional smooth duct and comparing these values with those obtained from Dittus Boelter and modified Blasius correlations. The average absolute percentage deviation of the experimental Nusselt number and friction factor has been found to be 2.70 % and 2.67 % respectively as compared to those obtained from these correlations. This comparison ensures accuracy of the experimental data collected with the present set-up.

2. An uncertainty analysis as proposed by Kline and McClintock [157] was carried out for selection of instruments and prediction of uncertainty associated with the experimental results based on the accuracy of various

instruments used. The maximum uncertainties in the values of major parameters for all sets of test runs as follows:

Reynolds number = ± 3 %

Nusselt number = ± 6.31%

Friction factor = ± 5.97 %

3. For the entire range of Reynolds number, Nusselt number and friction factor increase monotonically with increase in relative roughness height. It is attributed to the fact that increase in relative roughness height makes the rib to protrude more into turbulent core of the flow resulting in an increase in turbulence as also Nusselt number and friction factor.

4. Nusselt number increases with increase in relative roughness width, attains a maximum value corresponding to relative roughness width value of 6 and with further increase in the value of relative roughness width, Nusselt number decreases. However, friction factor increases with increase in relative roughness width and attains a maximum value corresponding to relative roughness width value of 10. As the relative roughness width is increased, heat transfer increases on account of formation of higher number of leading ends and secondary flow cells while very large number of secondary flow calls beyond a certain limit impedes the development of such cells resulting in a decrease of Nusselt number.

5. Nusselt number and friction factor increase with increase in angle of attack and attain the maximum values corresponding to angle of attack value of 60^0. With further increase in the value of angle of attack beyond 60^0, Nusselt number and friction factor decrease. It has been observed that there exists an angle of attack value for which both Nusselt number and the friction factor attain maximum values.

6. Nusselt and friction factor attain maximum values corresponding to relative roughness pitch value of 8 and on either side of this value, decrease in Nusselt number and friction factor has been observed. It is due to the fact that flow separation occurs downstream of a rib and reattachment of free shear layer may not occur if relative roughness pitch is less than about 6-8 and maximum heat transfer occurs in the vicinity of reattachment point.

7. The values of geometrical parameters of multiple v-rib roughness geometry for which enhancement ratios of Nusselt number and friction factor attain maximum values are:

Roughness parameter	**Fixed parameter**	**Value of roughness parameter**	**Maximum value of enhancement ratio, Nu/Nu_s**
Relative roughness height, e/D	P/e = 10 W/w = 6 $\alpha = 30^{o}$	0.043	4.0
Relative roughness width, W/w	e/D = 0.043 P/e = 10 $\alpha = 30^{o}$	6	4.80
Angle of attack, α	e/D = 0.043 P/e = 10 W/w = 6	60^{0}	5.70
Relative roughness pitch, P/e	e/D = 0.043 W/w = 6 $\alpha = 60^{o}$	8	6.18

Roughness parameter	Fixed parameter	Value of roughness parameter	Maximum value of enhancement ratio, f/f_s
Relative roughness height, e/D	P/e = 10 W/w = 6 $\alpha = 30^0$	0.043	3.7
Relative roughness width, W/w	e/D = 0.043 P/e = 10 $\alpha = 30^0$	10	3.90
Angle of attack, α	e/D = 0.043 P/e = 10 W/w = 6	60^0	4.70
Relative roughness pitch, P/e	e/D = .043 W/w = 6 $\alpha = 60^0$	8	5.20

8. Following correlations have been developed for Nusselt number and friction factor in terms of roughness geometry parameters (relative roughness height, relative roughness width, angle of attack and relative roughness pitch) and flow parameters (Reynolds number) from the experimental data by using regression analysis:

$$Nu = 3.35\times10^{-5}\ \mathrm{Re}^{0.92}\left(\frac{e}{D}\right)^{0.77}\left(\frac{W}{w}\right)^{0.43}\left(\frac{\alpha}{90}\right)^{-0.49}\exp[-0.1177(ln(W/w))^2]$$
$$\times\exp[-0.61(ln(\alpha/90))^2]\left(\frac{P}{e}\right)^{8.54}\exp[-2.0407\ (ln(P/e))^2]$$

$$f = 4.47x10^{-4}\ \mathrm{Re}^{-0.318}\left(\frac{e}{D}\right)^{0.73}\left(\frac{W}{w}\right)^{0.22}\left(\frac{\alpha}{90}\right)^{-0.39}\exp\left(-0.52(ln(\alpha/90))^2\right)\left(\frac{P}{e}\right)^{8.9}\exp\left(-2.133\,(ln(P/e))^2\right)$$

The comparison of experimental values of Nusselt number and friction factor with those predicted by the respective correlation shows that about 95 % of the data points lie within ±10 % deviation lines for Nusselt number and average

absolute percentage deviation is 4.45 % for all data points, while in case of friction factor, 96 % of data points are within ± 10 % deviation lines and average absolute percentage deviation is 4.00 % for all data points.

9. Analytical prediction of thermal as well as thermohydraulic performance of artificially roughened solar air heater ducts has been carried out using heat transfer coefficient and friction factor values as predicted by correlations developed in this work. The values of thermal efficiency, effective efficiency and exergetic efficiency have been determined as function of roughness parameters (e/D, W/w, α and P/e) and operating parameters ($\Delta T/I$ and I) of the solar air heater.

10. It has been found that thermal efficiency increases with increase in Reynolds number and becomes almost asymptotic in higher range of Reynolds number. The maximum absolute value of thermal efficiency has been found to be 77.13% corresponding to relative roughness height value of 0.043, relative roughness width value of 6, angle of attack value of 60^0 and relative roughness pitch value of 8.

11. Use of multiple v-ribs brings about considerable enhancement in the thermal performance of solar collector system. The thermal efficiency of multiple v-rib roughened solar collector system has been found to be 1.13-2.45 times that of a smooth solar collector system in the range of parameters investigated.

12. Based on the effective efficiency optimization criterion, the optimum values of relative roughness height has been found to be 0.019 and 0.043 for temperature rise parameter values less than 0.00375 K-m^2/W and higher than 0.006 K-m^2/W respectively. For temperature rise parameter value between 0.00375 and 0.006 K-m^2/W, the optimum value of relative roughness height varies between 0.019 and 0.043.

13. Based on the effective efficiency optimization criterion, it was found that for temperature rise parameter value less than 0.003 K-m^2/W relative roughness width value of 1 yield the optimum performance and for temperature rise parameters higher than 0.01375 K-m^2/W, the optimum values of relative roughness width is found to be 6. The optimum values of relative roughness width have been found vary between 1 and 5 for temperature rise parameter value between 0.003 and 0.01375 K-m^2/W.

14. Based on the effective efficiency optimization criterion, it was found that for temperature rise parameter values less than 0.00325 K-m^2/W and greater than 0.00675 K-m^2/W, the optimum values of angle of attack are 30^0 and 60^0 respectively. For temperature rise parameter value between 0.00325 and 0.00675 K-m^2/W, the optimum values of angle of attack vary between 30^0 and 60^0.

15. Based on the effective efficiency optimization criterion, it was found that for temperature rise parameter value less than 0.00575 K-m^2/W and greater than 0.008 K-m^2/W, the optimum values of relative roughness pitch have been found to be 12 and 8 respectively. The optimum value of relative roughness pitch has been found to vary between 8 and 12 for temperature rise parameter value between 0.00575 and 0.008 K-m^2/W.

16. There exists a set of optimum values of roughness geometry parameters, which yields the highest value of exergetic efficiency corresponding to a given set of operating conditions. The optimum values of relative roughness height for temperature rise parameter lower than 0.008 K-m^2/W and higher than 0.0013 K-m^2/W have been found to be of 0.019 and 0.043 respectively. The optimum values of relative roughness width have been found to vary between 0.019 and 0.043 for temperature rise parameter range of 0.008 to 0.0013 K-m^2/W.

17. On the basis of exergetic efficiency, it was found that the optimum values of relative roughness width for temperature rise parameter lower than 0.006 K-m^2/W and higher than 0.02425 K-m^2/W are 1 and 6 respectively, while for the temperature rise parameter value between 0.008 and 0.02425 K-m^2/W, the optimum relative roughness width values vary between 1 and 6.

18. On the basis of exergetic efficiency, it was found that the optimum values of angle of attack for temperature rise parameter values lower than 0.007 K-m^2/W and higher than 0.01575 K-m^2/W are 30° and 60° respectively. For temperature rise parameter values between 0.007 and 0.01575 K-m^2/W, the optimum value of angle of attack has been found to vary between 30^0 and 60^0.

19. On the basis of exergetic efficiency, it was found that the optimum values of relative roughness pitch for temperature rise parameter values less than 0.011 K-m^2/W and greater than 0.01625 K-m^2/W have been found to be 12 and 8 respectively, while for the temperature rise parameter values between 0.011 and 0.01625 K-m^2/W, the optimum value of relative roughness pitch varies between 8 and 12.

20. It has been observed that there exists an upper and lower limit of temperature rise parameter value, beyond which the optimum roughness geometry parameters obtained on the basis of effective efficiency and exergetic efficiency criteria are same.

21. The optimization method based on effective efficiency criterion seems to be more suitable for solar air heaters as compared to exergetic efficiency criterion as exergetic criterion is more suitable when a thermodynamic conversion of heat into work is involved.

22. Plots have been prepared to depict the values of individual roughness geometry parameters that represent the optimum condition as a function of temperature rise parameter and insolation. The designer can obtain the optimum values of individual roughness geometry parameters for given set of operating conditions.

Summarizing on the basis of the experimental investigation carried out on a solar air heater roughened with multiple v-ribs, it can be stated that considerable amount of enhancement in Nusselt number has been obtained in comparison with a smooth conventional solar air heater. Empirical correlations developed on the basis of extensive experimental data on heat transfer and friction characteristics can be used to estimate the heat transfer coefficient and friction factor as a function of roughness geometry parameters and operating conditions in a rectangular duct. Optimum values of roughness geometry parameters have been determined on the basis of thermal efficiency, effective efficiency and exergetic efficiency criteria. Design plots have been prepared which can be utilized to obtain a set of optimum values of roughness geometry parameters that will result in the best thermohydraulic performance for given operating conditions. A design procedure has been specified to arrive at the optimum roughness geometry for given set of operating parameters of solar air heater.

APPENDIX-A

SAMPLE CALCULATION FOR ROUGHENED DUCT

Sample calculation for the raw data of test Run Number 6, as listed in Table 2.3 for the roughened duct is given below:

Plate and Duct geometrical data

Duct height, H = 25 mm

Duct width, W = 300 mm

Length of test section, L = 1000 mm

Rib height, e = 1.62 mm

Relative roughness width, W/w = 6.0

Relative roughness pitch, P/e = 10.0

Angle of attack, α = 30°

General data

Diameter of orifice meter, d_2 = 38 mm

Diameter of pipe, d_1 = 81 mm

Density of manometer fluid, ρ_m = 769.8 kg/m^3

A-1 Mean outlet air temperature

The outlet air temperature, T_o is a simple arithmetic mean of the air temperature values measured at the exit of the test section of the duct and is estimated as below.

$$T_o = \frac{T_{26}+T_{27}+T_{28}+T_{29}+T_{30}}{5} \qquad \text{(A-1)}$$

This gives $T_o = \frac{42.3+41+41.6+41.1+43}{5}$

T_o = 41.8 °C or 314.8 K

A-2 Mean bulk air temperature

The bulk mean air temperature, T_f is a simple arithmetic mean of the measured values at the inlet and the exit temperatures of air flowing through the test section. Thus (A-2)

$$T_f = \frac{T_o + T_i}{2}$$

$$T_f = \frac{41.8 + 32.2}{2}$$

T_f = 37 °C or 310 K

A-3 Mean temperature of the absorber plate

The mean plate temperature, T_P is the average of the temperatures recorded at various locations on the absorber plate .The mean plate temperature is evaluated by following relationship,

$$T_p = \frac{T_1 + T_2 + T_3 + T_4 + T_5 + T_6 + T_7 + T_8 + T_9 + T_{10} + T_{11} + T_{12} + T_{13} + T_{14} + T_{15} + T_{16} + T_{17} + T_{18} + T_{19}}{19} \quad \text{(A-3)}$$

This result in

T_p = 52.13 °C or 325.13 K

A-4 Air properties at mean bulk air temperature

The thermo-physical properties of air are determined by using standard correlations [62] as given below,

Kinematics viscosity, $\mu = 1.81 \times 10^{-5} \times \left(\frac{T_f}{293}\right)^{0.735}$ (A-4)

$\mu = 1.88 \times 10^{-5}$ N-s/m^2

Specific heat at constant pressure, $C_p = 1006 \left(\frac{T_f}{293} \right)^{0.0155}$ (A-5)

$C_p = 1006.86$ J/kg K

Thermal conductivity of air, $k = 0.0257 \left(\frac{T_f}{293} \right)^{0.86}$ (A-6)

k = 0.02695 W/m-K

Density of air, $\rho = 97500 / (287.045\ T_f)$ (A-7)

$\rho = 1.097$ kg/m^3

A-5 Mass Flow Rate Measurement

Mass flow rate of air is determined from the pressure drop measurement across the calibrated orifice meter using the following relationship.

$$m = 0.624\, A_o \left[\frac{2\,\rho_a\,(\Delta P)_o}{1-\beta^4} \right]^{0.5} \quad \text{(A-8)}$$

where $(\Delta P)_o = (\Delta h)_o\ \rho_m\ g\ \sin(45°)$

$(\Delta P)_o = 0.225 \times 769.8 \times 9.81 \times \sin(45°)$

$(\Delta P)_o = 1201.47$ N/m^2

Area of orifice $A_o = 1.134 \times 10^{-3}$ m^2

$$m = 0.624 \times 0.001134 \times \left[\frac{2 \times 1.0971201.47}{0.9512} \right]^{0.5}$$

m = 0.03725 kg/sec

A-6 Velocity of Air through duct

The velocity of air is calculated from the values of mass flow rate and area of flow as,

$$V = \frac{m}{\rho\ W\ H} \quad \text{(A-9)}$$

$$V = \frac{0.03725}{1.097 \times 0.3 \times 0.025} = 4.527 \text{ m/s}$$

A-7 Equivalent Hydraulic Diameter

The hydraulic diameter of the rectangular section of the duct is determined from the relationship as given below,

D = (4 x Area of flow) / Wetted perimeter

$$= \frac{4(W \times H)}{2(W + H)} \qquad \text{(A-10)}$$

This gives,

$$D = \frac{4 \times (0.30 \times 0.025)}{2 \times (0.30 + 0.025)}$$

D = 0.04615 m

A-8 Reynolds Number (Re)

The Reynolds number of air flow in the duct is calculated from the following relationship,

$$\text{Re} = \frac{\rho V D}{\mu} \qquad \text{(A-11)}$$

$$\text{Re} = \frac{1.097 \times 4.527 \times 0.04615}{1.88 \times 10^{-5}}$$

Re = 12191

A-9 Friction Factor (f)

The friction factor is determined from the measured values of pressure drop $(\Delta P)_d$ across the test section length using Darcy-Weisbach equation as,

$$f = \frac{2(\Delta P)_d D}{4 \rho L V^2} \qquad \text{(A-12)}$$

$$f = \frac{2\times(21.9)\times 0.04615}{4\times 1.097\times 1\times(4.527)^2} = 0.02247$$

A-10 Heat Transfer Coefficient (h)

Heat transfer rate "Q_u" from the roughened plate to the air is determined as

$$Q_u = m\, C_p\, (T_o - T_i) \qquad \text{(A-13)}$$

$$Q_u = 0.03725 \times 1006.86 \times (41.8-32.2)$$

$$Q_u = 360 \text{ W}$$

The heat transfer coefficient for the heated test section is calculated from the relationship as below,

$$h = \frac{Q_u}{A_p.(T_p - T_f)} \qquad \text{(A-14)}$$

This gives,

$$h = \frac{360}{0.3\times(325.13-310)}$$

$h = 79.31 \text{ W/m}^2\text{-K}$

A-11 Nusselt Number (Nu)

The heat transfer coefficient is used to determine the Nusselt number, which is expressed as below,

$$Nu = \frac{h\,D}{k} \qquad \text{(A-15)}$$

This gives

$$Nu = \frac{79.31\times 0.04615}{0.02697}$$

$Nu = 135.71$

APPENDIX-B

UNCERTAINTY ANALYSIS

B-1 INTRODUCTION

Regardless of the fact that maximum possible care and precautions are normally taken during the experimentation, errors do creep into the measurement of parameters as the least count of the instruments used and the methods employed to measure give rise to some degree of error or inaccuracy in the measurements. Therefore, estimation of inaccuracy in measurement during any experiment is necessary. The degree of inaccuracy or the total measurement error is the difference between the measured quantity and true value. The total error is the sum of the bias error and the precision errors. The bias error is fixed, systematic or constant component of the total error and sometimes referred to simply as the bias. This can be reduced through careful calibration of probes and instruments in terms of a correction. The precision error is the random component of the total error and is sometimes called the repeatability error. This may be quantified statistically and may be combined by the quadrate rule (Pythagorean summation). It can not be eliminated altogether, but may be reduced to an extent by replication, i.e. by repeated measurements with time and space. Since the true value of the quantity is not known, the true magnitude of the error can not be evaluated. The best possible way to estimate the magnitude of the error is therefore termed as "Uncertainty". It gives a range in which the true value lies. The best estimation of a parameter is therefore, associated with the uncertainty range as equi-probable plus and minus value in which the value of the parameter is expected to lie.

A methodology of estimating uncertainty in experimental results has been suggested by Kline and McClintock [157], which is used in this work. The procedure is listed as below,

B-2 UNCERTANTY IN MEASURED PARAMETER

The possible error in the experiment must be examined before the experiments are conducted and this helps in selection of proper instruments for the experiment. Hence error analysis initially has been carried out, using hypothetical data to identify the critical instruments. The final analysis carried out using experimental data is only being presented here. Uncertainty in various measured parameters for the present experimental work is given in Table B.1. The list of various measured parameters, instruments used for their measurements with their least counts and uncertainty used are given in Table B.2. Uncertainty due to instrument should be equal to the half of the least count of the instrument. This means that the measurements from a particular instrument are expected to lie within ± half of its least count. However, in general, uncertainty in measurements is taken equal to the least count of the instrument to ensure the mean of the repeated measurements to lie within the uncertainty domain. Therefore, the uncertainty due to linear scale, vernier calipers, micro-manometer, inclined U-tube manometer is taken as the least count of the measuring instrument.

Table B.1: Uncertainty interval of various measurements [161]

Sl. No.	Measurement	Symbol	Instrument	Least count of instruments	Uncertainty
1	Dimension of duct:				
	Width	W	Vernier Calipers	0.05 mm	± 0.05 mm
	Depth	H	Vernier Calipers	0.05mm	± 0.05 mm
	Length	L	Linear scale	1 mm	± 1 mm/1m
2	Pressure drop in the duct.	$(\Delta P)_d$	Micro-manometer	0.001 mm of kerosene	± 0.001
3	Pressure drop across the orifice plate	$(\Delta P)_o$	Inclined U-tube Manometer	1 mm of kerosene	± 1 mm
4	Temperature measurement		Cu-Cn thermocouples		± 0.25 °C
5	Rib dimensions				
	Rib height	e	Vernier Calipers	0.05mm	± 0.05 mm
	Rib width	w	Vernier Calipers	0.05mm	± 0.05 mm
	Rib pitch	P	Vernier Calipers	0.05mm	± 0.05 mm
6	Atmospheric pressure		Mercury barometer	0.05 mm	± 0.05 mm of Hg
7	Orifice plate and Throat diameter		Vernier Calipers	0.05 mm	± 0.05 mm
8	Current and	I	Digital Ammeter,	0.01 A	± 0.01 A
	voltage	V	Voltmeter	0.1 V	± 0.1 V

B-3 COMPUTATION OF UNCERTAINTY IN PARAMETERS

The uncertainty analysis as proposed by Kline and McClintock [157] was used to calculate the uncertainty associated with experimental results, based on the observations of the scatter in the measured values used in calculating the result.

If a parameter is calculated using certain measured quantities as,

$$y = y(x_1, x_2, x_3, \ldots\ldots\ldots\ldots, x_n) \quad \text{(B-1)}$$

Then uncertainty in measurement of "y" is given as follows:

$$\frac{\delta y}{y} = \left[\left(\frac{\delta y}{\partial x_1} \delta x_1 \right)^2 + \left(\frac{\delta y}{\partial x_2} \delta x_2 \right)^2 + \left(\frac{\delta y}{\partial x_3} \delta x_3 \right)^2 + \ldots\ldots\ldots + \left(\frac{\delta y}{\partial x_n} \delta x_n \right)^2 \right]^{0.5} \quad \text{(B-2)}$$

where, δx_1, δx_2, δx_3, ..., δx_n are the possible errors in measurements of $x_1, x_2, x_3, \ldots\ldots, x_n$

δy is known as absolute uncertainty

$\delta y/y$ is known as relative uncertainty.

In the present investigation, the important parameters are:

(i) Reynolds number (Re) $\mathrm{Re} = \dfrac{\rho V D}{\mu}$ (B-3)

(ii) Heat transfer coefficient (h) $h = \dfrac{mC_p \Delta T}{A_p (T_p - T_f)}$ (B-4)

(iii) Nusselt number (Nu) $Nu = \dfrac{hD}{k}$ (B-5)

(iv) Friction factor (f_r) $f_r = \dfrac{2 (\Delta P)_d D}{4 \rho L V^2}$ (B-6)

To illustrate the procedure for the uncertainty analysis, the relevant data for the sample calculation is given in Table B.2.

Table B.2 Values of measured parameters

S.N.	Measured parameters	Symbol	Value
1	Test length of duct	L	1000 mm
2	Width of duct	W	300 mm
3	Height of the duct	H	25 mm
4	Diameter of pipe	D_1	81 mm
5	Diameter of orifice-meter	D_2	38 mm
6	Head drop across orifice-meter	$(\Delta h)_o$	225 mm of kerosene column
7	Pressure drop across test section	$(\Delta P)_d$	21.9 Pascal
8	Atmospheric pressure	P_{atm}	98.95 kN/ m^2
9	Outlet temperature of air	To	41.8 °C
10	Inlet temperature of air	Ti	32.2 °C
11	Rise in temperature of air	ΔT	9.6 °C
12	Mean bulk air temperature	T_f	36.7 °C
13	Mean plate temperature	Tp	52.13 °C
14	Mass flow rate of air	M	0.03725 kg/s
15	Heat transfer to air	Qu	360 W
16	Heat transfer coefficient	h	79.31 W/m^2K
17	Nusselt number	Nu	135.71
18	Friction factor	f	0.02247

The thermo-physical properties of air were determined using standard correlations (Eqs. B-3 to B-6) as given below,

$$\mu = 1.81 \times 10^{-5} \times (T_f/293)^{0.735}$$

$$C_p = 1006 \times (T_f/293)^{0.0155}$$

$$k = 0.0257 \times (T_f/293)^{0.86}$$

$$\rho = 97500 / (287.045 \times T_f)$$

B-3.1 Area of the absorber plate (A_p)

$$A_p = W L$$

$$\delta A_p = \left[\left(\frac{\delta A_p}{\delta L} \times \delta L \right)^2 + \left(\frac{\delta A_p}{\delta W} \times \delta W \right)^2 \right]^{0.5}$$

$$\delta A_p = \left[(W \times \delta L)^2 + (L \times \delta W)^2 \right]^{0.5}$$

$$\frac{\delta A_p}{A_p} = \left[\left(\frac{W \times \delta L}{W \times L} \right)^2 + \left(\frac{L \times \delta W}{W \times L} \right)^2 \right]^{0.5}$$

$$\frac{\delta A_p}{A_p} = \left[\left(\frac{\delta L}{L} \right)^2 + \left(\frac{\delta W}{W} \right)^2 \right]^{0.5}$$

$$\frac{\delta A_p}{A_p} = \left[\left(\frac{1}{1000} \right)^2 + \left(\frac{0.05}{300} \right)^2 \right]^{0.5}$$

$= 0.00101$ or 0.101%

Therefore the area of absorber plate, $A_p = 0.3 \times 1.0 \pm 0.00101$ m^2

$= 0.3 \pm (3.03 \times 10^{-4})$ m^2

B-3.2 Area of flow (A_c)

$A_c = W\,H = 300 \times 25 = 7500$ mm^2

$$\delta A = \left[\left(\frac{\delta A}{\delta W} \times \delta W \right)^2 + \left(\frac{\delta A}{\delta H} \times \delta H \right)^2 \right]^{0.5}$$

$$\delta A = \left[(H \times \delta W)^2 + (W \times \delta H)^2 \right]^{0.5}$$

$$\frac{\delta A}{A} = \left[\left(\frac{H \times \delta W}{W \times H} \right)^2 + \left(\frac{W \times \delta H}{W \times H} \right)^2 \right]^{0.5}$$

$$\frac{\delta A}{A} = \left[\left(\frac{\delta W}{W} \right)^2 + \left(\frac{\delta H}{H} \right)^2 \right]^{0.5}$$

or $$\frac{\delta A}{A} = \left[\left(\frac{0.05}{300} \right)^2 + \left(\frac{0.05}{25} \right)^2 \right]^{0.5}$$

= 0.002 or 0.2%

Finally the area of flow $A_c = 7500 \pm 15\ mm^2$

B-3.3 Hydraulic diameter, (D)

$$D = \frac{4 \times A}{P} = \frac{4 \times W \times H}{2 \times (W + H)}$$

$= (WH)\ (W+H)^{-1}$

$\partial D/\partial H = 2WH(-1)(W+H)^{-2} + (W+H)^{-1}\ (2W)$

$$\frac{\partial D}{\partial H} = \frac{-2WH}{(W+H)^2} + \frac{2W}{W+H}$$

$$= \frac{2W}{W+H} - \frac{2WH}{(W+H)^2}$$

$$\frac{\partial D}{\partial H} = \frac{2 \times 300}{300 + 25} - \frac{2 \times 300 \times 25}{(300 + 25)^2}$$

= 1.70

$$\frac{\partial D}{\partial W} = \frac{2H}{W+H} - \frac{2WH}{(W+H)^2}$$

$$\frac{\partial D}{\partial W} = \frac{2 \times 25}{300 + 25} - \frac{2 \times 300 \times 25}{(300 + 25)^2}$$

= 0.012

$$\delta D = \left[\left(\frac{\delta D}{\delta H} \times \delta H \right)^2 + \left(\frac{\delta D}{\delta W} \times \delta W \right)^2 \right]^{0.5}$$

$$\frac{\delta D}{D} = \frac{\left[\left(\frac{\delta D}{\delta H} \times \delta H \right)^2 + \left(\frac{\delta D}{\delta W} \times \delta W \right)^2 \right]^{0.5}}{2 \times (W \times H)(W+H)^{-1}}$$

$$\frac{\delta D}{D} = \frac{\left[(1.70 \times 0.05)^2 + (0.012 \times 0.05)^2 \right]^{0.5}}{2 \times (300 \times 25)(300+25)^{-1}}$$

= 0.00184 or 0.184%

Therefore hydraulic diameter D = 0.04615 ± 0.000085 m

B-3.4 Area of orifice meter (A_2)

$A_2 = (\pi/4)d_2^2$

$$\frac{\partial A_2}{\partial d_2} = \frac{2 \times \pi \times d_2}{4}$$

$$\delta A_2 = \left[\left(\frac{\delta A_2}{\delta d_2} \times \delta d_2 \right)^2 \right]^{0.5}$$

$$\text{or } \delta A_2 = \left[\left(\frac{\pi \times d_2}{2} \times \delta d_2 \right)^2 \right]^{0.5}$$

$$\text{or } \delta A_2 = \frac{\pi \times d_2 \times \delta d_2}{2}$$

$$\frac{\delta A_2}{A_2} = \frac{(\pi/2) d_2 \times \delta d_2}{(\pi/4) d_2^{\,2}} = \frac{2 \times \delta d_2}{d_2}$$

$=2(0.05)/38$

$= 0.0026$ or 0.26%

Therefore, area of orifice meter including uncertainty can be written as

$A_2 = 0.001134 \pm (2.95 \times 10^{-6})\ m^2$

B-3.5 Density (ρ_o)

$$\rho_0 = \frac{P_{atm}}{R \times T_o}$$

$$\frac{\partial \rho_o}{\partial P_{atm}} = \frac{1}{RT_o} \quad \alpha \quad \frac{P_{atm}}{T_o} \quad \text{or} \quad \frac{\partial \rho_o}{\partial P_{atm}} = \frac{1}{(RT_o)^2} \quad \text{or} \quad \frac{\partial \rho_o}{\partial T_o} = \frac{P_{atm}}{(RT_o)^2}$$

$$\delta \rho_o = \left[\left(\frac{\delta \rho_o}{\delta P_{atm}} \times \delta P_{atm} \right)^2 + \left(\frac{\delta \rho_o}{\delta T_o} \times \delta \rho_o \right)^2 \right]^{0.5}$$

$$\delta\rho_o = \left[\left(\frac{1}{RT_o}\times\delta P_{atm}\right)^2 + \left(\frac{-P_{atm}}{(RT_o)^2}\times\delta T_o\right)^2\right]^{0.5}$$

$$\frac{\delta\rho_o}{\rho_o} = \left[\left(\frac{\delta\rho_{atm}\times RT_o}{RT_oP_{atm}}\right)^2 + \left(\frac{-P_{atm}\times\delta T_oRT_o\delta\rho_o}{(RT_o)^2\times P_{atm}}\right)^2\right]^{0.5}$$

$$\frac{\delta\rho_o}{\rho_o} = \left[\left(\frac{\delta P_{atm}}{P_{atm}}\right)^2 + \left(-\frac{\delta T_o}{RT_o}\right)^2\right]^{0.5} \quad \alpha \quad \left[\left(\frac{\delta P_{atm}}{P_{atm}}\right)^2 + \left(-\frac{\delta T_o}{T_o}\right)^2\right]^{0.5}$$

$$= \left[\left(\frac{0.1}{740.4}\right)^2 + \left(-\frac{0.25}{36.7}\right)^2\right]^{0.5}$$

$= 6.81 \times 10^{-3}$ or 0.681%

Finally the density of air including uncertainty $\rho_0 = 1.097 \pm 0.0075$ kg/m^3

B-3.6 Mass flow rate, m

$$m = C_d \times A_o \times \left[\frac{2\times P_a\times(\Delta P)_o}{RT_O}\right]^{0.5}$$

Or $m = m\left(C_d, A_2, P_a, T_o, (\Delta P)_o\right)$

$$\frac{\partial m}{\partial C_d} = A_2(K)^{0.5}$$

where $K = \sqrt{\dfrac{2\times P_a\times(\Delta P)}{R\times T_O}}$

$$\frac{\partial m}{\partial A_2} = C_d(K)^{0.5}$$

$$\frac{\partial m}{\partial P_a} = \frac{(K)^{0.5}\times A_2\times C_d\times(P_a)^{-1}}{2}$$

$$\frac{\partial m}{\partial(\Delta P)_o} = \frac{(K)^{0.5}\times A_2\times C_d\times(\Delta P)_o^{-1}}{2}$$

$$\frac{\partial m}{\partial T_0} = \frac{(K)^{0.5} \times A_2 \times C_d \times (T_o)^{-1}}{2}$$

$$\delta m = \left[\left(\frac{\delta m}{\delta C_d} \times \delta C_d \right)^2 + \left(\frac{\delta m}{\delta A_2} \times \delta A_2 \right)^2 + \left(\frac{\delta m}{\delta T_o} \times \delta T_o \right)^2 + \left(\frac{\delta m}{\delta P_a} \times \delta P_a \right)^2 + \left(\frac{\delta m}{\delta (\Delta P)_o} \times \delta (\Delta P)_o \right)^2 \right]^{0.5}$$

$$\frac{\delta m}{m} = \left[\left(\frac{\delta C_d}{C_d} \right)^2 + \left(\frac{\delta A_2}{A_2} \right)^2 + \frac{1}{4}\left(\frac{\delta T_o}{T_o} \right)^2 + \frac{1}{4}\left(\frac{\delta P_a}{P_a} \right)^2 + \frac{1}{4}\left(\frac{\delta (\Delta P)_o}{(\Delta P)_o} \right)^2 \right]^{0.5}$$

From calibration chart of orifice meter, the value of $\delta C_d/C_d$=1.6%, The uncertainty $(\Delta P)_o$, for U-tube manometer = 0.2 mm [65], Manometer inclination angle = 45°

$(\Delta P)_o$ = 9.81x 0.7698 x 225 x sin 45

= 159 mm

$$\frac{\delta m}{m} = \left[\left(\frac{1.6}{100} \right)^2 + (0.0026)^2 + \frac{1}{4}\left(\frac{0.25}{36.7} \right)^2 + \frac{1}{4}\left(\frac{0.05}{740.4} \right)^2 + \frac{1}{4}\left(\frac{0.2}{159} \right)^2 \right]^{0.5}$$

= 0.01658 or 1.65%

Therefore mass flow rate m = 0.03725 ± 0.00158 kg/s

B-3.7 Velocity of air in test section (V)

$$V = \frac{m}{\rho W H}$$

$$\frac{\delta V}{V} = \left[\left(\frac{\delta m}{m} \right)^2 + \left(\frac{\delta \rho}{\rho} \right)^2 + \left(\frac{\delta W}{W} \right)^2 + \left(\frac{\delta H}{H} \right)^2 \right]^{0.5}$$

$$\frac{\delta V}{V} = \left[(0.01657)^2 + (0.00681)^2 + \left(\frac{0.05}{300} \right)^2 + \left(\frac{0.05}{25} \right)^2 \right]^{0.5}$$

= 0.018 or 1.8%

Therefore the velocity of air including uncertainty V = 4.527 ± 0.0815 m/s

B-3.8 Useful heat gain (Q_u)

$Q_u = m\ Cp\ (T_o - T_i)$ or $Q_u = m\ Cp\ (\Delta T)$

$$\frac{\delta Q_u}{Q_u} = \left[\left(\frac{\delta m}{m}\right)^2 + \left(\frac{\delta C_p}{C_p}\right)^2 + \left(\frac{\delta(\Delta T)}{\Delta T}\right)^2\right]^{0.5}$$

The uncertainty in δC_p =0.1 [65]

The uncertainty in $\delta\mu$ $=0.001 \times 10^{-5}$[65]

The uncertainty in δk =0.00001[65]

The uncertainty in δPr =0.001[65]

$$\frac{\delta Q_u}{Q_u} = \left[(0.01657)^2 + \left(\frac{0.1}{1006.86}\right)^2 + \left(\frac{0.25}{9.6}\right)^2\right]^{0.5}$$

= 0.031 or 3.1%

Hence the useful heat gain including uncertainty Qu = 360 ± 11.1 W

B-3.9 Heat transfer Coefficient (h)

$$h = \frac{Qu}{A_p \cdot (T_p - T_f)} \text{ or } h = \frac{Qu}{A_p \cdot \Delta T}$$

$$\frac{\delta h}{h} = \left[\left(\frac{\delta Q}{Q}\right)^2 + \left(\frac{\delta A_p}{A_p}\right)^2 + \left(\frac{\delta(\Delta T_f)}{\Delta T_f}\right)^2\right]^{0.5}$$

$$\frac{\delta h}{h} = \left[(0.031)^2 + (0.00101)^2 + \left(\frac{0.25)}{15.2}\right)^2\right]^{0.5}$$

= 0.0351 or 3.51%

Finally the heat transfer coefficient h = 79.31 ± 2.78 $W/m^2 K$

B-3.10 Nusselt number (Nu)

$$Nu = \frac{hD}{k}$$

$$\frac{\delta Nu}{Nu} = \left[\left(\frac{\delta h}{h} \right)^2 + \left(\frac{\delta D}{D} \right)^2 + \left(\frac{\delta k}{k} \right)^2 \right]^{0.5}$$

$$\frac{\delta Nu}{Nu} = \left[(0.031)^2 + (0.00185)^2 + \left(\frac{0.00001}{0.02694} \right)^2 \right]^{0.5}$$

$= 0.0351$ or 3.51%

Therefore the Nusselt number Nu = 135.71 ± 4.76

B3.11 Reynolds Number (Re)

$$\mathrm{Re} = \frac{V \cdot D}{\upsilon}$$

$$\frac{\delta \mathrm{Re}}{\mathrm{Re}} = \left[\left(\frac{\delta V}{V} \right)^2 + \left(\frac{\delta \rho}{\rho} \right)^2 + \left(\frac{\delta D}{D} \right)^2 + \left(\frac{\delta \mu}{\mu} \right)^2 \right]^{0.5}$$

$$\frac{\delta \mathrm{Re}}{\mathrm{Re}} = \left[(0.018)^2 + (0.00681)^2 + (0.00184)^2 + \left(\frac{0.001}{1.88} \right)^2 \right]^{0.5}$$

$= 0.01934$ or 1.934%

Finally the Reynolds number Re = 12191 ± 236

B-3.12 Friction factor (f)

$$f = \frac{2 \times (\Delta \mathrm{P})_d \times D}{4 \times \rho \times L \times V^2}$$

$$\frac{\delta f}{f} = \left[\left(\frac{\delta V_d}{V_d} \right)^2 + \left(\frac{\delta \rho}{\rho} \right)^2 + \left(\frac{\delta D}{D} \right)^2 + \left(\frac{\delta L}{L} \right)^2 + \left(\frac{\delta (\Delta P)_d}{(\Delta P)_d} \right)^2 \right]^{0.5}$$

$$\frac{\delta f}{f} = \left[(2 \times 0.018)^2 + (0.00681)^2 + (0.00184)^2 + \left(\frac{1}{1000} \right)^2 + \left(\frac{0.001}{3.493} \right)^2 \right]^{0.5}$$

$= 0.0367$ or 3.67%

Hence the friction factor including uncertainty $f = 0.02247 \pm (8.24 \times 10^{-4})$

Similar procedure has been adopted for the calculation of all the parameters of 380 experimental runs. Table B.2 and Table B.3 show the range of uncertainty of the important parameters. The uncertainty in measurement of Nusselt number is the range of 2.18 to 6.32% and uncertainty of friction factor is varied from 3.44 to 5.97%. The values of uncertainty in Nusselt number and friction factor for all the data points are plotted in Figs. B.1 and B.2, respectively.

Table B.3 Range of uncertainty in the computed parameters for all the experimental data

S. No.	Parameters	Value	Range of uncertainty (%)
1	Air mass flow rate, m (kg/s)	0.0058-0.064	1.66-2.88
2	Mass velocity, G (kg/sm^2)	0.736-7.68	1.7-2.9
3	Reynolds number, Re	2000-20000	1.7-3.0
4	Useful heat gain, Qu (W)	83.5-649	2.0-6.0
5	Heat transfer coefficient, h (W/m^2K)	5.92-186.2	2.1-6.3
6	Nusselt number, Nu	9.5-319	2.18-6.31
7	Friction factor, f	0.008189-0.05785	3.4-5.97

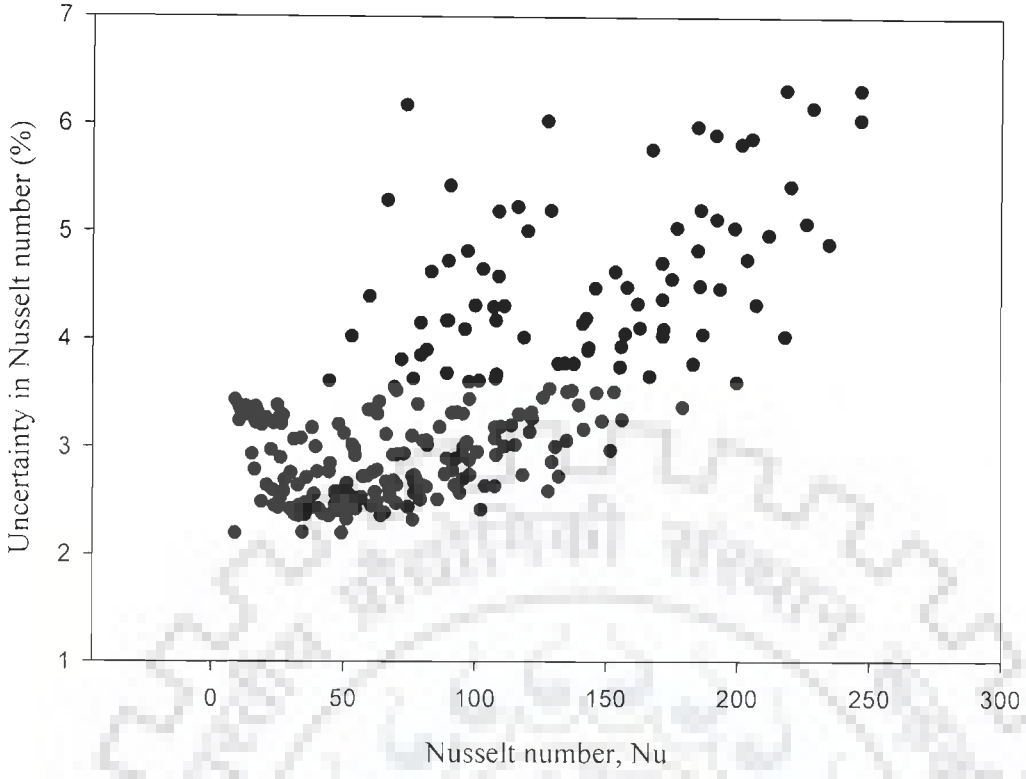

Fig.B.1 Percentage uncertainty in Nusselt number

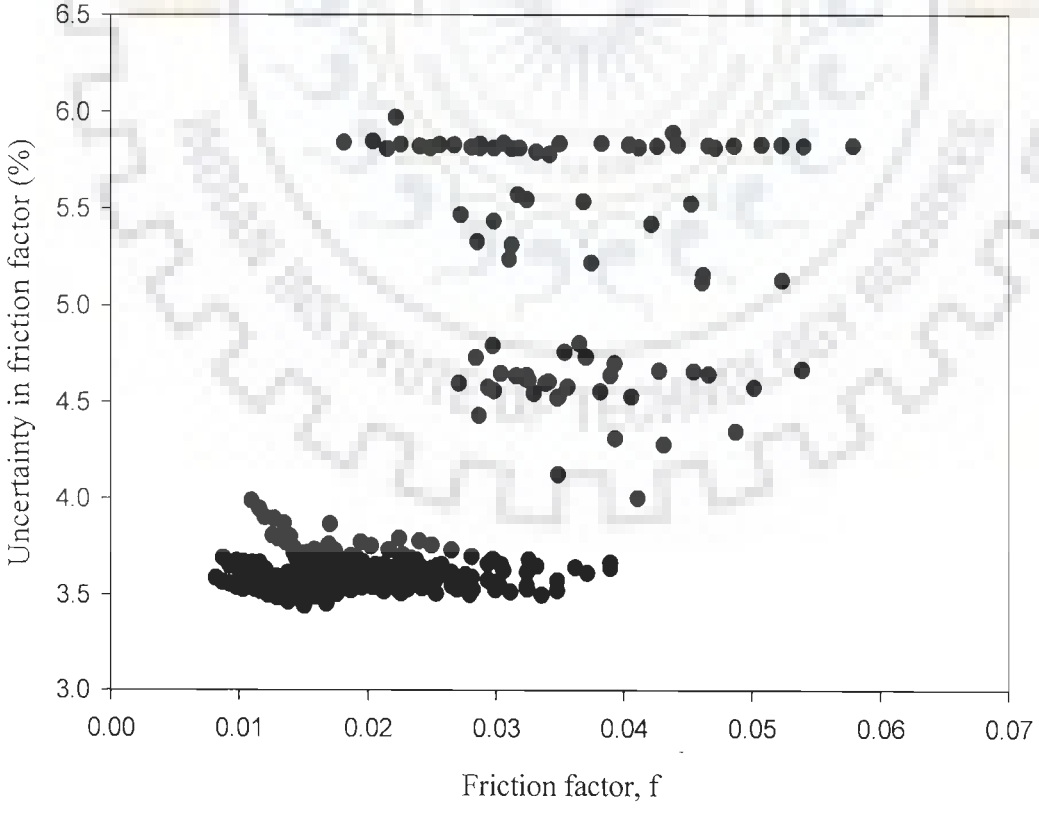

Fig.B.2 Percentage uncertainty in friction factor

REFERENCES

1. Sukhatme, S. P. and Nayak, J. K., Solar Energy, Principles of Thermal Collection and Storage, Tata McGraw-Hill Publishing Limited, New Delhi, 2009.

2. Duffie, J. A. and Beckman, W. A., Solar Engineering of Thermal processes, John Wiley and Sons, Inc. Publication, New York, 1991.

3. Aggarwal, M. K., Agarwal, R. S. and Sastry, Y. V. S. R., "Solid absorbents for solar powered refrigeration systems", Solar Energy, 34 (4/5), 423-426, 1985.

4. Al-Kharabsheh, S. and Goswami, D. Y., "Experimental study of an innovative solar water desalination system utilizing a passive vacuum technique", Solar Energy, 75, 395–401, 2003.

5. Bansal, N. K., "Solar energy and building architect", Proceedings of International Workshop on Energy Conservation in Buildings, CBRI, Roorkee, pp. 54-57, April 2-7, 1984.

6. Bansal, N. K. and Uhlemann, R., "Development and testing of low cost solar energy collectors for heating air", Solar Energy, 33, 197 -208, 1984.

7. Ettouney, H., "Brine entrainment in multistage flash desalination", Desalination, 182, 87–97, 2005.

8. Krishnamurthy, M. V. and Srinivasa Murthy, S., "Solar cooling systems: An overview, Active solar cooling systems", Proc. of Indo-Australian solar cooling Workshop, Madras, Published by James Cook University of NQ, Australia, pp. 2-39, 1984.

9. Sawhney, R. L., Sarsavadia, P. N. and Pangavhane, D. R., "Development of a multipurpose solar crop dryer", Proc. of National Solar Energy Convention, University of Roorkee, Roorkee, pp. 315 - 322, 1998.

10. Sawhney, R. L., and Sarsavadia, P. N., "A review on solar drying", Proc. of the 24th National Renewable Energy Convention, I.I.T. Bombay, pp. 482-485, 2000.

11. Suri, R. K., Chandra, S., Krishna Murthy, M. V., Hopmann, H., Berndorfer, K. and Wolf, D., "Development of small solar power plant for rural area in India", 'Sun', Proc. Int. Solar Energy Congress, New Delhi, India, Vol. 3, Ed F. De Winter and M. Cox, pp. 1722-1727, 1978.

12. Cooper, P., Boyd, D., Thring, J. B. and Maw, R. G., "The high lands, close group solar heating scheme", International Journal of Ambient Energy, 7, 197-206, 1986.

13. Cooper, P., "Group solar heating in U.K.", Solar 87, Annual conference of Australia and New Zealand Solar Energy Society, Nov. 26-28, 1987.

14. Mills, D. R., Bassett, I. M. and Derrick, G. H., "Relative cost effectiveness of CPC reflector designs suitable for evacuated absorber tube solar collectors", Solar Energy, 36, 199-206, 1986.

15. Mills, D. R. and Giutronich, J. E., "Ideal prism solar concentrators", Solar Energy, 21, 423-430, 1986.

16. Hsieh, J. S., "Solar Energy Engineering", Prentice Hall Inc., New Jersy, 1986.

17. Biondi, P., Cicala, L. and Farina, G., "Performance analysis of solar air heaters of conventional design", Solar Energy, 41, 101 – 107, 1988.

18. Reddy, T. A. and Gupta, C. L., "Generating application design data for solar air heating systems", Solar Energy, 25, 527- 530, 1980.

19. Whillier, A., "Black-painted solar air heaters of conventional design", Solar Energy, 8, 31-37, 1964.

20. Hottel, H. C. and Woertz, B. B., "The performance of flat plate solar heat collectors", Trans. ASME, 64, 91-104, 1942.

21. Klein, S. A., "Calculation of flat plate collector loss coefficients", Solar Energy, 17, 79-80, 1975.

22. Malhotra, A., Garg, H. P. and Patil, A., "Heat loss calculation of flat plate solar collectors", Journal of Thermal Engineering, 2, 59-62, 1981.

23. Garg, H. P. and Datta, G., "The top loss calculation for flat plate solar collectors", Solar Energy, 32, 141- 143, 1984.

24. Mullick, S. C. and Samdarshi, S. K., "An improved technique for computing the top heat loss factor of a flat plate collector with a single glazing", ASME/ Journal of Solar Energy Engineering, 110, 262-267, 1988.

25. Samdarshi, S. K. and Mullick, S. C., "Generalized analytical equation for top heat loss factor of a flat-plate solar collector with N glass covers", Trans. ASME Journal of Solar Energy Engineering, 116, 43-46, 1994.

26. Akhtar, N. and Mullick, S. C., "Approximate method for computation of glass cover temperature and top heat-loss coefficient of solar collectors with single glazing", Solar Energy, 66 (5), 349-354, 1999.

27. Hahne, I.E., "Parameter effects on design and performance of flat plate solar collectors, Solar Energy, 34 (6), 497-504, 1985.

28. Helmbold, W., "Independent house heating in temperature climate", Proc. Int. Workshop on Energy Conservation in Buildings, CBRI, Roorkee, 33-40, April 2-7, 1984.

29. Tabor, H., "Mirror boosters for solar collectors", Solar Energy, 10, 111-118, 1966.

30. Tabor, H., "Stationary mirror systems for solar collectors", Solar Energy, 2 (3-4), 27-33, 1958.

31. Patrick, N. E., "Performance analysis for collector side reflector system", Proc. Sun II, ISES, pp. 1208-1211, 1979.

32. Dang, A., "Collector, collector-reflector systems- an analytical and practical study", Energy Conversion and Management, 26 (1), 33-39, 1986.

33. Garg, H. P. and Harishikesan, D. S., "Enhancement of solar energy on flat-plate collectors by plane booster mirrors", Solar Energy, 40 (4), 295-307, 1988.

34. Kumar, R., Kaushik, S. C., and Garg, H. P., "Analytical study of collector solar-gain enhancement by multiple reflectors", Energy, 20 (6), 511-522, 1995.

35. Hussein, H. M. S., Ahmad, G. E., and Mohamad, M. A., "Optimization of operational and design parameters of plane reflector-tilted flat plate solar collector systems", Energy, 25 (6), 529-542, 2000.

36. Souka, A. F., "Double exposure flat plate collector", Solar Energy, 9 (3), 117-118, 1965.

37. Suri, R. K. and Saini, J. S., "Performance prediction of single and double exposure solar air heaters", Solar Energy, 12, 525-530, 1969.

38. Bhargava, A. K., Garg, H. P. and Sharma, V. K., "Theoretical analysis of some configurations of double exposure solar air heaters", Energy, 7 (4), 377-388, 1982.

39. Hollands, K. G. T., "Honeycomb devices in flat plate collectors", Solar Energy, 9 (3), 159-164, 1965.

40. Pellette, P., Cobble, M. and Smith, P., "Honeycomb thermal trap", Solar Energy, 12, 263-265, 1968.

41. Buchberg, H. and Edwards, D. K., "Design considerations for solar collectors with cylindrical honeycombs", Solar Energy, 18, 193-206, 1976.

42. Panos, K., Ehab S. and Farrinton, D., "Effect of artificial roughness on heat transfer and friction factor in a solar air heater", Solar Energy, 3, 19-23, 1959.

43. Herrick, C. S., "An air-cooled solar collector using all-cylindrical elements in a low-loss body", Solar Energy, 30 (3), 217-224, 1983.

44. Choudhury, C., Andersen, S. L. and Rekstad, J., "A solar air heater for low temperature applications", Solar Energy, 40, 335-343, 1988.

45. Gupta, C. L. and Garg H. P., "Performance studies on solar air heaters", Solar Energy, 11, 25-31, 1966.

46. Satcunanathan, S. and Deonarine, S., "A two pass solar air heater," Solar Energy, 15, 41- 49, 1973.

47. Wijeysundera, N. E., Ah, L. E. and Tjioe, L. E., "Thermal performance study of two pass solar air heaters," Solar Energy, 28, 363-370, 1982.

48. Persad, P. and Satcunanathan. S., "The thermal performance of the two-pass, two glass-cover solar air heater," ASME/Journal of Solar Energy Engineering, 105, 254 – 258, 1983.

49. Liu, Y. D, Diaz, L. A. and Suryanarayana, N. V., "Heat transfer enhancement in air heating flat plate solar collectors", ASME /Journal of Solar Energy Engineering, 106, 358-363, 1984.

50. Yeh, H. M., Ho, C. D. and Hou, J. Z., "Collector efficiency of double flow solar air heaters with fins attached", Energy, 27, 715-727, 2002.

51. Issacci, F., Zvirin, Y. and Grossman, G., "Heat transfer analysis of a finned solar air heater", ASME Journal of Solar Energy Engineering, 110, 145-155, 1988.

52. Pottler, K., Sippel, C. M., Beck and A., Fricke, J., "Optimized finned absorber geometries for solar air heating collectors", Solar Energy, 67, 35-52, 1999.

53. Selcuk, K., "Thermal and economic analysis of the overlapped-glass plate solar air heater", Solar Energy, 13, 165-191, 1971.

54. Kays, W. M. and London, A. L., "Compact Heat Exchangers," McGraw-Hill, New York, 1964.

55. Hamid, Y. H. and Beckman, W. A., "Performance of air-cooled radiatively heated screen matrices," Journal of Engineering Power, 93, 221–224, 1971.

56. Chiou, J. P., El-Wakil, M. M., and Duffie, J. A., "A slit and expanded aluminium foil matrix solar collector", Solar Energy, 9, 73-80, 1965.

57. Chiou, J. P. and El-Wakil, M. M., "Heat transfer and flow characteristics of porous matrices with radiations as heat source," Journal of Heat Transfer, 88, 69–76, 1966.

58. Öztürk, H. H. and Demirel, Y., "Exergy-based performance analysis of packed bed solar air heaters," International Journal of Energy Research, 28, 423–432, 2004.

59. Mittal, M. K. and Varshney, L., "Optimal thermo-hydraulic performance of a wire mesh packed bed solar air heater," Solar Energy, 80, 1112–1120, 2006.

60. Prasad, S. B., Saini, J. S. and Singh K. M., "Investigation of heat transfer and friction characteristics of packed bed solar air heater using wire mesh as packing material", Solar Energy, 83 (5), 773-783, 2009.

61. Saini, J. S., "Use of artificial Roughness for Enhancing Performance of solar air heater", Proceedings of XVII National and VI ISHME/ASME Heat and Mass Transfer Conference, IGCAR, Kalpakam (India), pp. 103-112, 2004.

62. Gupta, D., "Investigation on fluid flow and Heat Transfer in solar air heaters with roughened absorber", Ph.D. Thesis, University of Roorkee, Roorkee, India, 1993.

63. Gupta, D., Solanki, S. C. and Saini, J. S., "Thermo-hydraulic performance of solar air heaters with roughened absorber plates." Solar Energy, 61 (1), 33-42, 1997.

64. Jaurker A. R., Saini J. S. and Gandhi B. K., "Heat transfer coefficient and friction characteristics of rectangular solar air heater duct using rib-grooved artificial roughness", International Journal of Solar Energy, 80, 895-907, 2006.

65. Karwa, R., "Investigation of thermo-hydraulic performance of solar air heaters having artificially roughened absorber plate", Ph.D. Thesis University of Roorkee, Roorkee, 1997.

66. Karwa, R., Solanki, S. C. and Saini, J. S., "Heat transfer coefficient and friction factor correlation for the transitional flow regime in rib-roughened rectangular duct", International Journal of Heat and Mass Transfer, 42, 1597-1615, 1999.

67. Layek, A., Saini, J. S. and Solanki, S. C., "Heat transfer coefficient and friction characteristics of rectangular solar air heater duct using rib-grooved artificial roughness, International Journal of Heat and Mass Transfer, 50, 4845-4854, 2007.

68. Momin, A. M. E., "Thermo-hydraulic performance of solar collector using artificial roughness", Ph.D. Thesis, University of Roorkee, Roorkee, 1999.

69. Momin, A. M. E., Saini, J. S. and Solanki, S. C., "Heat transfer and friction in solar air heater duct with V-shaped rib roughness on absorber plate", International Journal of Heat and Mass Transfer, 45, 3383-3396, 2002.

70. Mulluwork, K. B., "Investigation on fluid flow and heat transfer in roughened absorber solar heaters", Ph.D. Thesis, University of Roorkee, Roorkee, 2000.

71. Mulluwork, K. B., Solanki, S. C. and Saini J. S., "Study of heat transfer and friction factor in solar air heaters roughened with staggered discrete ribs", Proceeding of 4th ISHMT-ASME and 15th National Conference on Heat and Mass Transfer, Pune, Jan.12-14, 2000.

72. Prasad, B. N. and Saini, J. S., "Effect of artificial roughness on heat transfer and friction factor in a solar air heater", Solar Energy, 41 (6), 555–560, 1988.

73. Prasad, B. N. and Saini, J. S., "Optimal thermo-hydraulic performance of artificially roughened solar air heaters", Solar Energy, 47 (2), 91-96, 1991

74. Saini, R. P., "Study of enhancement of energy collection rates of solar collectors using artificial roughness in the air duct", Ph.D. Thesis, University of Roorkee, Roorkee, 1996.

75. Saini, R. P. and Saini, J. S., "Heat transfer and friction factor correlations for artificially roughened ducts with expanded metal mesh as roughness element", International Journal of Heat and Mass Transfer, 40 (4), 973-986, 1997.

76. Aharwal, K. R., Gandhi B. K. and Saini J. S., "Experimental investigation on heat-transfer enhancement due to a gap in an inclined continuous rib arrangement in a rectangular duct of solar air heater", Renewable Energy, 33, 585-596, 2008.

77. Bhatti, M. S. and Shah, R. K., "Turbulent and Transition flow convective heat transfer in ducts," chapter 4, Hand book of single-phase convective heat Transfer, Editors Kakac S, Shah R. K., Aung W., John Willey & sons, New York, 1987.

78. Taslim, M. E. and Spring, S. D., "Measurement of heat transfer coefficients and friction factors in rib-roughened channels simulating leading-edge cavities of a modern turbine blades", ASME Journal of Turbomachinery, 119, 411-419, 1997.

79. Taslim, M. E., Li. T. and Krecher, D. M., "Experimental heat transfer and friction in channels roughened with angled, v-shaped and discrete ribs on two opposite walls", Trans. ASME, Journal of Turbomachinery, 118, 20-28, 1996.

80. Sparrow E. M. and Hossfeld L. M., "Effect of rounding of protruding edges on heat transfer and pressure drop in a duct", International Journal of Heat and Mass Transfer, 27, 1715-1723, 1984.

81. Nikuradse, J., "Law of flow in rough pipes", National Advisory Committee for Aeronautics, Technical Memorandum 1292, 1950.

82. Kadar, B. A., and Yaglom, A. M., "Heat and mass transfer laws for fully turbulent wall flow", International Journal of Heat and Mass Transfer, 15, 2329-2351, 1972.

83. Dipprey, D. P. and Sabersky, R. H., "Heat & momentum transfer in smooth and rough tubes at various Prandtl numbers", International Journal of Heat and Mass Transfer, 6, 329-353, 1963.

84. Webb, R. L., Eckert, E. R. G. and Goldstein, R. J., "Heat transfer and friction in tubes with repeated rib roughness", International Journal of Heat and Mass Transfer, 14, 601-617, 1971.

85. Webb, R. L. and Eckert, E. R. G., "Application of rough surface to heat exchanger design", International Journal of Heat and Mass Transfer, 15, 1647-1658, 1972.

86. Dalle D. M. and Meyer, L., "Turbulent convective heat transfer from rough surface with two- dimensional rectangular ribs", International Journal of Heat and Mass Transfer, 20, 583 - 620, 1977.

87. Webb, R. L., Eckert, E. R. G. and Goldstein, R. J., "Generalized heat transfer friction correlations for tubes with repeated rib roughness", International Journal of Heat Mass Transfer, 15, 80-184, 1971.

88. Han, J. C. and Park, J. S., "Developing heat transfer in a rectangular channel with rib turbulators", International Journal of Heat Mass Transfer, 31,183-195, 1988.

89. Han J. C. "Heat transfer and friction in channels with two opposite rib roughened walls", Trans. ASME Journal of Heat Transfer, 106, 774-781, 1984.

90. Han, J. C., Glicksman, L. R. and Rosenow, W. M. "An investigation of heat transfer and friction for rib-roughened surfaces", International Journal of Heat & Mass Transfer, 21, 1143-1156, 1978.

91. Han, J. C., Zhang, Y. M. and Lee, C. P., "Influence of surface heat flux ratio on heat transfer augmentation in square channels with parallel, crossed and v-shaped angled ribs", Journal of Turbomachinery, 114, 872-880, 1992.

92. Han, J. C., Park, J. S. and Lei, C. K., "Augmented heat transfer in rectangular channel of narrow aspect ratios with rib turbulators", International Journal of Heat and Mass Transfer, 32 (9), 1619-1630, 1989.

93. Han, J. C., Ou, S., Park, J. S. and Lei, C. K., "Augmented heat transfer in rectangular channels of narrow aspect ratios with rib turbulators," International Journal of Heat Mass Transfer, 32, 1619-1630, 1989.

94. Han, J. C. and Zhang, Y. M., "High performance heat transfer ducts with parallel, broken V- shaped broken ribs", International Journal of Heat and Mass Transfer, 35 (2), 513-523, 1992.

95. Kukreja, R. T., Lau, S. C. and McMillin, R. D., "Local heat/ mass transfer distribution in a square channel with full V- shaped ribs", International Journal of Heat and Mass Transfer, 36, 2013-2020, 1993.

96. Liou T. M. and Hwang, J. J., "Turbulent heat transfer augmentation friction in periodic fully developed channel flows", Trans. Journal of Heat Transfer, 114, 56-64, 1993.

97. Liou, T. M. and Hwang, J. J., "Effect of ridge shapes on turbulent heat transfer friction in a rectangular channel", International Journal of Heat and Mass Transfer, 36, 931-940, 1993.

98. Kiml, R., Mochizuki, S., Murita A. and Stoica, V., "Effect of rib-induced secondary flow on heat transfer augmentation inside a circular tube", Journal of Enhanced Heat Transfer, 10 (1), 9-19, 2003.

99. Chandra, P. R., Alexer, C. R., and Han, J.C., "Heat transfer and friction behavior in rectangular channels with varying number of ribbed walls", International Journal of Heat and Mass Transfer, 46, 481-495, 2003.

100. Lau, S. C., Kukreja, R. T. and McMillin, R. D., "Effect of V shaped rib arrays on turbulent and heat transfer and friction of fully developed flow in a square channel", International Journal of Heat and Mass Transfer, 34 (7), 1605-1616, 1991.

101. Gao X. and Sudden B., "Heat transfer and pressure drop measurements in rib-roughened rectangular ducts", Experimental Thermal and Fluid Science, 24, 25-34, 2001.

102. Tanda, G., "Heat transfer in rectangular channels with transverse V-shaped broken ribs", International Journal of Heat and Mass Transfer, 47, 229 - 243, 2004.

103. Wright, L. M., Fu Wen-Lung and Han, J.C. "Thermal performance of angled V-shaped and W-shaped rib turbulators in rotating rectangular cooling channels", Trans. ASME Journal of Heat Transfer, 126, 604 - 614, 2004.

104. Gao X. and Sudden B., "Effect of inclination angle of ribs on the flow behavior in rectangular ducts", Trans. ASME Journal of Fluids Engineering, 126, 692-699, 2004.

105. Bonhoff, B., Parneix, S., Leusch, J., Johnson, B.V., Schabacker, J. and Boles, A., "Experimental and numerical study of developed flow and heat transfer in coolants with channels with 45 degree ribs", International Journal of Heat and fluid flow, 20, 311-319, 1999.

106. Gao X. and Sudden B., "PIV measurement of flow field in rectangular ducts with 60° parallel, crossed and V-shaped ribs", Experimental Thermal and Fluid Science, 28, 369-653, 2004.

107. Lau, S. C., McMillin, R. D. and Han, J. C., "Heat transfer characteristics of turbulent flow in a square channel with angled rib", Trans. ASME Journal of Turbo-machinery, 113, 367-374, 1991.

108. Lau, S. C., McMillin, R. D. and Han, J. C., "Turbulent heat transfer and friction in a square channel with discrete rib tabulators", Trans. ASME Journal of Heat Transfer, 113, 360 - 366, 1991.

109. Wang L. and Sudden B., "An experimental investigation of heat transfer and fluid flow in a rectangular ducts with broken V-shaped ribs", Experimental Heat Transfer, 17, 243-259, 2004.

110. Chyu V. and Natrajan V., "Effect of slit in a rib on the heat transfer from a rib-mounted wall", Trans. ASME Journal of Heat transfer, 115, 792-796, 1993.

111. Cho, H. H., Kim, Y. Y., Rhee, D. H., Lee, S. Y., Wu, S. J. and Choi, C, "The effect of gap position in discrete ribs on local heat/ mass transfer in a square duct", Journal of Enhanced Heat Transfer, 10 (3), 287-300, 2003.

112. Cho, H. H., Wu, S. J. and Kwon, H. J., "Local heat/ mass transfer measurements in a rectangular duct with discrete ribs", Journal of Turbo-machinery, 122 (3), 579 - 586, 2000.

113. Olsson, C. O. and Sunden, B., "Thermal hydraulic performance of a rectangular duct with multiple v-shaped ribs", Journal of Heat Transfer, 120, 1072-1077, 1998.

114. Aliaga, D. A., Lamb, J. P. and Klein, D. E., "Convection heat transfer distributions over plates with square ribs from infrared thermography

measurements", International Journal of Heat And Mass Transfer, 17, 363-374, 1994.

115. Khanna, S. K. and Kant, K., "Forced convection heat transfer and pressure drop for air flowing throughn an enhanced tube", Proc. First ISHMT-ASME, Bhabha Atomic Research Centre, Bombay, 231-235, January 5-7, 1984.

116. Wu, L. and Cooper, P., "Heat transfer and pressure drop in an artificially roughened rectangular duct", 4th International Symposium on Transport Phenomenon in Heat and Mass Transfer, Sydney, 1-9, July 1991.

117. Hosni, M. H and Coleman, H. W., "Roughness element shape effects on heat transfer and skin friction in rough wall turbulent boundary layers", International Journal of Heat Mass Transfer, 36, 147-153, 1993.

118. Hsieh, S. S. and Hong, Y. J., "Separating flow over repeated surface mounted ribs in a square duct", AIAA Journal, 27, 770-776, 1989.

119. Kim, K.Y. and Kim, S. S., "Shape optimization of rib roughened surface to enhance turbulent heat transfer," International Journal of Heat Mass Transfer, 45, 2719 - 2727, 2002.

120. Prasad, K. and Mullick, S. C., "Heat transfer characteristics of a solar air heater used for drying purposes", Applied Energy, 13, 83-93, 1985.

121. Verma, S. K. and Prasad, B. N., "Investigation for the optimal Thermohydraulic performance of artificially roughened solar air heaters", Renewable Energy, 20, 9-36, 2000.

122. Karwa, R. K., "Experimental studies of augmented heat transfer and friction in asymmetrically heated rectangular ducts with ribs on heated wall in transverse, inclined, v-continuous and v-discrete pattern", International Comm. Heat Mass Transfer, 30 (2), 241-250, 2003.

123. Sahu, M. M. and Bhagoria, J. L., "Augmentation of heat transfer coefficient by using 90° broken transverse ribs on absorber plate of solar air heater", Renewable Energy, 30, 2057-2063, 2005.

124. Karwa, R., Bairwa, R. D., Jain, B. P. and Karwa, N., "Experimental study of the effects of rib angle and discretization on heat transfer and friction in an asymmetrically heated rectangular duct", Journal of Enhanced Heat Transfer, 12 (4), 343-355, 2005.

125. Bhagoria, J. L., Saini, J. S. and Solanki, S. C., "Heat transfer coefficient and friction factor correlation for rectangular solar air heater duct having transverse wedge shaped rib roughness on absorber plate," Renewable Energy, 25, 341-369, 2002.

126. Saini, S. K. and Saini, R. P., "Development of correlations for Nusselt number and friction factor for solar air heater with roughened duct having arc-shaped wire as artificial roughness", Solar Energy, 83 (12), 1118-1130, 2008.

127. Saini, R. P. and Verma, J., "Heat transfer and friction factor correlations for a duct having dimple-shaped artificial roughness for solar air heaters", Energy, 33 (8), 1277-1287, 2008.

128. Karmare, S. V. and Tikekar, A. N. "Heat transfer and friction factor correlation for artificially roughened duct with metal grit ribs", International Journal of Heat and Mass transfer, 50, 4342-4351, 2007.

129. Kumar, A. and Bhagoria, J. L., "Heat transfer and friction factor correlations for artificially roughened solar air heater duct with discrete W-shaped ribs", Energy Conversion and Management, 50 (8), 2106-2117, 2009.

130. Varun, Saini, R. P. and Singal, S. K., "Investigation of thermal performance of solar air heater having roughness elements as a combination on inclined and

transverse ribs on absorber plate", Renewable Energy, 33 (6), 1398-1405, 2008.

131. Bopche, S. B. and Tandale, M. S., Experimental investigations on heat transfer and friction characteristics of a turbulator roughened solar air heater" International Journal of Heat and Mass Transfer, (2009), doi:10.1016/j.ijheatmasstransfer.2008.09.039

132. Chaube, A., Sahoo, P. K. and Solanki, S. C., "Analysis of heat transfer augmentation and flow characteristics of a solar air heater", Renewable Energy, 31, 317-331, 2006.

133. Sharadkumar, "CFD based heat transfer analysis of artificially roughened solar air heater", M.Tech Dissertation, AHEC, IIT Roorkee, June 2008.

134. Sherrif, N and Gumley, P., "Heat transfer and friction properties of surfaces with discrete roughness", International Journal of Heat Mass Transfer, 9, 1297-1320, 1966.

135. Kovarik, M. and Lesse, P. F., "Improvement of the efficiency of a bare solar collector by means of turbulence promoters", Applied Energy, 36, 253-256, 1990.

136. Winn, C. B. and Hull, D. E., "Optimal controller of the second kind", Solar Energy, 23, 529-534, 1979.

137. Lewis, M. J., "Optimizing the thermohydraulic performance of rough surfaces", International Journal of Heat and Mass Transfer, 18, 1243-1248, 1975.

138. Williams, F., Pirie, M. A. M. and Warburton, C., "Heat transfer from surfaces roughened by ribs", ASME/Augmentation of Heat Transfer, New York, pp. 36-43, 1970.

139. Cortes, A. and Piacentini, R., "Improvement of the Efficiency of a Bare Solar Collector by Means of Turbulence Promoters", Applied Energy, 36, 253-261, 1990.

140. Fujiwara, M., "Exergy analysis for the performance of solar collectors", Journal of Solar Engineering, 105, 163-167, 1983.

141. Suzuki, A., "A fundamental equation for exergy balance on solar collectors", Journal of Solar Engineering, 110, 102-106, 1988.

142. Said, S. A. M. and Zubair, S. M., "On second-law efficiency of solar collectors", Journal of Solar Engineering, 115, 2-4, 1993.

143. Kurtbas, I. and Durmus, A., "Efficiency and exergy analysis of a new solar air heater", Renewable Energy, 29, 1489-1501, 2004.

144. Naphon, P., "On the performance and entropy generation of the double-pass solar air heater with longitudinal fins", Renewable Energy, 30, 1345-1357, 2005.

145. Ucar, A. and Inalli, M., "Thermal and exergy analysis of solar air collectors with passive augmentation techniques", International Comm. in Heat and Mass Transfer, 33, 1281-1290, 2006.

146. Gupta, M. K. and Kaushik, S. C., " Performance evaluation of solar air heater for various artificial roughness geometries based on energy, effective and exergy efficiencies", 34 (3), 465-476, 2009.

147. Altfeld, K., Leiner, K. A. and Fiebig, M., "Second law optimization of flat-plate solar air heaters, part I: The concept of net exergy flow and the modeling of solar air heaters," Solar Energy, 41, 127–32, 1988.

148. Bejan, A., Advanced Engineering Thermodynamics, Wiley–Interscience Publication, New-York, 1988.

149. Jaurker, A. R., "Heat and fluid flow characteristics of rib-groove artificially roughened solar air heaters", Ph.D. Thesis, Indian Institute of Technology, Roorkee, 2005.

150. Layek, A., Saini, J. S. and Solanki, S. C., "Second law optimization of a solar air heater having chamfered rib-groove roughness on absorber plate, Renewable Energy, 32, 1976-1980, 2007.

151. ASHARE Standard 93–97, "Method of Testing to Determine the Thermal Performance of Solar Collector," 1977.

152. Benedict, R. P., Fundamentals of Temperature Pressure and Flow Measurements, Third edition, Wiley-Interscience Publication, New-York, 1984.

153. Technical manual of "Dry block calibrator" (Presys Instruments T-25), 2004.

154. Moore, B. M., Theory and Application of Mechanical Engineering Measurements, Affiliated East-West Press Pvt. Limited, New Delhi, 1969.

155. Ehlinger, A. H., Flow of Air and Gases, Kent's Mechanical Engineering Handbook, John Wiley Publication, New-York, pp. 1.10 -1.20, 1950.

156. Rosenhow, W. M. and Hartnett, J. P., Hand Book of Heat Transfer, McGraw Hill, New York, pp. 7- 122, 1973.

157. Kline, S. J. and McClintock, F. P., "Describing uncertainties in single-sample experiments", Mech. Engg., 75, 3-8, 1953.

158. Ravigururajan, T. S. and Bergles, A. E., "Development and verification of general correlations for pressure drop and heat transfer in single-phase

turbulent flow in enhanced tubes", Experimental Thermal and Fluid Science, 13, 55-70, 1996.

159. Bergles, A. E., "Some perspectives on enhanced heat transfer second-generation heat transfer technology", Trans. of ASME, Journal of Heat Transfer, 110, 1082-1096, 1988.

160. Manfrida, G., "The choice of an optimal working point for solar collectors", Solar Energy, 34 (6), 513-515, 1985.

161. Colemann, H. W. and Steele, W. G., "Experimentation and uncertainty analysis for engineers", A Wiley Inter-science publication, John Wiley and sons, 1989.

PUBLICATIONS FROM THIS WORK

Journal Publications

1. Hans, V. S., Saini, R. P. and Saini, J. S., "Performance of artificially roughened solar air heaters-A review", Renewable and Sustainable Energy Reviews, 13 (8), 1854-1869, 2009.

2. Hans, Vishavjeet Singh, Saini, R. P. and Saini, J. S., "Heat transfer and friction factor correlations for a solar air heater duct roughened artificially with multiple v-ribs". Accepted for publication in Solar Energy.

Conference Publications

1. Hans, V. S., Saini, R. P. and Saini, J. S., "Experimental investigation of heat transfer and friction characteristics of a multiple v-rib roughened solar air heater", 20th National and 9th ISHMT-ASME Heat and Mass Transfer conference, IIT, Bombay, January 4-6, 2010, Accepted for publication.

2. Hans, V. S., Saini, R. P. and Saini, J. S., "Thermal performance of multiple v-rib roughened solar air heater". ICEM 2009, IT-BHU, December 18-20, 2009, Accepted for publication.

3. Hans, V. S., Saini, R. P. and Saini, J. S., "Thermohydraulic performance of artificially roughened solar air heaters". International Conference on Energy Engineering, ICEE 2009, PEC, Pondicherry, Paper No. EEM 2312, January 7-9, 2009.

4. Hans, V. S., Saini, R. P. and Saini, J. S., "Experimental investigation of thermal performance of a solar air heater roughened with multiple v-ribs"

International Conference on Advances in Mechanical Engineering, ICAME 2009, SVNIT Surat, pp. 153-158, December 15-17, 2008.

5. Hans, V. S., Saini, R. P. and Saini, J. S., "Performance evaluation of artificially roughened channels with different v-shaped ribs". 19th National and 8th ISHMT-ASME Heat and Mass Transfer conference, JNTU Hyderabad, Paper No. HTE-13, January 3-5, 2008.

6. Hans, Vishavjeet Singh, Saini, R. P. and Saini, J. S., "Heat transfer and friction factor in artificially roughened rectangular ducts for solar energy applications-A review". International Conference on Advances in Energy Research, ICAER 2007, IIT Bombay, pp. 135-142, December 12-14, 2007.

7. Hans, Vishavjeet Singh, Saini, R. P. and Saini, J. S., "Heat transfer enhancement techniques- A Saviour of energy in solar air heaters". National conference on energy: The future scenario, March 10 -11, 2007.